A CFD methodology for mass transfer of soluble species in incompressible two-phase flows: modelling and applications

by

Gabriele Gennari

Thesis Supervisors	Dr. Richard Jefferson-Loveday
	Prof. Stephen J. Pickering

The Gas Turbine and Transmissions Research Centre

Department of Mechanical, Materials and Manufacturing Engineering

The University of Nottingham

Thesis submitted to the University of Nottingham for the degree of Doctor of Philosophy

January 2023

To my family

God made the bulk; the surface was invented by the devil.

Wolfgang Ernst Pauli

Acknowledgments

First of all, I would like to thank my supervisors, Dr. Richard Jefferson-Loveday and Prof. Steve J. Pickering, who gave me the opportunity to work on this PhD project. Their support and invaluable help throughout the past three years have been fundamental for the development of my research skills and the analytical mindset that are necessary to tackle scientific problems. I would further like to thank my internal reviewer, Dr. Donald Giddings, for his feedback during the annual reviews, which has influenced the way this thesis is written, and Dr. Mirco Magnini for the fruitful discussions on numerical modelling of multiphase flows.

This project was funded through the EPSRC grant EP/P013341/1 and most of the simulations were run on the supercomputer of the University of Nottingham and the HPC centre Sulis (EPSRC grant EP/T022108/1). I would like to thank all the people involved in such projects, who made this work possible.

All the simulations performed in this thesis were run with the open source solver Basilisk and I am very grateful to the developers and user community for the great support they have provided and for freely sharing their code. Without their help, most of the code development carried out in this project would not have been possible.

I would also like to thank all my friends who have supported me throughout these challenging years of research. Thanks Luc, William, Benedikt, Ryan, Zak, Rajab, Neville, Dennis, Kuldeep and Sandeep for the many interesting discussions and coffee breaks, but, most importantly, for making the G2TRC such a friendly lab to work in. A Special thanks goes to my friends from Italy (Santiago, Dody, Lorenzo, Duccio and Luca) for being so close despite the distance between us and, of course, for the many online meetings during the pandemic!

Finally, I am grateful to my family for their love and support and to my partner, Diana, for all of her love, patience and for always encouraging me throughout this journey: I would not be here (literally!) without you.

Abstract

Continuous flow chemistry is an interesting technology that allows to overcome many of the limitations in terms of scalability of classical batch reactor designs. This approach is particularly relevant for both photochemistry and electrochemistry as new optimal solutions can be designed to limit, for example, the issues related to light penetration, reactor fouling, excessive distance between electrodes and management of hazardous compounds, whilst keeping the productivity high. Such devices operate often in a two-phase regime, where the appearance of a gas in the form of a disperse bubbly flow can be either a desirable feature (e.g. when the gas is needed for the reaction) or the result of a spontaneous reaction (e.g. electrochemistry). Such systems are very complicated flows where many bubbles populate the reactor at the same time and deform under the effect of several forces, such as surface tension, buoyancy and pressure and viscosity terms. Due to the solubility of gas in the liquid solvent, the disperse phase exchanges mass with the liquid (where the reactions generally occur) and the volume of the bubbles changes accordingly. Such physics is mainly a convection-dominated process that occurs at very small length scales (within the concentration boundary layer, which is generally thinner than the hydrodynamic one) and numerical tools for routine design are based on simplifying assumptions (reduced order methods) for the modelling of this region. However, such approaches often lead to errors in the prediction of the mass transfer rate and a fully-resolved method is generally needed to capture the physics at the interface. This last approach comes with a high computational cost (which makes it non suitable for common design processes) but can be employed in simplified scenarios to explore fundamental physics and derive correlation formulae to be used in reduced order models.

For the above reasons, this work aims at developing a high-fidelity numerical simulation framework for the study of mass transfer of soluble species in two-phase systems. The numerical modelling of these processes has several challenges, such as the small characteristic spatial scales and the discontinuities in both concentration and velocity profiles at the interface. All these points need to be properly taken into account to obtain an accurate solution at the gas-liquid interface. In this thesis, a new methodology, based on a two scalar approach for the transport of species, is combined with a geometric Volume of Fluid method in the open source software Basilisk (http://basilisk.fr/). A new algorithm is proposed for the treatment of the interfacial velocity jump, which consists of the redistribution of the mass transfer term from the interfacial cells to the neighbouring pure gas ones, in order to ensure the conservation of mass during the advection of the interface. This step is a crucial point of the methodology, since it allows to accurately describe the velocity field near the interface and, consequently, to capture the distribution of species within the concentration boundary layer.

The solver is extensively validated against analytical, experimental and numerical benchmarks, which include suspended bubbles in both super- and under-saturated solutions, the Stefan problem for a planar interface, dissolving rising bubbles and competing mass transfer of mixtures in mixed super- and under-saturated liquids.

Finally, the methodology is used for the study of real applications, namely the growth of electrochemically generated bubbles on a planar electrode and the mass transfer of a single bubble in a Taylor-Couette device. The effects of the main parameters that characterise the systems (e.g. contact angle, current density and rotor speed) on the growth/dissolution rate of bubbles are investigated. Although these systems need to be necessarily simplified to allow for direct numerical simulations, these examples show that the insight gained into the fundamental physics is valuable information that can be used to develop reduced order models.

Contents

Acknowledgments **iv**

Abstract **vi**

List of Tables **xiii**

List of Figures **xxv**

Nomenclature **xxxiii**

1 Introduction **1**

1.1 The Photo-Electro project: background and motivation of the present work 1

1.2 Objectives and contributions 6

1.3 Thesis outline 10

2 Literature Review **12**

2.1 Rising bubbles in a quiescent liquid: hydrodynamics 13

2.1.1 Non-dimensional groups 14

2.1.2 Terminal velocity 16

2.1.3 Shape, break-up and path instability 24

2.2 Bubbles in shear flows: Couette and Taylor-Couette 36

2.2.1 Bubble deformation and breakup in a Couette flow 37

2.2.2 Taylor-Couette flow: patterns and interaction with bubbles . . 47

2.3 Mass transfer of soluble species 66
2.3.1 Physisorption: a diffusion-driven process 67
2.3.2 Two film theory 74
2.3.3 Numerical methods for fully resolved simulations 80

3 Governing equations of two-phase incompressible flows 95
3.1 Two-phase Navier-Stokes equations 96
3.2 One-fluid formulation 99
3.2.1 Overview of the governing equations 102
3.3 Soluble species in two-phase flows 103
3.3.1 Overview of the transport of species 108

4 The BASILISK code 110
4.1 The grid structure 111
4.2 The Volume of Fluid method 115
4.2.1 Reconstruction step 117
4.2.2 Advection step 121
4.3 The Navier-Stokes solver 124
4.4 Overview of the time step integration 130

5 The phase-change model 134
5.1 The VOF method with phase-change 135
5.2 The velocity extension algorithm: a novel approach 137
5.3 Species transport: the two-scalar method 142
5.3.1 Species advection 145
5.3.2 Species diffusion 148
5.4 Mass transfer scheme 150
5.5 Overview of the phase-change model 153

6 Validation of the numerical framework 155
6.1 Non-dimensional groups 156

6.2 Pure species . . . 158
6.2.1 Bubbles with fixed mass transfer rates . . . 160
6.2.2 The Stefan problem . . . 164
6.2.3 Suspended bubbles . . . 171
6.2.4 Rising bubbles . . . 183
6.3 Mixtures . . . 195
6.3.1 Competing mass transfer in an infinite cylinder . . . 197
6.3.2 Competing mass transfer in a rising bubble . . . 208

7 Applications 219
7.1 Growing bubbles on planar electrodes . . . 219
7.2 Mass transfer in two-phase Taylor-Couette reactors . . . 230
7.2.1 Available approaches for quantifying mass transfer in chemical reactors . . . 232
7.2.2 Single-phase Taylor-Couette flow . . . 239
7.2.3 Mass transfer of a bubble in a Taylor-Couette reactor . . . 256

8 Conclusions and Future Work 276

A Spatial grid convergence 283

B A note on the consistency between the transport of volume fraction and momentum 287

Bibliography 290

Publications 314

List of Tables

2.1 Comparison between the terminal and critical Reynolds numbers for some of the bubbles studied in Cano-Lozano et al., 2016. For the cases where Re approaches an oscillating behaviour, the corresponding average value is assumed as terminal Re. Some of the bubbles reported here are in a regime very close to the critical one. It is reported that the Reynolds number drops when the instability occurs (see text). Therefore, at the onset of the instability, the difference between Re and Re_{cr} is larger than what is shown in this table. 29

6.1 Threshold values of the selected fields for the adaptive mesh refinement algorithm (see criterion 4.6). The value for c_d is reported here for the reader's convenience, but is used in section 6.3 only, where mixtures of species are modelled. The solid volume fraction field refers to the modelling of complex geometries via immersed boundaries (see section 7.2.2). Values of ξ are non-dimensional, consistently with the following simulations. 159

6.2 Gas-liquid properties for the bubble with fixed mass transfer rates. . . 160

6.3 Reference dimensions for the bubble with fixed mass transfer rates. . 160

6.4 List of cases for the bubble with fixed mass transfer rates. 161

6.5 Gas-liquid properties for the Stefan problem. 165

6.6 Reference dimensions for the Stefan problem. 166

6.7 List of cases for the grid convergence analysis of the Stefan problem. . 168

6.8 Gas-liquid properties for the suspended bubbles. 172

6.9 Reference dimensions for the suspended bubble cases. 172
6.10 Growth factors (β) and times ($\bar{t}$) to reach the bubble size $R_b^{t=\bar{t}} = 0.005\,\mathrm{m}$ for different super-saturation levels. 174
6.11 List of cases for the grid convergence analysis of the Scriven problem with $\zeta = 2$. 174
6.12 List of cases for the Scriven problem with different saturation levels. . 176
6.13 List of cases for the Epstein-Plesset model. 180
6.14 Gas-liquid properties for rising bubbles at different Péclet numbers. . 184
6.15 Reference dimensions for rising bubbles at different Péclet numbers. . 185
6.16 List of cases for rising bubbles at different Péclet numbers. 185
6.17 Grid refinements and concentration boundary layer thicknesses for rising bubbles at different Péclet numbers. 189
6.18 Gas-liquid properties for a rising bubble in a creeping flow. 189
6.19 Numerical setup for a rising bubble in a creeping flow. 191
6.20 Reference dimensions for a rising bubble in a creeping flow. 192
6.21 Gas-liquid properties for competing mass transfer in an infinite cylinder. 198
6.22 Numerical setup for a cylinder of gas expanding in an infinite liquid annulus. 201
6.23 Reference dimensions for a cylinder of gas expanding in an infinite liquid annulus. 201
6.24 Numerical setup for a cylinder of gas confined by a liquid annulus. . . 205
6.25 Gas-liquid properties for the competing mass transfer in a rising bubble. 208
6.26 Gas-liquid properties for the competing mass transfer in a rising bubble. 208
6.27 Reference dimensions for the competing mass transfer in a rising bubble. 210
6.28 Grid convergence study for the competing mass transfer in a rising bubble. The concentrations in both phases refer to the initial ($t = 0$) chemical composition. 210

7.1 Gas-liquid properties for a rising bubble in a creeping flow. 221
7.2 Numerical setup for growing bubbles on planar electrodes. 225
7.3 Single-phase Taylor-Couette cases. 240

7.4 Mesh sensitivity study for the configuration $\eta = 0.5$ and $Re = 5000$. N_z, N_r, N_θ are the number of cells along the axial, radial and azimuthal directions, respectively. The superscripts N^{b}, N^{in}, N^{out} refer to the bulk, inner and outer regions within the domain (see Figure 7.6). 241
7.5 Mesh characteristics in terms of wall units and number of cells in the viscous sublayer for the configuration $\eta = 0.5$, $Re = 5000$. 243
7.6 Selected mesh characteristics for the single-phase Taylor-Couette cases. 244
7.7 Gas-liquid properties for a dissolving bubble in a TCR. 257
7.8 List of cases for the grid convergence analysis of a dissolving bubble in a TCR with no rotation. 259
7.9 List of cases for the study of a dissolving bubble in a TCR at different rotating speeds and gravitational accelerations. 261

List of Figures

1.1 Sketches of the cross-section (not to scale) of the Taylor-Couette reactors for photochemistry developed within the Photo-Electro project. The design on the left automatically takes the air from the laboratory, whilst the solution on the right uses apposite ducts for the supply of oxygen. Some details are omitted. Figures adapted from Lee et al., 2017 (a) and Lee et al., 2020 (b). 4

1.2 Hierarchy of numerical approaches for multiphase simulations. Fully-resolved interfacial simulations (a - with Front Tracking in this example) are used to model small scales, Eulerian-Lagrangian (b) methods for intermediate scales and Euler-Euler (c) simulations for full size systems. Figure taken from Roghair et al., 2011. 8

2.1 Comparison between experiments (from Clift et al., 1978) and correlation models from Tomiyama et al., 1998 and Clift et al., 1978 for the terminal velocity of rising bubbles in a quiescent liquid. The curves from Tomiyama et al., 1998 for pure and contaminated systems correspond to equation 2.20 and 2.22, respectively. 22

2.2 Bubble deformation and breakup. Figures from Gumulya et al., 2016 (a - c) and Tripathi et al., 2015 (d - e). 25

2.3 Regions in the Bo - Ga plane. The continuous lines are taken from the work of Tripathi et al., 2015, whilst the dashed line corresponds to the onset of the path instability reported in Cano-Lozano et al., 2013. The red curve is the iso-Mo line with $Mo = 10^{-3}$. Figure adapted from Tripathi et al., 2015. (Note that in the work of Tripathi et al., 2015, Ga and Bo are computed with the bubble radius instead of the diameter. Data have been opportunely scaled here.) 27

2.4 Different trajectories from Cano-Lozano et al., 2016. The dash line represents the onset of path instability reported in the work of Cano-Lozano et al., 2013. A good quantitative match is observed since (almost) all the non-rectilinear trajectories are above the suitability line. Figure adapted from Cano-Lozano et al., 2016. 28

2.5 The black lines represent the stability curves for the onset of the wake instability: continuous (Cano-Lozano et al., 2013), dashed (Zenit and Magnaudet, 2008) and dot-dashed (Magnaudet and Mougin, 2007). The red plots are the standing eddy curves: continuous (Cano-Lozano et al., 2013) and dashed (Blanco and Magnaudet, 1995). Figure adapted from Cano-Lozano et al., 2013. 32

2.6 Wake structure (iso-contours of streamwise vorticity) for the planar zigzag (a) and spiraling (b) regimes. Bubbles rise horizontally from left to right. Figure adapted from Cano-Lozano et al., 2016. 34

2.7 Droplet/bubble parameters for the low deformation regime (ellipsoidal) in a Couette flow. 38

2.8 Main geometrical parameters of the parallel band (a) and cylindrical Couette (b) apparatus. The velocity profile in the cylindrical device has been approximated to a linear law. 39

2.9 Sigmoidal bubble shape from the experiments of Müller-Fischer et al., 2008 in the parallel band apparatus, with: $\mu_r = 1.292 \times 10^{-7}$, $Ca = 5.35$ and $E = 0.8$. Figure taken from Müller-Fischer et al., 2008. 40

2.10 Deformation parameter (a), elongation (b) and orientation (c) for a bubble in Couette flow Vs Capillary number. Black and red curves represent experiments (profiles are fitted to data) and analytical models, respectively. 43
2.11 Critical Capillary number Vs viscosity ratio for bubble/droplet breakup in Couette flow. The curves from Grace, 1982 refer to fracture (top) and tip streaming (bottom). 45
2.12 Geometrical parameters of a Taylor-Couette apparatus and representation of counter-rotating Taylor vortices. 49
2.13 Evolution of flow regimes in a Taylor-Couette apparatus at: $Re/Re_{\mathrm{cr}} = 1.1$ (a), $Re/Re_{\mathrm{cr}} = 6$ (b), $Re/Re_{\mathrm{cr}} = 16$ (c) and $Re/Re_{\mathrm{cr}} = 23.5$ (d). A chaotic (turbulent) component is already visible in the MWVF state. Figures taken from Fenstermacher et al., 1979 ($\eta = 0.877$) 50
2.14 Torque reduction ratio Vs Re. Two different behaviours are observed in the ranges $Re < 5 \times 10^3$ and $Re > 7 \times 10^4$. The vertical line at $We = 1$ separates the small and strong drag reduction regimes in the experiments of Van den Berg et al., 2005. The same line is shifted towards $Re = 5.1 \times 10^5$ in the measurements of Van Gils et al., 2013. Data from Van den Berg et al., 2005 and Van Gils et al., 2013 are reported here for a gas volume fraction of 3%. 61
2.15 Bubble accumulation patterns at different Reynolds numbers. The black body is the inner cylinder. Figures taken from Murai et al., 2005. 62
2.16 Concentration profiles and mass transfer for saturated (a), supersaturated (b) and under-saturated (c) solutions. 69
2.17 Two film theory for the physisorption of species A. 76
2.18 Two film theory for the chemisorption of species A. The reaction with species B occurs instantaneously in the liquid film. 77

3.1 Two-phase gas-liquid domain. 96
3.2 Control volume around the interface used to derive the jump conditions. The volume moves with the interface velocity $\mathbf{u}_\Sigma$. 97

3.3 1D concentration profile of a soluble (pure) species in a two-phase system. The density profile is discontinuous at the interface and the concentration is assumed constant in Ω_d due to the incompressibility of the phases. 107

4.1 Example of a quadtree grid (left) and the corresponding tree structure (right). The black points represent the active cell centres, whilst the blue ones (right) refer to the parent cells (see text). 111

4.2 Example of restriction/prolongation operators. In order to apply discretization schemes on regular Cartesian stencil, the solution needs to be extrapolated in ghost points (blue and red circles) at different grid levels. 112

4.3 Different variable staggering in Basilisk. 115

4.4 Continuous gas-liquid interface (left) and its corresponding VOF representation (right). The reconstructed interface has been obtained with the PLIC method (see text). 117

4.5 Cell centred reference system for the definition of the reconstructed (PLIC) interface. 118

4.6 Vertical (left) and horizontal (right) heights estimation for the centered-columns scheme. 119

4.7 Advection scheme for the geometric VOF method. The fluxes across each cell boundary are computed from the upwind cells (left), where the exact amount of fluid that crosses the cell edge is computed based on the PLIC interface reconstruction (right). The VOF fluxes are: $F_L = F_{x(i-1/2,j)}$, $F_R = F_{x(i+1/2,j)}$, $F_B = F_{y(i,j-1/2)}$, and $F_T = F_{y(i,j+1/2)}$. 123

4.8 Prediction of face velocity field at time $t^{n+1/2}$. The velocity on the cell boundary $(i-1/2, j)$ is obtained through extrapolation (in space and time) from the upwind cell to point A (left). The velocity in the upwind cell is advanced to point B to take into account the effect of the cross flow velocity (right). 126

4.9 Curvature estimation with the HF method. 130

5.1 Normal displacement ($\mathbf{h}_\Sigma$) of the interface due to a (positive) global mass transfer rate $\dot{m}$. 138

5.2 a) Computation of the field avg for the donor cell (i, j) (red cell). The number of acceptors (green cells) is computed inside the 3×3 stencil and, in this case, $avg_{(i,j)} = 2$. b) Computation of the redistributed mass transfer term $\dot{m}'$ for the acceptor cell (i, j) (green cell). For this cells, the donors are the interfacial cells within the 3×3 stencil (red cells). 139

5.3 Contours of the divergence of the velocity field around a dissolving bubble. The redistributed mass transfer term ensures that the velocity field is divergence-free in pure liquid and interfacial cells and results in a smooth extension of the liquid velocity field across Σ. Variables are non-dimensional. 141

5.4 Integration volume (red area) for the species transport equation in Ω_c. Since the integral balance is performed in V_c, the velocity of the interface $\mathbf{u}_\Sigma$ needs to be taken into account. 143

5.5 Advection of species concentrations confined within the respective phases. The transport fluxes across the cell boundary are based on the PLIC advection of the respective volume of fluids (red and green volumes for the liquid and gaseous phases, respectively). 146

5.6 Diffusion of the species concentration confined within the continuous domain Ω_c. The diffusive flux across the interface is set to zero, since no mass transfer can occur at this stage. 149

5.7 Geometric mass transfer scheme. The extrapolated value in P_1 is obtained from the concentrations inside the red cells, whilst the value in P_2 is extrapolated from the green ones. 151

5.8 Overview of the phase-change solver. 154

6.1 Radial displacement of an infinitesimal element of the interface from time t to $t + dt$. The red volume dV represents the volume phase change between the phases (in this case $\dot{m}$ is assumed positive). . . . 162

6.2 Radius Vs time for the dissolving bubble cases. When the velocity field is not extended across the interface (Case B), the numerical solution deviates significantly from the analytical one. 163

6.3 Velocity field (vectors) and contours of the velocity divergence for cases A (a) and B (b) at $t^* = 0.01$. In Case A, the liquid velocity is smoothly extended across the interface (white line) and preserves the axisymmetric shape of the bubble. In Case B, the flow field is not compatible with the VOF method and produces a significant deviation from the reference solution (dotted line). 164

6.4 Radius Vs time for the growing bubble case. 165

6.5 Velocity field (vectors) and contours of horizontal velocity for Case A (a) and Case B (b) at $t^* = 0.01$. 166

6.6 Numerical domain for the Stefan problem. 167

6.7 Grid convergence analysis for the Stefan problem. Plot of interface displacement Vs time for Gas A (a) and Gas B (b). 169

6.8 Contours of species concentration for Case A.3 (a) and Case B.3 (b) at $t^* = 0.05$ (left) and $t^* = 0.8$ (right). 170

6.9 Velocity (left) and concentration (right) profiles for Case A.3 (a) and Case B.3 (b). The continuous lines represent the analytical curves, whilst the symbols ($\times$) are the numerical solutions. The interface locations are identified by the vertical dotted lines. 171

6.10 Grid convergence for the Scriven problem with $\zeta = 2$. Plot of bubble radius Vs time. 175

6.11 Radius Vs time for growing bubbles in super-saturated solutions at different saturation levels. 177

6.12 Interface (white line) and contours of species concentration on the XY plane at $t^* = 0.3$, for $\zeta = 2$ (a), $\zeta = 3$ (b) and $\zeta = 4$ (c). 178

6.13 Predicted radius (a) and concentration values (b) at three points with different radial distances from the centre of the bubble. The bubble size is kept fixed and the radius prediction is based on the species flux across the interface. Numerical simulations are compared against the exact EP model. 181

6.14 Radius Vs time for a dissolving bubble in an under-saturated solution. The full species transport (advection + diffusion) is solved in Case C, whilst only diffusion is taken into account in Case B. A corrected version of the EP model (see text) is derived, based on experimental findings. 182

6.15 Reynolds number Vs time for the rising bubble of Case A. After a transient period where the bubble accelerates from rest, a steady state regime is approached. 186

6.16 Sherwood number Vs time for rising bubbles at different Péclet numbers. After a transient regime, the numerical simulations approach the value predicted by Takemura and Yabe, 1998 (equation 6.28). . . 187

6.17 Equatorial concentration profiles at $t^* = 6$ for different Péclet numbers. 188

6.18 Contours of concentration (left) and mesh refinement (right) for Case A (a), Case B (b) and Case C (c), at $t^* = 6$. 190

6.19 Rising velocity profile for a bubble in a creeping flow. The bubble accelerates from rest until the steady state regime is reached (vertical dotted line). For $t^* > 25$, the volume of the bubble reduces and the rising velocity decreases accordingly. 193

6.20 Volume ratio Vs time for a rising bubble in a creeping flow. The volume of the bubble is let free to evolve for $t > \bar{t}$. 194

6.21 Bubble positions and contours of concentration at $t^* = 0$ (a), $t^* = 20$ (b) and $t^* = 40$ (c). 195

6.22 Mass transfer rate on the XZ plane at $t^* = 20$. Overview of the field distribution (a) and details for the top (b), equatorial (c) and bottom (d) regions. 196

6.23 Computational domain for an infinite gaseous cylinder (Ω_d) confined by a liquid annulus (Ω_c). 197

6.24 Inner radius of the liquid annulus Vs time for Case A. 202

6.25 Radial concentration profiles of species A at $t^* = 0.1$ (a), $t^* = 1$ (b), $t^* = 2.5$ (c) and $t^* = 5$ (d) for Case A. Crosses represent the numerical solution, whilst the continuous red line is the analytical one. The vertical dotted line shows the interface location, i.e. $r = R_{\text{in}}$. 203

6.26 Contours of concentration for species A at $t^* = 0$ (a), $t^* = 5$ (b) and species B at $t^* = 0$ (c), $t^* = 5$ (d) for case A. The gaseous region is initially composed of B only, then the concentration of A increases (due to the mass transfer) and B decreases accordingly. 204

6.27 Plot of mass fractions in Ω_d and radius R_{in} Vs time for Case B (a), Case C (b), Case D (c) and Case E (d). 206

6.28 Comparison between the present work and the results in Maes and Soulaine, 2020 for Case B (a), Case C (b), Case D (c) and Case E (d). 207

6.29 Grid convergence for the competing mass transfer in a rising bubble. Plot of bubble volume Vs time. 211

6.30 Plot of bubble rising velocity and species Péclet numbers Vs time for Case C. 212

6.31 Species mass fractions Vs time for Case C. 214

6.32 Comparison between the work of Fleckenstein and Bothe, 2015 and Case A for the bubble volume and mass fractions. 215

6.33 Contours of concentration at $t^* = 4$ (left) and $t^* = 29$ (right) for CO_2 (a, b), N_2 (c, d) and O_2 (e, f). 216

6.34 Equatorial concentration profiles Vs time for the soluble species at $t^* = 4$ (a) and $t^* = 29$ (b). The vertical dotted lines represent the location of the interface Σ. All the profiles are discontinuous at $y = y_\Sigma$ due to the different solubility of species in the liquid phase. 217

7.1 2D Computational domain (a) and adaptive mesh refinement (b) for a growing bubble on a planar wall. The contact angle ϑ is kept constant during the simulation. 224
7.2 Bubble radius evolution for $\vartheta = 90\,\text{deg}$ (a) and $\vartheta = 35\,\text{deg}$ (b) at different current densities. The growth rate follows Scriven's solution, i.e. $R_b \propto \sqrt{t}$. 227
7.3 Growth factor β Vs current density I. Comparison against the experimental data of Glas and Westwater, 1964. 228
7.4 Bubble growth and contours of gas concentration for cases A.1 (left) and B.1 (right) at $t = 0.40\,\text{s}$ (a-b), $t = 0.53\,\text{s}$ (c-d) and $t = 1.01\,\text{s}$ (e-f). 229
7.5 Schematic of a TCR with counter-rotating Taylor vortices. Only a section of the reactor is modelled and periodic boundary conditions are applied at the top and bottom faces. 231
7.6 Mesh refinements within two cylindrical regions (dashed lines) around the inner and outer walls. 241
7.7 Mesh sensitivity study for the configuration with $\eta = 0.5$ and $Re = 5000$. The radial profiles of the average azimuthal velocity (a) and fluctuation (b) are compared against the work of Chouippe et al., 2014.242
7.8 Inner and outer cylinder (non-dimensional) torques Vs time for the Taylor-Couette configuration with $\eta = 0.5$ and $Re = 5000$. The absolute value $|G_w|$ is plotted here to compare between the two walls. The statistically stationary regime is approximately reached after 50 revolutions. 245
7.9 Comparison of the (non-dimensional) torque exerted on the inner cylinder against the experimental work of Wendt, 1933 (equation 7.29).246
7.10 Average radial profiles of the azimuthal velocity component for the configurations with $\eta = 0.5$, $Re = 1000$ (a), $\eta = 0.5$, $Re = 3000$ (b), $\eta = 0.5$, $Re = 5000$ (c) and $\eta = 0.91$, $Re = 5000$ (d). 247
7.11 Average radial profiles of the azimuthal velocity fluctuation for the configurations with $\eta = 0.5$, $Re = 1000$ (a), $\eta = 0.5$, $Re = 3000$ (b) and $\eta = 0.5$, $Re = 5000$ (c). 248

7.12 Average radial profile of the azimuthal velocity component for the configuration $\eta = 0.5$, $Re = 3000$. Velocity and radial coordinate are made non-dimensional with the inner friction velocity and wall unit respectively. 249

7.13 Velocity boundary layer profiles at the inner (left) and outer (right) walls for the configuration with $\eta = 0.5$ and $Re = 1000$ (a-b), $Re = 3000$ (c-d) and $Re = 5000$ (e-f). For the inner wall $U_{\text{wall}} = U_{\text{in}}$, whilst for the outer cylinder $U_{\text{wall}} = 0$. 250

7.14 Contours of axial velocity on the $z-\theta$ plane for the configurations with $\eta = 0.5$, $Re = 1000$ (a), $Re = 3000$ (b), $Re = 5000$ (c) and $\eta = 0.91$, $Re = 5000$ (d). These plots are obtained from the corresponding cylindrical surface with radius $r_{\text{in}} + 0.1(r_{\text{out}} - r_{\text{in}})$ for cases a,b,c and radius $r_{\text{in}} + 0.25(r_{\text{out}} - r_{\text{in}})$ for case d. 251

7.15 Inner and outer cylinder (non-dimensional) torques Vs time for the Taylor-Couette configuration with $\eta = 0.73$ and $Re = 1014$. The torques follow the start up procedure of the rector and the formation of Taylor vortices is clearly visible from the sudden increases in the torque profiles between the sixth and seventh revolution. 253

7.16 Average profiles of radial (top) and axial (bottom) velocity for the configurations with $\eta = 0.73$, $Re = 338$ (left) and $Re = 1014$ (right). The profiles are averaged in time and over the azimuthal direction at a distance from the rotor of $0.35(r_{\text{out}} - r_{\text{in}})$ and $0.37(r_{\text{out}} - r_{\text{in}})$ for $Re = 338$ and $Re = 1014$, respectively. Note that the reference velocity U_{in} is the same for both configurations ($U_{\text{in}} = 1$), but the fluid viscosity is not, i.e. $\mu^{Re=338} = 3\mu^{Re=1014}$. 254

7.17 Contours of radial (top) and axial (bottom) velocities for the configurations with $\eta = 0.73$, $Re = 338$ (left) and $Re = 1014$ (right). 255

7.18 Opening of the outer cylinder for the passage of liquid (section taken at $z = L_z/2$). This modification is necessary to ensure the continuity of mass when the volume of the gas fraction decreases. 258

7.19 Grid convergence for a dissolving bubble in a TCR with no rotation. Plot of bubble volume ratio Vs time. 260
7.20 Volume ratio Vs time for a dissolving bubble in a TCR at different rotating speeds. For the selected configuration, gravity is dominant and the TC flow plays a marginal role in the dissolution rate. 262
7.21 Sherwood number Vs time for a dissolving bubble in a TCR at different rotating speeds. The Sh number is based on the diameter of the equivalent sphere (see text). 263
7.22 Bubble trajectories on the horizontal XY plane in a TCR at different rotating speeds. Bubbles are initialised at $x = 0, y = -1.5r_{\text{in}}$. 264
7.23 Iso-surfaces ($c_c = 0.1\rho_d/M$) of dissolved gas concentration and contours of axial velocity on the YZ plane in a TCR at $Re = 0$ (a), $Re = 1000$ (b), $Re = 3000$ (c) and $Re = 5000$ (d). Snapshots taken at $t = 0.1\,\text{s}$. 265
7.24 Plots of Sh and Re numbers Vs time for a dissolving bubble in a TCR at $Re = 0$ (a), $Re = 1000$ (b), $Re = 3000$ (c) and $Re = 5000$ (d). The similarity of the profiles suggests a functional relationship between Sh and Re, as found for rising bubbles in (unbounded) quiescent flows. . 267
7.25 Comparison of the corrected Sherwood number against the theoretical formulae proposed by Oellrich et al., 1973 for $Re = 0$ (a), $Re = 1000$ (b), $Re = 3000$ (c) and $Re = 5000$ (d). 269
7.26 Shape factor and bubble shapes Vs time for a dissolving bubble in a TCR at $Re = 0$ (a), $Re = 1000$ (b), $Re = 3000$ (c) and $Re = 5000$ (d). 270
7.27 Volume ratio Vs time for a dissolving bubble in a TCR at different rotating speeds. Gravity is not taken into account. 272
7.28 Sherwood number Vs time for a dissolving bubble in a TCR at different rotating speeds. Gravity is not taken into account. 273
7.29 Contours of species concentration and bubble interface in a TCR without gravity at $Re = 1000$ (a-b), $Re = 3000$ (c-d) and $Re = 5000$ (e-f). Top view (left) and side view (right). The outer cylinder has been removed for a better visibility. 274

A.1 Characteristic concentration profile of the Stefan problem (a) and grid convergence analysis of the gradient scheme (b). For this specific problem, the method is second-order accurate. 284
A.2 Grid convergence analysis of the overall solver (NS + phase-change) for the Stefan problem (Case A, section 6.2.2). The global accuracy is second-order. 285

B.1 Growing bubble with a constant mass transfer rate. As the bubble expands, part of the surrounding liquid leaves the domain. 288
B.2 Relative error of the imbalance between the amount of liquid that leaves the domain based on the boundary fluxes of momentum (dm^{flux}) and volume fraction field (dm^{f}). 289

Nomenclature

Acronyms

AMR Adaptive Mesh Refinement

CFL Courant–Friedrichs–Lewy

DNS Direct Numerical Simulation

FT Film theory

FV Finite Volume

HF Height functions

LHS Left hand side

LS Level Set

MWVF Modulated wavy vortex flow

MYC Mixed-Youngs-Centered

NS Navier-Stokes

PLIC Piecewise Linear Interface Construction

RHS Right hand side

TCR Taylor-Couette reactor

TFT Two-film theory

TRR Torque reduction ratio

TTVF Turbulent Taylor vortex flow

TVF Taylor vortex flow

VOF Volume of Fluid

WVF Wavy vortex flow

Greek Letters

α	Interface intercept	
β	Growth factor for Scriven problem	
χ	Wavelet-based error	
χ_b	Bubble (ellipsoid) aspect ratio	
Δc	Concentration difference	$\mathrm{mol\,m^{-3}}$
Δ	Mesh size	m
δ^*	Viscous length scale	m
δ_Σ	Interface Dirac delta function	$\mathrm{m^{-1}}$
δ_c	Concentration boundary layer	m
δ_h	Hydrodynamic boundary layer	m
$\dot{\gamma}$	Shear rate	$\mathrm{s^{-1}}$
η	Radius ratio (Reactor)	
Γ	Aspect ratio (Reactor)	

κ	Interface curvature	m^{-1}
λ	Vortex wavelength	m
μ	Dynamic viscosity	$\mathrm{N\,s\,m}^{-2}$
μ_r	Gas to liquid viscosity ratio	
ν	Kinematic viscosity	$\mathrm{m}^2\,\mathrm{s}^{-1}$
Ω	Generic fluid domain	
ω	Rotor speed (Reactor)	$\mathrm{rad\,s}^{-1}$
ϕ	Volume-average molar concentration	$\mathrm{mol\,m}^{-3}$
ρ	Density	$\mathrm{kg\,m}^{-3}$
ρ_r	Gas to liquid density ratio	
Σ	Gas-Liquid interface	
σ	Surface tension coefficient	$\mathrm{N\,m}^{-1}$
τ_w	Wall shear stress	$\mathrm{N\,m}^{-2}$
θ	Azimuthal coordinate or droplet orientation	rad
ε_p	Phase (p) holdup	
ϑ	Contact angle	deg
ξ	Error threshold for mesh adaption	
ζ	Saturation ratio	

Roman Letters

$\dot{m}$	Mass transfer rate	$\mathrm{kg\,m}^{-2}\,\mathrm{s}^{-1}$

$\dot{m}'$	Redistributed mass transfer term	$\mathrm{kg\,s^{-1}}$
$\mathbf{a}$	Generic acceleration term	$\mathrm{m\,s^{-2}}$
$\mathbf{e}_r$	Unit vector along the radial direction	
$\mathbf{e}_x$	Unit vector along the x-direction	
$\mathbf{e}_y$	Unit vector along the y-direction	
$\mathbf{e}_z$	Unit vector along the z-direction	
$\mathbf{f}_\sigma$	Surface force per unit area	$\mathrm{N\,m^{-2}}$
$\mathbf{g}$	Gravitational acceleration	$\mathrm{m\,s^{-2}}$
$\mathbf{I}$	Unit tensor	
$\mathbf{J}$	Diffusive flux	$\mathrm{kg\,m^{-2}\,s^{-1}}$
$\mathbf{N}$	Molar flux	$\mathrm{mol\,m^{-2}\,s^{-1}}$
$\mathbf{n}$	Normal vector	
$\mathbf{S}$	Deformation tensor	$\mathrm{s^{-1}}$
$\mathbf{T}$	Stress tensor	$\mathrm{N\,m^{-2}}$
$\mathbf{u}$	Velocity	$\mathrm{m\,s^{-1}}$
$\mathbf{x}$	Location vector	m
A_Σ	Interfacial area	$\mathrm{m^2}$
a_Σ	Specific interfacial area	$\mathrm{m^{-1}}$
A_p	Projected bubble area	$\mathrm{m^2}$
B	Ellipse minor axis	m

Bo	Bond number	
c	Molar concentration	$\mathrm{mol\,m^{-3}}$
C_D	Drag coefficient	
C_T	Torque coefficient	
Ca	Capillary number	
D	Diffusion coefficient	$\mathrm{m^2\,s^{-1}}$
D_b	Bubble diameter	m
D_s	Sauter diameter	m
D_{eq}	Bubble equivalent diameter	m
E	Deformation parameter	
F	Faraday constant	$96\,485.3\,\mathrm{A\,s\,mol^{-1}}$
f	Volume fraction	
F_D	Drag force	N
Fr	Froude number	
G_w	Non-dimensional torque	
Ga	Galilei number	
$H(\mathbf{x}, t)$	Heaviside function	
H_e	Henry's law coefficient	
I	Current density	$\mathrm{A\,m^{-2}}$
k	Reaction rate constant	$\mathrm{s^{-1}(mol\,m^{-3})^{1-n}}$

k_m	Mass transfer coefficient	$\mathrm{m\,s^{-1}}$
L	Ellipse major axis	m
l	Mesh hierarchical level	
$L0$	Domain length	m
L_z	Reactor length	m
L_{ref}	Reference length	m
M	Molar mass	$\mathrm{kg\,mol^{-1}}$
m	Mass fraction	
M_H	Hatta number	
Mo	Morton number	
p	Pressure	$\mathrm{N\,m^{-2}}$
Pe	Péclet number	
Q	Number of moles	mol
R	Reaction term	$\mathrm{kg\,m^{-3}\,s^{-1}}$
r	Species rate of disappearance	$\mathrm{mol\,m^{-3}\,s^{-1}}$
R_b	Bubble radius	m
Re	Reynolds number	
Re_b	Bubble Reynolds number	
Sc	Schmidt number	
Sh	Sherwood number	

Sr	Shape factor	
T	Temperature	K
t	Time	s
t_e	Exposure time	s
T_w	Torque	N m
Ta	Taylor number	
u	x-velocity	$\mathrm{m\,s^{-1}}$
u'	Fluctuating velocity	$\mathrm{m\,s^{-1}}$
u^*	Friction velocity	$\mathrm{m\,s^{-1}}$
U_b	Bubble terminal velocity	$\mathrm{m\,s^{-1}}$
V	Control volume	$\mathrm{m^3}$
v	y-velocity	$\mathrm{m\,s^{-1}}$
V_b	Bubble volume	$\mathrm{m^3}$
w	z-velocity	$\mathrm{m\,s^{-1}}$
We	Weber number	
y	Species to phase density ratio	

Subscripts/Superscripts

Σ	Interface
c	Continuous (liquid) phase
cc	Centered-columns method

d	Disperse (gaseous) phase
f	Face field
k	k-th species
p	Phase indicator
Y	Youngs method
*	Non-dimensional
b	Bubble
cr	Critical
in	Inner wall (reactor)
out	Outer wall (reactor)
ref	Reference

Chapter 1

Introduction

The present thesis is part of the Photo-Electro project, which is described in section 1.1 along with the motivation of this work. The main objectives and contributions of the thesis are discussed in section 1.2, whilst the structure of the following chapters is outlined in section 1.3.

1.1 The Photo-Electro project: background and motivation of the present work

The Photo-Electro project is a multi-disciplinary and multi-institutional research group based on a partnership between the Universities of Nottingham, Bristol and Southampton. The vision is to innovate how chemicals (for a broad range of applications that include, but are not limited to, the pharmaceutical and agrochemical sectors) are manufactured by exploiting the use of continuous flow chemistry. The focus is on the production of complex molecules by combining photochemical and electrochemical reactions with thermal flow chemistry. The ultimate goal of this project is to deliver an innovative approach that minimises the use of chemicals, solvents and steps needed for the production of chemical compounds, reducing in this way the environmental impact of such industrial processes.

Contrary to standard batch reactors, which are closed systems that contain the

whole amount of chemicals needed for the process, continuous flow devices are continuously fed with the reactants and the desired product flows out of the reactor with a controllable flow rate. This approach offers a better control of the reactions and opens the way to the implementation of automated systems that can be operative for longer times. Another advantage of continuous flow chemistry over batch processes consists of the possibility of linking multiple reactors to perform multi-step chemistry (see, for example, Britton and Raston, 2017).

Photochemistry is generally considered as a green approach due to the use of photons, which are indeed environmentally friendly reactants. One of the most significant limitations of the use of batch reactors for photochemistry consists of the light penetration issue within the reaction vessel. Batch devices are generally designed as large systems in order to meet the production targets. However, in this case, light (which comes form external lamps) cannot easily penetrate across the whole vessel and a significant amount of chemicals is not processed. As a result, the scale-up of such devices is generally difficult. On the other hand, the use of continuous flow chemistry allows to process a small amount of material at one time and smaller reactors can be designed where the distribution of light is optimal and the production rate increases accordingly. The requirements in terms of global production rate (i.e. kg of product per day) can be more easily met (compared to batch reactors), since the scale-up of such devices is generally easier (see Lee et al., 2020).

Another advantage of continuous flow reactors emerges when hazardous reagents are used. This happens, for example, when oxygen is needed for the reaction, which is a well-known inflammable substance but, at the same time, highly desirable for its low environmental impact. In such cases, oxygen is introduced as a gaseous phase within the reactor and the molecules need to be first transferred to the liquid solvent where the reaction can take place (this process will be described in section 2.3). The use of pure oxygen is clearly desirable from the productivity point of view, since a large concentration of O_2 allows to reach high production rates. However, the presence of a large amount of oxygen is generally not possible, due to the risk of hazardous events. A common solution consists of the use of laboratory air (where the concentration of O_2 is limited). The penalty of this approach is clearly a smaller productivity, since

the lower partial pressure of oxygen inside the gas phase limits the mass transfer towards the solvent. Due to the small quantities of O_2 that can be processed at the same time, a batch reactor does not represent an optimal design, since it cannot be easily scaled up. On the other hand, continuous flow devices generally offer a more robust control over the process and represent an interesting alternative, since the smaller amount of chemical mixtures that are processed (in a continuous way) reduces the hazard of the operation, whilst keeping the productivity high. This has been achieved in the Photo-Electro project by developing two different versions of a continuous Taylor Couette reactor, where oxygen can be either automatically drawn into the device from the surrounding air (in this case O_2 is only a small component of the mixture - see Lee et al., 2017) or injected through ducts, which allows for a better control over the concentration (Lee et al., 2020). This type of reactor consists of two coaxial cylinders, where the inner one rotates and the outer wall is generally kept fixed. When the rotating speed reaches a critical value, the fluid within the reactor undergoes an instability that produces pairs of counter-rotating toroidal vortices superimposed on the main (azimuthal) flow. This pattern is particularly efficient for the mixing of chemical species and an accurate description of its features is given in section 2.2.2. For photochemical application, a strong mixing within the reaction vessel is particularly beneficial, since the reaction tends to occur mainly at the external wall, where the intensity of the light is stronger. A sketch of the two Taylor-Couette reactors introduced above is shown in Figure 1.1.

Due to the significant shear rate and small gaps between the cylinders (a few millimeters in the examples above), the gas phase is organised into a large number of small bubbles. This is an optimal configuration for the enhancement of mass transfer between the phases, since the global surface of the gas-liquid interface is relatively large, given the volume fraction of gas inside the reactor. Clearly, the configuration reported in Figure 1.1b offers a better control over the amount of oxygen whilst, in the other design, the amount of air drawn into the vessel is reported to be a function of the rotor speed. As will be shown in section 2.2.2, the fluid pattern of a Taylor-Couette reactor depends on the product between the gap size and the peripheral velocity of the rotor. This offers a natural and convenient way for the scale-up of

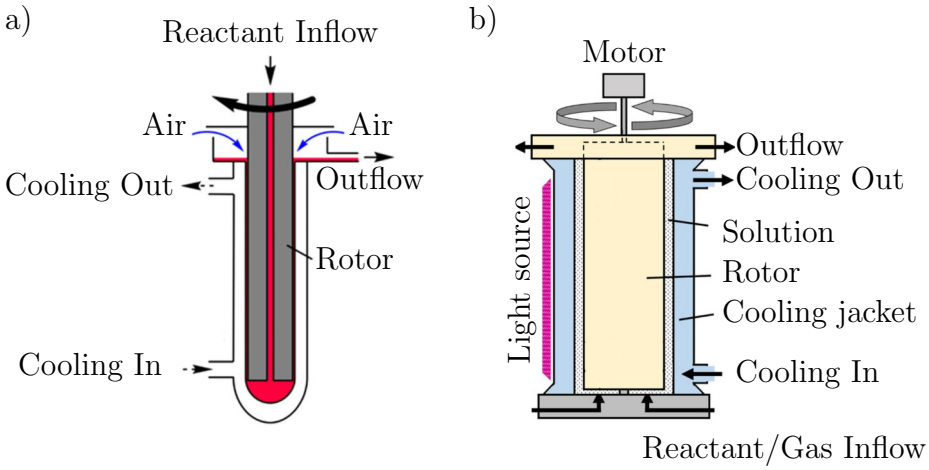

Figure 1.1: Sketches of the cross-section (not to scale) of the Taylor-Couette reactors for photochemistry developed within the Photo-Electro project. The design on the left automatically takes the air from the laboratory, whilst the solution on the right uses apposite ducts for the supply of oxygen. Some details are omitted. Figures adapted from Lee et al., 2017 (a) and Lee et al., 2020 (b).

such devices, since the radii of the cylinders can be increased whilst keeping the gap fixed. For larger sizes, the angular speed of the rotor can be decreased, since the peripheral velocity increases with the radius. This feature offers a clear advantage from a structural point of view. Clearly, in the configuration of Figure 1.1a, this comes with a cost, since for smaller rotating speed, less air is adsorbed. Another reported advantage of this type of reactor is a sort of self-cleaning mechanism of the outer wall due to the large shear rate generated by the vortices, which is helpful to prevent the reactor fouling.

From a sustainability point of view, electrochemistry offers a valuable methodology too. This is mainly due to the fact that chemical reagents can be replaced by electrons and, if the electric current needed for the process is generated from renewable sources, the overall environmental footprint can be significantly low. A strong limitation to the adoption of this approach in industrial settings is related to the production of bubbles on the electrode surface, which makes electrochemical reactors difficult to scale up (see Pereiro et al., 2019). Bubbles are the result of the

production of a dissolved gas from a chemical reaction, which then eventually diffuses into microscopic gas nuclei (this process will be discussed in section 2.3). This phenomenon is detrimental for the performance of the reactor (see Angulo et al., 2020), since the presence of bubbles reduces the active (uncovered) area of the electrodes and induces a non uniform current density in the electrolytic solution. The effective resistance of the solution is also affected (it increases) since the gas phase has a lower conductivity and reduces the transport of ions across the electrochemical cell.

Continuous flow chemistry can also be adopted to improve the design of electrochemical reactors, which benefit from smaller gaps between the electrodes and larger electrode surfaces for a given volume of solution. A significant achievement of the Photo-Electro project is the development of a continuous Taylor-Couette reactor for electrochemistry (Love et al., 2021, Lee et al., 2022). The principle of the reactor is the same as the one presented before for photochemistry but, in this case, the cylinders are used as electrodes. The formation of vortices is particularly useful for this type of applications since the reaction that occurs at the electrode surfaces benefits from the enhanced mixing (i.e. more solution is processed and the mass transfer increases accordingly).

The scenarios discussed so far (i.e. photochemistry with a gaseous reagent and electrochemistry) share the common feature that two-phase (gas-liquid) systems are involved. Some generic features that characterise such processes include the presence of a large number of bubbles with different volume fractions, mass transfer between the phases (due to the solubility of the chemical species) and, clearly, the presence of reactions. Many other aspects are needed to fully characterise the system (e.g. the type of reaction and the design of the reactor), but these are mainly configuration specific. Another relevant example of two-phase electrochemical systems is the production of hydrogen via electrolysis (i.e. the splitting of water into hydrogen and oxygen). This is an extremely interesting technology, since H_2 has a central role (as an alternative to fossil fuels) in the roadmap to carbon neutrality, and has a potentially low environmental impact as long as the energy used for the system comes from carbon-neutral sources. However, as reported in Vachaparambil, 2020 (which is based on a recent report from the European Commission about the hy-

drogen strategy for a climate-neutral Europe - see European Commission, 2020) the cost of this technology in 2020 was still too high (approximately 2.5 - 5 €$\,kg^{-1}$ of hydrogen) compared to standard approaches (e.g. steam-methane reforming or partial oxidation reforming), which cost around 1.5 €$\,kg^{-1}$, but are not carbon neutral. Therefore, the cost of H_2 production via (green) electrolysis should nearly be halved, in order to make this technology competitive on the market. Although the costs reported previously are highly dependent on the energy market, it appears evident that a lot of work is needed to develop such reactors. In the same report from the European Commission, it is reported that the way to reach this target is to scale up electrolysers to more efficient devices, which is definitely not a trivial task given the issues discussed above about bubble formation and their impact on the overall performance of electrochemical cells.

From the introduction to the Photo-Electro project discussed so far, it emerges clearly that a significant amount of research is needed to advance the design of continuous flow reactors. These devices have the potential to contribute to the decarbonisation of part of the chemical manufacturing sector but need to be scaled up and made more efficient in order to meet the industrial productivity standards. The present thesis deals with the study of these systems from an engineering perspective. As was mentioned before, extremely complicated two-phase flows with mixtures of chemical species characterise these types of reactors and no simple analytical models can be used for their design.

1.2 Objectives and contributions

The characterisation of two-phase chemical reactors can be performed by using two approaches, namely experiments and numerical simulations. These two techniques have both advantages and disadvantages (which will be discussed in section 2.3.3) and should be coupled together in order to gain as much insights as possible into the physics of the systems. Due to the continuous increase in computational power and availability of large High-Performance Computing (HPC) centres, numerical simulations have become an attractive tool for the modelling of two-phase systems, since

they offer a cheaper alternative to experiments (compared to the cost of experimental facilities) and provide access to local information that are difficult to measure experimentally. However, despite the enormous advancement of numerical schemes and efficient algorithms, direct numerical simulations (DNS), where all the temporal and spatial scales are fully resolved, are still limited to simplified scenarios. This is especially true when industrial-size systems (which have characteristic dimensions of meters) are modelled and thousands of small bubbles (with diameters of the order of a few millimeters) populate the reactor. In this case, the required mesh size (and the associated time step) are very small and fully resolved simulations are not feasible for routine design due to the high computational cost. Researchers have developed alternative approaches based on simplifying assumptions that allow to reduce the computational cost of the simulations. Such reduced order techniques rely on the use of models for the characterisation of several features (e.g. turbulence, mass transfer, gas-liquid interaction), which are generally valid for a specific application but cannot be easily generalised to different systems. Such models can be derived from different ways that generally combine theoretical considerations with either experimental data or high-fidelity simulations.

The last approach, i.e. the use of DNS in simple scenarios to inform reduced order models, has been applied successfully, for example, in the study of drag forces in bubble column reactors, that usually operate at large scales and contain a large number of bubbles (Roghair et al., 2011). These authors discuss the hierarchy of the available numerical approaches and a summary (from their work) is reported in Figure 1.2. Direct numerical simulations of fully-resolved interfaces (Figure 1.2a) can be used to model small length scales (of the order of centimeters) and are generally limited to a few hundreds of bubbles. Several approaches exist for the resolution of the interface (see section 2.3.3) that allow to capture the complex phenomena that occur at the gas-liquid interface.

At intermediate scales (of the order of meters), bubbles can be approximated as rigid particles and their positions tracked in a Lagrangian way (Figure 1.2b). Clearly, the motion of bubbles depends on several forces that act on the particles, which include buoyancy, drag, lift, added mass and pressure gradient. Many of these

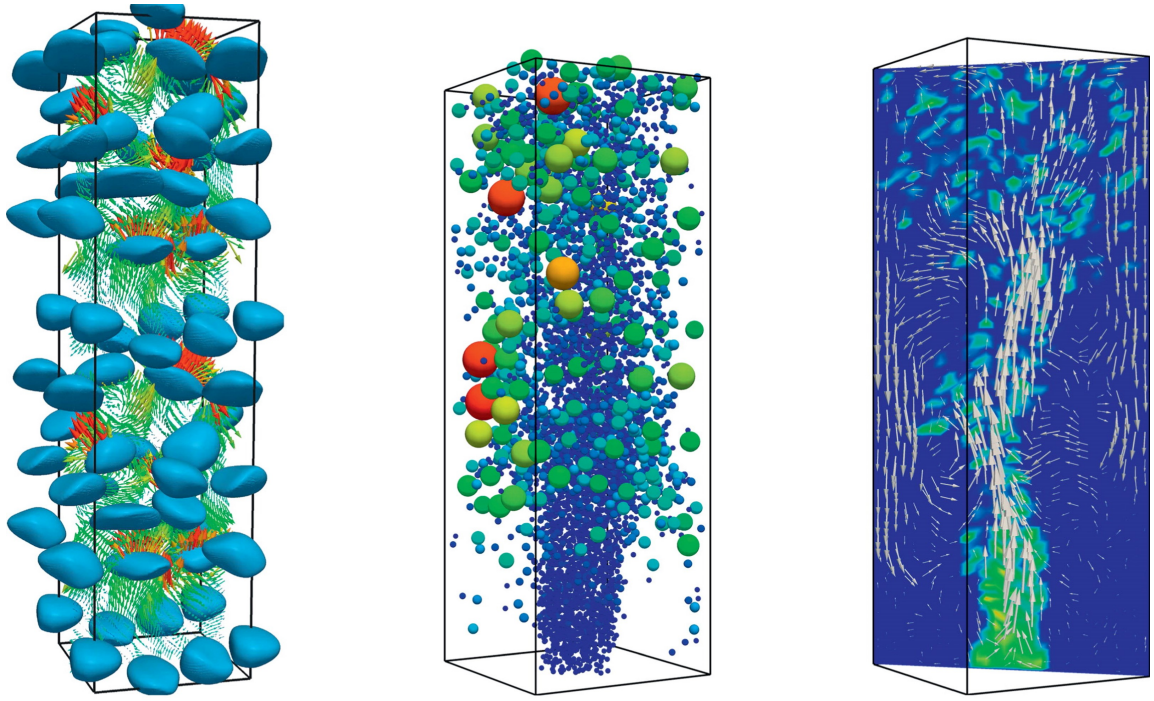

(a) Resolved interface (b) Euler-Lagrange (c) Euler-Euler

Figure 1.2: Hierarchy of numerical approaches for multiphase simulations. Fully-resolved interfacial simulations (a - with Front Tracking in this example) are used to model small scales, Eulerian-Lagrangian (b) methods for intermediate scales and Euler-Euler (c) simulations for full size systems. Figure taken from Roghair et al., 2011.

terms rely on coefficients that need to be estimated through the use of correlation models. This approach is often referred to as Eulerian-Lagrangian model and can be classified depending on whether the particles affect the motions of the fluid (two-way coupling) or not (one-way coupling).

Finally, for larger scales, the Euler-Euler model (Figure 1.2c) is often used, where one set of governing equations is solved for each phase and the distribution of the gas (and liquid) phase is obtained by tracking the transport of the corresponding volume fraction. Clearly, also in this case, closure models are needed to take into account the exchange of momentum between the phases at the interface. This approach is

classified as a two-fluid model.

From the discussion about the numerical approaches presented so far, it appears evident that high-fidelity simulations play a central role in the advancement of computational fluid dynamics modelling. When dealing with mass transfer problems in two-phase systems, additional phenomena appear at the interface, e.g. concentration and velocity discontinuities (which will be carefully discussed in section 2.3). This physics occurs at extremely small length scales (fractions of the bubble diameter) and needs to be fully resolved to characterise the processes in two-phase chemical reactors. Unfortunately, these features add additional challenges to numerical modelling and only few works have been recently published where different methodologies are proposed for an accurate description of the interfacial dynamics (see section 2.3.3 for a review on the state of the art). The main objective of the present thesis is to contribute to the advancement of high-fidelity numerical simulations of mass transfer of soluble species in two-phase systems. In this work, the open source software Basilisk (see Popinet and collaborators, 2013–2023), which is a Finite Volume solver for partial differential equations on adaptive Cartesian grids, is used for the solution of direct numerical simulations of incompressible two-phase flows. A new solver is developed and implemented in Basilisk to take into account the transport of soluble species and the related mass transfer between the phases, with the corresponding volume change. The novelty of the proposed methodology consists of the development of an original algorithm to treat interfacial velocity discontinuities (see section 5.2), which allows for an accurate representation of the flow field around the interface. The proposed approach is different from the others methodologies available in the literature and has the advantage that it requires minimum computational effort and is readily implementable in existing codes (with similar characteristics to Basilisk, e.g. Cartesian meshes). The main contribution of the work is, therefore, the delivery of an open source (state of the art) numerical framework for high-fidelity simulations of flows with phase-change. The methodology is extensively validated against several benchmarks related to bubbly flows and an additional contribution consists of the study on the mesh resolution needed to capture the mass transfer of rising bubbles and its dependence on the system parameters (e.g. bubble size and terminal veloc-

ity). The solver is able to deal with mixtures of different species and reaction terms for the modelling of chemical reactions can be naturally implemented. Finally, the methodology is applied to (simplified) engineering systems, namely electrochemically generated bubbles on flat electrodes and mass transfer in Taylor-Couette reactors, for the characterisation of the fundamental physics involved in these processes. As was discussed before, this approach is an important step towards the development of more accurate models for reduced order simulations. The case of a bubble exchanging mass in a Taylor-Couette reactor is particularly relevant for the Photo-Electro project and represents an important contribution of this work, since no previous studies on the detailed interfacial dynamics of mass transfer in this device has been reported before (to the best of the author's knowledge).

1.3 Thesis outline

The thesis is organised as follows.

Chapter 2 contains the relevant literature review for the characterisation of the flow physics this thesis deals with. The focus is on the main aspects of rising bubbles, the effects of shear forces on bubble deformability and breakup, the description of the flow patterns in Taylor-Couette reactors, the physics of mass transfer processes and the state of the art numerical techniques for fully resolved simulations.

Chapter 3 discusses the governing equations (Navier-Stokes) for two-phase flows with phase-change and derives the one-fluid formulation, which is at the basis of the numerical implementation of the Volume of Fluid method. The chapter also derives the governing equations for the transport of soluble species in gas-liquid systems.

Chapter 4 introduces the Basilisk flow solver. The goal is to present the relevant features for the implementation of the new solver developed in the present work. The focus is on the grid structure, the geometric Volume of Fluid method and the Navier-Stokes solver.

Chapter 5 presents the phase-change solver developed in this thesis. This chapter contains the derivation of the original algorithm used for the treatment of the velocity discontinuity. The Volume of Fluid method is extended to take into account

the volume change and the details related to the transport of species and prediction of the mass transfer rate are discussed.

Chapter 6 provides an extensive validation of the numerical methodology. The proposed benchmarks are based on analytical solutions, experiments and previous numerical studies and include: bubbles with constant mass transfer rates, the Stefan problem for planar interfaces, suspended bubbles in super- and under-saturated solutions, rising bubbles and competing mass transfer in systems with mixtures of species.

Chapter 7 presents two applications of the proposed methodology to real systems. The chapter is dived into two parts. In the first part, growing bubbles on planar electrodes are modelled and the dependence of the growth rate on the contact angle and current density is investigated. In the second part, a single bubble in a Taylor-Couette reactor is studied and the effects of the Reynolds number and gravity on the mass transfer rate are discussed.

Chapter 8 outlines the main findings (and limitations) of the present thesis and presents some suggestions for future work.

Appendix A discusses the characteristics in terms of spatial grid convergence of the proposed solver.

Appendix B provides some considerations related to the consistency between the transport of volume fraction and momentum in the proposed methodology.

Chapter 2

Literature Review

The present thesis deals with the numerical modelling of soluble bubbles exchanging mass with a liquid solution. The focus of this work is on the development of an accurate phase-change solver for high-fidelity simulations, where an original algorithm is proposed for the treatment of velocity discontinuities that occur at the interface in the presence of mass transfer. In this chapter, the most relevant features of bubbly flows that will be modelled in the rest of the thesis (especially in chapter 6 for the validation of the numerical solver and chapter 7 for some engineering applications) are presented and the relevant literature is discussed.

The chapter is organised as follows. In section 2.1 the case of a single bubble rising in a quiescent liquid is introduced and the main characteristics in terms of terminal velocity, shapes and trajectories are discussed. The case of bubbles deforming under shear forces is a relevant topic for the present work since this thesis contributes to the modelling of bubbles in Taylor-Couette reactors. This subject, along with the description of the features of single-phase Taylor-Couette flows, is treated in section 2.2. Finally, the physics of diffusion-driven mass transfer of soluble species in two-phase systems and the state of the art of numerical methods for fully resolved simulations are discussed in section 2.3. Since this work is focused on disperse bubbly flows in liquid solutions, the gas and liquid phases are referred to as disperse and continuous phases, respectively, and these terms will be used interchangeably in the rest of the work.

2.1 Rising bubbles in a quiescent liquid: hydrodynamics

This section will address the following points:

- Non-dimensional groups for the description of bubbly flows.
- Analytical and empirical models for the prediction of terminal velocities in both low and high speed regimes.
- Effect of surface active contaminants.
- Shape deformation and breakup.
- Path instability and rising trajectories.

The case of a rising bubble in a quiescent liquid has captured the attention of scientists for a long time due to the several complicated features of this type of flow and its applications in many technological processes. The first documented case of interest dates back to Leonardo Da Vinci, who reported about the path instability of a rising bubble, known as Leonardo's paradox after the work of Prosperetti, 2004. In this section, a brief overview of the main features of this type of flow is provided and the interested reader is referred to Magnaudet and Eames, 2000 and Clift et al., 1978 for the underlying fundamental physics and review on the topic. Shape deformation, break-up, instability of the rising trajectory and effect of surface active contaminants (i.e. surfactants, generally referred to as contaminants in this work) are amongst the features that make this topic fascinating from a scientific point of view, and, at the same time, very difficult to investigate theoretically.

In this section, the problem is first addressed from a dimensional point of view, where the main non-dimensional numbers are introduced (section 2.1.1). Then, the main characteristics of this type of flow, namely rising velocity, shape deformation and path instability are discussed in sections 2.1.2 - 2.1.3.

2.1.1 Non-dimensional groups

As is generally done for many physical phenomena, it is convenient to approach the problem by introducing non-dimensional groups that compare the magnitude of the main parameters that affect the bubble behaviour. In this work, the liquid and gas phases are also referred to as continuous and disperse phases respectively, and the subscripts c,d refer to the properties of the respective phase, whilst the subscript b is used for the characteristics of the bubble (e.g., D_b and R_b are the bubble diameter and radius, respectively). In two-phase systems, common choices for the non-dimensional groups include (see Tryggvason et al., 2011) the Reynolds number:

$$Re = \frac{\text{inertial force}}{\text{viscous force}} = \frac{\rho_c U_b^2 D_b^2}{\mu_c U_b / D_b D_b^2} = \frac{\rho_c U_b D_b}{\mu_c} \tag{2.1}$$

the Froude number:

$$Fr = \frac{\text{inertial force}}{\text{buoyancy force}} = \frac{\rho_c U_b^2 D_b^2}{g \rho_c D_b^3} = \frac{U_b^2}{g D_b} \tag{2.2}$$

the Weber number:

$$We = \frac{\text{inertial force}}{\text{surface tension force}} = \frac{\rho_c U_b^2 D_b^2}{\sigma D_b} = \frac{\rho_c U_b^2 D_b}{\sigma} \tag{2.3}$$

and the density and viscosity ratios:

$$\rho_r = \frac{\rho_d}{\rho_c}, \quad \mu_r = \frac{\mu_d}{\mu_c} \tag{2.4}$$

where U_b is the terminal velocity of the bubble, σ is the surface tension coefficient and g is the gravitational acceleration (the buoyancy force has been simplified assuming $\Delta\rho = \rho_c - \rho_d \approx \rho_c$). Due to the deformability of bubbles, the shape of the interface can deviate significantly from a sphere along its trajectory, making the definition of the diameter not trivial. For this reason, it is a common choice to refer to the equivalent sphere, i.e. a sphere with the same volume of the bubble (V_b), whose

diameter is:

$$D_{eq} = 2\left(\frac{3V_b}{4\pi}\right)^{1/3} \tag{2.5}$$

In equations 2.1 - 2.3, the non-dimensional groups depend on the rising velocity of the bubble (U_b), which is generally not-known a priori and, under certain circumstances, never reaches a steady-state value (see, for example, some of the cases reported in Cano-Lozano et al., 2016). Therefore, a combination of the non-dimensional numbers introduced above is generally adopted to eliminate the dependence on U_b, leading to the definition of the Galilei number:

$$Ga = \frac{Re}{\sqrt{Fr}} = \frac{\rho_c}{\mu_c}\sqrt{gD_b^3} \tag{2.6}$$

and the Bond number:

$$Bo = \frac{We}{Fr} = \frac{\rho_c g D_b^2}{\sigma} \tag{2.7}$$

Another useful parameter is the Morton number, which has the characteristic of being dependent on the properties of the gas-liquid system only:

$$Mo = \frac{We^3}{Re^4 Fr} = \frac{\mu_c^4 g}{\rho_c \sigma^3} \tag{2.8}$$

Depending on the system properties, the range of variation of Mo can be as large as twenty orders of magnitude. Following a dimensional analysis, the rising velocity of the bubble is generally a function of seven parameters:

$$U_b = U_b(\rho_c, \rho_d, \mu_c, \mu_d, \sigma, g, D_b) \tag{2.9}$$

which means that only four independent non-dimensional groups are needed to fully describe the problem (see Buckingham π theorem). Given the above discussion, the four numbers used in this work to describe the setup of the numerical simulations are ρ_r, μ_r, Ga and Bo.

2.1.2 Terminal velocity

When a bubble is released in a liquid medium, the first part of the motion is characterised by a strong acceleration, where the added mass force plays a significant role. As the acceleration decreases and the bubble reaches a steady-state regime (which could also never occur, as noted before), the buoyancy and drag forces balance out and the terminal velocity results from this balance as:

$$U_b = \sqrt{\frac{2\Delta\rho V_b g}{\rho_c C_D A_p}} \tag{2.10}$$

where C_D is the drag coefficient (i.e. $F_d = (1/2)\rho_c C_D A_p U_b^2$) and A_p is the projected bubble area, which for a sphere is $A_p = \pi D_b^2/4$. Due to the complexity of the problem, only few theoretical solutions can be obtained for the prediction of the drag coefficient and these generally introduce strong assumptions on the flow physics (see Clift et al., 1978). For a slow viscous flow around a spherical particle (also known as creeping flow), Hadamard, 1911 and Rybczynski, 1911 independently obtained an analytical solution of the Navier-Stokes equations and the resulting drag coefficient is:

$$C_D = \frac{8}{Re}\left(\frac{2+3\mu_r}{1+\mu_r}\right) \tag{2.11}$$

In the case of bubbles ($\mu_r \to 0$), equation 2.11 converges to $C_D = 16/Re$. Substituting the value of the drag coefficient into equation 2.10 gives the Hadamar-Rybczynski rising velocity (which is used in section 6.2.4 for the study of mass transfer in a creeping flow):

$$U_b = \frac{2}{3}\frac{\Delta\rho g R_b^2}{\mu_c}\left(\frac{1+\mu_r}{2+3\mu_r}\right) \tag{2.12}$$

Experimental investigations into the validity of this solution for rising bubbles have shown that equation 2.12 tends to become less accurate as the size of the bubble decreases. The main reason for this is related to the combined effect of small bubbles and contaminants (which are generally present in experiments) that makes the bubble behave in a way close to rigid particles. Under these circumstances, a better

correlation is obtained by assuming $\mu_r \to \infty$, which leads to the drag coefficient for solid spherical particles (known since the work of Stokes, 1850), i.e.:

$$C_D = \frac{24}{Re} \tag{2.13}$$

However, experiments in pure liquids (i.e. with no contaminants) have shown that spherical bubbles are well represented by equation 2.11 with $\mu_r \to 0$ independently on their size, confirming thus the importance of liquid contaminants in this type of flow. A first correction to the formula in equation 2.13 was provided by Oseen, 1910:

$$C_D = \frac{24}{Re}\left(1 + \frac{3}{16}Re\right) \tag{2.14}$$

which results in a greater drag compared to Stokes, 1850. The interested reader is referred to the work of Dey et al., 2019 for more contributions on the topic. However, these analytical formulae have a limited range of validity and can generally be applied only to spherical rising bubbles in the flow regime with $Re < 1$ (Clift et al., 1978).

For larger Reynolds numbers, the behaviour of a spherical bubble is significantly different from the creeping flow case. As Re increases, the effect of viscosity becomes less relevant for the conservation of momentum and this makes the potential flow theory a suitable approach to investigate the problem. When a solid body and the surrounding fluid are in a relative motion, the no-slip boundary condition at the wall produces some vorticity that is confined within the boundary layer region, whilst outside the flow is irrotational, i.e. $\nabla \times \mathbf{u} = 0$ (which is mathematically equivalent to the non-physical assumption of inviscid fluid - see Buresti, 2012). For high Reynolds numbers, the boundary layer thickness decreases and the potential flow theory can be used to obtain a first approximation of the flow field around the body, by setting a free-slip boundary condition at the wall (which is equivalent to the assumption of irrotational flow everywhere, i.e. vanishing boundary layer thickness). One of the main consequences of this approach is that no flow separation occurs (i.e. no wake is generated). Therefore, this methodology is representative of the cases where the boundary layer is thin and (almost) completely attached,

but fails when significant separated wakes occur (e.g. bluff bodies). In the case of a bubble, the boundary conditions at the bubble surface consist of the continuity of tangential velocity and stress across the gas-liquid interface. The internal flow circulation that develops within the bubble enhances the momentum on the liquid side of the interface, which results in less vorticity produced at the interface and thinner (liquid) boundary layers. The main consequence of this phenomenon is that the flow separation is delayed and the wake is significantly reduced compared to an equivalent solid sphere where the no-slip boundary condition applies at the wall. Clift et al., 1978 report that no separation occurs for bubbles in pure liquids (i.e. with no surfactants) up to $Re = 200$, whilst for a solid sphere at $Re = 100$ flow separation is expected at approximately $\theta \approx 130\,\text{deg}$ from the stagnation point. The specific boundary condition at the gas-liquid interface makes the assumption of irrotational flow more consistent for bubbles compared to solid particles. In Clift et al., 1978 the pressure distributions on the interface for a bubble and a particle in a potential flow are compared at $Re = 100$, and no significant differences can be observed until $\theta \approx 130\,\text{deg}$, whilst the case of a solid sphere shows a stronger deviation from the potential solution. The above considerations led Levich, 1949 to apply the potential flow theory for rising bubbles at large Reynolds numbers and the drag coefficient is estimated from the viscous dissipation in the irrotational flow:

$$C_D = \frac{48}{Re} \tag{2.15}$$

The solution of equation 2.15 was further extended by Moore, 1963, who included the contributions of the boundary layer and wake regions and obtained:

$$C_D = \frac{48}{Re}\left(1 - \frac{2.21}{Re^{1/2}}\right) + O\left(Re^{-11/6}\right) \tag{2.16}$$

Equation 2.16 has shown a good agreement with many studies for rising bubbles in the range $50 < Re < 500$ (see Magnaudet and Eames, 2000, Clift et al., 1978 and the references therein). For $Re > 500$, bubbles in common gas-liquid systems tend to deform and the assumption of spherical shape is no longer valid. On the other hand,

for $1 < Re < 50$, neither the creeping flow and potential theory are representative of the flow behaviour and no analytical solutions have been obtained. An attempt to derive a formula valid in both regimes for spherical bubbles with no contaminants is proposed in Mei et al., 1994, who derive the following empirical correlation:

$$C_D = \frac{16}{Re}\left\{1 + \left[\frac{8}{Re} + \frac{1}{2}\left(1 + 3.315Re^{-1/2}\right)\right]^{-1}\right\} \tag{2.17}$$

Equation 2.17 recovers the asymptotic solutions of equations 2.11 (when $\mu_r \to 0$) and 2.15 for $Re \to 0$ and $Re \to \infty$, respectively, providing thus a reference solution for spherical bubbles at every Reynolds number. The formulae discussed so far share the common assumption that the bubble preserves a spherical shape. However, it is a well documented fact that for sufficiently large bubbles the surface tension force is no longer able to maintain a spherical shape and deformations take place (see, for example, Davies and Taylor, 1950). A particularly relevant case occurs when We is of the order of unity, where small deformations into oblate spheroids are observed. In this case, the minor axis is aligned with the rising trajectory, whilst the major one is in the cross-stream direction. In the work of Moore, 1965, the ratio of major and minor axes (χ_b) is found to be a function of the Weber number:

$$\chi_b = 1 + \frac{9}{64}We + O\left(We^2\right) \tag{2.18}$$

and, in the same article, the author proposes a correction to his previous formula for spherical bubbles (equation 2.16), which reads

$$C_D = \frac{48}{Re}G(\chi_b)\left[1 + \frac{H(\chi_b)}{Re^{1/2}} + O\left(\frac{1}{Re^{1/2}}\right)\right] \tag{2.19}$$

where $G(\chi_b)$ and $H(\chi_b)$ are coefficients reported in Moore, 1965. The validity of equation 2.19 is tested in the experimental work of Duineveld, 1995, where the author measures the rising speed and aspect ratio (χ_b) for several bubbles, with radius in the range $0.33 - 1\,\text{mm}$, rising in hyper clean water. Results show an excellent agreement between theory and experiments when $R < 0.63\,\text{mm}$ but, for larger bubbles, theory

under-predicts the terminal velocity. The explanation for such discrepancy comes from the assumption in the potential flow solution that the fore- and after- bodies of the bubble are symmetric, which leads to an over-estimation of the aspect ratio with a corresponding increase in the drag resistance. These results confirm that the range of validity of equation 2.19 is restricted to small spherical or slightly deformed ellipsoid bubbles (i.e. low Weber number). Cases with larger bubbles (and, therefore, larger Re and We) are often of practical interest for many industrial applications. However, in these circumstances, the potential flow theory cannot be applied due to the large deformation that might occur, which eventually generates separated wakes that cannot be described by the irrotational flow assumption.

Another aspect that must be taken into account when experiments are compared against theoretical predictions is the presence of surfactants in the liquid. Their effect has been briefly introduced before for the low Re regime and a few more considerations from the physiochemical point of view are provided here. However, a detailed analysis of surfactants is beyond the scope of this work and the interested reader is referred to Pesci et al., 2018, Magnaudet and Eames, 2000, Fdhila and Duineveld, 1996, Clift et al., 1978 and the references therein for a comprehensive review on the effects of contaminants on the dynamics of rising bubbles. It is an experimentally observed fact that the terminal velocity of bubbles decreases as the presence of surfactants in the liquid increases. The justification for this phenomenon comes from the observation that the convective transport of contaminants is generally predominant over diffusion and these tend to accumulate at the rear end of the bubble. The surfactants reduce the surface tension at the gas-liquid interface and, therefore, generate a gradient of surface tension between the top and bottom of the bubble. This phenomenon, also known as Marangoni effect, is balanced by an increase in the viscous shear stress at the interface that makes the bubble behave in a similar way to solid particles (where vorticity is produced within the boundary layer by the no-slip boundary condition). This effect is more relevant for small bubbles since they maintain a spherical shape, for which the terminal velocity is mainly affected by the viscous force and an increase in surface vorticity has indeed a strong impact on drag. On the other hand, large bubbles tend to deform more and the

corresponding effect in terms of drag generation is generally more relevant than the increase in the viscous drag related to the presence of surfactants (Yamamoto and Ishii, 1987). These considerations lead to the conclusion that for large bubbles (or, for the same reason, small surface tension), the drag coefficient is mainly determined by buoyancy and surface tension forces and that correlation formulae for C_D should be function of the Bond number rather than Re (Tomiyama et al., 1998).

In the experimental work of Tomiyama et al., 1998, three correlation formulae of the drag coefficient for different levels of contamination are proposed, namely, for pure systems:

$$C_D = \max\left\{\min\left[\frac{16}{Re}\left(1+0.15Re^{0.687}\right), \frac{48}{Re}\right], \frac{8}{3}\frac{Bo}{Bo+4}\right\} \tag{2.20}$$

for slightly contaminated systems:

$$C_D = \max\left\{\min\left[\frac{24}{Re}\left(1+0.15Re^{0.687}\right), \frac{72}{Re}\right], \frac{8}{3}\frac{Bo}{Bo+4}\right\} \tag{2.21}$$

and for fully contaminated systems:

$$C_D = \max\left\{\frac{24}{Re}\left(1+0.15Re^{0.687}\right), \frac{8}{3}\frac{Bo}{Bo+4}\right\} \tag{2.22}$$

Equations 2.20 - 2.22 reflect the considerations made so far about the role of bubble size, Reynolds number and concentration of surfactants. Indeed, in pure systems, small (spherical) bubbles approach Hadamard-Rybczynski solution for low Reynolds flows (equation 2.11), whilst the high Re regime is described by Levich's solution (equation 2.15). In fully contaminated systems, small bubbles behave similarly to solid particles and the solution approaches an extended version of Stokes' formula, which recovers equation 2.13 for low Reynolds numbers. For large bubbles, the deformation of the interface is predominant over viscous effects and drag is dependent on the Bond number, regardless of the level of contamination. These formulae are compared against experiments in Tomiyama et al., 1998 and a good agreement is observed for a large range of applications, namely $10^{-2} < Bo < 10^{3}$, $10^{-14} < Mo <$

10^7 and $10^{-3} < Re < 10^5$, as reported in Figure 2.1.

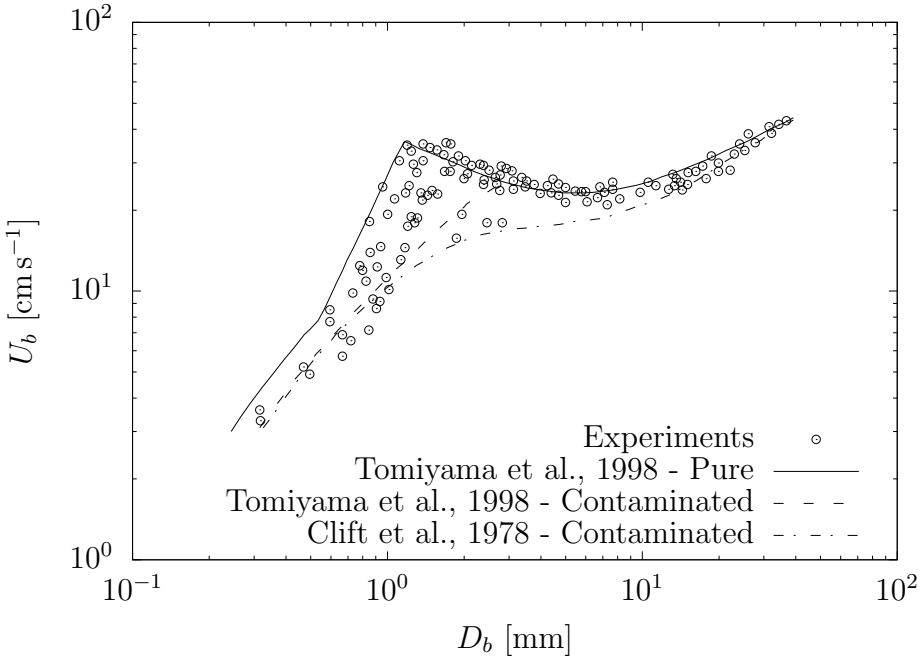

Figure 2.1: Comparison between experiments (from Clift et al., 1978) and correlation models from Tomiyama et al., 1998 and Clift et al., 1978 for the terminal velocity of rising bubbles in a quiescent liquid. The curves from Tomiyama et al., 1998 for pure and contaminated systems correspond to equation 2.20 and 2.22, respectively.

Dijkhuizen et al., 2010 perform numerical and experimental investigations of rising bubbles and propose a drag model that combines the effects of Reynolds (for small bubbles) and Bond (for larger non-spherical particles) numbers in pure systems, and reads:

$$C_D = \sqrt{C_D(Re)^2 + C_D(Bo)^2}, \quad C_D(Bo) = \frac{4Bo}{Bo + 9.5} \tag{2.23}$$

where $C_D(Re)$ is based on the formula of Mei et al., 1994 (equation 2.17). The Bo related part in equation 2.23 differs from the corresponding term in equation 2.20 (i.e. $8Bo/3(Bo+4)$) and it is shown to give a better agreement against experiments for non-spherical bubbles. The authors also perform experiments in contaminated systems and report an excellent agreement with the extended formula of Stoke for

nearly spherical bubbles, but more dispersion is observed for larger particles.

A comprehensive review on the available drag models in the literature is reported in the work of Zhou et al., 2020, where comparisons against experimental data for a large range of flow parameters are reported. The authors observe that, for large bubbles that undergo shape deformations, the Bond number related contribution to drag first decreases with Bo for small Bond values at different Morton numbers and then increases with Bo for larger Bond numbers. Therefore, the range of validity of equation 2.23 is extended by taking into account the effect of the Morton number:

$$C_D(Bo) = \max\left\{10^{-1.23\log(Bo)+0.37\log(Mo)+1.6}, \min\left[\frac{4Bo}{Bo+9.5}, \frac{8}{3}\frac{Bo}{0.8762Bo+4.887}\right]\right\} \tag{2.24}$$

where the first term in equation 2.24 represents the role of Mo at low Bo values. The effectiveness of this correlation formula is proved against several studies in a comprehensive range of flow regimes ($10^{-2} < Bo < 10^3$, $10^{-14} < Mo < 10^7$ and $10^{-3} < Re < 10^5$).

From the consideration reported so far, it appears evident that predicting the terminal velocity of rising bubbles is a non trivial task, since many parameters play a central role. The level of surfactants in experiments must be carefully controlled especially for slightly contaminated systems, where the time needed for absorption increases with the surface area of the interface. However, above a certain amount of surfactants, increasing the concentration of contaminants does not affect anymore the rising velocity of bubbles. The formulae for the drag coefficients discussed in this section have a limited range of validity, since they are generally based on restrictive assumptions (e.g. small deformations, rectilinear trajectory, potential flow theory). In the next section, it will be shown that bubbles can deform significantly under the effect of different forces and that the wake plays a central role in the rising trajectory. Therefore, under general circumstances, experiments and fully resolved numerical simulations should be used to evaluate the effective terminal velocity of rising bubbles.

2.1.3 Shape, break-up and path instability

Initially spherical bubbles deform under the effect of buoyancy and surface tension forces, until normal and tangential shear stresses acting on the gas-liquid interface balance each other. For small surface tensions, larger deformations are observed, whilst high values of σ tend to maintain a spherical shape. Therefore, significant deviations from the spherical shape are expected for large Weber or Bond numbers. Many experimental (see, for example, de Vries, 2001, Duineveld, 1995 or Bhaga and Weber, 1981) and numerical (Cano-Lozano et al., 2016, Gumulya et al., 2016 or Tripathi et al., 2015) investigations have been devoted to the study of deformations of bubbles rising in a quiescent liquid and the different shapes have been correlated to the characteristic non-dimensional numbers introduced in section 2.1.1. A well-known description of bubble shapes is reported in Clift et al., 1978, where a Bond-Reynolds-Morton map is discussed for a large range of flow parameters, namely $10^{-2} < Bo < 10^{3}$, $10^{-1} < Re < 10^{5}$ and $10^{-14} < Mo < 10^{8}$. The observed shapes in this Bo-Re-Mo space are:

- Spherical. For low Re and/or We numbers (i.e. when inertial forces are marginal), bubbles maintain a spherical shape.
- Ellipsoidal. Oblate bubbles with the minor axis aligned with the rising trajectory. Fore- and aft- symmetry is not necessarily satisfied. Therefore, different shapes with the same aspect ratio can be observed.
- Spherical-cap or ellipsoidal cap. Large bubbles often deform into a spherical or ellipsoidal body, cut by a planar base (Figure 2.2a). In the case where the base is not planar but it extends towards the inner of the bubble, the shape is called dimpled (Figure 2.2b). Bubbles in this configuration can also develop thin structures from the bottom side, referred to as skirts (Figure 2.2c).
- Wobbling. Shapes characterised by strong fluctuations driven by capillary forces.

A comprehensive investigation into the shapes described above can be found in the experimental and numerical works of Bhaga and Weber, 1981 and Gumulya et al.,

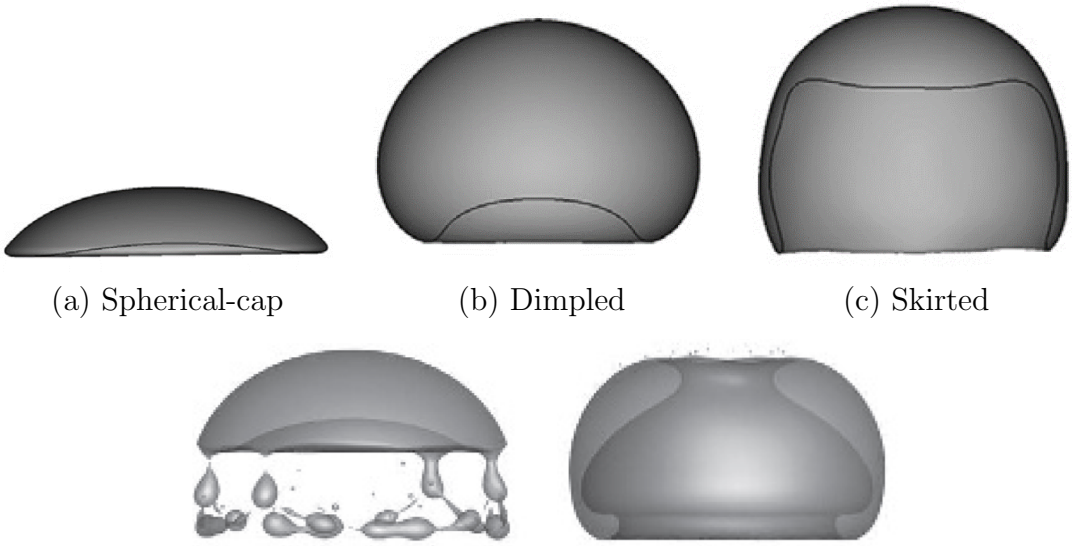

(a) Spherical-cap (b) Dimpled (c) Skirted

(d) Peripheral breakup (e) Central breakup

Figure 2.2: Bubble deformation and breakup. Figures from Gumulya et al., 2016 (a - c) and Tripathi et al., 2015 (d - e).

2016, respectively. This shape classification is further extended in the work of Tripathi et al., 2015 where bubbles (in a gas-liquid system with fixed density and viscosity ratios, i.e. $\rho_r = 0.001$, $\mu_r = 0.01$) are investigated in the range $20 < Ga < 1415$ and $0.4 < Bo < 800$ by means of direct numerical simulations and two additional deformation mechanisms that lead to the breakup of bubbles are reported, namely:

- Peripheral breakup. Bubbles that adopt a spherical-cap shape after a skirt structure or the base perimeter break up into several smaller (satellites) bubbles (Figure 2.2d).

- Central breakup. A central hole forms in bubbles that adopt a doughnut or toroidal shape (Figure 2.2e).

The authors in Tripathi et al., 2015 identify five different regions in the Bo - Ga plane (see Figure 2.3), namely:

- Region I. For low Bo and Ga numbers, bubbles do not break up and rise along a rectilinear trajectory. Shapes are spherical or ellipsoidal.

- Region II. For large Bo and low Ga values, bubbles follow a straight path and adopt an axisymmetric cap with a thin skirt at the rear.

- Region III. For low Bo and large Ga numbers, a non-axisymmetric oblate shape is approached and bubbles rise with a zigzag or spiraling trajectory.

- Region IV. For moderate values of the product $Bo \times Ga$, bubbles break up according to the peripheral mechanism.

- Region V. For large Bo and Ga numbers, bubbles are characterised by the central breakup dynamics.

Particular attention is devoted to the boundary between regions II and III, since this corresponds to the highest Morton number where the onset of path instability (which leads to either zigzag or spiraling trajectories) is observed. This boundary is found to correspond to the iso-Mo line with $Mo = 10^{-3}$ and no instabilities (i.e. only rectilinear paths) are expected for bubbles in gas-liquid systems with $Mo > 10^{-3}$. The same conclusion is reported in Hartunian and Sears, 1957, but for $Mo > 10^{-4}$.

The break of the axisymmetric flow around nearly spherical (rising) bubbles and departure from the rectilinear trajectory has captured the attention of many scientists in the last five decades. Several experimental first, and numerical studies then, have been devoted to the analysis of the causes and mechanisms that lead to path instabilities. Here, the main findings are summarised and the interested reader is referred to the works of Cano-Lozano et al., 2016, Cano-Lozano et al., 2013, de Vries, 2001, Magnaudet and Eames, 2000 and the references therein for more information. Cano-Lozano et al., 2016 have preformed several three-dimensional numerical simulations of spheroidal bubbles close to the boundary between stable and unstable regions and, apart from the well known rectilinear, planar zigzagging and spiraling paths, two additional trajectories have been observed, namely the flattened spiral and chaotic ones. Here, a brief description of the main trajectories is discussed:

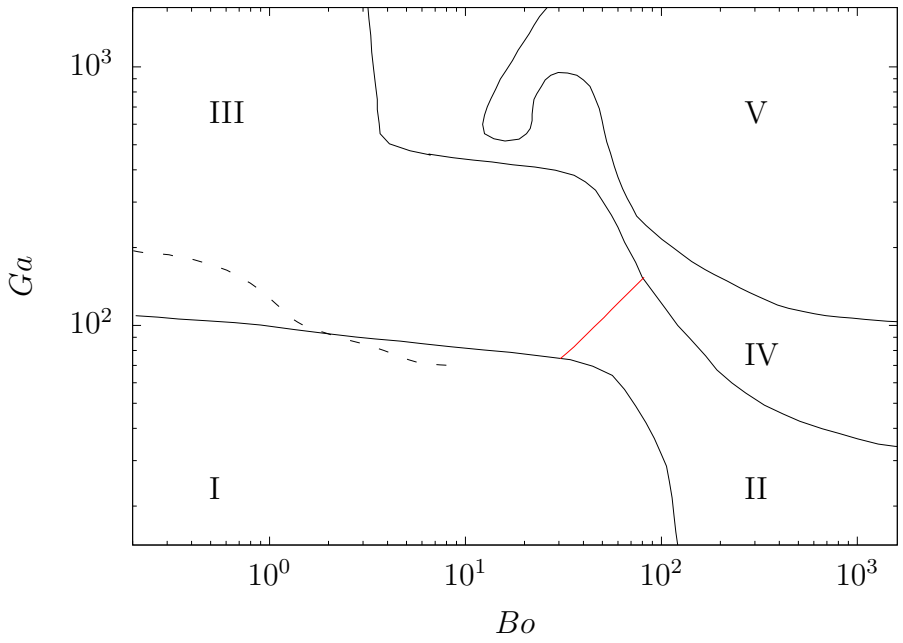

Figure 2.3: Regions in the Bo - Ga plane. The continuous lines are taken from the work of Tripathi et al., 2015, whilst the dashed line corresponds to the onset of the path instability reported in Cano-Lozano et al., 2013. The red curve is the iso-Mo line with $Mo = 10^{-3}$. Figure adapted from Tripathi et al., 2015. (Note that in the work of Tripathi et al., 2015, Ga and Bo are computed with the bubble radius instead of the diameter. Data have been opportunely scaled here.)

- Planar zigzag. Two-dimensional planar motion characterised by a periodic sinusoidal trajectory.
- Spiral (or helical). Three-dimensional spiral regime, which generally occurs for large bubbles after a transient zigzag regime.
- Flattened spiral. In this configuration, the bubble approaches a spiral trajectory with an elliptical projection on a plane perpendicular to the rising direction. This is generally a transient regime before the bubble approaches either a zigzag or helical path.
- Chaotic. In this regime, the bubble exhibits random (chaotic) and sudden

changes to its rising direction.

A summary of the results from Cano-Lozano et al., 2016 is shown in Figure 2.4, where the observed trajectories are reported in the Bond - Galilei plane, along with the stability curves obtained from (less-accurate) 3D numerical simulations of realistic frozen bubbles (Cano-Lozano et al., 2013). Results are shown to agree well with

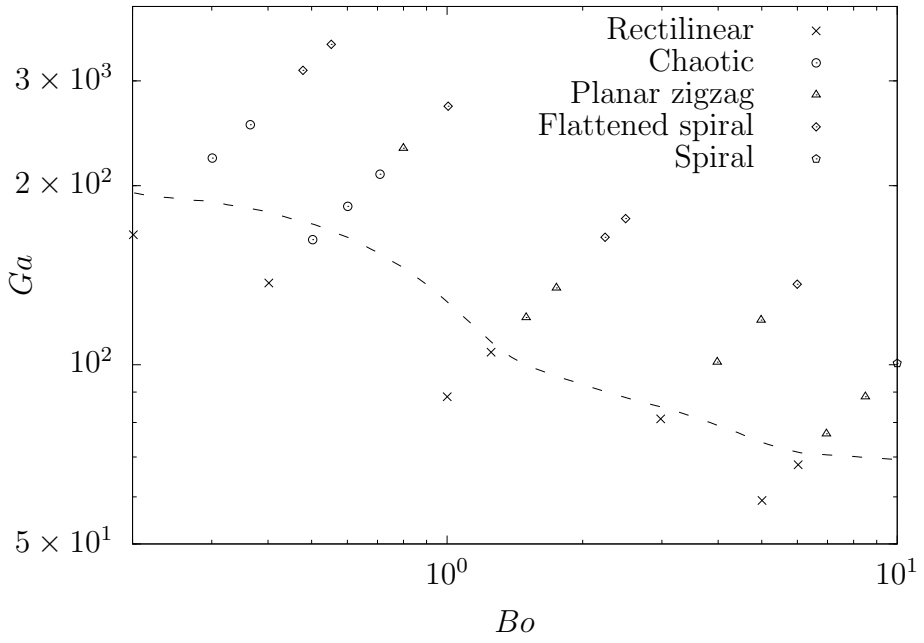

Figure 2.4: Different trajectories from Cano-Lozano et al., 2016. The dash line represents the onset of path instability reported in the work of Cano-Lozano et al., 2013. A good quantitative match is observed since (almost) all the non-rectilinear trajectories are above the suitability line. Figure adapted from Cano-Lozano et al., 2016.

the predictions of Cano-Lozano et al., 2013 and a similar comparison can be made against the data from Tripathi et al., 2015 (see Figure 2.3). In this case, results are qualitatively in agreement, although some quantitative differences (attributed to an under-resolved mesh by the authors in Cano-Lozano et al., 2016) are observed.

Shape deformation and path instability appear to be related, since the region of stability grows as the Bond number decreases, i.e. the bubble can deform less due to

a larger surface tension. Tsuge and Hibino, 1977 derived the following formulae for the prediction of the critical Reynolds and Weber numbers for the departure from the rectilinear trajectory:

$$We_{\mathrm{cr}} = 21.5 Re_{\mathrm{cr}}^{-0.32} \tag{2.25}$$

$$Re_{\mathrm{cr}} = 9.0 Mo^{-0.173} \tag{2.26}$$

Equations 2.25 - 2.26 show that the critical Weber number depends on the gas-liquid system and that for lower Morton numbers, lower We_{cr} are expected. These results are in agreement with the findings of Cano-Lozano et al., 2016 reported in Table 2.1, where the value of the terminal Reynolds numbers for bubbles with different trajectories is compared against the critical ones (from equation 2.26) and is shown that instabilities occur only for $Re > Re_{\mathrm{cr}}$. Duineveld, 1995 reports that path

Trajectory	Mo	Terminal Re	Re_{cr} (eq. 2.26)
Rectilinear	9.90×10^{-6}	59	66
Chaotic	1.11×10^{-11}	715	708
Planar zigzag	6.20×10^{-7}	110	106.7
Flattened spiral	1.80×10^{-10}	500	436.6
Flattened spiral	1.60×10^{-8}	215.5	200.9
Spiral	9.90×10^{-6}	82	66

Table 2.1: Comparison between the terminal and critical Reynolds numbers for some of the bubbles studied in Cano-Lozano et al., 2016. For the cases where Re approaches an oscillating behaviour, the corresponding average value is assumed as terminal Re. Some of the bubbles reported here are in a regime very close to the critical one. It is reported that the Reynolds number drops when the instability occurs (see text). Therefore, at the onset of the instability, the difference between Re and Re_{cr} is larger than what is shown in this table.

instability from rectilinear to zigzag trajectory is first observed in pure water ($Mo = 2.4 \times 10^{-11}$) for a bubble with radius 0.91 mm at $Re = 660$ and $We = 3.3$. This is consistent with equations 2.25 - 2.26 (which predict $Re_{\mathrm{cr}} = 619$, $We_{\mathrm{cr}} = 2.75$), given the accuracy reported in Tsuge and Hibino, 1977 of $\pm 25\%$ and $\pm 15\%$ for We_{cr} and

Re_{cr}, respectively. However, these results differ significantly from others experimental investigations in air-water systems as, for example, the works of Saffman, 1956 and Hartunian and Sears, 1957, who measured the onset of path instability for bubbles with radii of 0.7 mm ($Re = 400$) and 0.63 mm ($Re = 202$), respectively. In general, many other investigations report about critical values in the range between the works of Hartunian and Sears, 1957 ($Re = 202$) and Duineveld, 1995 ($Re = 660$) - see Magnaudet and Eames, 2000 and the references therein. This discrepancy has been mainly attributed to the presence of surfactants in early studies, since techniques to produce clean water were not well developed at that time (it is reminded here that water is particularly sensitive to this type of contaminants). This argumentation is consistent with the observation that surfactants make bubbles behave in a similar way to solid spheres and that the flow around a spherical body is no longer axisymmetric for $Re > 210$ (Ghidersa and Dušek, 2000). This analogy led scientists to conclude that the path instability of bubbles is caused by the alternating shedding of vortices in the wake behind the bubble (see, for example, Lunde and Perkins, 1998). This is indeed the only way in which solid spheres can approach non-rectilinear trajectories and vortex shedding is the consequence of a wake instability that originates from the presence of a standing (toroidal) eddy attached to the after-body of the sphere. For solid spheres, the standing eddy, which is a direct result of boundary layer separation, forms at $Re = 10$ and becomes unstable at $Re = 210$. In the case of clean bubbles, however, the mechanism for the generation of the standing eddy is driven by the accumulation of vorticity that is generated at the interface due to the shear-free condition (see section 2.1.2), which is then advected towards the rear of the bubble (Leal, 1989). The difference in the mechanism with which the standing eddy is generated in clean bubbles and solid spheres (or strongly contaminated bubbles) explains the large dispersion in the measurements of critical Reynolds numbers from the experimental works discussed above.

Therefore, the production of surface vorticity in rising bubbles plays a central role for the path stability. Blanco and Magnaudet, 1995 performed direct numerical simulations of ellipsoidal bubbles with a fixed aspect ratio χ_b (i.e. non deformable) at large Reynolds numbers and found that a standing eddy can exist only if enough

vorticity is generated at the interface and the convective transport is not too strong to completely evacuate the rotational flow into the wake. Therefore, for a given χ_b a standing eddy exists only for a limited range of Re and, interestingly, no eddy can be generated for $\chi_b < 1.65$. These results are further extended in Magnaudet and Mougin, 2007 who investigated the region of wake stability in the χ_b - Re plane, by keeping the aspect ratio of ellipsoidal bubbles fixed. The authors found that no wake instability can occur for $\chi_b < 2.21$ and that the flow is unstable for $\chi_b > 2.21$ only in a limited range of Re. The reason is that the surface vorticity generated at the interface reaches a finite value for large Reynolds numbers and the amount of vorticity injected into the wake evolves as $Re^{-1/2}$, so that the flow recovers a stable configuration when Re is large enough. For large Reynolds numbers, the aspect ratio needed to trigger the instability increases (i.e. bubbles are more oblate), since more vorticity, which is found to evolve as $\chi^{8/3}$, needs to be produced at the gas-liquid interface. An interesting result is that a spherical bubble (i.e. $\chi_b = 1$) is always stable, regardless of the Reynolds number. This result was first obtained for large Re by Moore, 1959 who considered the flow around the bubble to be completely irrotational and is also confirmed in the more recent work of Cano-Lozano et al., 2013. Given the considerations above, it appears evident that bubbles and solid bodies behave differently in terms of vorticity production and generation of the standing eddy. However, once the eddy is generated, the type of instability that characterises the wake is found to be independent on the type of boundary condition at the interface, i.e. free-shear or no-slip (Magnaudet and Mougin, 2007). This is also confirmed by some of the wake visualisations reported in Cano-Lozano et al., 2016 for bubbles in a zigzag regime, which exhibit the typical hairpin vortical structure.

The results presented so far from the works of Blanco and Magnaudet, 1995 and Magnaudet and Mougin, 2007 are based on bubbles with a fixed shape. The case of freely rising bubbles is investigated in the experimental work of Zenit and Magnaudet, 2008, where the effect of bubble deformability results in a lower critical aspect ratio ($\chi_b \approx 2$), i.e. the onset of the wake instability occurs for less oblate bubbles.

Finally, Cano-Lozano et al., 2013 perform 3D direct numerical simulations of the

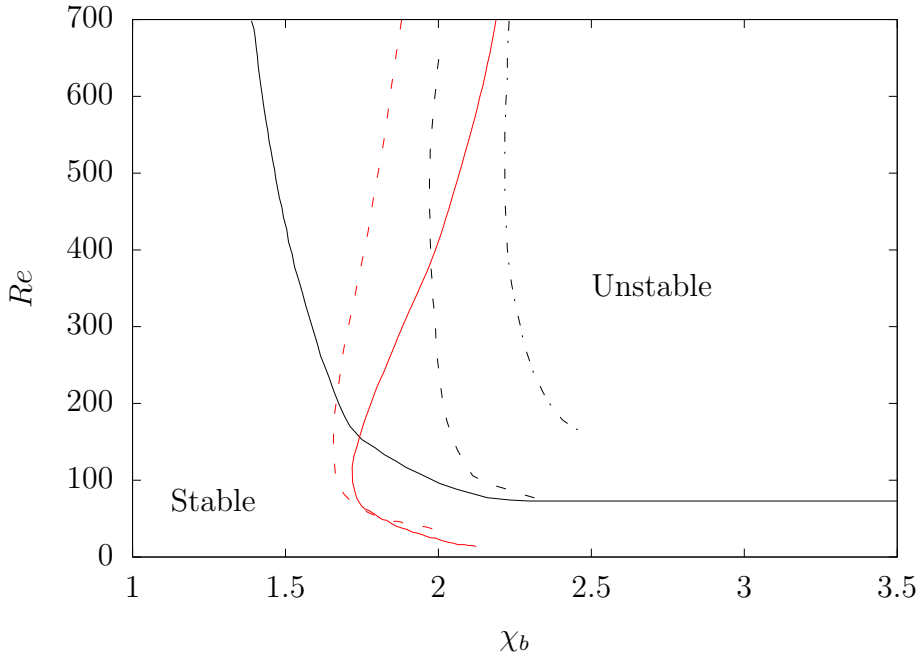

Figure 2.5: The black lines represent the stability curves for the onset of the wake instability: continuous (Cano-Lozano et al., 2013), dashed (Zenit and Magnaudet, 2008) and dot-dashed (Magnaudet and Mougin, 2007). The red plots are the standing eddy curves: continuous (Cano-Lozano et al., 2013) and dashed (Blanco and Magnaudet, 1995). Figure adapted from Cano-Lozano et al., 2013.

flow field around bubbles with realistic shapes (obtained from 2D axisymmetric computations of deformable rising bubbles) and compare the stability and standing eddy curves against the results of Blanco and Magnaudet, 1995, Magnaudet and Mougin, 2007 and Zenit and Magnaudet, 2008. The authors report that the curve that determines the presence of the standing eddy is shifted towards larger deformations (no eddy is observed for $\chi_b < 1.71$, whilst the same behaviour occurs for $\chi_b < 1.65$ in Blanco and Magnaudet, 1995), and the extension of the wake stability region in the χ_b - Re plane is significantly reduced compared to Zenit and Magnaudet, 2008 and Magnaudet and Mougin, 2007. A summary of the main findings discussed so far in terms of stability and standing eddy curves is reported in Figure 2.5. The reason for the discrepancy with the works of Blanco and Magnaudet, 1995 and Magnaudet and

Mougin, 2007 is attributed to the non-realistic assumption in their works of fore-and-aft symmetry, which is observed to produce an increment in the vorticity strength. However, no justification is provided for the disagreement with the experimental results of Zenit and Magnaudet, 2008.

Once the wake instability is triggered (e.g., due to an horizontal displacement or shape deformation), the bubble departs from the rectilinear trajectory and approaches either a planar zigzag or a spiraling path. Several studies report that a spiral trajectory is often observed after a zigzag transient regime, mainly in the case of large bubbles (see, for example, Cano-Lozano et al., 2016, Shew et al., 2005, Mougin and Magnaudet, 2001 or Magnaudet and Eames, 2000 and the references therein), whilst the opposite behaviour has never been documented (to the best of the author's knowledge). The reason why a bubble approaches a planar zigzag trajectory has been investigated by many authors and is related to the structure of the wake that develops after the onset of the instability. In the experimental work of de Vries, 2001, the author introduces a temperature gradient within the tank and schlieren optic is used to visualise the cold water dragged into the bubble's wake. This procedure allows for a visualisation of the wake structure and it is observed that, as soon as the instability takes place, the wake evolves from a single-threaded structure (rectilinear path) to a double-threaded one (zigzag), where the two threads consist of counter-rotating vortical filaments. The same pattern is observed, for instance, in the numerical works of Cano-Lozano et al., 2016, Tripathi et al., 2015, Cano-Lozano et al., 2013 and Mougin and Magnaudet, 2001, where the wake is analysed in terms of iso-contours of vorticity ω_x (the rising trajectory is assumed here to be aligned along the $x-$direction). An example of a two-threaded wake associated with the planar zigzag regime is shown in Figure 2.6a. The two threads contain vorticity with opposite sign and the experimental visualisations of de Vries, 2001 show that, as soon as the curvature of the trajectory becomes null, a single-thread forms, which merges the two previously generated ones. This is reported to happen at the midpoint of the zigzag and, when the bubble goes beyond such point, a two-threaded wake reappears, where the sign of the counter-rotating vortical structures is inverted compared to the first half of the trajectory (see Figure 2.6a between t_3

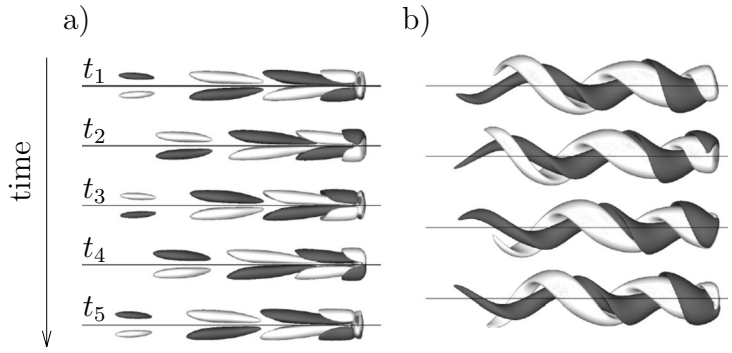

Figure 2.6: Wake structure (iso-contours of streamwise vorticity) for the planar zigzag (a) and spiraling (b) regimes. Bubbles rise horizontally from left to right. Figure adapted from Cano-Lozano et al., 2016.

and t_4). By applying momentum conservation principles, de Vries, 2001 shows that this wake configuration is responsible for the generation of a transversal force (i.e. lift) perpendicular to the trajectory. When buoyancy and lift forces balance out, the curvature becomes null and the lift changes its direction, forcing the bubble into a periodic zigzag regime. Following a different argumentation based on the balance of forces and vorticity production at the gas-liquid interface, Shew et al., 2005 provide a similar explanation to de Vries, 2001 for the zigzag motion, although the location where the lift changes sign is different. The works of Mougin and Magnaudet, 2006 and Cano-Lozano et al., 2016 confirm the results of Shew et al., 2005 in terms of time behaviour of lift, as they show that the change in direction of the transversal force occurs at some point in the first or second half of the zigzag (and not at the midpoint of the cycle).

After a transient zigzag regime, bubbles might approach a spiraling rising trajectory, where the wake structure still consists of two counter-rotating vortices. However, the filaments are continuously produced (contrary to the zigzag case, where the threads switch at every cycle) and are wrapped around each other, in a sort of corkscrew structure (Cano-Lozano et al., 2016). This wake pattern results in a constant lift force directed towards the center of the trajectory, which forces the bubble

into a spiral with a constant velocity (Mougin and Magnaudet, 2006, Shew et al., 2005, de Vries, 2001). An example of the wake past a spiraling bubble is shown in Figure 2.6b.

So far, the departure from the rectilinear trajectory has been associated with the presence of an unstable standing eddy that evolves into two counter-rotating vortical filaments as soon as an instability is triggered. Under this view, the path instability is caused by a wake instability and the corresponding way in which the vorticity is shed into the liquid. However, some studies report of non-rectilinear trajectories in cases where a standing eddy is not present behind the bubble (de Vries, 2001, Cano-Lozano et al., 2013, Cano-Lozano et al., 2016). This is mainly the case of the experiments reported in de Vries, 2001, which occur in the χ_b - Re region where no standing eddy exists. The same behaviour (i.e. absence of flow recirculation behind the bubble) is observed in Cano-Lozano et al., 2016 for the bubbles in the chaotic regime (where the wake is still characterised by two counter-rotating vortices). The authors observe that, in this case, the chaotic trajectory is not caused by the wake instability but rather from a global instability of the bubble-liquid system. Therefore, the wake pattern is the consequence (and not the cause) of the (chaotic) lateral displacements.

It is finally reported (from the work of Cano-Lozano et al., 2016) that instabilities generally occur after the bubble has approached a terminal rising velocity and a drop of approximately 10% of its value is observed when the bubble departs from the rectilinear trajectory. In the cases where the instability originates from the standing eddy, a time delay is reported between the quasi-steady state and the wake instability. This time interval corresponds to the time needed by the standing eddy to develop into the two-thread pattern.

From the literature discussed in this section, it can be concluded that the path instability of bubbles is a rather complicated phenomenon that depends on several parameters, like the aspect ratio, Reynolds number, purity of the liquid and bubble size. Shape instability (i.e. shape oscillations) is generally not seen as a primary cause of path instability (see, for example, Cano-Lozano et al., 2016, Mougin and Magnaudet, 2001, Duineveld, 1995), although bubble deformations can certainly interact or even trigger the instability of the wake. However, some authors see

a more intimate connection amongst path instability, wake instability and shape deformation (Tripathi et al., 2015, Wichterle et al., 2014). It is therefore concluded here that further research is required to fully understand the unstable behaviour of bubbles. High-fidelity numerical simulations (where bubbles are free to adapt their shape) appear to be the preferred way to investigate such phenomenon, since the experimental techniques used to visualise the wake can affect the instability of bubbles (e.g., dye visualisations or particle image velocimetry). On the other hand, numerical methods must be able to resolve the thin structures that might appear (e.g. bubbles skirts) as well as the wake of the bubble, which has a central role for path stability. This represents a challenge for numerical simulations, since very fine meshes are generally required in a relatively large domain. A possible solution is offered by adaptive mesh refinement techniques, which will be introduced in chapter 4.

2.2 Bubbles in shear flows: Couette and Taylor-Couette

This section will address the following points:

- Non-dimensional numbers for the description of bubbles deforming in shear flows.
- Analytical and empirical models for the elongation, orientation and breakup of droplets/bubbles in simple shear flows.
- Characteristics of single-phase Taylor-Couette flows: instabilities, flow regimes and Taylor vortices.
- Models for the prediction of the torque in Taylor-Couette apparatus.
- Numerical modelling of Taylor-Couette flows: reduced order models and high-fidelity simulations.

- Bubbles in Taylor-Couette reactors: drag reduction, accumulation patterns, and effect on Taylor vortices.

- Numerical approaches for the modelling of disperse bubbles in Taylor-Couette flows.

So far, only bubbles rising in a quiescent liquid (driven by gravity) have been considered. However, in several applications (chemical reactors, foaming processes, gas exchange at the interface between the sea and atmosphere), bubbles undergo deformation and breakup due to different mechanisms, like turbulent fluctuations or shear forces. The case of shear flows is particularly relevant for the Photo-Electro project (see chapter 1), since great effort has been made to develop a chemical reactor based on the Taylor-Couette flow (Lee et al., 2017, Lee et al., 2020, Love et al., 2021, Lee et al., 2022), where shear forces are predominant. The same type of reactor is modelled in this thesis (section 7.2.3) for the study of mass transfer of a single bubble.

Here, the fundamentals of bubble deformation and breakup in a simple Couette flow are first introduced (2.2.1). Then, the principles of single-phase Taylor-Couette flows are presented and some studies on the interaction between bubbles and the flow pattern are discussed in section 2.2.2.

2.2.1 Bubble deformation and breakup in a Couette flow

The literature about deformation and breakup induced by viscous forces in simple shear flows is not as comprehensive as for turbulent flows (see, for example, the review of Chu et al., 2019), since the interaction with turbulent eddies is generally the primary cause of deformation. However, in the case of multiple bubbles rising together (e.g. bubble column reactors), the wake of the upstream bubbles can induce a significant shear force if the bubble that follows is partially immersed in their wake and partially exposed to a less turbulent flow (Liao and Lucas, 2009). A comprehensive review on bubble deformation and breakup mechanisms can be found in the works of Liao and Lucas, 2009, Liao, 2013 and Chu et al., 2019, whilst detailed

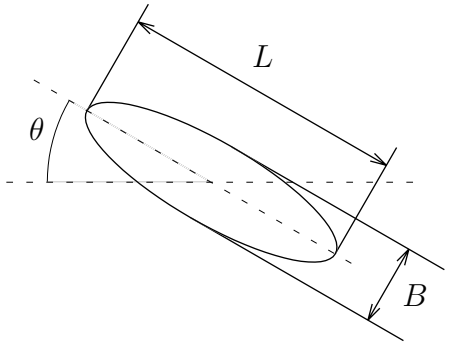

Figure 2.7: Droplet/bubble parameters for the low deformation regime (ellipsoidal) in a Couette flow.

studies on simple Couette flows for low viscosity ratios and Reynolds numbers (fully laminar) are reported in Canedo et al., 1993, Rust and Manga, 2002 and Müller-Fischer et al., 2008. According to the above-mentioned studies, extensive literature for droplets in shear flows has been published (see, for example, Hinch and Acrivos, 1980, Grace, 1982, Rallison, 1984 Bruijn, 1989, Guido and Greco, 2001) and the same conclusions are generally applied to the characterisation of bubbles under the same type of forces. Therefore, the main models for droplets deformation and breakup are briefly introduced here and their validity for deformable bubbles is then discussed.

A droplet/bubble in a Couette flow undergoes a transient deformation under the effect of the shear force until a steady shape (or, eventually, a breakup) is reached. At the equilibrium point, viscous shear forces (which tend to elongate the particle) and surface tension (which tries to maintain a spherical shape) balance out. For low deformations, a droplet adopts a steady ellipsoidal shape, inclined with respect to the direction of the Couette flow (see Figure 2.7). Under these circumstances, the dynamics of a deformable particle depends on the disperse-continuous viscosity ratio (μ_r), the flow shear rate ($\dot{\gamma}$) and the Capillary number (i.e. the ratio between viscous

shear and surface tension forces). The Capillary number is defined as:

$$Ca = \frac{\text{viscous shear force}}{\text{surface tension force}} = \frac{\mu_c \dot{\gamma} R_b^2}{R_b \sigma} = \frac{\mu_c \dot{\gamma} R_b}{\sigma} \tag{2.27}$$

where the bubble radius has been used instead of the diameter to be consistent with the relevant literature (see, for example, Müller-Fischer et al., 2008).

The experimental apparatus generally used for the study of bubble (or droplet) deformation in Couette flows are the parallel band (e.g. Rust and Manga, 2002, Müller-Fischer et al., 2008) and cylindrical devices (Grace, 1982, Bruijn, 1989, Canedo et al., 1993, Müller-Fischer et al., 2008); a schematic of both apparatus is shown in Figure 2.8. In the parallel band experiment, the shear rate is computed

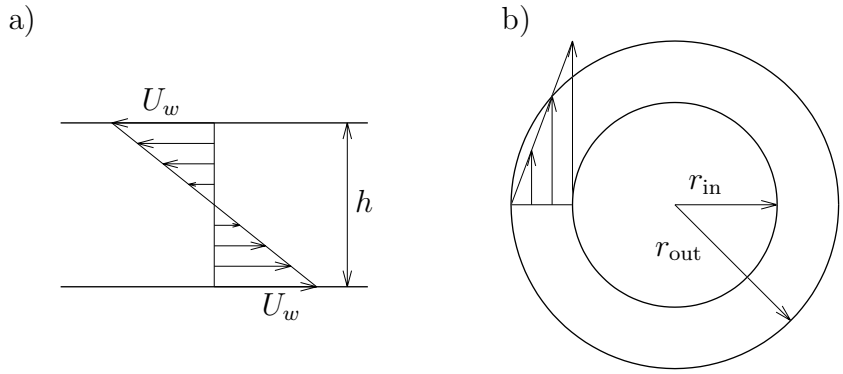

Figure 2.8: Main geometrical parameters of the parallel band (a) and cylindrical Couette (b) apparatus. The velocity profile in the cylindrical device has been approximated to a linear law.

as:

$$\dot{\gamma} = \frac{2U_w}{h} \tag{2.28}$$

whilst for the cylindrical device is:

$$\dot{\gamma} = \frac{\omega}{r_m^2} \frac{2\left(r_{\text{in}} r_{\text{out}}\right)^2}{r_{\text{out}}^2 - r_{\text{in}}^2} \tag{2.29}$$

where r_m is the average radius, i.e. $r_m = (r_{\text{in}} + r_{\text{out}})/2$, and ω is the rotor speed.

For low values of the Capillary number, surface tension forces are dominant and small (ellipsoidal) deformations are expected. In this case, the shape of the droplet (see Figure 2.7) is completely defined by the deformation parameter (Taylor, 1934):

$$E = \frac{L - B}{L + B} \tag{2.30}$$

and the rotation angle θ. For nearly spherical droplets, $E \approx 0$, whilst for highly elongated bodies $E \approx 1$. However, in the case of large deformations (which occur for high shear rates and/or low surface tensions, i.e. large Ca), the droplet departs significantly from an ellipsoid and adopts a sigmoidal shape with pointed ends (see Figure 2.9). Under these extreme conditions, authors (see, for example, Hinch and Acrivos,

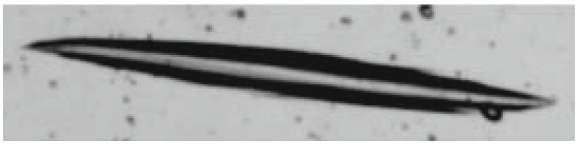

Figure 2.9: Sigmoidal bubble shape from the experiments of Müller-Fischer et al., 2008 in the parallel band apparatus, with: $\mu_r = 1.292 \times 10^{-7}$, $Ca = 5.35$ and $E = 0.8$. Figure taken from Müller-Fischer et al., 2008.

1980) generally define the deformation of the particle with the non-dimensional length L/D_b (instead of E), where D_b is the diameter of the non-deformed droplet.

For small deformations (i.e. nearly spherical droplets) in slow flows, Taylor, 1934 derived the following formula:

$$E = Ca \frac{19\mu_r + 16}{16\mu_r + 16} \tag{2.31}$$

which, in the case of low viscosity ratios (i.e. $\mu_r \to 0$), reduces to $E \approx Ca$.

In the case of large deformations, a widely used relationship is the one proposed by Hinch and Acrivos, 1980, obtained by applying the slender body theory to droplets with a circular cross section:

$$\frac{L}{D_b} = 3.45 Ca^{0.5} \tag{2.32}$$

For the steady orientation of a droplet in simple shear flows, several models have been proposed. For small deformations and viscosity ratios (i.e. $Ca << 1$ and $\mu_r << 1$), the theory proposed by Rallison, 1981 predicts (see Guido and Greco, 2001 for the derivation of the following linear equation and the validation against experimental data):

$$\theta = \frac{\pi}{4} - \frac{3}{5}Ca \tag{2.33}$$

However, experimental investigations in a large range of Capillary numbers have shown that the orientation θ has a non-linear dependence on the Capillary number. Hinch and Acrivos, 1980 derived the following formula for large Ca and small μ_r:

$$\theta = \arctan\left(0.359Ca^{-0.75}\right) \tag{2.34}$$

The two models in equations 2.33 - 2.34 cover small and large values of Ca, respectively. For very small deformations ($Ca \to 0$), equation 2.33 recovers the equilibrium solution, i.e. $\theta = \pi/4$ (see Rallison, 1984).

The models presented above for deformation (equations 2.31 - 2.32) and orientation (equations 2.33 - 2.34) were derived for droplets in simple shear flows. In the following, their validity for the characterisation of bubbles is discussed.

Canedo et al., 1993 used the cylindrical Couette apparatus (with both cylinders rotating) with a gap of 9.3 mm, capable of generating shear rates up to $20\,\mathrm{s}^{-1}$, and performed experimental observations on bubbles with diameters in the range $1.5 - 3$ mm. The authors investigated a large range of Capillary numbers ($3 < Ca < 47$) and reached the maximum deformation $L/D_b \approx 15.2$ at $Ca \approx 47$, whilst no breakup was observed. Results for the elongation (L/D_b) are compared against the formula for droplets of Hinch and Acrivos, 1980 (equation 2.32) and smaller deformations are reported for the same Capillary number. Based on their measurements, Canedo et al., 1993 proposed the following formula:

$$\frac{L}{D_b} = 3.1Ca^{0.43} \tag{2.35}$$

Rust and Manga, 2002 used the parallel band apparatus with very low viscosity

ratios ($\mu_r \approx 10^{-7}$) and explored a smaller range of Capillary numbers ($0.02 < Ca < 7.1$) compared to Canedo et al., 1993. The shear rate generated by the planar Couette device spans the range $0.009 < \dot{\gamma} < 1.77\,\mathrm{s}^{-1}$ and bubbles with diameters of $1.76 - 5.1\,\mathrm{mm}$ are tested in two different liquids with viscosity of 118 and $137\,\mathrm{N\,s\,m}^{-2}$. In this range of viscosity ratios, no breakup is expected up to $Ca \approx 10^3$. The authors observed a maximum deformation of $E \approx 0.94$ (or, equivalently, $L/D_b \approx 9$) at $Ca = 7.1$. A good agreement with Taylor's formula for small μ_r (i.e. $E \approx Ca$) is reported for $Ca < 0.5$; for larger values of Capillary numbers, the deformation parameter approaches a plateau around $E \approx 0.95$. For $Ca > 1$, measurements match the prediction of Hinch and Acrivos, 1980 (equation 2.32), whilst equation 2.35 is found to under-estimate the deformation. The authors also investigated the orientation and found that the bubble approaches the equilibrium angle $\theta = 45\,\mathrm{deg}$ for $Ca \to 0$, whilst, for $Ca > 0.5$, the data follow the relationship in equation 2.34.

Finally, Müller-Fischer et al., 2008 performed investigations in both the parallel band and cylindrical Couette (with the inner cylinder rotating only) apparatus, with gas-liquid viscosity ratios in the range $10^{-6} < \mu_r < 10^{-7}$. The shear rates used for the experiments are $1.8 < \dot{\gamma} < 17.4\,\mathrm{s}^{-1}$ and $1.8 < \dot{\gamma} < 52.1\,\mathrm{s}^{-1}$ in the parallel and cylindrical devices, respectively; bubbles with diameters $D_b < 5.5\,\mathrm{mm}$ are generally used. A maximum deformation (in the parallel band device) of $E = 0.89$ at $Ca = 38.52$ is obtained, were the bubble adopts the typical elongated sigmoidal shape with pointed ends. As the shear rate increases, the orientation moves from $\theta = 45\,\mathrm{deg}$ to $\theta \approx 0\,\mathrm{deg}$. The measurements confirm that Taylor's formula (equation 2.31) provides a good prediction for small deformations ($Ca < 1$), whilst for large Capillary numbers a steady value around $E \approx 0.9$ is observed. A good qualitative agreement for the measured parameters (i.e. E, L/D_b and θ) is generally observed against the previously-mentioned experimental studies and theoretical models. However, quantitative differences are reported and bubble deformation as well as alignment with the flow are found to be under-estimated compared to the other works. Possible reasons for deviations from theoretical models include the experimentally-observed non-circular cross section of elongated bubbles, contrary to what is generally assumed in analytical formulae, whilst discrepancies with other works are attributed to sys-

tematic errors in experiments. A summary of the experimental works of Canedo et al., 1993, Rust and Manga, 2002 and Müller-Fischer et al., 2008, as well as the analytical formulae discussed so far, is reported in Figure 2.10.

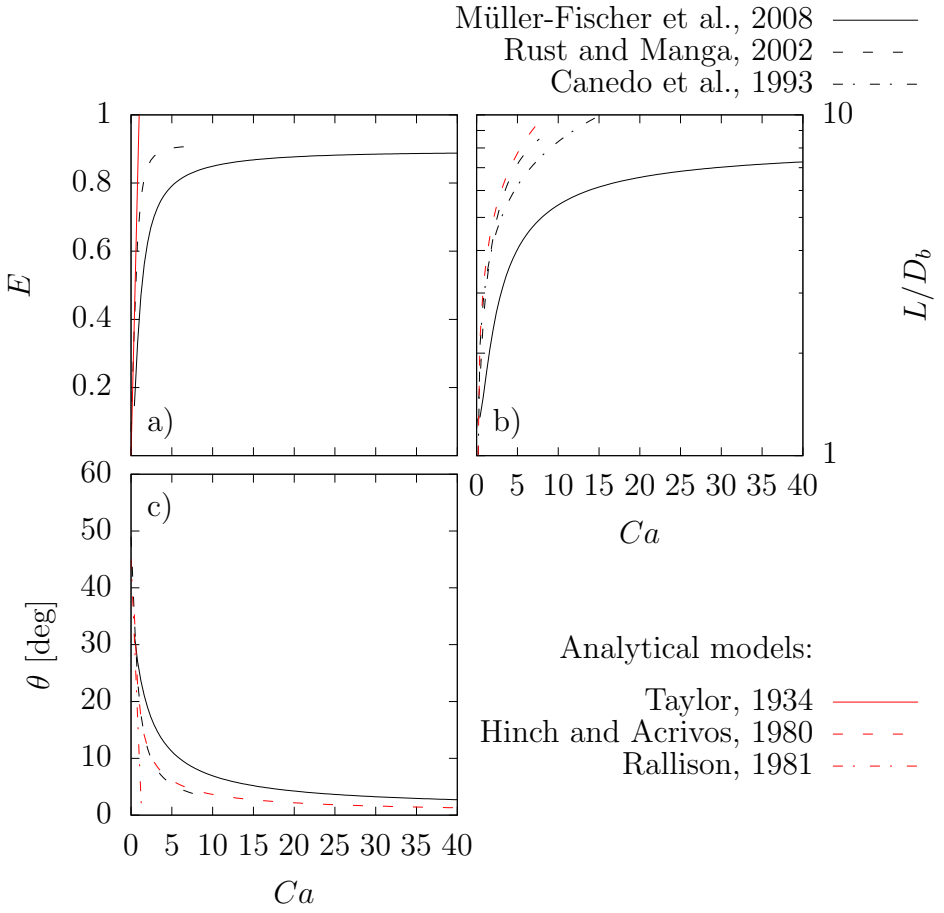

Figure 2.10: Deformation parameter (a), elongation (b) and orientation (c) for a bubble in Couette flow Vs Capillary number. Black and red curves represent experiments (profiles are fitted to data) and analytical models, respectively.

Bubble breakup is observed by Müller-Fischer et al., 2008 in the cylindrical apparatus, where large shear rates can be achieved. As was done before for the discussion on bubble deformation, droplet breakup is first briefly introduced and then the applicability of the same models to bubbles is discussed.

When surface tension is no longer able to balance the shear force, droplets undergo a transient deformation until they break up. When fraction (see text below) occurs, the Capillary number is referred to as the critical Capillary (Ca_{cr}). In the work of Grace, 1982, the effect of viscosity ratio on the breakup of droplets is investigated using the cylindrical Couette device. The value of μ_r is varied between 10^{-6} and 3.5 and a minimum of critical Capillary ($Ca_{\mathrm{cr}} \approx 0.56$) is found in the range $0.1 < \mu_r < 1$. For $\mu_r < 0.1$ and $\mu_r > 1$, a larger value of Ca (e.g., increased shear rate and/or reduced surface tension) is required to break up the droplet. These results are compared in Figure 2.11 against the extensive experimental campaign of Bruijn, 1989, who derived the following empirical formula:

$$\log Ca_{\mathrm{cr}} = -0.506 - 0.0994 \log \mu_r + 0.124(\log \mu_r)^2 - \frac{0.115}{\log \mu_r - \log 4.08} \qquad (2.36)$$

An interesting fact that arises from Figure 2.11 is that, for $\mu_r > 4$, no breakup is observed in both works of Grace, 1982 and Bruijn, 1989. The breakup mechanism described by equation 2.36 (which occurs for $Ca_{\mathrm{cr}} < Ca < 2Ca_{\mathrm{cr}}$ in simple shear flows - see Liao and Lucas, 2009) is referred to as fracture and consists of a necking process that breaks the droplet into two main children droplets (of similar sizes) with smaller fragments (satellites) between them.

A different type of breakup mechanism is also reported in Grace, 1982 for lower values of Capillary numbers ($0.55 < Ca < 0.69$) and a relatively large range of viscosity ratios ($10^{-5} < \mu_r < 5 \times 10^{-2}$) and consists of the so-called tip streaming. This process occurs when the droplet is deformed into a sigmoidal shape with pointed ends and small satellites detach from the tips. The tip streaming mechanism has been deeply investigated in the work of Bruijn, 1989 who came to the conclusion that the level of contamination of the solution is more important than the viscosity ratio itself. This breakup behaviour occurs due to interfacial tension gradients (generally induced by the presence of surfactants - see section 2.1.2), which result in smaller values of surface tension at the tips of the droplet.

Finally, when the Capillary number is significantly greater than the critical value (i.e. $Ca >> Ca_{\mathrm{cr}}$), the droplet adopts an elongated cylindrical shape and breaks into

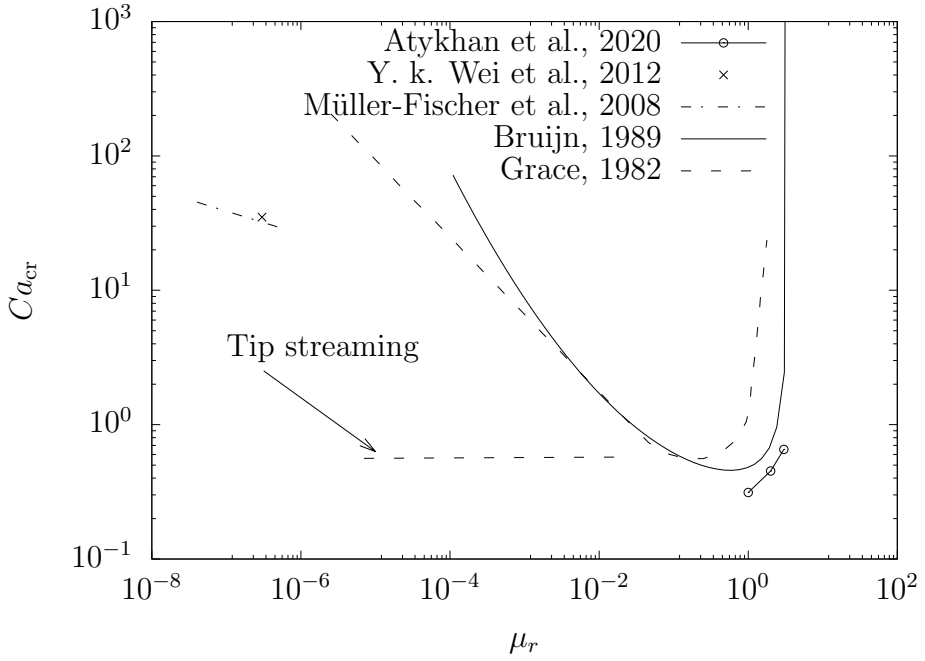

Figure 2.11: Critical Capillary number Vs viscosity ratio for bubble/droplet breakup in Couette flow. The curves from Grace, 1982 refer to fracture (top) and tip streaming (bottom).

several smaller units due to the propagation of a capillary-wave instability (see Liao and Lucas, 2009, Chu et al., 2019); this mechanisms is also referred to as continuous breakup (see Atykhan et al., 2020).

For the case of a single bubble deforming under the effect of a simple Couette flow, Müller-Fischer et al., 2008 report a tip breakup of an extremely elongated bubble with pointed ends. The shape of the bubble is ellipsoidal rather than sigmoidal (as generally observed for droplets) and the breakup occurs in a region of Capillary numbers where neither fracture or tip streaming is expected for droplets (see Figure 2.11). Bubble breakup is observed in the cylindrical Couette device for viscosity ratios between 6.67×10^{-8} and 3.09×10^{-7}, at Capillary numbers in the range $44.7 > Ca > 29.1$. The empirical formula for the onset of the breakup, based on the

measurements of Müller-Fischer et al., 2008, reads:

$$Ca = 2.456\mu_r^{-0.171} \tag{2.37}$$

Since no surfactants are added to the solution, the authors conclude that a different mechanism from the one based on the gradient of surface tension triggers the breakup of the bubble. From their visualisations, it is also reported that the size of the fragments shed off from the tips increases with the flow shear rate.

Y. k. Wei et al., 2012 performed Lattice Boltzmann simulations of a single bubble in a parallel band Couette apparatus. They found good qualitative and quantitative agreements with the data of Müller-Fischer et al., 2008 for both bubble deformation and orientation. The authors also modelled the breakup of a bubble with a viscosity ratio of $\mu_r = 3 \times 10^{-7}$, at a Capillary number of $Ca = 35$. The breakup occurs in the same region reported by Müller-Fischer et al., 2008 (see Figure 2.11), but a fracture mechanism is observed in this study instead of tip streaming. A possible explanation is due to the different types of Couette apparatus used in the works of Y. k. Wei et al., 2012 and Müller-Fischer et al., 2008, i.e. parallel band and cylindrical device, respectively.

In the recent work of Atykhan et al., 2020, the authors adopted a Lattice Boltzmann method to investigate bubbles deformation and breakup in planar Couette flows at different viscosity ratios and bubble diameters. The three main breakup mechanisms (i.e. fracture, tip and continuous breakups) are reproduced and the Capillary number at which breakup occurs is found to increase for more viscous solutions (from $\mu_r = 1$ to $\mu_r = 2$) due to a larger shear rate needed for the deformation of the bubble (consistently with the findings of Grace, 1982). The ratio of bubble diameter to channel height (i.e. D_b/h) is also found to affect the breakup, since larger Capillary numbers are needed for both fracture and tip streaming when D_b/h increases, whilst an opposite trend is observed for continuous breakup. Finally, it is reported that the shape of the bubble that undergoes a continuous breakup (found here at $Ca \approx 2.5Ca_{\mathrm{cr}}$) is still a sigmoidal one rather than a cylindrical thread, as generally observed for $Ca >> Ca_{\mathrm{cr}}$, and the critical Capillary values predicted

by Atykhan et al., 2020 are generally smaller than the equivalent ones for droplets (Figure 2.11).

It is finally concluded that, although models for droplet deformation and breakup can successfully describe (from a qualitative point of view) the behaviour of bubbles under the same flow conditions, quantitative differences are often observed and specific experiments and/or computations for bubbles are generally necessary to characterise their behaviour in simple shear flows. As for the case of rising bubbles in a quiescent liquid (section 2.1), surfactants can significantly affect the dynamics of bubbles under shear forces (by reducing the surface tension and promoting breakup - see Janssen et al., 1994) and their presence must be carefully taken into account when comparing different experiments and simulations.

2.2.2 Taylor-Couette flow: patterns and interaction with bubbles

The flow within the gap between two coaxial rotating cylinders, named as Taylor-Couette flow after the works of Couette, 1890 and Taylor, 1923, is a well studied configuration that exhibits several consecutive states during the transition from the laminar regime (low rotating speeds) to a fully turbulent flow. In the last decades, Taylor-Couette flow has captured the attention of both scientists active in the study of laminar to turbulent transition (see, for example, Gollub and Swinney, 1975, Smith and Townsend, 1982 or Townsend, 1984) as well as engineers involved in the design of rotating devices, like rotating machinery (Nicoli et al., 2022) or specific types of chemical reactors (Schrimpf et al., 2021). Originally, an experimental apparatus consisting of two coaxial cylinders was used by Couette, 1890 to measure the viscosity of different fluids. Approximately 30 years later, Taylor, 1923 demonstrated, by means of linear stability analysis, that the Couette flow between rotating cylinders is unstable above a certain critical speed. Taylor used dyes to visualise the flow structure after the onset of the instability and observed that the flow approaches a configuration where pairs of counter-rotating toroidal vortices are superimposed on the main azimuthal component. An extensive literature has been published on

the characterisation of Taylor-Couette flows and the interested reader is referred to the works of Di Prima and Swinney, 1981, Andereck et al., 1986, H. Wang, 2015, Grossmann et al., 2016, and the references therein for a detailed review. In this thesis, only the configuration where the inner cylinder is rotating and the outer one is kept stationary is considered, as this is the setup adopted for the chemical reactor developed within the Photo-Electro project (see the introduction to section 2.2) and the same configuration will be used in section 7.2.3 for the study of mass transfer from bubbles in Taylor-Couette reactors.

The non-dimensional groups generally used for the characterisation of this flow configuration take into account both the geometry of the apparatus (see Figure 2.12), which is defined by the radius ratio:

$$\eta = \frac{r_{\text{in}}}{r_{\text{out}}} \tag{2.38}$$

and the aspect ratio:

$$\Gamma = \frac{L_z}{r_{\text{out}} - r_{\text{in}}} \tag{2.39}$$

as well as the ratio of inertial to viscous forces (i.e. the Reynolds number):

$$Re = \frac{\rho_c U_{\text{in}} \left(r_{\text{out}} - r_{\text{in}}\right)}{\mu_c} \tag{2.40}$$

where r_{in}, r_{out} are the inner and outer radii, respectively, L_z is the axial extension of the device and $U_{\text{in}} = r_{\text{in}}\omega_{\text{in}}$ is the peripheral speed of the inner rotor. In some works, the Reynolds number is replaced by the Taylor number:

$$Ta = \left(\frac{\rho_c U_{\text{in}}(r_{\text{out}} - r_{\text{in}})}{\mu_c}\right)^2 \left(\frac{r_{\text{out}} - r_{\text{in}}}{r_{\text{in}}}\right) = Re^2 \left(\frac{1}{\eta} - 1\right) \tag{2.41}$$

Experiments were the preferred way (since the work of Taylor, 1923) for the investigation of instabilities and transition in Taylor-Couette flows, until computational techniques became efficient enough to complement experimental methods. Here the main results based on visualisation techniques and power spectral analysis are first

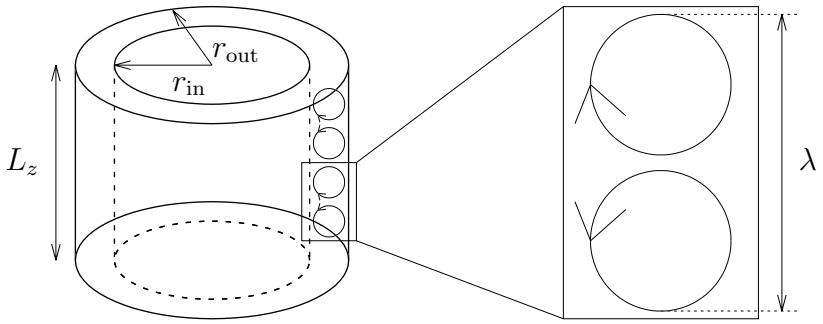

Figure 2.12: Geometrical parameters of a Taylor-Couette apparatus and representation of counter-rotating Taylor vortices.

discussed and then some more recent numerical investigations are presented.

Instabilities of Taylor-Couette flows and experimental investigations

As was already mentioned before, the first instability that occurs in a (planar, time-independent and axisymmetric) cylindrical Couette flow, when the rotating speed exceeds a critical value, consists of pairs of counter-rotating vortices (also known as Taylor cells) superimposed on the main flow (Taylor, 1923). This flow regime is referred to as Taylor Vortex flow (TVF) and the cells have a characteristic toroidal-like shape (see Figure 2.13a). The flow is periodic in the axial direction, axisymmetric and time-independent. The Reynolds number at which this instability occurs is referred to as critical Reynolds (Re_{cr}). From stability analysis (see, for example, the Appendix by P. H. Roberts in Donnelly et al., 1965 or Di Prima and Swinney, 1981), the expected wavelength (λ) of the disturbance (i.e. the axial extension of two consecutive Taylor cells - see Figure 2.12) is approximately twice the gap between the cylinders, i.e. $\lambda \approx 2(r_{\text{out}} - r_{\text{in}})$, which corresponds to nearly squared vortices (consistently with the observations of Taylor, 1923). However, it is anticipated here that multiple states can exist where different wavelengths are observed and a significant dispersion in the measurements of λ, by varying the aspect ratio and/or

the Reynolds number, is reported in the literature (see, for example, the results collected in Chouippe et al., 2014). The critical Reynolds number (or, equivalently, Taylor number) depends on the geometry of the apparatus and is found to decrease with larger gaps, i.e. decreasing aspect ratios (see the data summarised in Childs, 2011).

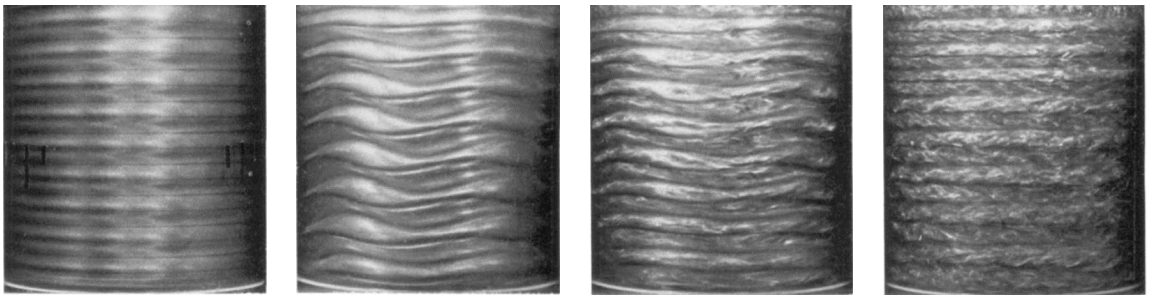

(a) TVF (b) WVF (c) MWVF (d) TTVF

Figure 2.13: Evolution of flow regimes in a Taylor-Couette apparatus at: $Re/Re_{\mathrm{cr}} = 1.1$ (a), $Re/Re_{\mathrm{cr}} = 6$ (b), $Re/Re_{\mathrm{cr}} = 16$ (c) and $Re/Re_{\mathrm{cr}} = 23.5$ (d). A chaotic (turbulent) component is already visible in the MWVF state. Figures taken from Fenstermacher et al., 1979 ($\eta = 0.877$)

As the rotating speed is further increased beyond the critical Reynolds, a second instability is observed, which leads the vortices to travel along the azimuthal direction, following a wavy trajectory (see Figure 2.13b). The boundaries between two adjacent Taylor cells have a sinusoidal shape (wave) and the flow is no longer time-independent; the waves are periodic along the azimuthal direction. This configuration is referred to as Wavy Vortex flow (WVF) and the Reynolds number at which is observed is defined as Re'_{cr}. An extensive experimental investigation of Taylor-Couette flow in the WVF state (and the subsequent regimes) can be found in Coles, 1965, who used both visualisation techniques and the hot-wire anemometry for the study of the instability in a device with $\eta = 0.874$ and $\Gamma = 27.9$. The author reports that at the onset of the WVF, the wavy vortex boundaries travel with a rotating speed of approximately $0.5\omega_{\mathrm{in}}$, which then decreases down to $0.34\omega_{\mathrm{in}}$ as the rotor is further accelerated. One of the main contribution from the work of Coles, 1965 consists of the analysis of the non-uniqueness behaviour of Taylor-Couette flow in the

WVF regime. In fact, the author reports of several states (completely defined by the number of Taylor cells and azimuthal waves) that can occur for the same Reynolds number. The wavelength is found to be in the range $(1.7 - 3.1) \times (r_{\text{out}} - r_{\text{in}})$, whilst the number of waves is reported to vary between 3 and 7. The specific configuration adopted by the flow depends on both the geometrical parameters and previous history of the apparatus (e.g. acceleration and/or deceleration of the rotors) and a significant hysteresis is observed when moving between two consecutive states. This feature led L. Wang, Marchisio, et al., 2005 to develop a specific start up procedure for their reactor in order to reproduce the same number of vortices in all the experiments (see section 7.2.2).

As in the case of TVF, also for the WVF regime the geometrical dimensions affect the onset of the related instability (Re'_{cr}). Some of the results reported in Di Prima and Swinney, 1981 show that, for large aspect ratios ($\eta \approx 0.95$), the transition from TVF to WVF is quite close to the first instability, being $Re'_{\text{cr}} \approx (1.05 - 1.1)Re_{\text{cr}}$. On the other hand, for larger gaps the distance between the two regimes increases and can be as large as $Re'_{\text{cr}} \approx 10Re_{\text{cr}}$ for $\eta = 0.5$. The effect of the aspect ratio was deeply investigated by Cole, 1976 (by means of visualisations and torque measurements) in an apparatus where radius and aspect ratios could vary in the ranges $\eta = 0.894{-}0.954$ and $\Gamma = 1 - 107$. No effect of varying Γ was reported for the onset of Taylor vortices (TVF), but the critical speed for the appearance of waves was found to increase for smaller aspect ratios.

Temporal measurements of the flow field allowed researchers to analyse the power spectra of the signals and identify the related characteristic frequencies (see, for example, Gollub and Swinney, 1975, Fenstermacher et al., 1979, Gorman and Swinney, 1982). A sharp frequency at the onset of WVF is reported by Fenstermacher et al., 1979 in the signal of the radial velocity component (obtained by means of laser-Doppler velocimetry) in a device with $\eta = 0.877$ and $\Gamma = 20$. The same result is found in Gorman and Swinney, 1982, where the authors followed the temporal evolution of the light scattered by small particles used for flow visualisations, in an apparatus with $\eta = 0.883$ and $\Gamma = 20$. This frequency is associated with the travelling of azimuthal waves and confirms the singly-periodic nature of WVF.

As the rotating speed is further increased beyond Re'_{cr}, a second frequency appears in the power spectra. Gorman and Swinney, 1982 investigated this configuration and found out that the new frequency is related to a modulation of both the amplitude (i.e. the amplitude oscillates) and the frequency of the waves. This flow configuration is referred to as Modulated Wavy Vortex flow (MWVF - Figure 2.13c) and the presence of two sharp frequencies (the first one is still related to the travelling waves in the azimuthal direction) clearly indicates that the flow is doubly-periodic. Similar to the non-uniqueness of states reported by Coles, 1965, multiple modulation frequencies can be achieved for the same state. In the experiments of Fenstermacher et al., 1979, the appearance of the second frequency is observed at $Re = 10.1Re_{\mathrm{cr}}$.

For the first three regimes (i.e. TVF, WVF and MWVF), Koschmieder, 1979 reported that the axial wavelength increases with the rotating speed up to approximately $Re = 10Re_{\mathrm{cr}}$ (for an apparatus with $\eta = 0.896$), after which λ is found to be independent of the rotating speed. For $Re > 10Re_{\mathrm{cr}}$ the azimuthal waves progressively disappear and the flow transitions towards a turbulent regime. The same dynamics is observed from the power spectra of radial velocity signals in Fenstermacher et al., 1979, where a chaotic component emerges at $Re = 12Re_{\mathrm{cr}}$, whilst the frequencies related to the MWVF and WVF regimes disappear at $Re = 19.3Re_{\mathrm{cr}}$ and $Re = 21.9Re_{\mathrm{cr}}$, respectively. Therefore, for $Re > 21.9Re_{\mathrm{cr}}$ no waves are observed and the flow regime is fully turbulent and chaotic. This is the last state of Taylor-Couette flow and is generally referred to as Turbulent Taylor Vortex flow (TTVF). From visual observations, the flow is still structured into azimuthal cells, although the velocity field is no longer well organised into a toroidal pattern, due to the presence of strong velocity fluctuations (see Figure 2.13d). The persistence of highly turbulent Taylor cells has been reported in the literature for large Reynolds numbers ($Re > 1000Re_{\mathrm{cr}}$ - see Di Prima and Swinney, 1981). A characteristic feature of the TTVF is the herringbone-like structure that can be observed in experiments at the outer wall for large Reynolds numbers (Barcilon et al., 1979). This pattern was associated to the presence of the so-called Görtler vortices and this hypothesis has been confirmed in later works (see, for example, T. Wei et al., 1992 or Dong, 2007).

The majority of the studies reported so far, focuses on large radius ratios ($\eta > 0.85$), but the description of the main instabilities (e.g. appearance of Taylor vortices and azimuthal waves) is valid for a large range of η (see, for example, the works of Razzak et al., 2019 and Dong, 2007 for $\eta = 0.5$). Clearly, the critical Reynolds numbers at which the instabilities occurs are largely dependent on the geometrical parameters of the apparatus. However, some qualitative differences in the transition to turbulence can be expected for extremely low radius ratios, where the flow was found to undergo the transition from laminar Taylor vortices to a turbulent regime without the appearance of waves (Snyder, 1968).

In many practical applications that involve the design of coaxial rotating cylinders, the torque exerted by the fluid on the inner rotor is a crucial parameter (e.g. rotating shafts in bearing chambers). Several authors have proposed formulae for the prediction of the torque coefficient expressed as (Bilgen and Boulos, 1973):

$$C_T = \frac{T_w}{0.5\pi\rho_c\omega_{\text{in}}^2 r_{\text{in}}^4 L_z} \tag{2.42}$$

where T_w is the torque at the cylindrical wall. In the following, a few relationships for the turbulent regime (which is the most relevant for industrial cases) are presented. Wendt, 1933 derived the following empirical formula (which will be used for the validation of the numerical model in section 7.2.2) for the regime $4 \times 10^2 < Re < 10^4$:

$$C_T = 0.92 \left(\frac{(r_{\text{out}} - r_{\text{in}}) r_{\text{out}}}{r_{\text{in}}^2} \right)^{0.25} Re^{-0.5} \tag{2.43}$$

In the work of Donnelly and Simon, 1960, the variation of the torque with the gap size, for Reynolds numbers well above the first instability, is expressed as:

$$C_T \propto \left(\frac{r_{\text{out}} - r_{\text{in}}}{r_{\text{in}}} \right)^{0.31} Re^{-0.5} \tag{2.44}$$

Finally, for the same turbulent regime up to $Re < 10^4$, Bilgen and Boulos, 1973

propose:

$$C_T = 1.03 \left(\frac{r_{\text{out}} - r_{\text{in}}}{r_{\text{in}}} \right)^{0.3} Re^{-0.5} \tag{2.45}$$

Equations 2.43 - 2.45 have the same functional dependence on the Reynolds number (i.e. $C_T \propto Re^{-0.5}$) and provide basically the same results.

Numerical investigations

Numerical methods have been successfully applied to explore the physics of the several regimes that characterise Taylor-Couette flow. Reynolds-averaged Navier–Stokes (RANS) simulations are the preferred way for industrial applications (where flows are typically turbulent), due to the reduced computational cost compared to high-fidelity approaches, e.g. large eddy simulations (LES) or direct numerical simulations (DNS). Therefore, researchers have investigated the reliability of RANS models for the characterisation of Taylor-Couette flows and some of the results are briefly discussed in the following.

Wild et al., 1996 used the standard $k - \varepsilon$ model to study the effect of turbulent Taylor vortices on the axial distribution of shear stress on the cylindrical walls. Their conclusion shows that the variation in the average azimuthal shear stress (induced by the vortices) is more relevant for reactors with relatively low aspect ratios. Results for the torque measurement are also compared against equations 2.43 and 2.45, and a good agreement is reported.

Laminar to turbulent transition is studied in Batten et al., 2002 for three radius ratios, namely $\eta = 0.734$, 0.941 and 0.985, in a range of Reynolds numbers between 5×10^3 and 5×10^4. Based on the observation that for fully turbulent regimes (TTVF) Taylor cells persist without waves, the authors adopted a two-dimensional axisymmetric domain, coupled with the $k - \omega$ model for turbulence. However, comparison against the formula proposed by Bilgen and Boulos, 1973 for the torque (equation 2.45) shows a significant deviation from the experimental data (up to 50%).

L. Wang, Marchisio, et al., 2005 and L. Wang, Vigil, et al., 2005 performed numerical (and experimental) investigations of aggregation processes in a Taylor-Couette reactor (with $\eta = 0.73$) for several regimes, namely TVF ($Re = 4Re_{cr}$), WVF

($Re = 12Re_{cr}$) and TTVF at Re =(34, 100, 160 and 220)Re_{cr}. The authors adopted 2D steady-state axisymmetric models (although waves are time-dependent and non-axisymmetric) and, for the turbulent cases, the Reynolds stress model (RSM) is found to produce the most accurate results. Comparison against Particle Image Velocimetry shows a good agreement for both axial and radial velocity profiles.

H. Wang, 2015 modelled the same Taylor-Couette device as L. Wang, Marchisio, et al., 2005 (i.e. $\eta = 0.73$, $\Gamma = 34$) and compared two- and three-dimensional unsteady RANS simulations (URANS), based on the $k - \varepsilon$ and $k - \omega$ turbulence models, against experimental data, up to $Re = 190Re_{cr}$. The author concluded that both turbulence closures result in an accurate description of the main features of Taylor-Couette flow and that 2D geometries provide a reliable alternative to the more expensive 3D simulations.

Nicoli et al., 2022 investigated the accuracy of several turbulence models by running unsteady RANS simulations. The authors modelled the geometry of L. Wang, Marchisio, et al., 2005 and a realistic aero engine bearing chamber (with $\eta = 0.577$ and $\Gamma = 0.47$). The main conclusion of the study is that a full 3D geometry is generally required to capture the complex features of turbulent Taylor-Couette flows and both the standard $k-\omega$ and RSM stress-BSL models are found to provide good results for the Taylor-Couette apparatus. In the case of the bearing chamber (where end effects are particularly relevant, due to the small aspect ratio), the SST $k - \omega$ turbulence model is the recommended approach.

Although RANS models have been proven to provide an accurate description of the main features of Taylor-Couette flows (e.g. average torque and velocity profiles), the detailed investigation into the turbulent characteristics and small-length structures require the use of high-fidelity approaches. Direct numerical simulations represent the most accurate methodology and several studies of Taylor-Couette flows with DNS have been published in the literature. In order to provide a general overview of the insights that can be achieved by means of DNS, some of the works based on direct numerical simulations are reviewed here. An exhaustive analysis of the literature of high-fidelity simulations of Taylor-Couette flows is out of the scope of the present thesis, and the interested reader is refereed to the following studied and the

references therein for a more comprehensive review.

Bilson and Bremhorst, 2007 performed direct numerical simulations of turbulent Taylor-Couette flow at $Re = 3200$ with $\eta = 0.617$ and $\Gamma = 4.58$. The authors reported of the onset of a secondary vortex motion in the near-wall region, where the primary Taylor cells are not present. This secondary flow is demonstrated to affect the shear stress distribution on the cylinder.

Pirrò and Quadrio, 2008 combined spectral and fourth-order finite difference methods and performed DNS in both laminar and turbulent regimes. For $\eta = 0.5$ and $\eta = 0.95$ they found a good agreement with the previous studies for the onset of the first instability at $Re \approx 68$ and $Re \approx 185$, respectively. The fully turbulent regime is modelled for $\eta = 0.882$ at $Re = 10500$, where two different turbulent mechanisms are identified, namely large-scale vortices and small-scale fluctuations induced by shear forces near the wall.

Dong, 2007 used a DNS approach based on a spectral method and investigated small-scale turbulent structures in Taylor-Couette flows with $\eta = 0.5$ and $Re = 1000$, 3000, 5000 and 8000. For $Re = 1000$, the annulus is entirely occupied by well organised Taylor vortices but for $Re > 5000$ the appearance of randomly distributed small-scale vortices near the walls is observed. The author reported that these structures (the so-called Görtler vortices, observed in the work of Barcilon et al., 1979 for Taylor-Couette flows) first appear at the inner cylinder, in the location close to the boundary between two (consecutive) diverging Taylor cells, i.e. the outflow region, where the flow is pushed away from the rotor. The fluctuating component of the azimuthal velocity field is also investigated, and a typical profile with two peaks at both the inner and outer walls is reported. The normalised magnitude of the fluctuations is found to decrease for increasing Reynolds numbers. The same numerical method is used in Dong, 2008 to study the effect of counter-rotating cylinders.

A detailed analysis of the boundary layer dynamics from laminar TVF to the turbulent regime is presented in Ostilla-Mónico et al., 2014. The authors used a second-order finite difference method for Reynolds numbers up to 10^5 with a radius ratio of $\eta = 0.714$. As was observed in Dong, 2007, in the laminar regime the flow is characterised by well organised cells that occupy the whole space between

the cylinders. As the flow transitions towards turbulence, an intermediate state (identified with the MWVF) is first approached, where both laminar and turbulent boundary layers coexist.

Razzak et al., 2019 investigated the viscous layer thickness at the wall to study the source and propagation of non-axisymmetric instabilities, i.e. from TVF to WVF, with $\eta = 0.5$ and Reynolds number in the range $60 < Re < 650$. The flow is found to be no longer axisymmetric at $Re = 425$ and an increase in the viscous layer thickness in some specific locations at the outer wall is believed to trigger the instability. Coherently with the findings of Koschmieder, 1979, the vortex wavelength is found to increase in the WVF compared to TVF.

Taylor-Couette devices have attracted the attention of chemical engineers due to their excellent mixing properties (see the introduction to Taylor-Couette reactors in section 7.2). Nemri et al., 2016 used DNS (and experiments) to investigate the transport of a passive tracer in Taylor-Couette flows at different laminar to turbulent regimes. Two main mixing mechanisms are observed, namely intra-vortex and inter-vortex mixing, whose combination is observed to enhance the axial dispersion of the tracer. This study also demonstrates the central role that high-fidelity simulations could play in quantifying the mixing in Taylor-Couette reactors and inform reduced order models commonly used in their design.

Due to the significant cost of direct numerical simulations, a popular choice is to reduce the axial extension of the computational domain to a multiple of the vortex wavelength λ (see, for example, Chouippe et al., 2014 or Nemri et al., 2016) and apply periodic boundary conditions at both the top and bottom ends of the domain. This could lead to significant deviations from experiments in the cases where the wavelength is not correctly reproduced. A detailed analysis on the effect of the domain size in numerical simulations of Taylor-Couette flows is discussed in Ostilla-Mónico et al., 2015, whilst a study on the reliability of periodic boundary conditions can be found in Xu et al., 2022, where the choice between no-slip walls or periodic boundaries is found to affect the onset of the first instability (TVF).

Bubbles in Taylor-Couette flows

The presence of a disperse bubbly phase in a Taylor-Couette device (as well as other type of reactors) is a common scenario for chemical processes that either involve gases (e.g. Dłuska et al., 2001, Lee et al., 2017, Qiao et al., 2018, Lee et al., 2020) or induce a spontaneous (and, generally, not desired) production of gas molecules (Love et al., 2021). The interaction of bubbles with hydrodynamic boundary layers on solid walls has also found interesting applications for drag reduction (Murai, 2014, H. Wang et al., 2022) and Taylor-Couette flow has been often used (along with other configurations, e.g. channel flows or flat plates) to investigate into such phenomenon (Murai et al., 2005, Van den Berg et al., 2005, Sugiyama et al., 2008, Murai et al., 2008, Van Gils et al., 2013). The choice of Taylor-Couette apparatus has the advantage that drag reduction can be readily monitored by measuring the torque on the inner rotor and that the flow exhibits statistically stationary states (i.e. TVF, WVF, MWVF and TTVF), which are well understood and can be easily controlled by tuning the rotating speed. The gain in terms of drag reduction that can be achieved by injecting a disperse bubbly flow is measured through the torque reduction ratio (TRR - see Sugiyama et al., 2008), defined as:

$$\mathrm{TRR} = 1 - \frac{T_w^b}{T_w} \tag{2.46}$$

where T_w and T_W^b are the torques with and without bubbles, respectively.

Murai et al., 2005 and Murai et al., 2008 performed an experimental investigation into the effects of a bubbly flow injected in a Taylor-Couette device with $\eta = 0.833$ and $\Gamma = 20$. The different flow states are observed at $Re = 92$ (TVF), $Re = 138$ (WVF), $Re = 1020$ (MWVF) and $Re = 1380$ (TTVF). The authors examined the range $600 < Re < 4500$ and, therefore, investigated the regimes between WVF and TTVF. The TRR (which reaches a maximum of 36% at $Re = 770$) is found to decrease with increasing Reynolds number and the drag reduction vanishes at $Re \approx 4000$. For $Re > 4000$, the injection of bubbles is observed to enhance the drag. Flow visualisations showed that, in the range of Reynolds numbers where

drag reduction is achieved, the injection of bubbles increases the wavelength of the vortices, i.e. less Taylor cells are observed in the gap. This mechanism is stronger for lower Re (λ is increased by 32% and 11% at $Re = 900$ and $Re = 1800$, respectively) and is believed to be linked to drag reduction, since no alteration of the vortical structures is observed at $Re = 4000$.

These results are confirmed by Sugiyama et al., 2008 who investigated the same geometrical configuration in a reduced range of Reynolds numbers ($600 < Re < 2500$). The authors used a numerical Eulerian-Lagrangian model where the carrier fluid and the (rigid) particles influence each other in a two-way coupling. A good agreement is obtained between experiments and numerical computations for the TRR and the analysis of Sugiyama et al., 2008 suggests that drag reduction occurs due to the break of dissipative Taylor cells through rising particles. Therefore, buoyancy is the driving force responsible for the reduced wall friction as confirmed by the numerical simulations where gravity is switched off and no drag reduction is achieved. The choice of modelling rigid particles is justified by the small size of bubbles used in the experiments of Murai et al., 2005 (the radius is approximately 0.6 mm and the corresponding Weber number is $We < 0.6$), for which no significant deformations are expected. The good agreement between these two works proves the reliability of such assumption.

Bubbles can be made less rigid by reducing the surface tension and the effect of the deformability of small (sub-Kolmogorov) bubbles is found to play a significant role for drag reduction (Spandan et al., 2017). In this numerical work, bubbles are treated as deformable ellipsoids and a Taylor-Couette device with $\eta = 0.833$ is modelled at $Re = 2500$ and $Re = 8000$. Bubbles are observed to adopt a prolate shape that is responsible for accumulation near the inner cylinder, where the breakup of the dissipative structures is enhanced. At $Re = 2500$, drag reduction is reported to be more efficient as the deformability of bubbles increases. On the other hand, almost null drag reduction is observed for $Re = 8000$, where turbulent fluctuations prevail on the perturbations induced by the bubbles. This is consistent with the findings reported in the works of Murai et al., 2005, Murai et al., 2008 and Sugiyama et al., 2008.

A different trend in the drag reduction was observed for larger Reynolds numbers. Van den Berg et al., 2005 used a Taylor-Couette device with $\eta = 0.73$ and $\Gamma = 11.5$ in highly-turbulent Reynolds numbers ($7 \times 10^4 < Re < 10^6$). They observed a small drag reduction (TRR $= 0.01 - 0.08$) up to $Re \approx 6 \times 10^5$ and a strong drag reduction (TRR up to 0.2) for $Re > 6 \times 10^5$. The boundary between these two regimes is identified by the value $We = 1$, where the Weber number is based on the velocity fluctuations u' (i.e. $u' = iU_{\text{in}}$ and i is the turbulent intensity). For $We < 1$ (where bubbles mostly behave as rigid particles), the (small) drag reduction is achieved through the effective compressibility of the flow (Ferrante and Elghobashi, 2004), where the bubble distribution removes the dissipative structures from the wall. The modest gain in terms of TRR is justified by the small amount of gas volume fraction injected in the apparatus. When $We > 1$ (where the size of the bubbles is significantly larger than the Kolmogorov scale), the large drag reduction regime is observed and this is assumed to be due to the deformability of bubbles. This mechanism is investigated in Lu et al., 2005, where the authors report that, in turbulent flows, deformable bubbles near a solid wall are able to modify the streamwise vortices in such a way to compensate the vorticity generated by the viscous shear stresses, resulting in an effective drag reduction.

The results reported in Van den Berg et al., 2005 are supported by the similar findings of Van Gils et al., 2013 for a reactor with $\eta = 0.72$ and $\Gamma = 11.7$ in the Reynolds range $5 \times 10^5 - 2 \times 10^6$. The authors observed a small drag reduction regime (TRR $= 0.07$) for $Re = 5.1 \times 10^5$ and a strong drag reduction for $Re > 10^6$, with a peak of TRR $= 0.4$ at $Re = 2 \times 10^6$ (for a gas volume fraction of 4% within the apparatus). The boundary between the two drag reduction regimes is consistent with the results of Van den Berg et al., 2005, i.e. drag reduction increases when deformable bubbles are close to the wall ($We > 1$). Interestingly, the presence of bubbles near the wall is larger in the moderate drag reduction case, where $We \approx 1$. This further confirms the central role of bubbles deformability.

A summary of the main trends in drag reduction discussed so far is reported in Figure 2.14. From these studies, different behaviours seem to occur between the ranges $Re < 5 \times 10^3$ (Murai et al., 2005, Murai et al., 2008, Sugiyama et al., 2008)

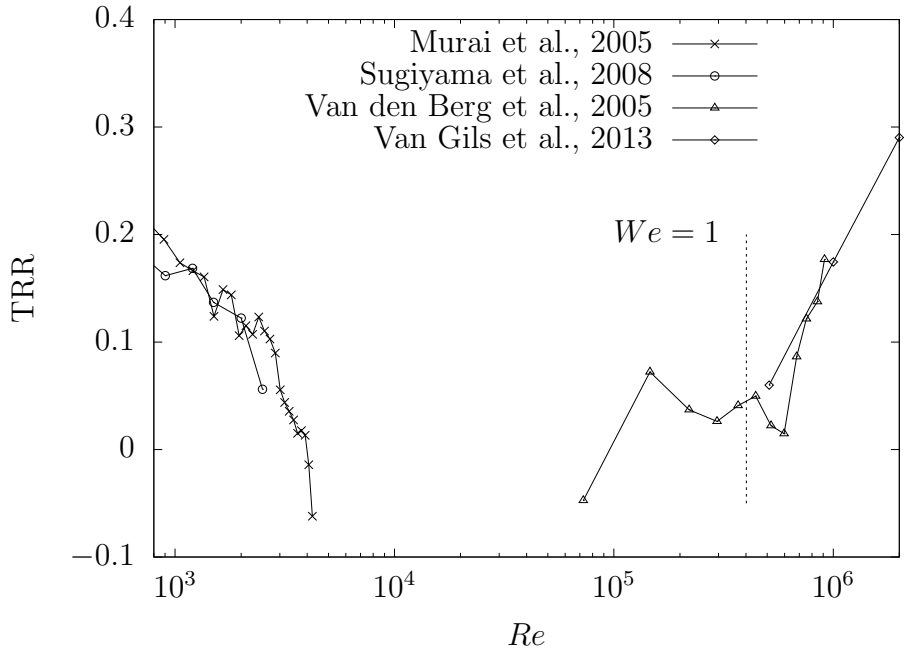

Figure 2.14: Torque reduction ratio Vs Re. Two different behaviours are observed in the ranges $Re < 5 \times 10^3$ and $Re > 7 \times 10^4$. The vertical line at $We = 1$ separates the small and strong drag reduction regimes in the experiments of Van den Berg et al., 2005. The same line is shifted towards $Re = 5.1 \times 10^5$ in the measurements of Van Gils et al., 2013. Data from Van den Berg et al., 2005 and Van Gils et al., 2013 are reported here for a gas volume fraction of 3%.

and $Re > 7 \times 10^4$ (Van den Berg et al., 2005, Van Gils et al., 2013) and more work is needed to understand the role of bubbles for $5 \times 10^3 < Re < 7 \times 10^4$. The shear stress exerted on the cylinders is clearly dependent on the distribution of bubbles within the reactor. In the following, the main observed patterns are briefly discussed.

Shiomi et al., 1993 investigated bubble patterns in Taylor-Couette flow with $\eta = 0.9$ and moderate gas and liquid volumetric fluxes up to $0.0647\,\mathrm{m\,s^{-1}}$ and $0.268\,\mathrm{m\,s^{-1}}$ (note that a flow configuration with a superimposed axial flow rate is generally referred to as Poiseuille-Taylor-Couette flow - see Nemri et al., 2013). When the rotating speed is low, bubbles tend to rise in a uniformly distributed way (disperse flow). As the rotor is accelerated, bubbles organise into a spiral pattern and, for

large rotating speeds, bubbles accumulate into stable locations and follow circular trajectories (ring pattern).

These preferential patterns are qualitatively confirmed by the visualisations reported in Murai et al., 2005, where the gas flow rate is varied up to $1.67 \times 10^{-6} \mathrm{m}^3\,\mathrm{s}^{-1}$. At $Re = 600$ ($Re/Re_{cr} = 6.5$), a disperse bubbly flow is observed, where the bubbles tend to rise close to the inner cylinder (Figure 2.15a). As the rotating speed is increased above $Re = 1200$, bubbles tend to migrate towards specific locations near the rotor (see Figure 2.15b). These preferential locations consist of the outflow

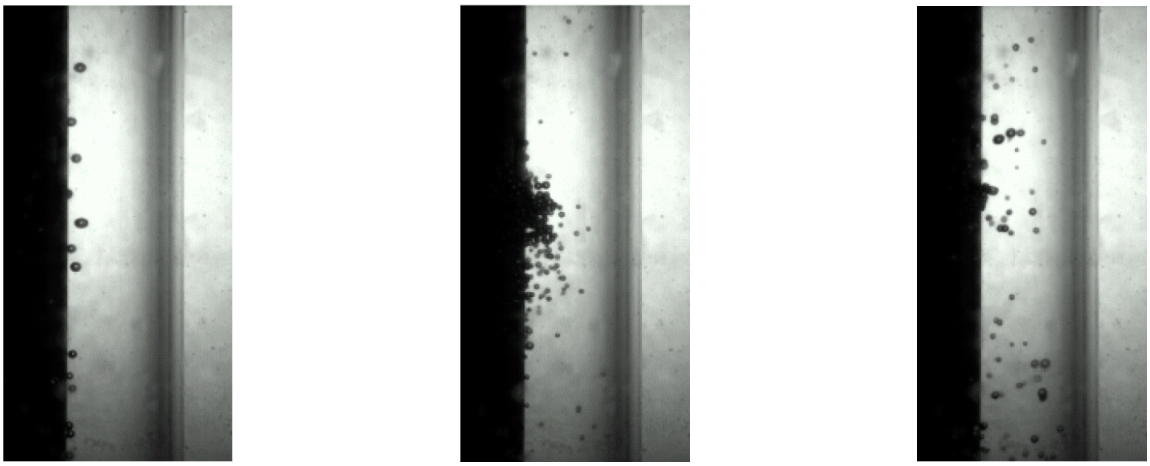

(a) $Re = 600$ (b) $Re = 1700$ (c) $Re = 3900$

Figure 2.15: Bubble accumulation patterns at different Reynolds numbers. The black body is the inner cylinder. Figures taken from Murai et al., 2005.

regions between Taylor cells, where the liquid is pushed away from the inner cylinder. When the downward velocity is large enough to counterbalance buoyancy, these locations transform into stagnant regions where bubbles form agglomerates. For increased Reynolds numbers, both spiral and ring patterns are reported and the radial distribution of bubbles tends to be more uniform (Figure 2.15c). As was already introduced before, the wavelength of Taylor cells is found to increase with respect to the single-phase configuration.

A similar elongation (as well as migration mechanism towards the outflow regions) of the vortices is observed in Djeridi et al., 2004 for $\eta = 0.857$ and $\Gamma = 20$, where the

wavelength increases by 45% at $Re/R_{cr} = 10$. In this work, bubbles are introduced in the device through either ventilation from the upper free surface or cavitation. A ring pattern is observed for Reynolds numbers as low as $Re = 350$, where the bubbles are trapped into the vortical structures and follow the azimuthal waves. In the work of Murai et al., 2005, for such low Re values, a bubbly disperse flow is observed instead. Differences can be potentially due to the size of the bubbles and/or the way they are generated (i.e. injection Vs ventilation or cavitation). Two different regimes are observed in the work of Djeridi et al., 2004, namely $2.5 < Re/Re_{cr} < 7.5$ and $7.5 < Re/Re_{cr} < 20$. In the first case, bubbles are passively transported by the flow, whilst in the second regime the interaction between the disperse phase and the carrier flow is observed to affect both the wavelength and azimuthal wave number.

The increased axial wavelength observed in bubbly Taylor-Couette flows under certain conditions was deeply investigated in the work of Mehel et al., 2007 in an apparatus with $\eta = 0.91$ and $\Gamma = 40$. Bubbles that accumulate in the outflow regions are observed to increase the size of Taylor cells due to a decrease in the vorticity. On the other hand, the bubbles that are trapped within the vortex cores tend to stabilise the cells, which results in a reduced size. The same mechanism is observed in the experimental work of Ymawaki et al., 2007 for a radius ratio of $\eta = 0.658$ in the range $336 < Re < 1442$, where bubbles are observed to move from a disperse pattern (low Re) to a spiral one (moderate Re) and finally approach a ring trajectory for large enough rotating speeds. Larger gas flow rates promote transition to a spiral pattern and the axial wavelength of vortices in the ring pattern is generally shorter than the spiral configuration.

A direct numerical method (DNS) based on an Euler-Lagrange approach where the carrier flow is not affected by the disperse phase (i.e. one-way coupling) is adopted in Climent et al., 2007 to investigate the relative magnitudes of the forces that drive the bubbles to preferential trajectories. The magnitudes of the downward velocity induced by the vortices and the upward one due to gravity are compared by means of the non-dimensional ratio:

$$C = \frac{u^{TV}}{U_b} \tag{2.47}$$

where u^{TV} is a characteristic velocity of the secondary flow (radial and axial components of the vortices), whilst U_b is the terminal bubble rising velocity. The transport in the radial direction is estimated by comparing the effects of the centripetal force induced by the rotor ($\propto U_{\text{in}}^2/r_{\text{in}}$) and the convective transport of momentum $\left(\propto \left(u^{TV}\right)^2/(r_{\text{out}}-r_{\text{in}})\right)$:

$$H = 4\left(\frac{u^{TV}}{U_{\text{in}}}\right)^2 \frac{r_{\text{in}}}{r_{\text{out}}-r_{\text{in}}} \tag{2.48}$$

Three regimes are identified in the (C, H) plane: for low values of C, buoyancy is predominant and bubbles tend to rise close the inner cylinder (consistent with the findings of Murai et al., 2005); for large C and low H the centripetal force attracts the disperse phase towards the stable outflow regions at the rotor, whilst for large C and H bubbles are trapped within the vortex cores.

The same direct numerical approach (i.e one-way Euler-Lagrange coupling) was used by Chouippe et al., 2014 for a large gap configuration ($\eta = 0.5$) in the TTVF regime ($Re = 5000$) and two different bubble radii, namely $R_b = 2 \times 10^{-4} r_{\text{out}}$ and $R_b = 2 \times 10^{-3} r_{\text{out}}$, are simulated. This methodology allows to model a large number of bubbles, which is set to 10^6 in this study. Bubbles are initialised close to the inner cylinder and the presence of outflow jets redistribute the concentration of bubbles towards the outer wall. For this high rotational speed, the centripetal force and buoyancy are predominant and bubbles adopt a spiral pattern, as confirmed by the visualisation reported in Murai et al., 2005. The transport towards the outflow regions (induced by the vortices) is not observed for this configuration.

The main limitation of standard Lagrangian approaches for the tracking of particles consists of the assumption of perfectly rigid bubbles. As was discussed in sections 2.1.3 and 2.2.1, bubbles can exhibit strong deformations (according to Bond, Weber and Capillary numbers) and their effect on Taylor vortices is generally not negligible (see the above discussion on the role of bubble deformability for drag reduction). Another limitation of the two previously discussed studies (Climent et al., 2007, Chouippe et al., 2014) is the one-way coupling approach, which neglects the pertur-

bations exerted on the carrier fluid by the disperse phase. An improvement to the Euler-Lagrange modelling discussed so far is presented in Spandan et al., 2017, where particles are still tracked through a Lagrangian scheme but they are assumed to be deformable ellipsoids. The deformation is computed with a subgrid-scale model and the two phases interact in a two-way coupling.

An alternative approach based on a Euler-Euler model where the two phases affect each other through interfacial momentum exchange terms is proposed in Gao, Kong, and Vigil, 2015 (2D and 3D) and Gao et al., 2016 (2D only). A RANS turbulence closure (Reynolds stress model - RSM) is used in Gao, Kong, and Vigil, 2015, where the same reactor from the experiments of Murai et al., 2005 is modelled ($\eta = 0.833$ and average bubble radius of $R_b = 0.6\,\mathrm{mm}$) by varying the Reynolds number in the range $600 < Re < 3900$. A good comparison between experiments and simulations is obtained for the radial distribution of gas within the annuls, confirming the appropriateness of this modelling choice. The effect of increasing the gas flow rate is found to be responsible for the axial elongation of Taylor vortices and, for sufficiently large flow rates, the disperse phase can disrupt the toroidal cells. Two different turbulence models ($k-\varepsilon$ and $k-\omega$) are compared in Gao et al., 2016 for a device with $\eta = 0.716$ and Reynolds numbers up to $Re = 5.1 \times 10^5$. The $k-\omega$ model is found to be more accurate for the prediction of the main azimuthal velocity component. From these two studies (Gao, Kong, and Vigil, 2015, Gao et al., 2016) the radial distribution of bubbles is found to be mainly determined by the effects of pressure gradient and turbulence dispersion force.

Although the numerical studies discussed in this review were able to predict and explain some of the phenomena observed in experiments with bubbly flows, the use of either Euler-Lagrange or Euler-Euler schemes relies on the choice of suitable models for the gas-liquid interaction, which are generally based on empirical correlations (e.g. drag and lift coefficients, virtual mass effects). Especially in the case of large bubbles, where deformations have a significant effect on Taylor-Couette flow, a fully resolved simulation (with methods like the Front Tracking, Level Set or Volume of Fluid) is probably needed to investigate the behaviour of bubbles and, eventually, inform Euler-Lagrange and Euler-Euler models. A drawback of such high-fidelity

approach is clearly related to the number of bubbles that can be modelled, which is strongly limited by the computational cost compared to what can be achieved with a Lagrangian method. To the best of the author's knowledge, no studies have been published on the modelling of bubbles in Taylor-Couette reactors by means of fully resolved approaches. The numerical study of a bubble in different Taylor-Couette regimes that is presented in section 7.2.3 is therefore one of the original contributions of the present thesis.

2.3 Mass transfer of soluble species

This section will address the following points:

- Diffusion-driven mass transfer process.
- Physisorption and chemisorption.
- Henry's law.
- Fick's law.
- Non-dimensional numbers for the description of mass transfer of soluble species.
- Analytical and empirical models for the prediction of mass transfer coefficients in bubbly flows.
- Concentration and hydrodynamic boundary layers.
- Two film theory for the prediction of mass transfer rates.
- State of the art numerical methods for fully resolved simulations of phase-change flows: treatment of velocity and concentration discontinuities.

The transfer of soluble species across the gas-liquid interface in two-phase systems is at the basis of several chemical processes, like the absorption of CO_2 in aqueous NaOH (Krauß and Rzehak, 2018) or the desorption of hydrogen sulphide (H_2S) from

water (Teuber et al., 2019). When absorption/desorption occurs without involving any chemical reactions, the process is referred to as physisorption. However, specific chemical components can be introduced to trigger a reaction with the transferable species in order to enhance the overall mass transfer rate; in this case the process is called chemisorption.

Physisorption is first discussed in section 2.3.1 along with the main assumptions used in this thesis for the treatment of soluble species. A simple analytical model (two film theory) is introduced in section 2.3.2 for the cases that involve chemical reactions. Finally, a literature review on the state of the art numerical methods for the interfacial transport of species in two-phase systems is presented in section 2.3.3.

2.3.1 Physisorption: a diffusion-driven process

A soluble gas in a two-phase gas-liquid system at equilibrium is partially dissolved into the liquid solution with a concentration (c_c [$\mathrm{mol\,m^{-3}}$]) that depends on the partial pressure (p) exerted by the gas on the interface between the phases:

$$c_c = pH'_e \tag{2.49}$$

Equation 2.49 is known as Henry's law and H'_e is Henry's law coefficient (measured in [$\mathrm{mol\,m^{-3}\,Pa^{-1}}$]). Assuming the gaseous species as a perfect gas, equation 2.49 can be rewritten as:

$$c_c = c_d RT H'_e = \frac{c_d}{H_e} \tag{2.50}$$

where R and T are the ideal gas constant and temperature, respectively. The concentration of gas in the disperse phase (c_d) is assumed uniform and this version of Henry's law coefficient H_e ($= 1/RTH'_e$) is a non-dimensional constant. The coefficient H_e is generally a function of the temperature and pressure fields in both phases (see Bothe and Fleckenstein, 2013). However, in this work it is assumed to be a constant property of the specific gas-liquid system. Equation 2.50 is also valid in the case of non-uniform disperse concentrations as long as the interface is at equilibrium

(i.e. saturated). In this case, Henry's law applies at the interface (Σ) and reads:

$$(c_c)_\Sigma = \frac{(c_d)_\Sigma}{H_e} \tag{2.51}$$

where $(c_d)_\Sigma$ and $(c_c)_\Sigma$ are the concentrations at the disperse and continuous sides of the interface, respectively. Henry's law coefficient is generally $H_e \neq 1$, meaning that the concentration is discontinuous at the interface. In this thesis, the interface is assumed saturated and Henry's law can always be applied at Σ. If not specified otherwise, Equation 2.51 and H_e are the versions of Henry's law and relative coefficient that will be used in the rest of the work.

If the concentration of species in the liquid phase is equal to the equilibrium value at the interface (i.e. $c_c = (c_c)_\Sigma = (c_d)_\Sigma / H_e$), the liquid is said to be saturated (note that this is different from a saturated interface, which refers only to the jump in concentrations across Σ) and no net mass transfer of gas will occur between the phases. However, in the cases where the concentration in the liquid solution is either lower or larger than the saturated value, the system is not at equilibrium and some exchange of gas across the interface will occur in order to re-establish a saturated system. To classify the system in terms of species equilibrium, the saturation ratio is generally used:

$$\zeta = \frac{c_{\text{bulk}}}{(c_c)_\Sigma} \tag{2.52}$$

which compares the amount of concentration in the bulk liquid against the saturated value at the interface. Here, the bulk liquid has been introduced (c_{bulk}) to remind that ζ is defined for an idealised system with a uniform concentration in the liquid phase. In a generic system, c_c is non-uniform and the saturation ratio could be eventually defined as a local quantity at the interface, by comparing $(c_c)_\Sigma$ with the near field concentration. Depending on the value of ζ, the solution can be classified as:

- saturated, if $\zeta = 1$
- super-saturated, if $\zeta > 1$

- under-saturated, if $\zeta < 1$

If the solution is super-saturated, an excess of gas is dissolved into the liquid and the system will transfer some of the gaseous species from the liquid side of the interface to the gas phase. In an under-saturated scenario, physisorption will act in the opposite way, redistributing some of the gas molecules from the disperse phase to the continuous one. These three scenarios ($\zeta = 1$, $\zeta > 1$ and $\zeta < 1$) are schematically represented in Figure 2.16 for the concentration around a bubble.

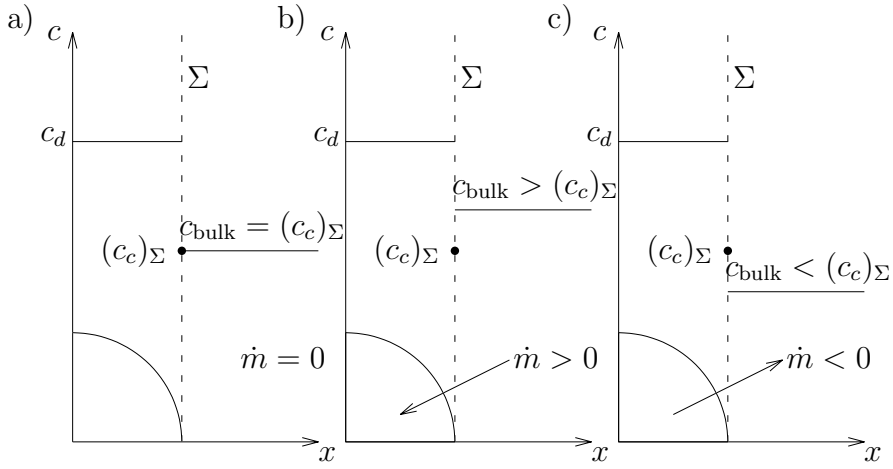

Figure 2.16: Concentration profiles and mass transfer for saturated (a), super-saturated (b) and under-saturated (c) solutions.

The mechanism at the basis of the interfacial transfer of gas molecules in super- and under-saturated systems is a diffusion-driven process that depends on the local concentrations at the interface (see, for example, Groß and Pelz, 2017). In this thesis, the gas phase is the only soluble species (i.e. the liquid is not volatile) and is assumed to be dilute. Under this assumption, the interfacial mass transfer rate [$\mathrm{kg\,m^{-2}\,s^{-1}}$] can be computed with Fick's law of diffusion (Fick, 1855):

$$\dot{m} = -MD_c \frac{\partial c_c}{\partial \mathbf{n}_\Sigma} \tag{2.53}$$

where M and D_c are the molar mass and diffusivity of the species in the liquid, respec-

tively. The gradient of concentration is computed at the liquid side of the interface, where $\mathbf{n}_\Sigma$ is the normal direction pointing towards the gas phase. The mass transfer rate is assumed positive for super-saturated solutions (see Figure 2.16). Equation 2.53 can be used in this form when the soluble species is a marginal component of the gaseous phase and its transport across the interface does not affect significantly the volume of the phases. For pure bubbles (or highly concentrated species in the disperse phase), an additional term appears in equation 2.53, which will be appropriately discussed in section 3.3 (this extra term is not relevant for the purposes of this section).

From equation 2.53, it appears evident that the magnitude of the mass transfer rate depends on the profile of concentration at the liquid-side of the interface. In the case of a bubble rising in an under-saturated solution, the species released into the liquid is transported through advection and diffusion, and forms a thin concentration boundary layer (δ_c) around the bubble interface. This mechanism is conveniently described by introducing the following non-dimensional groups. In diffusion-driven processes, the effects of momentum diffusion (due to viscosity) and diffusive transport of species in the liquid phase are compared through the Schmidt number:

$$Sc = \frac{\nu_c}{D_c} \tag{2.54}$$

For advection-diffusion problems, the relative importance between these two transport mechanism is estimated by the Péclet number:

$$Pe = Re_b Sc \tag{2.55}$$

where Re_b refers to the Reynolds number of the rising bubble (equation 2.1). The larger is the Péclet number, the stronger is the advective transport, which in turn results in a thinner concentration boundary layer. The problem of physisorption in rising bubbles is generally an advection-dominated problem (large Pe), as can be seen by considering the case of a 1 mm (diameter) bubble of oxygen rising in water at 20 °C. For this problem, Weiner and Bothe, 2017 report that the terminal velocity

is $U_b \approx 0.25\,\mathrm{m\,s^{-1}}$ and the characteristic non-dimensional numbers are $Re_b = 250$, $Sc = 500$ and $Pe = 1.25 \times 10^5$. In this range of Péclet numbers, the thickness of the concentration boundary layer is of the order of few microns. From equation 2.53 it appears evident that a smaller δ_c enhances the mass transfer rate, since the corresponding concentration profile is steeper.

The force that drives the diffusive transport across the interface is related to the difference in concentration between the interface and the bulk of the liquid, i.e. $\Delta c = (c_c)_\Sigma - c_{\mathrm{bulk}}$. Based on this difference, a mass transfer coefficient $[\mathrm{m\,s^{-1}}]$ can be defined as:

$$k_m = -\frac{\int_\Sigma \dot{m}\, dS}{A_\Sigma M \Delta c} \tag{2.56}$$

where A_Σ is the global area of the gas-liquid interface. A non-dimensional version of the mass transfer coefficient is obtained by comparison against the characteristic velocity of diffusion. The Sherwood number serves this purpose:

$$Sh = \frac{k_m L_{\mathrm{ref}}}{D_c} \tag{2.57}$$

where the reference length for bubbly flows is generally set to the bubble diameter, i.e. $L_{\mathrm{ref}} = D_b$.

The Sherwood number offers a convenient description of the mass transfer process and many research efforts were made to derive predictive formulae for this parameter in bubbly flows. For a generic spherical bubble with radius R_b immersed in a solution with a uniform concentration c_{bulk}, the diffusion of a species $(c_c(r,t))$ out of the interface is described by a convection-diffusion equation:

$$\begin{aligned} \partial_t c_c + \mathbf{u}\cdot\nabla c_c &= \nabla\cdot(D_c \nabla c_c) \\ c_c(r,0) &= c_{\mathrm{bulk}} \qquad \text{for} \quad r > R_b \\ c_c(R_b,t) &= (c_c)_\Sigma \qquad \text{for} \quad t > 0 \\ \lim_{r\to\infty} c_c(r,t) &= c_{\mathrm{bulk}} \qquad \text{for} \quad t > 0 \end{aligned} \tag{2.58}$$

For the simplified case of a fixed (i.e. not rising) spherical bubble in a steady

state, the transport equation reduces to (Crank, 1975):

$$\frac{d}{dr}\left(r^2\frac{dc_c}{dr}\right) = 0 \tag{2.59}$$

and the solution for the gradient of concentration at the interface ($r = R_b$) reads:

$$\left(\frac{dc_c}{dr}\right)_{r=R_b} = -\frac{(c_c)_\Sigma - c_{\text{bulk}}}{R_b} \tag{2.60}$$

Combining this with equations 2.53 and 2.57 gives $Sh = 2$.

The case of a fixed particle is clearly not representative of real applications, where bubbles generally rise. For a rising spherical bubble (with terminal velocity U_b) in a steady state regime, the following solution (see Lochiel and Calderbank, 1964) can be obtained for large Péclet numbers (which is an assumption generally representative of many applications):

$$Sh = \sqrt{\frac{2}{\pi}}\left[\int_0^\pi \frac{(u_\varphi)_{r=R_b}}{U_b}\sin^2\varphi\, d\varphi\right]^{1/2}\sqrt{Pe} \tag{2.61}$$

where u_φ is the tangential velocity component. Equation 2.61 is actually valid in the limit $Pe \to \infty$.

For low Reynolds applications, the Hadamar-Rybczynski solution (see section 2.1.2) for a bubble rising in a creeping flow (valid for $Re_b < 1$) can be substituted in equation 2.61 and the corresponding Sherwood number is (see Clift et al., 1978):

$$Sh = 0.651\sqrt{\frac{Pe}{1+\mu_r}} \tag{2.62}$$

In the opposite regime, i.e. $Re_b \to \infty$, the potential flow theory provides a sensible description of the flow field around the interface (see section 2.1.2). Using the potential solution in equation 2.61 gives (Clift et al., 1978):

$$Sh = \frac{2}{\sqrt{\pi}}\sqrt{Pe} \tag{2.63}$$

Other theoretical solutions were derived for the prediction of Sh in bubbly flows. In this thesis, the formulae proposed by Oellrich et al., 1973 are compared against the numerical solution for the mass transfer in a Taylor-Couette reactor. These correlations were formulated for two opposite regimes, namely small bubbles:

$$Sh = 2 + 0.651 \frac{Pe^{1.72}}{1 + Pe^{1.22}} \quad \text{for } Re_b \to 0, Sc \to \infty \tag{2.64}$$

and large bubbles:

$$Sh = 2 + \frac{0.232 Pe^{1.72}}{1 + 0.205 Pe^{1.22}} \quad \text{for } Re_b \to \infty, Sc \to 0 \tag{2.65}$$

Given the complex time-dependent features that a rising bubbles may exhibit in terms of shape, velocity and trajectory, theoretical formulae are often valid under severe assumptions (e.g. spheroidal bubbles, rectilinear trajectories, steady-state regime). Experiments and/or numerical simulations are therefore needed to compute accurate values of the mass transfer. Amongst the experimental formulae, it is reported here the empirical correlation proposed by Takemura and Yabe, 1998 (which will be used in section 6.2.4 for the validation of the numerical model), valid in the range $Re_b < 100$ and $Pe > 1$:

$$Sh = \frac{2}{\sqrt{\pi}} \left[1 - \frac{2}{3} \frac{1}{\left(1 + 0.09 Re_b^{2/3}\right)^{3/4}} \right]^{1/2} \left(2.5 + \sqrt{Pe}\right) \tag{2.66}$$

Equations 2.61 - 2.66 clearly show the importance of the Péclet number in the mass transfer process, and they all predict for large Pe a functional dependence of the type $Sh \propto \sqrt{Pe}$. A complete review on the available models for the prediction of Sherwood numbers in bubbly flows is out of the scope of the present work. The interested reader is referred to Clift et al., 1978, Deising et al., 2018 and the references therein for a detailed discussion on the topic.

The characteristic length scale of mass transfer is typically smaller than the corresponding hydrodynamic one. The hydrodynamic boundary layer thickness (δ_h) can

be approximated as (Levich, 1962):

$$\delta_h \approx \frac{D_b}{\sqrt{2Re}} \tag{2.67}$$

Considering a uniform concentration boundary layer, where the entire Δc is applied within δ_c, the following formula is readily obtained:

$$\delta_c = \frac{D_b}{Sh} \tag{2.68}$$

Given the functional relationship between Sh and Pe (i.e. $Sh \propto \sqrt{Pe}$) discussed above, the ratio of concentration to hydrodynamic boundary layer thicknesses evolves as $\delta_c/\delta_h \propto 1/\sqrt{Sc}$ (see, for example, Bothe and Fleckenstein, 2013). For the case of the oxygen bubble presented before (taken from Weiner and Bothe, 2017), the hydrodynamic boundary layer thickness is estimated to be (equation 2.67) $\delta_h \approx 45\,\mu m$, whilst Sherwood (equation 2.63) and the concentration boundary layer (equation 2.68) are approximately $Sh \approx 400$ and $\delta_c \approx 2.5\,\mu m$, respectively. This example clearly shows that the limiting factor in terms of numerical resolution of the length scales is dominated by the mass transfer of species (i.e. $\delta_c < \delta_h$). This indeed represents one of the biggest challenges for fully resolved numerical simulations of mass transfer in rising bubbles.

2.3.2 Two film theory

A generic heterogeneous (i.e. where two or more phases are involved) reaction in a gas-liquid system between two species A and B can be described by the following stoichiometric equation:

$$A_{(d\rightarrow c)} + bB_c \rightarrow P \tag{2.69}$$

where P is the product of the reaction and b is a coefficient. Species A is initially concentrated within the dispersed phase, whilst B is distributed in the liquid solution. Here, it is assumed that A is soluble in the liquid, but B cannot be transferred to the gaseous phase. Under these assumptions, the reaction can only take place within

the continuous phase, after A is transferred from the gas phase to the liquid one ($d \rightarrow c$). In the case of an elementary reaction, the rate of conversion of A and B depends on the number of collisions between these two species, which is proportional to the product of the concentrations. Therefore the rate of disappearance of A and B (r^A and r^B, respectively) in terms of moles per unit volume of liquid (V_c) and time [$\mathrm{mol\,m^{-3}\,s^{-1}}$] is given by:

$$-r^A = -\frac{1}{V_c}\frac{dQ^A}{dt} = kc_c^A c_c^B = -\frac{r^B}{b} \tag{2.70}$$

where Q^A is the number of moles of species A and k is the reaction rate constant. The nomenclature adopted here for the concentration reminds that the reaction is governed by the concentrations of A and B in the continuous phase only and, for the specific case of equation 2.70, the reaction is assumed of second order. For a generic n-th order reaction, the reaction rate is expressed in [$\mathrm{s^{-1}(mol\,m^{-3})^{1-n}}$]. Another useful way of representing the rate of disappearance of A in heterogeneous reactions is obtained by looking at the rate of moles that are transferred across the gas-liquid interface per unit interfacial area (which are assumed to react entirely in the liquid solution):

$$-r''^A = -\frac{1}{A_\Sigma}\frac{dQ^A}{dt} \tag{2.71}$$

The two rates of equations 2.70 and 2.71 are clearly related through the expression: $r^A = r''^A A_\Sigma / V_c$.

A simple model to represent the physisorption of A consists of looking at the transport of the species from the gas to the bulk liquid as a process that undergoes two resistances in series that occur in two thin film regions next to the interface (see Figure 2.17). This model is the so-called two film theory (TFT), originally proposed by Whitman, 1923, and has the advantage of providing a simple approach to investigate the main parameters that affect the transfer of soluble species. The TFT can be applied to a wide range of scenarios; here only the key points are introduced and the reader is referred to Levenspiel, 1998 for a more detailed discussion.

The first resistance to mass transfer occurs in the gas phase, where the transfer

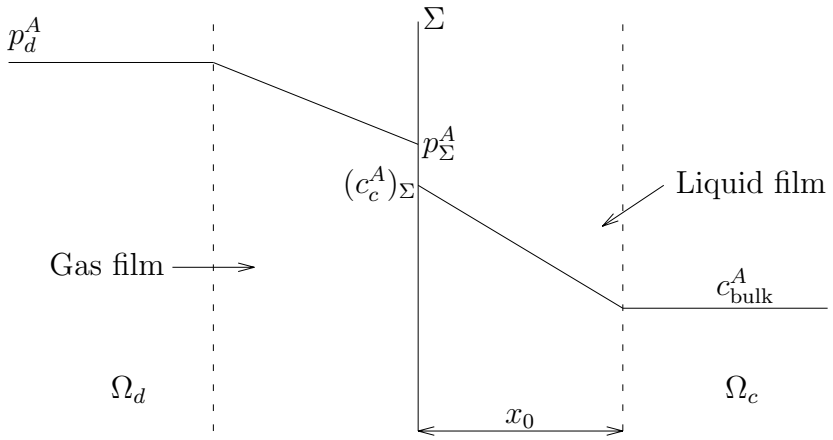

Figure 2.17: Two film theory for the physisorption of species A.

of A is driven by the difference between the partial pressures in the bulk gas (p_d^A) and at the interface (p_Σ^A), as shown in Figure 2.17:

$$r''^A = k_d^A \left(p_d^A - p_\Sigma^A\right) \tag{2.72}$$

where k_d^A is a version of the mass transfer coefficient related to the pressure difference and is expressed in $[\text{mol}\,\text{m}^{-2}\,\text{Pa}^{-1}\,\text{s}^{-1}]$. For the continuity of mass, the moles that cross the interface from the gas side reach the bulk liquid (where the concentration is c_{bulk}^A) through the liquid film, where a second resistance occurs. The mass transfer in this region is driven by the difference in concentrations:

$$r''^A = k_m^A \left(\left(c_c^A\right)_\Sigma - c_{\text{bulk}}^A\right) \tag{2.73}$$

where k_m^A is the same mass transfer coefficient first introduced in equation 2.56. Assuming a linear profile of concentration within the liquid film and applying Fick's law of diffusion (equation 2.53), k_m^A can be rewritten as:

$$k_m^A = \frac{D_c^A}{x_0} \tag{2.74}$$

where x_0 is the thickness of the liquid film (Figure 2.17) and D_c^A is the diffusivity of species A in the continuous phase. Finally, combining equations 2.72 - 2.73 with Henry's formula (in the form of equation 2.49), the rate of disappearance of A can be written as:

$$-r''^A = \frac{1}{\frac{1}{k_d^A} + \frac{1}{k_m^A H_e'^A}} \left(p_d^A - \frac{c_{\text{bulk}}^A}{H_e'^A} \right) \tag{2.75}$$

In the case where the reaction with species B (equation 2.69) occurs, the rate of disappearance of A depends also on the concentration of B available near the liquid film. Here, the reaction is assumed to be instantaneous and to take place in a location within the liquid film where both A and B are present. Such location is called the reaction plane (see Figure 2.18). The position of the reaction plane is clearly affected

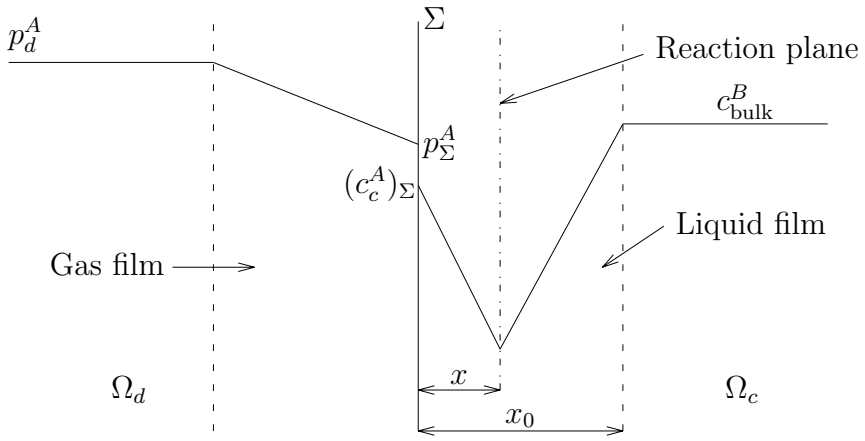

Figure 2.18: Two film theory for the chemisorption of species A. The reaction with species B occurs instantaneously in the liquid film.

by the partial pressure p_d^A within the disperse phase and the concentration of B in the bulk liquid (c_{bulk}^B). A larger pressure p_d^A increases the amount of available moles of A within the film liquid and, in this case, the limiting factor for the reaction is given by the concentration of B. Therefore, the reaction plane moves towards the liquid bulk where larger concentrations of B are available. In the opposite scenario of an increase in c_{bulk}^B, the limiting factor is given by the availability of A and the

reaction plane moves towards the interface accordingly. In the limiting case of a very large c^B_{bulk}, the reaction plane overlaps the interface, i.e. the reaction occurs at Σ.

In a steady state regime, where all the moles of A and B that diffuse into the liquid film react at the reaction plane, the rate of disappearance of species A and B can be written as:

$$-r''^A = -\frac{r''^B}{b} = k^A_d \left(p^A_d - p^A_\Sigma\right) = k^A_m \left(c^A_c\right)_\Sigma \frac{x_0}{x} = k^B_m c^B_{\text{bulk}} \frac{x_0}{x_0 - x} \tag{2.76}$$

where the last three terms represent the gas resistance for A and liquid resistances for A and B, respectively. The coefficients k^A_m and k^B_m refer to the case when no reaction occurs and the species diffuses across the whole film thickness x_0 (equation 2.74); for this reason the distance between the reaction plane and the interface (x) appears in equation 2.76 (see Figure 2.18). Taking into account the definitions of k^A_m, k^B_m and Henry's law, equation 2.76 can be rewritten as:

$$-r''^A = \frac{\frac{D^B_c}{D^A_c}\frac{c^B_{\text{bulk}}}{b} + p^A_d H'^A_e}{\frac{H'^A_e}{k^A_d} + \frac{1}{k^A_m}} \tag{2.77}$$

In applications involving pure incompressible gas phases, i.e. where the disperse phase consists of a single species (A in this example), the concentration of A inside the disperse phase is uniform, since the density is assumed constant. In this case, the pressure of A within the gas region is uniform (i.e. $p^A_d = p^A_\Sigma$) and the resistance to mass transfer given by the gas film vanishes (which is equivalent to assume $k^A_d \to \infty$). Under these assumptions, the rate of disappearance of A is entirely determined by the diffusion across the liquid film and the corresponding model is generally referred to as film theory (FT). A similar scenario occurs often in bubbly flows even in the presence of a mixture of species since, due to the typical size of bubble diameters in chemical reactors (few millimeters) and to the larger diffusivity in the gas phase compared to the liquid one (for CO_2 the diffusivity in air is approximately 10^4 times the diffusivity in water - see Pritchard and Currie, 1982 and Cadogan et al., 2014), the concentrations of the soluble species can be assumed uniform inside the bubbles.

Under these assumptions (i.e. negligible gas resistance), a simplified formula for the chemisorption can be obtained from equation 2.77:

$$-r''^{A} = k_m^A \left(c_c^A\right)_\Sigma \left(1 + \frac{D_c^B c_{\text{bulk}}^B}{b D_c^A \left(c_c^A\right)_\Sigma}\right) \tag{2.78}$$

From equation 2.78, it appears evident that the presence of a reaction enhances the transport of A from the gas phase, since the value within the parentheses is always larger than one. This is related to the the gradient of A (which is consumed by the reaction) within the liquid film, which is generally steeper compared to the case without reaction.

A quantitative way to estimate the mass transfer enhancement due to the reaction is given by the non-dimensional Hatta number, which compares the rate of reaction in a saturated solution, i.e. $c_{\text{bulk}}^A = \left(c_c^A\right)_\Sigma$, against the rate of maximum diffusion (i.e. $c_{\text{bulk}}^A = 0$) across the film thickness x_0:

$$M_H^2 = \frac{\text{rate of reaction}}{\text{rate of diffusion}} = \frac{k \left(c_c^A\right)_\Sigma c_{\text{bulk}}^B A_\Sigma x_0}{k_m^A \left(\left(c_c^A\right)_\Sigma - 0\right) A_\Sigma} = \frac{k c_{\text{bulk}}^B D_c^A}{\left(k_m^A\right)^2} \tag{2.79}$$

where a second order reaction has been assumed, consistently with the analysis presented in this section.

The two film theory offers a convenient way to describe the transport of soluble species in two-phase systems and explore the role of several parameters that affect the transfer rates. Other theories were developed to overcome some of the limiting assumptions behind the TFT, like the penetration theory (Higbie, 1935) or surface-renewal theory (Danckwerts, 1951), which anyway provide similar qualitative results. These models will be briefly introduced in section 7.2.1. However, all these analytical approaches share the common limitation that they do not provide a quantitative tool to estimate the mass transfer coefficients in both phases (for example, the liquid film thickness in the TFT is unknown but is needed to predict k_m^A). Experiments and/or numerical simulations are therefore necessary to quantitatively predict the mass transfer.

2.3.3 Numerical methods for fully resolved simulations

From the analysis presented so far of the main characteristics of bubbly flows, it appears evident that several features concur to determine the behaviour of two-phase chemical reactors, including the rising velocity, shape and trajectory of bubbles as well as the transfer of soluble species across the interface. These phenomena are extremely difficult to predict and, for this reason, analytical models can be derived only for simple cases. Although they are not representative of real applications (due to the simplified assumptions that are generally made), simple theoretical models are useful to predict the effects of the main parameters on the system and, at the same time, provide analytical benchmarks to validate numerical tools. Several analytical solutions (e.g. rising velocity in a creeping flow, growth and shrinkage of suspended bubbles in super- and under-saturated solutions) will be used in chapter 6 for the validation of the numerical method developed within the present thesis.

Experimental techniques have been applied successfully to the characterisation of real apparatus. Terminal velocities (drag coefficients) and global mass transfer rates (Sherwood numbers) for a rising bubble in a liquid column are measured in the works of Takemura and Yabe, 1998, Takemura and Yabe, 1999 and Takemura and Matsumoto, 2000 by means of an optical apparatus. A more advanced visualisation technique (Planar Laser Induced Fluorescence - PLIF) is used in Dani et al., 2007 and Francois et al., 2011 to visualise the concentration field of the species released into the liquid from a rising bubble. Although these approaches have provided fundamental insights into the characterisation of mass transfer in bubbly flows, the quantities that can be generally measured are limited to global values (e.g. global mass transfer rate, bubble volume), whilst access to local information at the gas-liquid interface (e.g. local mass transfer rate, concentration and hydrodynamic boundary layer thicknesses) as well as the actual interfacial area of highly deformed bubbles are difficult to obtain with the available experimental techniques. The level of contamination (e.g. presence of surfactants), which has a strong impact on the dynamics of rising bubbles (see section 2.1), is another parameter that is not always easy to control and may limit the accuracy of experimental measurements.

On the other hand, the continuous increase in computational resources and development of highly-scalable computational fluid dynamics (CFD) codes make high-fidelity numerical simulations an extremely interesting tool for the modelling of bubbly flows and mass transfer across deformable interfaces. Numerical methods offer the advantage that all the fields are readily available everywhere inside the computational domain. This is particularly relevant for mass transfer problems, where opposite directions of species transfer (i.e. from the gas to the liquid and vice versa) can occur at the same time in different parts of the bubble. In this scenario, experimental measurements can only provide the average mass transfer rate, but information on the local quantity is inherently lost. An example of such case will be discussed in section 6.2.4. It is worth reminding here that the comparison between experiments and numerical simulations is not always a trivial task, since many parameters that can significantly affect experimental measurements, including temperature, contamination and presence of dissolved species, need to be carefully monitored during experimental campaigns. For a more detailed discussion on possible uncertainties between experiments and simulations, the reader is referred to Weiner, 2020.

Numerical methods are clearly affected by several limitations, related to both the extremely complicated physics that needs to be modelled as well as the resolution requirements in terms of temporal and spatial length scales. Apart from the well known difficulties in reproducing turbulent fluctuations (which affect all kind of turbulent flows), the modelling of mass transfer in a two-phase system and the related volume effect on the size of bubbles pose some additional challenges. In this thesis the focus is on the modelling of diffusion-driven mass transfer problems and the terminology diffusion-driven phase-change is used to refer to the full process of transfer of moles of a soluble species across the interface and the corresponding volume change of the phases. A common assumption for highly dilute species in the disperse phase (i.e. when the soluble gas is a marginal component of the mixture) is to neglect the volume change of the bubble. In this case the species acts as a passive tracer and does not affect the solution of the Navier-Stokes equations (Bothe and Fleckenstein, 2013, Farsoiya et al., 2021). The advantage of this assumption consists of a simplified (continuous) velocity field near the interface, which is easier to han-

dle by means of standard two-phase numerical methods. The term diffusion-driven reminds that the mass transfer process is driven by the gradient of species concentration at the interface, contrary to temperature-driven phenomena (e.g. boiling) where the temperature field drives the phase-change. Evaporation can be classified as a diffusion-driven process since the mass transfer rate is determined by the interfacial gradient of a species concentration (vapour), although the temperature is also involved into the thermodynamic equilibrium of the interface. In the present work, the effect of the temperature field is always neglected and the terminology diffusion-driven is generally omitted.

The main challenges for numerical methods related to phase-change processes consist of the treatment of discontinuities that characterise both the velocity and concentration profiles at the interface. As was introduced in section 2.3.1, the interface is always assumed saturated and the concentration jump between the values at the gas and liquid sides of the interface is determined by Henry's law (equation 2.51). The discontinuity in the velocity component normal to the interface is due to the exchange of mass between two phases with different densities and is described by the Rankine-Hugoniot condition (this relationship will be introduced and discussed in section 3.1). For flows without mass transfer ($\dot{m} = 0$) or phases with the same density, the velocity is continuous across the interface. However, for bubbly flows in aqueous solution the density ratio is typically $\rho_r \approx 10^{-3}$ and the velocity discontinuity may be relevant for the dynamics of the interface. The velocity jump is the result of an extra (discontinuous) flow that is activated by the exchange of species between the phases and is necessary to preserve mass; this additional component is generally referred to as Stefan flow.

In the following, the main numerical methodologies for the treatment of velocity and concentration discontinuities for phase-change flows are reviewed and discussed.

Treatment of velocity discontinuity at the interface

The problem of a discontinuity in the normal velocity profile at the interface affects all types of phase-change flows between phases of different densities, regardless of the

process that drives the transfer of mass (i.e. temperature or concentration gradients). The mathematical formulation of the governing equations for the conservation of mass and momentum (which will be discussed in chapter 3) is the same for both types of phase-change flows and the numerical schemes designed for boiling or evaporating flows can be applied to the study of phase-change of soluble species as well (and vice versa). For this reason, works related to all the previously mentioned types of flow are included in this review.

Amongst the most popular numerical methods for the advection of the interface in two-phase systems are the Front Tracking (Tryggvason et al., 2001), Level Set (Sussman et al., 1994) and Volume of Fluid (VOF - Hirt and Nichols, 1981, Scardovelli and Zaleski, 1999) approaches. A comprehensive review on numerical methods for direct numerical simulations of multiphase flows can be found in Tryggvason et al., 2011. The VOF method has been applied successfully to a variety of multiphase problems with complex interfaces and one of its major strengths is the capability to preserve mass. This approach is the method used in the present thesis for the treatment of the interface and the present review will focus on this methodology.

The VOF method consists of capturing the position of the interface by solving the following transport equation:

$$\partial_t H + \nabla \cdot (H\mathbf{u}) = -\frac{\dot{m}}{\rho_c}\delta_\Sigma \tag{2.80}$$

where H is a marker function (the Heaviside function) that assumes a value of one or zero in the primary and secondary phases, respectively, whilst the term on the RHS is related to the volume change (δ_Σ is the interface Dirac delta function). In this work the primary and secondary phases are the continuous and disperse ones, respectively. This equation will be carefully introduced and discussed in section 3.2. According to the way equation 2.80 is numerically integrated, two main versions of the VOF method have been proposed, namely the algebraic and geometric approaches. In the algebraic version, the numerical fluxes of the volume fraction field (i.e. the cell volume-average value of H) are computed considering its value uniformly distributed within the computational cell. On the other hand, in the geometric approach, the

interface between the phases is first reconstructed and the amount of volume that is transported across the cell boundary is exactly (in the sense of the interface approximation) computed. In this thesis a geometric VOF approach is used for the modelling of two-phase systems and its properties will be discussed in detail in section 4.2. For the purposes of this review, the difference between algebraic and geometric VOF methods is fundamental for the choice of the most suitable approach for the treatment of concentration discontinuities at the interface (as will be discussed later in this section).

Several works have been published in the literature that use the VOF method to model incompressible phase-change flows (both diffusion- and temperature-driven). Some of these studies can be found in Welch and Wilson, 2000, Schlottke and Weigand, 2008, Kunkelmann and Stephan, 2009, Magnini et al., 2013, Ma and Bothe, 2013, Fleckenstein and Bothe, 2015, Vachaparambil and Einarsrud, 2020, Maes and Soulaine, 2020, Taqieddin et al., 2020, Scapin et al., 2020, Malan et al., 2021, Zanutto, Evrard, et al., 2022, Zanutto, Paladino, et al., 2022 and Farsoiya et al., 2023. Although many authors have deployed the VOF method for this class of flows, only few studies have combined a rigorous treatment of the velocity discontinuity with a sharp advection of the interface.

In the VOF method, a one-fluid velocity field ($\mathbf{u}$) obtained through a weighted average (based on the volume fraction fields) of the phase velocities ($\mathbf{u}_c$, $\mathbf{u}_d$) is defined everywhere in the domain, i.e. $\mathbf{u} = \mathbf{u}_c H + \mathbf{u}_d(1 - H)$ (One-fluid formulation - see section 3.2). The most common approach consists of advecting the marker function with the one-fluid velocity and apply a source term to take into account the volume change. A first problem with this approach is related to the stability of VOF schemes, which are generally designed for continuous flows. A popular workaround to deal with this type of instability is presented in the work of Hardt and Wondra, 2008, where the authors propose a smearing of the interfacial source term for mass transfer in a few layers of cells around the interface. This is achieved by solving an additional inhomogeneous Helmholtz equation and the method is implemented in a geometric VOF scheme to study the evaporation of droplets.

Another issue is related to the nature of the Stefan flow, which is non divergence-

free at the interface. The non solenoidal feature is due to the change in volume that a mass of material experiences when its phase (and, therefore, density) changes. The volume effect related to the divergence of the one-fluid velocity is known to cause the smearing of the interface in algebraic methods. This issue is common in this class of VOF schemes even for divergence-free flows and compression terms acting at the interface are generally used to maintain the interface sharp (see, for example, Ubbink and Issa, 1999). Clearly, an accurate treatment of the continuity of mass at the interface is crucial for geometric schemes too. Schlottke and Weigand, 2008 proposed an iterative method to improve the conservation of mass, based on the computation of the interface and gas velocities, in such a way to fulfill the kinematic constraint of the velocity field at the interface.

Several geometric VOF schemes integrate the transport equation of H in the non-conservative form, by using an operator-split advection scheme (see, for example, the method of Weymouth and Yue, 2010, which is used in the present thesis and is described in section 4.2). These methods generally rely on the assumption of divergence-free velocity field to ensure the conservation of mass, which is always true for incompressible flows without mass transfer. Therefore, an inconsistency arises when the one-fluid velocity is used for the transport of H (with the non-conservative form) in the presence of phase-change. In fact, a cumulative (and artificial) volume effect is automatically included during the split advection of H, as a result of the non-solenoidal nature of the discontinuous flow. Such effect must be removed after all the transport steps along the spatial directions are executed. If this correction is missed, an artificial volume change is produced, since the volume changes twice: through the advection step and via the source term (related to $\dot{m}$) in equation 2.80, which is the only term that must be kept, since it is representative of the actual mass transfer (Fleckenstein and Bothe, 2015). Another simpler (but less accurate) approach consists of neglecting the discontinuous Stefan flow (as if $\dot{m} = 0$) and apply the whole volume change that corresponds to the mass transfer rate in a single step via a source term. However, the resulting velocity field is not accurate near the interface (since the Stefan flow is missing) and this has a direct consequence on the accuracy of the solution, because the convective transport of species near the

interface directly affects the concentration boundary layers and, therefore, the mass transfer rate.

A formally accurate way to transport the marker function with a split geometric scheme would rely on the use of the primary phase velocity field ($\mathbf{u}_c$), which is divergence-free everywhere in the liquid domain (due to the incompressibility assumption). However, the phase velocities are not suitable for a Finite Volume (FV) framework with an Eulerian grid, where the variables are averaged over the volume cell rather than the phase volume. Therefore, some attempts to define an extended velocity field of the primary phase, in such a way to result divergence-free on all the mixed cell faces, have been proposed in the literature and are briefly discussed in the following. The advantage of such approaches is that the velocity field is not altered far from the interface and the marker function is transported by a solenoidal velocity field, taking advantage, in this way, of the conservation properties of VOF schemes for incompressible flows.

Although developed for different reasons, the Ghost Fluid method (Fedkiw et al., 1999) has been used to develop several algorithms to handle the interfacial discontinuity in phase-change flows and enforce the correct phase velocity divergence near the interface. Examples of this approach can be found in Nguyen et al., 2001 and Sussman, 2003 for the Level Set method, and Tanguy et al., 2007 for a coupled Level Set and Volume of fluid approach.

More recently, Scapin et al., 2020 proposed a method to make the velocity field continuous and divergence-free near the interface by subtracting the Stefan flow component (which is responsible for the discontinuity) from the one-fluid velocity field. The individual contribution of the Stefan flow is obtained from the solution of an elliptic equation (potential flow). The corrected velocity field is then used for the advection of the interface and excellent mass conservation properties are reported. The authors implemented this algorithm into an algebraic VOF method, but the same strategy can be used with geometric schemes.

The same result (i.e. a divergence free-velocity field) is obtained in the work of Malan et al., 2021 for the study of evaporating droplets. The authors propose an algorithm to extend the liquid velocity field across the interface, by solving a Poisson

equation for an artificial pressure in a small subdomain built around the interface. This pressure field is designed in a way to produce a velocity component that, when added to the liquid velocity field, makes it divergence-free near the interface. A similar method is used in Guo, 2020 for evaporating and boiling flows, with the difference that the artificial pressure is solved everywhere in the domain rather than in the interfacial region only.

These treatments for the velocity field are particularly relevant for flows with large mass transfer rates and/or density ratios, where significant Stefan flows are expected. Several works reviewed so far rely on the either iterative algorithms (Schlottke and Weigand, 2008) or on the solution of elliptic equations (Scapin et al., 2020, Guo, 2020, Malan et al., 2021). The main contribution of the present thesis is the derivation of an original algorithm for the extension of the liquid velocity field, which does not require the solution of an additional partial differential equation and is readily implementable in available VOF codes. The goal is to transport the marker function with a solenoidal field and the method is coupled with a geometric VOF based on the Piecewise Linear Interface Construction (PLIC) scheme. This algorithm will be introduced in section 5.2.

Treatment of concentration discontinuity at the interface

As was introduced earlier, the transport of a soluble species adds an additional challenge for numerical methods, which have to preserve the jump between the concentration values at the interface (given by Herny's law), during the transport of the species. In this section, the focus is on the available approaches for the coupling of VOF methods with the transport of soluble species, since this is the methodology used in the present thesis.

In the absence of chemical reactions, the time-evolving concentration of a chemical component in the incompressible liquid and gas phases (interface excluded) is described by a standard advection-diffusion equation (which will be discussed in section 3.3):

$$\partial_t c + \mathbf{u} \cdot \nabla c - \nabla \cdot (D \nabla c) = 0 \quad \text{in } \Omega \setminus \Sigma \tag{2.81}$$

where Ω is the whole domain and the diffusion coefficient generally assumes a different value depending on the carrier phase (i.e. $D_c \neq D_d$). Two main families of numerical methods have been developed for the solution of equation 2.81, namely one-scalar and two-scalar methods. The main difference between these two approaches consists of the number of transport equations that are solved for each soluble species (i.e. one and two for one- and two-scalar methods, respectively) and the choice of the most suitable approach is intrinsically related to the type of VOF scheme used (i.e. algebraic or geometric). Some of the works that make use of both methodologies and their characteristics are discussed in the following.

In one-scalar methods, only one equation is solved for each transferable species and the unique concentration variable c is defined everywhere in the domain. One of the first attempts with this approach was proposed by Bothe et al., 2004, where the concentration field is represented by a single scalar quantity that is made continuous across the interface by applying a proper variable transformation. Such scaling procedure was also applied successfully in other works and the interested reader is referred to the references in Bothe and Fleckenstein, 2013 for more information.

A fundamental contribution to the development of one-scalar schemes is presented in the work of Haroun et al., 2010 for the study of reactive liquid films. The authors adopted the one-fluid formulation for both the concentration field and diffusion coefficient, i.e. $c = c_c H + c_d(1 - H)$ and $D = D_c H + D_d(1 - H)$, respectively. This leads to the following transport equation:

$$\partial_t c + \mathbf{u} \cdot \nabla c - \nabla \cdot (D \nabla c + \Phi) = 0 \quad \text{in } \Omega \tag{2.82}$$

where the additional term Φ enforces the concentration discontinuity at the interface and is related to Henry's law coefficient through the following formula:

$$\Phi = -D \frac{c(1 - H_e)}{H + H_e(1 - H)} \nabla H \tag{2.83}$$

The one-fluid field c is globally conserved in the domain Ω, unless reaction terms are introduced. The authors reported that the use of the arithmetic mean for the global

diffusion coefficient produces numerical instabilities and better results are obtained through an harmonic average, i.e. $D = D_c D_d/(D_d H + D_c(1 - H))$.

The one-scalar approach is also developed in the works of Marschall et al., 2012 and Deising et al., 2016. Marschall et al., 2012 used the conditional volume-averaging technique to derive a one-fluid formulation for the transport of species, which results in a single transport equation where additional terms appear compared to the work of Haroun et al., 2010 (equation 2.82). Their approach is entitled Continuous Species Transfer (CST). This method is further developed by Deising et al., 2016, where an extra term is included to take into account the effect of the curvature of the interface.

Maes and Soulaine, 2018 showed that the CST produces a significant amount of numerical diffusion for flows dominated by convection ($Pe > 100$). For this reason, the authors have extended the range of applicability of the CST method by including a compressive velocity term in the single-field transport equation for species concentration, which comes from a more accurate treatment of the numerical fluxes of the advection term. This method is referred to as Compressive Continuous Species Transfer (C-CST).

One-scalar formulations have been successfully coupled with algebraic VOF methods. Some recent examples include the works of Taqieddin et al., 2020 and Vachaparambil and Einarsrud, 2020, where the scheme of Haroun et al., 2010 and the C-CST method are used, respectively, for the study of growing bubbles rising in supersaturated solutions.

The C-CST method is also used in the work of Maes and Soulaine, 2020 for the study of multicomponent mass transfer, where multiple species can be transferred in opposite directions across the interface. The authors propose a more general formulation of the one-field diffusion coefficient that is valid also in the case of pure species (where the self-diffusion coefficient within the disperse phase tends to $D_d \rightarrow 0$).

The coupling of an algebraic VOF with the CST model is further discussed in the works of Zanutto, Evrard, et al., 2022 and Zanutto, Paladino, et al., 2022. The authors show the importance of treating the advection of the concentration field with the same numerical scheme used for the transport of the marker function in order to

avoid artificial mass transfer and ensure global conservation of species. Their method is validated for evaporating flows and non-ideal mixtures with large discontinuities in the concentration profiles across the interface.

In two-scalar methods, two different transport equations are solved for each transferable species. One equation describes the distribution of concentration in the continuous phase (Ω_c):

$$\partial_t c_c + \mathbf{u}_c \cdot \nabla c_c - \nabla \cdot (D_c \nabla c_c) = -\frac{\dot{m}}{M}\delta_\Sigma \quad \text{in } \Omega_c \tag{2.84}$$

and the other one is solved inside the disperse phase (Ω_d):

$$\partial_t c_d + \mathbf{u}_d \cdot \nabla c_d - \nabla \cdot (D_d \nabla c_d) = \frac{\dot{m}}{M}\delta_\Sigma \quad \text{in } \Omega_d \tag{2.85}$$

Contrary to the one-scalar approach (where the one-fluid concentration variable is globally conserved in Ω), the two concentration fields c_c and c_d are not individually conserved in Ω_c and Ω_d, respectively, even in the absence of reactions. This is due to the fact that each field represents the amount of concentration within the respective phase and, in case of mass transfer, such quantity is clearly not conserved due to the transport of moles across the interface. In terms of mathematical modelling, this is represented by the source terms on the RHS of equations 2.84 - 2.85. However, the method is clearly mass conservative in the sense that the same amount of species that is added or subtracted from Ω_c is subtracted or added to Ω_d, since the source terms have the same magnitude, but opposite signs. The variables c_c and c_d exist only within the respective domain (Ω_c and Ω_d, respectively) and, strictly speaking, they represent phase-average variables. In order to make the transport of such quantities consistent with FV discretization schemes, the following transformation is adopted in the work of Alke et al., 2009:

$$\phi_c(\mathbf{x}, t) = \begin{cases} c(\mathbf{x}, t) & \text{if } \mathbf{x} \in \Omega_c \\ 0 & \text{if } \mathbf{x} \in \Omega_d \end{cases} \tag{2.86}$$

$$\phi_d(\mathbf{x},t) = \begin{cases} 0 & \text{if } \mathbf{x} \in \Omega_c \\ c(\mathbf{x},t) & \text{if } \mathbf{x} \in \Omega_d \end{cases} \tag{2.87}$$

where the one-sided (i.e. confined to one side of the interface) fields c_c and c_d are extended to zero in the other phase (Ω_d and Ω_c, respectively), whilst $\phi_c(t)$, $\phi_d(t)$ represent the cell volume-average version of the corresponding phase-average quantities:

$$\phi_c(t) = \frac{1}{V}\int_{V\cap\Omega_c(t)} c(t)\, dV \tag{2.88}$$

$$\phi_d(t) = \frac{1}{V}\int_{V\cap\Omega_d(t)} c(t)\, dV \tag{2.89}$$

where V is the volume of the computational cell. The formal derivation of the two-scalar approach will be introduced, and its properties discussed, in section 5.3. The variables ϕ_c and ϕ_d are VOF-like variables in the sense that they are discontinuous across the interface, with a null value in the other phase (like the marker function H) and they are advected in the work of Alke et al., 2009 with the same (geometric) fluxes used for H. This is a crucial point of two-scalar methods where, in order to preserve mass, no mass transfer can occur during the advection (and diffusion) of the concentration fields, since the whole interfacial transport is given by the source terms $\pm\dot{m}/M\delta_\Sigma$. The definition of equations 2.88 - 2.89 allows to recover the phase-average quantities and, when the method is coupled with a geometric VOF, the exact (according to the reconstruction of the interface) amount of moles from both sides of the interface can be advected within the corresponding domain by applying the same geometric fluxes as used for the advection of the marker function. This makes the transport of the phase-average species consistent with the displacement of the interface and ensures that both concentration fields are kept confined to their respective side of the interface during the advection step, preventing, in this way, any artificial mass transfer. For the same reason, the species should not be transferred across the interface during the integration of the diffusive term as well. This is achieved in the work of Bothe and Fleckenstein, 2013 by an appropriate treatment of the diffusive fluxes.

Contrary to one-scalar approaches, this method requires a direct evaluation of the mass transfer rate ($\dot{m}$) for each interfacial cells. In the work of Bothe and Fleckenstein, 2013, two different methods are compared. The first approach consists of assuming the whole concentration within each interfacial cells at the thermodynamic equilibrium given by Henry's law. In the second approach, only the interface is assumed to be saturated and $\dot{m}$ is accurately computed by evaluating the normal gradient of concentration at the interface (equation 2.53) through an unsplit geometrical scheme. Results show that the global equilibrium method (first approach) generally overestimates the mass transfer rate, whilst direct evaluation of local concentration gradients provides a more accurate prediction of $\dot{m}$. This methodology is further extended in the work of Fleckenstein and Bothe, 2015 for multicomponent mass transfer problems with volume effects (i.e. full phase-change simulations of mixtures), where an accurate treatment of jump discontinuities at the interface shows that mass transfer is generally composed of two terms, namely a convective contribution and a diffusive one, which are both taken into account in their simulations.

A novel implementation of the two-scalar method is presented in Schulz et al., 2022, where the authors use the geometrical reconstruction of the interface to split the mesh between the phases. The newly created cell faces match the interface and accurate boundary conditions can be set for the transport of species, according to their chemical repartition.

A hybrid method, where one- and two-scalar approaches are combined, was recently proposed by Farsoiya et al., 2021 and implemented in a geometric VOF scheme. The chemical equilibrium at the interface is treated with the one-scalar approach proposed by Haroun et al., 2010, where the extra diffusive term enforces the concentration jump given by Henry's law. The convective transport of species is made consistent with the displacement of the interface by recovering the two phase-average concentration fields (two-scalar approach) and transporting them with the geometrical fluxes used for the marker function. The same authors have recently proposed an alternative approach that takes into account the volume effect due to the mass transfer between the phases (see Farsoiya et al., 2023). An immersed boundary method

is used to set a Dirichlet boundary condition at the interface for the concentration, which ensures that Henry's law is satisfied at the gas-liquid interface, whilst the value within the disperse phase is kept uniform. A phase-change velocity field is computed in the interfacial cells (based on the gradient of concentration at the liquid side) and used to update the volume fraction to take into account the volume change. The convective transport of the concentration field is performed with a two-scalar method.

From the above discussion about numerical methods for the transport of soluble species in two-phase systems, it emerges that a crucial requirement for accurate simulations is the consistency between the transport of the marker function and the advection of the concentration field. This is fundamental to ensure that the mass transfer process is entirely driven by the diffusive fluxes of concentration and no artificial mass transfer occurs due to numerical errors. As pointed out by Deising et al., 2016, the choice between one- and two-scalar approaches is inherently related to the type of VOF methodology (i.e. algebraic or geometric) used. For algebraic VOF methods, the most convenient choice is the one-scalar approach, where the one-fluid formulation of the concentration field in interfacial cells is naturally suited to be advected with the same scheme used for the algebraic marker function. On the other hand, when a geometric VOF method is used, the reconstruction of the interface allows to clearly distinguish between the continuous and disperse domains within each interfacial cell. In this situation, a two-scalar approach is the most suitable treatment for the concentration field as it allows to separately transport the species within their respective phase and avoid any exchange of moles between the phases during the movement of the interface (as long as the same geometric fluxes are used for both H and the concentrations).

The choice between one- and two-scalar methods is then inherently related to the VOF scheme used. The two-scalar approach is expected to be more expensive from a computational point of view (since two equations are solved instead of just one for each species). However, it offers a natural way to access information about local quantities at the interface (since the mass transfer rate $\dot{m}$ is computed individually for each interfacial cell) and is also more suited for the implementation of subgrid-scale

models for the concentration boundary layer (Bothe and Fleckenstein, 2013, Weiner and Bothe, 2017). The capability of computing the local mass transfer rate was also recently extended to one-scalar approaches in the work of Maes and Soulaine, 2020, where this is necessary when volume effects are taken into account (i.e. for full phase-change simulations). Finally, the two-scalar approach is known to suffer from the small cell problem, which occurs when a cell is almost filled with one phase and conservation problems may arise within the small volume occupied by the other phase (Deising et al., 2016). Both methods present advantages and disadvantages, but the most limiting factor for this type of simulations (which is common to both methodologies) consists of the mesh size that is generally needed to capture the concentration boundary layer in convection-dominated cases (large Pe, see section 2.3.1), which is a crucial requirement for high-fidelity simulations.

In this thesis, a geometric VOF method is used and the two-scalar approach presented in Fleckenstein and Bothe, 2015 is adopted. The numerical methodology for the transport of species is discussed in detail in section 5.3.

Chapter 3

Governing equations of two-phase incompressible flows

In this chapter, the governing equations for the dynamics of two-phase incompressible flows are introduced and the relevant assumptions are discussed. Although the mathematical modelling presented in this chapter and the numerical methodology developed in the present thesis apply to a generic multiphase (incompressible) system, this work is mainly focused on disperse bubbly flows and the gas and liquid phases are referred to as disperse and continuous phases respectively. A generic two-phase (gas-liquid) system is represented in Figure 3.1. The regions occupied by the two phases are called $\Omega_d(t)$, for the disperse phase, and $\Omega_c(t)$ for the continuous phase, and these two sub-domains are separated by an infinitely thin interface $\Sigma(t)$, so that the entire domain is given by $\Omega = \Omega_d(t) \cup \Omega_c(t) \cup \Sigma(t)$. The normal vector ($\mathbf{n}_\Sigma$) at the interface is defined as the unit vector which points into $\Omega_d(t)$. To simplify the notation in the following, the time dependence from the phase domains (Ω_d, Ω_c) and interface (Σ) are omitted. The terms continuous (disperse) and liquid (gas) will be used interchangeably in the rest of the work.

The chapter is organized as follows. In section 3.1 the system of conservation laws (Navier-Stokes equations) for mass and momentum is presented along with the additional boundary conditions that must be taken into account at the interface.

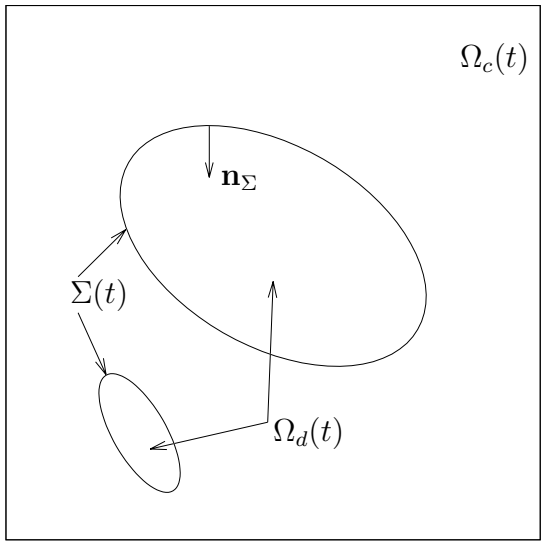

Figure 3.1: Two-phase gas-liquid domain.

The One-Fluid formulation of the Navier-Stokes equations, which serves as the basis for the numerical methodology presented in chapter 4, is introduced in section 3.2 and the transport of soluble species in a two-phase system is discussed in section 3.3.

3.1 Two-phase Navier-Stokes equations

For each phase, the system of governing laws for an incompressible flow is given by the Navier-Stokes (NS) equations:

$$\nabla \cdot \mathbf{u} = 0 \quad \text{in } \Omega \setminus \Sigma \tag{3.1}$$

$$\partial_t(\rho \mathbf{u}) + \nabla \cdot (\rho \mathbf{u} \otimes \mathbf{u}) = -\nabla p + \nabla \cdot (2\mu \mathbf{S}) + \rho \mathbf{a} \quad \text{in } \Omega \setminus \Sigma \tag{3.2}$$

where the fluid has been assumed Newtonian and the material properties, e.g. density (ρ) and dynamic viscosity (μ), have constant values in Ω_d, Ω_c and depend on the respective phase. Equation 3.1 is the continuity equation (conservation of mass), where $\mathbf{u}$ represents the fluid velocity field ($\mathbf{u} = (u, v, w)$). In the conservation of

momentum (equation 3.2), p is the static pressure, $\mathbf{a}$ contains the acceleration terms which come from external body forces (e.g gravitational force) and $\mathbf{S}$ is the deformation tensor $[\nabla\mathbf{u} + (\nabla\mathbf{u})^T]/2$. The only body force which is considered in the present work is the gravitational force; the acceleration term $\mathbf{a}$ is then replaced by $\mathbf{g}$ in the following chapters. Equations 3.1 and 3.2 are valid everywhere in the domain, except at the interface, where additional jump conditions are needed to close the system (see Tryggvason et al., 2011). To derive such relations, conservation balances are applied to the control volume V shown in Figure 3.2, where the interface is represented as an infinitely thin region that cannot store any mass or momentum. The first jump

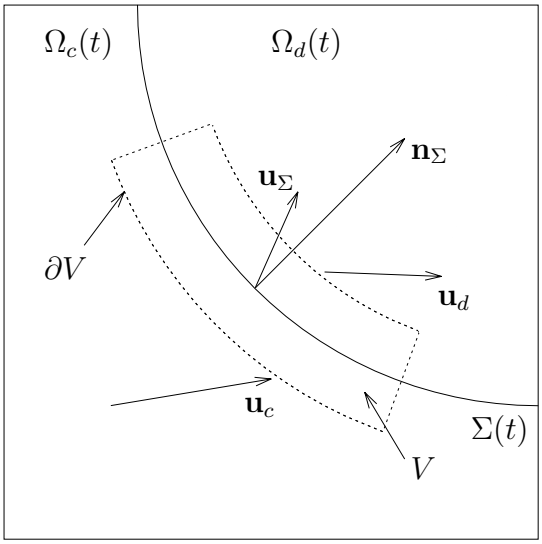

Figure 3.2: Control volume around the interface used to derive the jump conditions. The volume moves with the interface velocity $\mathbf{u}_\Sigma$.

condition derives from the principle of mass conservation and states that the amount of mass which leaves Ω_d (Ω_c) must be entirely transferred to Ω_c (Ω_d) since no mass can be stored in the interface. The balance of mass for the control volume V (that moves with the interface Σ) reads:

$$\frac{d}{dt}\int_V \rho\, dV = -\oint_{\partial V} \rho(\mathbf{u} - \mathbf{u_\Sigma}) \cdot \mathbf{n}\, dS \tag{3.3}$$

where $\mathbf{u}_\Sigma$ is the interface velocity. If we take the control volume with a vanishing thickness (i.e. $V \to 0$), the transient term on the left hand side (LHS) of equation 3.3 is null and the balance can be integrated only along the edges parallel to the interface (the other edges give a null contribution) and simplifies as:

$$\rho_c(\mathbf{u}_c - \mathbf{u_\Sigma}) \cdot \mathbf{n_\Sigma} = \rho_d(\mathbf{u}_d - \mathbf{u_\Sigma}) \cdot \mathbf{n_\Sigma} = \dot{m} \tag{3.4}$$

where $\dot{m}$ is the mass transfer rate [$\mathrm{kg\,m^{-2}\,s^{-1}}$]. Equation 3.4 can be reformulated by employing the jump notation (e.g. $\|\rho\| = \rho_c - \rho_d$) as:

$$\|\rho(\mathbf{u} - \mathbf{u}_\Sigma) \cdot \mathbf{n}_\Sigma\| = \|\dot{m}\| = 0 \quad \text{at } \Sigma \tag{3.5}$$

This relation is also known as the Rankine-Hugoniot condition and for flows without phase-change ($\dot{m} = 0$) it implies that no relative velocity along the normal direction can occur between the fluids and the interface.

The second jump condition comes from the balance of momentum applied to the same control volume of Figure 3.2 (moving with the interface velocity $\mathbf{u_\Sigma}$):

$$\frac{d}{dt}\int_V \rho\mathbf{u}\, dV \; = -\oint_{\partial V} \rho\mathbf{u}(\mathbf{u} - \mathbf{u_\Sigma}) \cdot \mathbf{n}\, dS \; + \oint_{\partial V} \mathbf{T} \cdot \mathbf{n}\, dS \; + \int_\Sigma \mathbf{f}_\sigma\, dS \tag{3.6}$$

where $\mathbf{T}$ is the stress tensor and $\mathbf{f}_\sigma$ is the surface force per unit area that can be formulated as (see Tryggvason et al., 2011):

$$\mathbf{f}_\sigma = \sigma\kappa\mathbf{n_\Sigma} + \nabla_\Sigma\sigma \tag{3.7}$$

In equation 3.7 the surface tension coefficient (σ) and interface curvature (κ) have been introduced. Applying the same integration approach as for the conservation of mass (i.e. control volume with an infinitely small thickness) the following condition for the conservation of momentum across the interface is obtained:

$$\|\rho\mathbf{u} \otimes (\mathbf{u} - \mathbf{u}_\Sigma) + p\mathbf{I} - 2\mu\mathbf{S}\| \cdot \mathbf{n}_\Sigma = \sigma k\mathbf{n}_\Sigma + \nabla_\Sigma\sigma \quad \text{at } \Sigma \tag{3.8}$$

where $\mathbf{I}$ is the unit tensor. Since both phases are treated as Newtonian incompressible fluids, the stress tensor has the form:

$$\mathbf{T} = -p\mathbf{I} + 2\mu\mathbf{S} \tag{3.9}$$

For the applications considered in the present thesis (i.e. gas bubbles that exchange mass with the surrounding liquid), some assumptions can be introduced to simplify equation 3.8. The surface tension is assumed uniform and, following the dimensional analysis presented in Fleckenstein and Bothe, 2015 for gas bubbles with a radius of 1mm immersed in water, the first term on the LHS of Equation 3.8 is of several orders of magnitude smaller than the first term on the RHS. Given the physical properties of these types of flow and assuming a no-slip condition for the tangential velocities at the interface (coherently with the assumption of phases with non-vanishing viscosity), equation 3.8 can be further simplified to:

$$\|p\mathbf{I} - 2\mu\mathbf{S}\| \cdot \mathbf{n}_\Sigma = \sigma k \mathbf{n}_\Sigma \quad \text{at } \Sigma \tag{3.10}$$

The system of governing equations (3.1, 3.2) along with the jump conditions at the interface (equations 3.5, 3.10) describe the dynamics of two-phase incompressible flows with mass transfer. This approach is also known as two-fluid formulation, since two sets of equations (one for each phase) need to be solved and coupled through the interfacial boundary conditions. In the following section, an alternative formulation of the conservation laws is introduced, which reduces the governing equations to one set of equations valid everywhere in the domain (i.e. $\mathbf{x} \in \Omega$).

3.2 One-fluid formulation

The One-fluid formulation consists of the derivation of a single set of governing equations where the interfacial jump conditions (equations 3.5, 3.10) are automatically included in the Navier-Stokes equations. This approach is the basis for the implementation of the numerical method adopted in the present thesis (i.e. the Volume of

Fluid (VOF) method, see chapter 4). When one set of equations is used for the whole domain, the properties of the fluid (e.g. density, viscosity) change abruptly across the interface and additional source terms that act at the interface as singularities (δ-functions) need to be included to take into account the jump conditions. Since the properties of the fluid assume different values in their respective phase (Ω_c, Ω_d), the starting point for the derivation of the One-fluid approach is the definition of a marker function to determine the location of the interface and to identify whether a point $\mathbf{x} \in \Omega_c$ or Ω_d. The Heaviside function serves this purpose:

$$H(\mathbf{x}, t) = \begin{cases} 1, & \text{if } \mathbf{x} \in \Omega_c \\ 0, & \text{if } \mathbf{x} \in \Omega_d \end{cases} \tag{3.11}$$

where the continuous phase is assumed to be the primary phase, i.e. where $H(\mathbf{x}, t) = 1$. Once $H(\mathbf{x}, t)$ is known everywhere, the values of ρ and μ can be computed as:

$$\rho = \rho_c H + \rho_d (1 - H) \tag{3.12}$$

and

$$\mu = \mu_c H + \mu_d (1 - H) \tag{3.13}$$

where, in this case, the arithmetic mean has been used (different formulations are clearly possible, e.g. the harmonic mean). To track the position of the interface, the transport equation for $H(\mathbf{x}, t)$ is obtained from the following integral balance for a generic control volume V that contains Σ:

$$\int_V \partial_t H \, dV \; + \oint_{\partial V} H \mathbf{u} \cdot \mathbf{n} \, dS \; + \int_\Sigma (\mathbf{u}_c - \mathbf{u}_\Sigma) \cdot \mathbf{n}_\Sigma \, dS \; = 0 \tag{3.14}$$

where the second term on the LHS represents the convective transport and the last term is a source term that accounts for the mass transfer across the interface, which is null when $\dot{m} = 0$. Since equation 3.14 is valid for a generic domain, applying the

integral balance to an infinitesimal control volume gives the differential form:

$$\partial_t H + \nabla \cdot (H\mathbf{u}) + \frac{\dot{m}}{\rho_c}\delta_\Sigma = 0 \tag{3.15}$$

where δ_Σ is the surface Dirac function which has a nonzero value only at the interface, i.e. $\delta_\Sigma = \delta(\mathbf{x} - \mathbf{x_\Sigma})$.

The starting point for the derivation of the mass balance within the One-fluid formulation, which must take into account the jump condition for mass conservation (equation 3.5), is the introduction of the one-fluid velocity field, which follows the one-fluid properties definition (equations 3.12, 3.13):

$$\mathbf{u} = \mathbf{u}_c H + \mathbf{u}_d(1 - H) \tag{3.16}$$

where the continuous and disperse velocity fields ($\mathbf{u}_c$ and $\mathbf{u}_d$ respectively) are assumed to have a smooth incompressible extension across the interface (see Tryggvason et al., 2011). By computing the divergence of the velocity field and applying the incompressibility kinematic constraint (i.e. $\nabla \cdot \mathbf{u}_c = \nabla \cdot \mathbf{u}_d = 0$), it follows:

$$\nabla \cdot \mathbf{u} = -(\mathbf{u}_c - \mathbf{u}_d) \cdot \mathbf{n_\Sigma}\delta_\Sigma \tag{3.17}$$

where the relation $\nabla H = -\mathbf{n_\Sigma}\delta_\Sigma$ has been used. The phase velocities $(\mathbf{u}_c, \mathbf{u}_d)$ can be removed by applying the Rankine-Hugoniot condition (equation 3.5) and equation 3.17 turns into:

$$\nabla \cdot \mathbf{u} = \dot{m}\left(\frac{1}{\rho_d} - \frac{1}{\rho_c}\right)\delta_\Sigma \tag{3.18}$$

Equation 3.18 represents the one-fluid formulation of the continuity equation for the general case of two-phase incompressible flows with mass transfer. The source term on the RHS can assume a non-null value only at the interface (where mass transfer occurs) and equation 3.18 recovers the standard form of the continuity equation ($\nabla \cdot \mathbf{u} = 0$) in the bulk domains ($\Omega_c$, Ω_d) or when no mass is transferred between the phases.

To derive the one-fluid form of the momentum equation, the integral balance is

applied to a control volume that contains part of the interface Σ. In this case, the effect of the surface tension (from the jump condition in equation 3.10) is turned into a volume contribution by means of the surface Dirac function:

$$\int_{\Sigma} \mathbf{f}_{\sigma}\, dS \;= \int_{V} \mathbf{f}_{\sigma}\delta_{\Sigma}\, dV \tag{3.19}$$

The conservation of momentum then reads:

$$\partial_t \mathbf{u} + \nabla \cdot (\mathbf{u} \otimes \mathbf{u}) = \frac{1}{\rho}\left[-\nabla p + \nabla \cdot (2\mu \mathbf{S})\right] + \mathbf{g} + \frac{\sigma k \mathbf{n}_{\Sigma}}{\rho}\delta_{\Sigma} \tag{3.20}$$

where $\mathbf{f}_{\sigma}$ has been replaced with $\sigma\kappa\mathbf{n}_{\Sigma}$, according to the assumption of constant surface tension (see section 3.1). Equation 3.20 represents the one-fluid formulation of the momentum equation, where the jump condition for momentum (equation 3.10) is introduced as a source term based on the volumetric formulation of surface tension (last term on the RHS).

3.2.1 Overview of the governing equations

For the reader convenience, the one-fluid formulation of the governing equations discussed in the present section is summarized here:

$$\partial_t H + \nabla \cdot (H\mathbf{u}) = -\frac{\dot{m}}{\rho_c}\delta_{\Sigma} \tag{3.21}$$

$$\nabla \cdot \mathbf{u} = \dot{m}\left(\frac{1}{\rho_d} - \frac{1}{\rho_c}\right)\delta_{\Sigma} \tag{3.22}$$

$$\partial_t \mathbf{u} + \nabla \cdot (\mathbf{u} \otimes \mathbf{u}) = \frac{1}{\rho}\left[-\nabla p + \nabla \cdot (2\mu \mathbf{S})\right] + \mathbf{g} + \frac{\sigma k \mathbf{n}_{\Sigma}}{\rho}\delta_{\Sigma} \tag{3.23}$$

Equations 3.21 - 3.23 are valid everywhere in the domain ($\mathbf{x} \in \Omega$) and, far from the interface, the one-fluid approach recovers the form of the two-fluid formulation.

Equations 3.21 and 3.22 are characterized by source terms that depend on the mass transfer rate $\dot{m}$. Mass transfer might occur for different physical phenomena, e.g. evaporation, boiling, chemical reactions, gas solubility. In the present work, the

focus is on the solubility of gaseous species in liquid solutions, where the mass transfer is driven by a diffusive process that occurs at the interface (diffusion-driven phase-change) and depends on the species concentration around Σ. Therefore, to close the system of governing equations, the conservation law for soluble species in two-phase systems needs to be included. The corresponding mathematical formulation, along with the relevant assumptions, are discussed in section 3.3.

3.3 Soluble species in two-phase flows

In this section, the transport equation for a soluble species in a two-phase gas-liquid flow is presented. The main assumptions are introduced and the boundary conditions at the interface are discussed.

In a generic two-phase system both phases can be a mixture of several chemical species. For the generic species k, the individual mass balance reads:

$$\partial_t \rho^k + \nabla \cdot (\rho^k \mathbf{u}^k) = R^k \quad \text{in } \Omega \setminus \Sigma \tag{3.24}$$

where ρ^k is the partial (species) density, $\mathbf{u}^k$ denotes the species velocity and R^k is a generic reaction term that can be used to model chemical reactions. Equation 3.24 is coupled with the jump condition at the interface for conservation of mass (equation 3.5), that is reported here for the k-th species:

$$\|\rho^k(\mathbf{u}^k - \mathbf{u}_\Sigma) \cdot \mathbf{n}_\Sigma\| = \|\dot{m}^k\| = 0 \quad \text{at } \Sigma \tag{3.25}$$

where $\dot{m}^k$ is the individual mass transfer rate. In order to get a consistent formulation of the species transport with the governing equations of two-phase flows (equations 3.21 - 3.23), the phase density (ρ) and phase velocity ($\mathbf{u}$) need to be related to their respective species quantities (ρ^k and $\mathbf{u}^k$, respectively). This is done by applying the following relations:

$$\rho = \sum_k \rho^k \tag{3.26}$$

and

$$\rho\mathbf{u} = \sum_k \rho^k \mathbf{u}^k \tag{3.27}$$

Introducing the definition of diffusive velocity as the difference between the species and phase velocities (i.e. $\mathbf{u}^k - \mathbf{u}$), the individual mass balance of species k (equation 3.24) can be rewritten as:

$$\partial_t \rho^k + \mathbf{u} \cdot \nabla \rho^k + \nabla \cdot \mathbf{J}^k = R^k \quad \text{in } \Omega \setminus \Sigma \tag{3.28}$$

where the phase velocity $\mathbf{u}$ appears and the diffusive flux $\mathbf{J}^k = \rho^k(\mathbf{u}^k - \mathbf{u})$ accounts for the relative velocity between the species and the phase medium. Equation 3.28 has the form of a standard advection-diffusion-reaction equation and the diffusive term needs to be modelled to remove the dependency on the species velocity $\mathbf{u}^k$ (which is not solved for in the system of governing equations). Under the assumption of dilute liquid solutions, the diffusive flux $\mathbf{J}^k$ can be well modelled by Fick's law of diffusion:

$$\mathbf{J}^k = -D^k \nabla \rho^k \tag{3.29}$$

where D^k is the species coefficient of diffusion which assumes different but constant values for each phase. For a detailed discussion on the assumption of Fickian diffusion and its range of applicability, the reader is referred to Bothe, 2015.

In a similar way to the species transport equation, the formula for the individual mass transfer rate $\dot{m}^k$ (equation 3.25) needs to be reformulated to remove the dependency on the species velocity $\mathbf{u}^k$. Here, a generic system of n components is considered, where the first $n-1$ elements are soluble species (that can be transferred across the interface and appear as dilute components in the liquid phase), and the n-th component is the solvent, which is assumed to be not volatile (i.e. no solvent species exists in the disperse phase). Under these assumptions, the mass transfer

rate of a single species can be rearranged into:

$$\begin{aligned}\dot{m}^k &= \rho^k(\mathbf{u}^k - \mathbf{u}_\Sigma)\cdot\mathbf{n}_\Sigma \\ &= \rho^k(\mathbf{u} - \mathbf{u}_\Sigma)\cdot\mathbf{n}_\Sigma + \rho^k(\mathbf{u}^k - \mathbf{u})\cdot\mathbf{n}_\Sigma \\ &= \frac{\rho^k}{\rho}\dot{m} + \mathbf{J}^k\cdot\mathbf{n}_\Sigma\end{aligned} \tag{3.30}$$

Equation 3.30 shows that the mass transfer of each soluble species contains both convective and diffusive terms. Since the total mass transfer rate is given by the contributions of all the $n-1$ transferable species (i.e. $\dot{m} = \sum_{l=1}^{n-1}\dot{m}^l$), equation 3.30 can be reformulated as:

$$\dot{m}^k = \frac{\rho^k}{\rho}\sum_{l=1}^{n-1}\dot{m}^l - D^k\nabla\rho^k\cdot\mathbf{n}_\Sigma \tag{3.31}$$

where $\mathbf{J}^k$ has been replaced with the Fickian diffusive flux. Equation 3.31 is equivalent to the $(n-1)\times(n-1)$ system:

$$\begin{aligned}&\begin{bmatrix} 1-y^1 & -y^1 & \dots & -y^1 \\ -y^2 & 1-y^2 & \dots & -y^2 \\ \dots & \dots & \dots & \dots \\ \dots & \dots & \dots & \dots \\ -y^{n-2} & \dots & 1-y^{n-2} & -y^{n-2} \\ -y^{n-1} & \dots & -y^{n-1} & 1-y^{n-1} \end{bmatrix}\begin{pmatrix} \dot{m}^1 \\ \dot{m}^2 \\ \dots \\ \dots \\ \dot{m}^{n-2} \\ \dot{m}^{n-1} \end{pmatrix} = \\ &= \begin{pmatrix} -D^1\nabla\rho^1\cdot\mathbf{n}_\Sigma \\ -D^2\nabla\rho^2\cdot\mathbf{n}_\Sigma \\ \dots \\ \dots \\ -D^{n-2}\nabla\rho^{n-2}\cdot\mathbf{n}_\Sigma \\ -D^{n-1}\nabla\rho^{n-1}\cdot\mathbf{n}_\Sigma \end{pmatrix}\end{aligned} \tag{3.32}$$

where $y^k = \rho^k/\rho$. It is important to remind here that system 3.32 can be solved in

both phase domains (Ω_c, Ω_d) and that the mass transfer rate must be continuous across Σ, i.e. $\dot{m}_c^k = \dot{m}_d^k$. A special case arises when the disperse phase is made of a single species only (i.e. no mixtures). In this case, the system contains two components ($n = 2$): the pure gas ($k = 1$) and the solvent (liquid phase, $k = 2$) and the overall mass transfer ($\dot{m}$) is entirely given by the transfer rate of the single species which exists in the disperse phase, i.e. $\dot{m} = \dot{m}^1$. It is worth pointing out that, in this case, the density of the soluble species is the same as the phase density in the disperse domain, which is constant in Ω_d, accordingly to the assumption of incompressible flows (i.e. $\rho_d^1 = \rho_d = \text{const}$). Therefore, there is no need to solve the species transport equation (3.28) in Ω_d. The mass transfer rate for a pure disperse phase can be computed from equation 3.31 as:

$$\dot{m} = -\frac{D_c^1}{1 - y_c^1} \frac{\partial \rho_c^1}{\partial \mathbf{n}_\Sigma} \tag{3.33}$$

where the subscript c has been added to remind that the mass transfer rate must be computed from the liquid side of the interface (computing $\dot{m}$ from equation 3.31 in Ω_d gives the identity $\dot{m} = \dot{m}$).

One more condition needs to be taken into account at the interface for the chemical partitioning of species densities. In a generic two-phase system, the species distribution at the interface is discontinuous and a typical density profile for a pure gaseous phase is represented in Figure 3.3 (a similar profile would be representative of a mixture with several components). As was introduced in section 2.3.1, in a gas-liquid system at equilibrium (saturated interface) the jump in the species distribution profile across the interface is given by Henry's Law, which states that the k-th species concentration on the liquid side of Σ is directly proportional to the partial pressure of the same gaseous species on the liquid. By taking advantage of the perfect gas law, Henry's formula can be written in terms of a jump condition for the species densities at the interface:

$$(\rho_c^k)_\Sigma = \frac{(\rho_d^k)_\Sigma}{H_e^k} \tag{3.34}$$

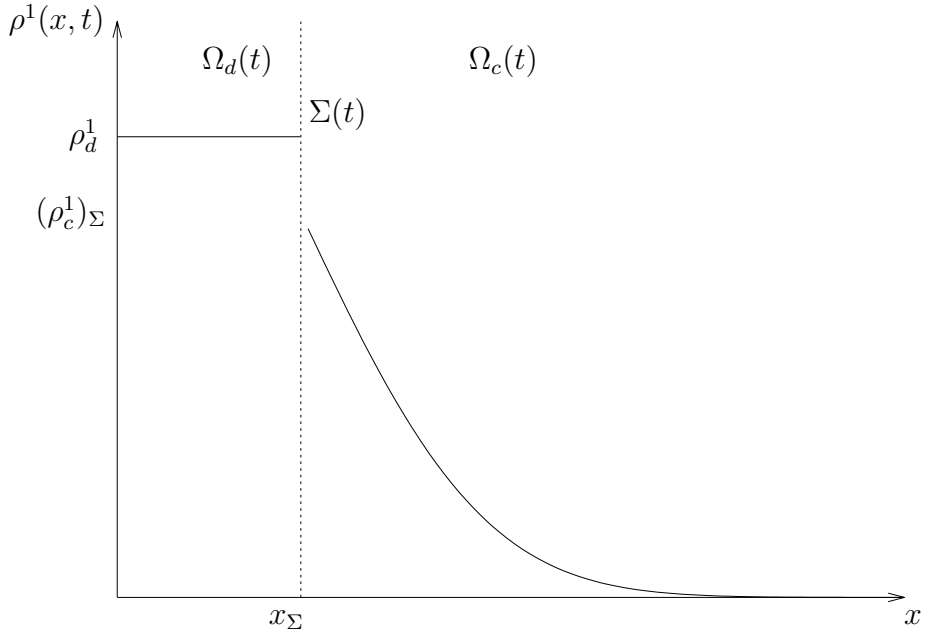

Figure 3.3: 1D concentration profile of a soluble (pure) species in a two-phase system. The density profile is discontinuous at the interface and the concentration is assumed constant in Ω_d due to the incompressibility of the phases.

where H_e^k is the Henry's law coefficient for the k-th species and it is a material property of the system, which generally depends on the temperature and pressure fields near the interface (see Bothe and Fleckenstein, 2013 for a detailed discussion about the generalized Henry's law). For the applications considered in the present work, H_e^k is assumed to be constant for each species and the interface is always treated as saturated. In the special cases of a pure soluble species, the liquid-side of the species concentration is constant and is immediately known from equation 3.34, i.e. $(\rho_c^1)_\Sigma = \rho_d / H_e^1$. Finally, it is reminded here that Henry's law provides accurate results as long as the system is a dilute solution near the equilibrium point, at moderate pressures. These conditions are met in the present work and the reader is referred to Prausnitz et al., 1998 for a discussion about the limitations of Henry's law and for alternative formulations (e.g. Raoult's law).

3.3.1 Overview of the transport of species

For the reader convenience, the set of governing equations for the transport of soluble species in two-phase flows is summarised here. In the present thesis, the molar concentration [$\mathrm{mol\,m^{-3}}$] is used to describe the distribution of species in the domain Ω and it is directly related to the species density as $c^k = \rho^k/M^k$, where M^k is the molar mass of the k-th species. In the following, the molar concentration is simply referred to as concentration.

The conservation of species is given by the following transport equation:

$$\partial_t c^k + \mathbf{u} \cdot \nabla c^k - \nabla \cdot \left(D^k \nabla c^k \right) = 0 \quad \text{in } \Omega \setminus \Sigma \tag{3.35}$$

where the reaction term is not taken into account here (no chemical reactions are considered in the present work).

The mass transfer rate is given by:

$$\dot{m}_p^k = \frac{c_p^k M^k}{\rho_p} \sum_{l=1}^{n-1} \dot{m}_p^l - M^k D_p^k \nabla c_p^k \cdot \mathbf{n}_\Sigma \quad \text{for } p = c, d \tag{3.36}$$

Equation 3.36 can be computed on both sides of the interface, but, due to the continuity of mass, the respective values must be equal, i.e. $\dot{m}_c^k = \dot{m}_d^k$. When the mass transfer rate is computed from the liquid side of the interface ($\dot{m}_c^k$), the ratio ρ_c^k/ρ_c is generally neglectable (consistently with the assumption of dilute solutions) and equation 3.36 can be simplified as $\dot{m}^k = -D^k \nabla \rho^k \cdot \mathbf{n}_\Sigma$.

Finally, the interface is always assumed at the chemical equilibrium and the jump in concentrations across the interface is given by Henry's Law:

$$(c_c^k)_\Sigma = \frac{(c_d^k)_\Sigma}{H_e^k} \tag{3.37}$$

It is worth remarking that equation 3.35 is not valid at the interface and numerical methods must deal with the discontinuity in the concentration profile across Σ. Two approaches are available to integrate numerically the transport equation, namely

one-scalar and two-scalar methods (see the review in section 2.3.3). The selected approach in the present thesis is the two-scalar method introduced by Bothe and Fleckenstein, 2013 and details of the numerical schemes used for the solution of equations 3.35 - 3.37 are provided in chapter 5.

Chapter 4

The BASILISK code

The numerical framework used to solve the governing equations presented in chapter 3 is the open source solver Basilisk (see Popinet and collaborators, 2013–2023). Basilisk is a Finite Volume (FV) solver for the solution of partial differential equations on adaptive Cartesian grids and implements a second-order accurate (time and space discretization) solver for Direct Numerical Simulations (DNS) of two-phase immiscibile fluids without mass transfer. The interface position is tracked with a geometric Volume of Fluid (VOF) method and state of the art numerical techniques are implemented for the computation of the interface curvature, which is particularly relevant to mitigate the numerical effect of spurious currents. The Cartesian mesh can be dynamically adapted (i.e. refined and/or coarsened) by means of an Adaptive Mesh Refinement (AMR) technique based on a wavelet estimation of the spatial discretization error for selected flow fields. The ability of adapting the mesh at each iteration in regions where strong gradients occur makes Basilisk an efficient solver for interfacial flows, where generally a fine mesh is required around the gas-liquid interface and a coarser discretization can be employed for the remaining part of the domain.

In this chapter a general overview of the Basilisk flow solver is provided, and the following sections are organized as follows. The mesh structure and AMR technique are introduced in section 4.1. The VOF method implemented in Basilisk is presented in section 4.2, whilst the numerical schemes for the solution of the Navier-Stokes

equations are described in section 4.3. Finally, the main steps of the flow solver are summarized in section 4.4.

4.1 The grid structure

The integration domain is a square (cube) for 2D (3D) simulations with dimensions $L0 \times L0$ ($L0 \times L0 \times L0$). The domain is discretized with a Cartesian quadtree (octree) mesh in 2D (3D) where each cell is identified by its hierarchical level in the corresponding tree-structure. The root cell is at level 0 and its size Δ is the same as the whole numerical domain ($\Delta = L0$), whilst a generic cell at level l has a resolution of $\Delta(l) = L0/2^l$. The grid structure in Basilisk allows neighbouring cells to vary up to one level, i.e. each cell edge/face cannot communicate with more than two finer edges/faces. A generic cell at level l can be further divided into four (2D) or eight (3D) cells at level $l + 1$; the coarser cell is called "parent" and the finer ones are its corresponding "children". An example of a quadtree grid with different levels of refinement and the relative tree structure are shown in Figure 4.1a and Figure 4.1b, respectively.

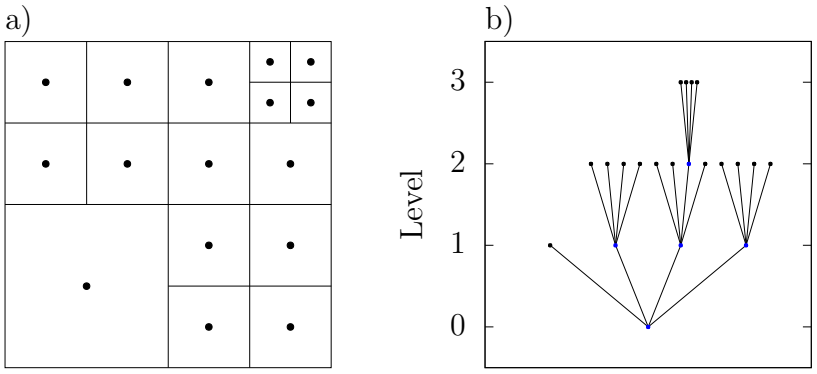

Figure 4.1: Example of a quadtree grid (left) and the corresponding tree structure (right). The black points represent the active cell centres, whilst the blue ones (right) refer to the parent cells (see text).

In order to perform numerical operations (e.g. computation of spatial derivatives, fluxes across cell boundaries) on this type of Cartesian stencils, some extra information needs to be extrapolated from the actual grid, where the solution is defined, and extended to ghost cells (in a similar way to the implementation of boundary conditions). This is done by the "prolongation" and "restriction" operators that compute field values in ghost cells from the available data. The prolongation function (P) predicts the values in children cells from the coarser grid, whilst the restriction operator (R) computes the data in parent cells from the finer grid (see Popinet, 2015 for more details). This operators are used to build regular stencils, where structured Cartesian schemes can be easily implemented in the case of non constant mesh resolution. An example of how these functions operate is shown in Figure 4.2 for a quadtree grid (extension to 3D is straightforward). The actual grid is composed of

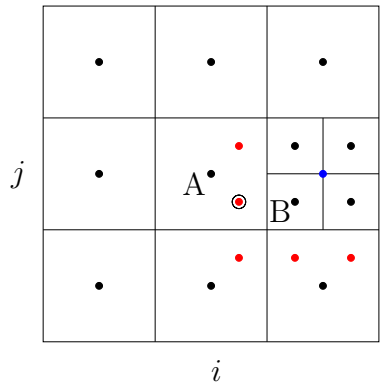

Figure 4.2: Example of restriction/prolongation operators. In order to apply discretization schemes on regular Cartesian stencil, the solution needs to be extrapolated in ghost points (blue and red circles) at different grid levels.

eight cells at level l and four cells at level $l+1$. The twelve points (cell centres) where the solution is defined are called "active" points (black circles in Figure 4.2). To get a 3×3 stencil centered on cell A, the solution in the blue ghost point at level l needs to be extrapolated from the finer grid. A simple way to do this is through a

direct average from the values at level $l+1$:

$$v(\text{ghost}) = \frac{\text{fine}(v,0,0) + \text{fine}(v,1,0) + \text{fine}(v,0,1) + \text{fine}(v,1,1)}{4} \tag{4.1}$$

where $\text{fine}(v,i,j)$ is the value of field v defined in the active child (i,j) of the same ghost cell. In a similar way, to perform operations on a 3×3 stencil centered on cell B, the five red ghost values at level $l+1$ are extrapolated from the coarser grid. This can be done by applying a linear interpolation operator and for the ghost cell marked by the circle in Figure 4.2, it reads:

$$\begin{aligned} v(\text{ghost}) = \text{coarse}(v,0,0) \\ + \frac{\text{coarse}(v,1,0) - \text{coarse}(v,-1,0)}{2\Delta(l)}\frac{\Delta(l)}{4} \\ + \frac{\text{coarse}(v,0,1) - \text{coarse}(v,0,-1)}{2\Delta(l)}\frac{\Delta(l)}{4} \end{aligned} \tag{4.2}$$

where $\text{coarse}(v,0,0)$ is the value of field v defined in the respective parent cell (cell A in this example) and $\text{coarse}(v,i,j)$ is located in cell (i,j) on the coarse grid. Equations 4.1 and 4.2 are only two of the several restriction and prolongation operators that are available in Basilisk. Depending on the type of field that is restricted/prolongated, other formulations might be necessary. This is the case for the refinement of the face-centered velocity field (see section 4.3), where the divergence-free condition (for flows without mass transfer) must be preserved when the solution is transferred between different grid levels.

The restriction and prolongation operators are at the basis of the Adaptive Mesh Refinement technique implemented in Basilisk. Here, a brief description of the AMR algorithm is presented; more details can be found in Popinet, 2015 and van Hooft et al., 2018. The purpose of the AMR algorithm is to decide whether a cell must be refined, coarsened or left unchanged. This is done based on a wavelet estimation of the spatial discretization error for variable fields. For a generic field f, the value $f_l(i,j)$ in a generic active cell of level l is known. The restriction operator can be

applied to estimate the value of f in the parent cell:

$$f_{l-1} = R(f_l) \tag{4.3}$$

where R is the restriction operator and l, $l-1$ represent the active and coarser tree levels, respectively. The prolongation (P) function can now be applied to predict the value of f on the active cell (i, j) from the coarser grid:

$$g_l(i, j) = P(f_{l-1}) \tag{4.4}$$

Since the exact solution $f_l(i, j)$ is known, the wavelet-based discretization error is:

$$\chi_l(i, j) = |f_l(i, j) - g_l(i, j)| \tag{4.5}$$

Given a threshold ξ for the error, a cell (i, j) can be adapted based on the following criteria:

$$\text{cell } (i,j) \text{ must be} = \begin{cases} \text{refined, if} & \chi_l(i,j) > \xi \\ \text{coarsened, if} & \chi_l(i,j) < \frac{2}{3}\xi \\ \text{left unchanged} & \text{Otherwise} \end{cases} \tag{4.6}$$

After all the active cells are assessed against criteria 4.6, the grid is adapted and the values on the updated mesh are computed through the "refinement" and restriction operators. The refinement function performs the same operation as the prolongation operator, i.e. it extrapolates values from a coarser grid to the finer one, but can have a different mathematical formulation than the prolongation function. The user can select multiple fields (e.g. velocity, volume fraction) and assess criteria 4.6 for all the selected fields. The grid is adapted accordingly.

The mesh topology in Basilisk allows for a staggered implementation of the variable fields. This is particularly relevant for the decoupling of pressure and velocity fields in the solution of the Navier-Stokes equations (see section 4.3). Scalar variables can be defined either as cell centered or vertex centered values, while vector fields can be computed either on cell centered or face centered locations (see Figure 4.3).

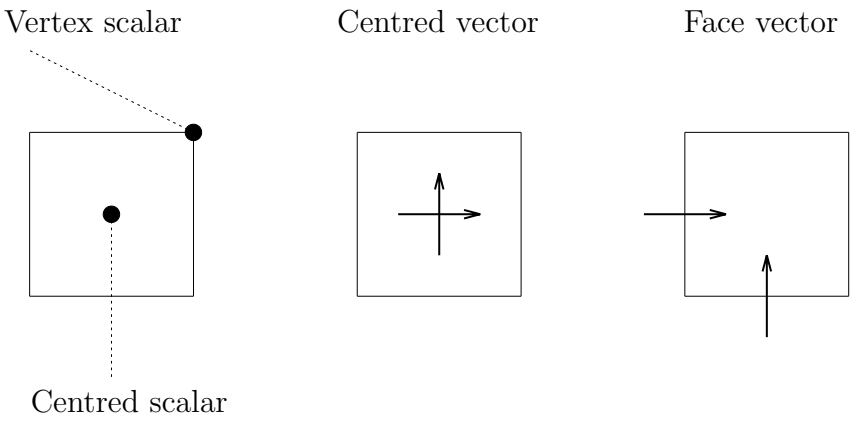

Figure 4.3: Different variable staggering in Basilisk.

4.2 The Volume of Fluid method

The Volume of Fluid (VOF) method was originally proposed by Hirt and Nichols, 1981 and is one of the most widely used numerical approaches for the modelling of two-phase immiscible fluids. The method is part of the so called "interface capturing" methods, along with the Level Set (LS) method (see Sussman et al., 1994). In this class of methods, the interface is identified by an indicator function and its position is tracked by solving a transport equation for the indicator field. The VOF method has been applied successfully to a variety of two-phase problems and amongst its major strengths are the capabilities to deal with complex interface shapes and preserve mass during the transport of the interface. Two formulations of the VOF method are available, namely the "algebraic" and "geometric" approaches, and they differ in the way the transport equation for the indicator field is solved. Basilisk implements the geometric VOF method of Weymouth and Yue, 2010 and, in this section, the main features of this method are presented.

The starting point for the derivation of the VOF approach is the one-fluid formulation presented in section 3.2, which consists of the governing equations 3.21 - 3.23. However, since the available VOF implementation in Basilisk does not take into account any mass transfer between the phases, the phase-change terms are ne-

glected in the present discussion. The details about the methodology developed in the present work to extend the capability of the VOF method to phase-change flows are presented in detail in chapter 5.

The indicator field is given by the Heaviside function (equation 3.11) and the related transport equation is reported here for the reader convenience (the incompressibility constraint has been applied, i.e. $\nabla \cdot \mathbf{u} = 0$):

$$\partial_t H + \mathbf{u} \cdot \nabla H = 0 \tag{4.7}$$

where $H = 1$ in the continuous phase and $H = 0$ in the disperse one. In order to derive the FV scheme, equation 4.7 is integrated over a generic cell with volume V:

$$\frac{\partial}{\partial t} \int_V H \, dV \; + \oint_{\partial V} H \mathbf{u} \cdot \mathbf{n} \, dS \; = \int_V H \nabla \cdot \mathbf{u} \, dV \tag{4.8}$$

where the second term on the LHS of equation 4.7 has been integrated by parts. The term on the RHS of equation 4.8 is null for incompressible flows, but it is kept here because this equation will be integrated with an operator-split method (see section 4.2.2). The volume-averaged value of H is the volume fraction of the continuous phase:

$$f_c = \frac{1}{V} \int_V H \, dV \tag{4.9}$$

and the value of f_c is within the set $[0, 1]$, depending on the amount of liquid in the cell:

$$f_c = \begin{cases} 0 & \text{if the cell is pure gas} \\ 1 & \text{if the cell is pure liquid} \\ ]0, 1[& \text{if the cell is mixed} \end{cases} \tag{4.10}$$

The volume fraction of the disperse phase is immediately known from f_c, i.e. $f_d = 1 - f_c$. Therefore, there is no need to solve an additional transport equation for f_d and, in the following, the phase indicator for the volume fraction is omitted, i.e. $f = f_c$. A representation of the volume fraction field for a generic interface is given in Figure 4.4.

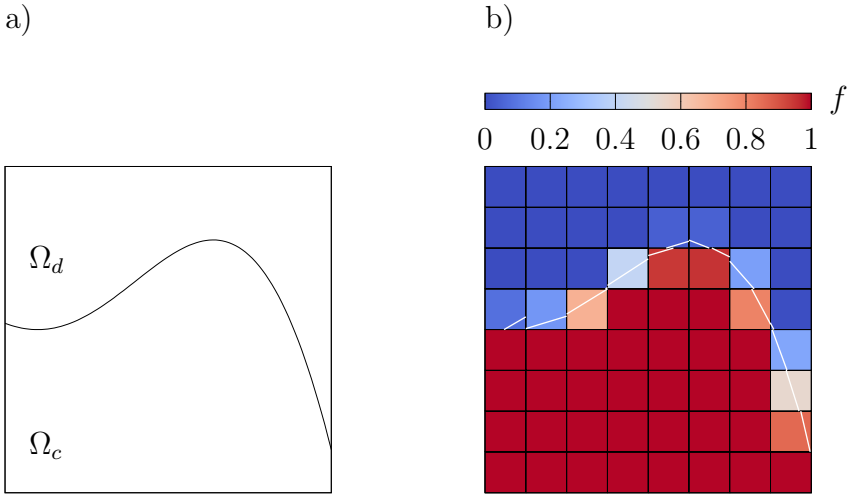

Figure 4.4: Continuous gas-liquid interface (left) and its corresponding VOF representation (right). The reconstructed interface has been obtained with the PLIC method (see text).

The integration of the transport equation 4.8 is performed in two steps (Scardovelli and Zaleski, 1999). First, the interface is approximated with a line/plane in each interfacial cell (reconstruction step, see section 4.2.1), then the fluxes of volume fraction across the cell boundaries are computed (in a geometric way) and equation 4.8 is integrated in time (advection step, see section 4.2.2).

4.2.1 Reconstruction step

The geometric reconstruction of the interface is based on the Piecewise Linear Interface Construction (PLIC) method, where the interface is approximated as a line (plane) in 2D (3D). For each interfacial cell, a local reference system centered on the cell centroid is defined and the interface is represented by the following equation (see Figure 4.5 for a 2D example; extension to 3D is straightforward):

$$xn_{\Sigma x} + yn_{\Sigma y} = \alpha \tag{4.11}$$

where the components of $\mathbf{n}_\Sigma$ are such that $|n_{\Sigma x}| + |n_{\Sigma y}| = 1$ and α is the intercept of the line that represents the interface. The unknowns in equation 4.11 are the

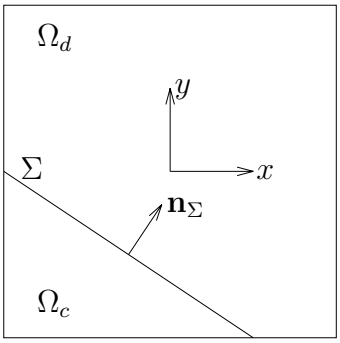

Figure 4.5: Cell centred reference system for the definition of the reconstructed (PLIC) interface.

normal vector $\mathbf{n}_\Sigma$ and the intercept α. First, the normal $\mathbf{n}_\Sigma$ is computed from the volume fraction field f and then α is uniquely defined from $\mathbf{n}_\Sigma$ and f. The algorithm used to compute the interface normal is a combination of the method proposed by Youngs, 1984 and the centered-columns scheme (see Tryggvason et al., 2011). A brief description of the present Mixed-Youngs-Centered (MYC) method is presented here for the 2D case shown in Figure 4.6.

The interface normal is first computed with the centered-columns scheme. The line equation 4.11 can be rewritten as:

$$y = -\text{sgn}(n_{\Sigma y}) m_x x + \alpha' \tag{4.12}$$

where sgn is the sign function and $|m_x|$ is the magnitude of the slope. The method performs a column integration to estimate the heights of the interface to the left (y_L)

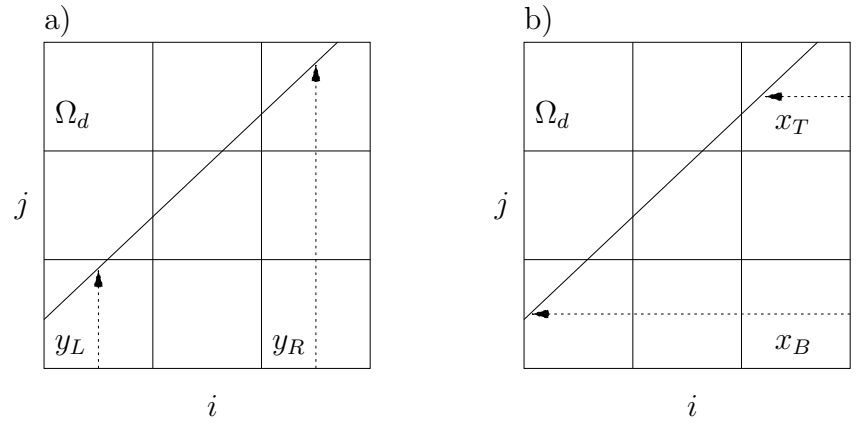

Figure 4.6: Vertical (left) and horizontal (right) heights estimation for the centered-columns scheme.

and right (y_R) sides of the central cell (i, j) where $\mathbf{n}_\Sigma$ is computed (see Figure 4.6a):

$$\begin{aligned} y_L &= \Delta \sum_{k=-1}^{1} f(i-1, j+k) \\ y_R &= \Delta \sum_{k=-1}^{1} f(i+1, j+k) \end{aligned} \tag{4.13}$$

Then, m_x^{cc} can be computed as:

$$m_x^{cc} = \frac{1}{2\Delta}\left(y_L - y_R\right) \tag{4.14}$$

where the superscript cc refers to the centered-columns method. In a similar way, the interface can be described with the function:

$$x = -\text{sgn}(n_{\Sigma x}) m_y y + \alpha'' \tag{4.15}$$

and the heights along the x-direction from the bottom (x_B) and top (x_T) rows (Figure

4.6b):

$$\begin{aligned} x_B &= \Delta \sum_{k=-1}^{1} f(i+k, j-1) \\ x_T &= \Delta \sum_{k=-1}^{1} f(i+k, j+1) \end{aligned} \tag{4.16}$$

are used to compute the slope:

$$m_y^{cc} = \frac{1}{2\Delta}\left(x_B - x_T\right) \tag{4.17}$$

At this point, the choice between the slopes 4.14 and 4.17 follows the criterion (see Tryggvason et al., 2011):

$$|m^{cc}| = \min(|m_x^{cc}|, |m_y^{cc}|) \tag{4.18}$$

Finally, the normal $\mathbf{n}_\Sigma$ is obtained as:

$$\mathbf{n}_\Sigma^{cc} = \begin{cases} \left(\frac{m_x}{|m_x|+1}, \frac{sgn(m_y)}{|m_x|+1}\right) & \text{if } m^{cc} = m_x^{cc} \\ \left(\frac{sgn(m_x)}{1+|m_y|}, \frac{m_y}{1+|m_y|}\right) & \text{if } m^{cc} = m_y^{cc} \end{cases} \tag{4.19}$$

The Youngs' method (see Youngs, 1984) is then applied to perform an additional estimation of the interface normal based on the gradient of the volume fraction field:

$$\mathbf{m}_\Sigma^Y = -\nabla f \tag{4.20}$$

where the symbol $\mathbf{m}_\Sigma$ is used instead of $\mathbf{n}_\Sigma$ to remind that the normal is not yet in its final formulation (i.e. $|m_{\Sigma x}| + |m_{\Sigma y}| \neq 1$); the superscript Y refers to the Youngs method. First, the gradients for each corner of the central cell are computed; for the

top-right vertex of cell (i, j) these read:

$$\begin{aligned} m^Y_{\Sigma x(i+1/2,j+1/2)} &= -\frac{1}{2\Delta}(f_{i+1,j+1} + f_{i+1,j} - f_{i,j+1} - f_{i,j}) \\ m^Y_{\Sigma y(i+1/2,j+1/2)} &= -\frac{1}{2\Delta}(f_{i+1,j+1} - f_{i+1,j} + f_{i,j+1} - f_{i,j}) \end{aligned} \tag{4.21}$$

Finally, the centred volume fraction gradient in cell (i, j) is obtained from the average of the four corner values:

$$\begin{aligned} \mathbf{m}^Y_{\Sigma(i,j)} = \frac{1}{4}(&\mathbf{m}^Y_{\Sigma(i+1/2,j+1/2)} + \mathbf{m}^Y_{\Sigma(i+1/2,j-1/2)} \\ &+ \mathbf{m}^Y_{\Sigma(i-1/2,j+1/2)} + \mathbf{m}^Y_{\Sigma(i-1/2,j-1/2)}) \end{aligned} \tag{4.22}$$

and the interface normal is obtained as:

$$\mathbf{n}^Y_\Sigma = \left(\frac{m^Y_{\Sigma x}}{|m^Y_{\Sigma x}| + |m^Y_{\Sigma y}|}, \frac{m^Y_{\Sigma y}}{|m^Y_{\Sigma x}| + |m^Y_{\Sigma y}|} \right) \tag{4.23}$$

Finally, the choice between the centered-columns (equation 4.19) and Youngs (equation 4.23) methods follows the criteria:

$$\mathbf{n}_\Sigma = \begin{cases} \mathbf{n}^{cc}_\Sigma & \text{if } m^{cc} = m^{cc}_x \text{ and } |m^{cc}| > |m^Y_{\Sigma x}|/|m^Y_{\Sigma y}| \\ \mathbf{n}^{cc}_\Sigma & \text{if } m^{cc} = m^{cc}_y \text{ and } |m^{cc}| > |m^Y_{\Sigma y}|/|m^Y_{\Sigma x}| \\ \mathbf{n}^Y_\Sigma & \text{Otherwise} \end{cases} \tag{4.24}$$

After the interface is computed, the intercept α can be uniquely determined from $\mathbf{n}_\Sigma$ and the volume fraction field (see Tryggvason et al., 2011).

4.2.2 Advection step

After the reconstruction step, the location of the interface is known and the integration in time of the advection equation 4.8 is performed using the operator-split method presented in Weymouth and Yue, 2010. The volume fraction field is advanced from $t^{n-1/2}$ to $t^{n+1/2}$, but the velocity field ($\mathbf{u}_f$) used to transport the interface is

defined at t^n, i.e. there is a delay of half time step between the volume fraction and velocity fields (see section 4.3). Here, the algorithm is briefly introduced for a 2D case; extension to 3D is straightforward.

Equation 4.8 is integrated sequentially along the x- and y- directions in the control volume defined by cell (i, j) (see Figure 4.7a):

$$\frac{f^*_{(i,j)} - f^{n-1/2}_{(i,j)}}{\Delta t} V = -(F_{x(i+1/2,j)} - F_{x(i-1/2,j)}) + \int_V H \frac{\partial u^n}{\partial x}\, dV \tag{4.25}$$

$$\frac{f^{n+1/2}_{(i,j)} - f^*_{(i,j)}}{\Delta t} V = -(F_{y(i,j+1/2)} - F_{y(i,j-1/2)}) + \int_V H \frac{\partial v^n}{\partial y}\, dV \tag{4.26}$$

where F_x, F_y are the fluxes of fluid volume that cross the cell boundaries. The last term on the RHS of equations 4.25 - 4.26 is a dilation term, which is null globally for incompressible flows, but must be taken into account during the operator-split procedure, since the flow is not divergence-free when it is advected along one dimension only. The order in which Equations 4.25 - 4.26 are integrated is changed at each time step, in order to minimize phase errors.

The present Volume of Fluid scheme belongs to the class of geometric VOF methods, because the interface is reconstructed before each one-dimensional advection and the fluxes F are computed in a "geometric" way, based on the exact (in the sense of the PLIC reconstruction) amount of fluid volume which crosses each cell boundary. An example of the flux computation across the $(i - 1/2, j)$ edge is shown in Figure 4.7b:

$$F_{x(i-1/2,j)} = \frac{\Delta V_c}{\Delta t} \tag{4.27}$$

where ΔV_c is the volume of liquid (continuous phase) that is donated by the upwind cell $(i - 1, j)$ to cell (i, j). In this example, the face-centred velocity $u_{f(i-1/2,j)}$ has been assumed positive; in case of negative velocity, the central cell would be donating part of its fluid to the left one and the volume ΔV_c would be computed from cell (i, j).

The terms on the RHS of equations 4.25 - 4.26 are integrated explicitly and this ensures that the fluxes are conservative, i.e. the amount of fluid that leaves one cell

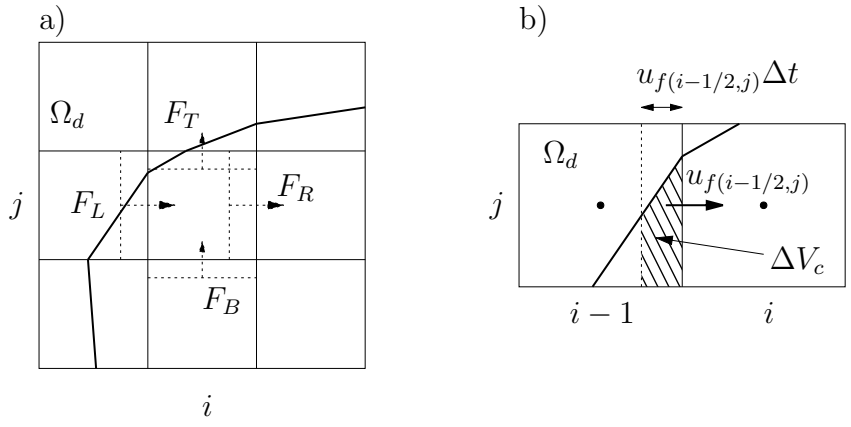

Figure 4.7: Advection scheme for the geometric VOF method. The fluxes across each cell boundary are computed from the upwind cells (left), where the exact amount of fluid that crosses the cell edge is computed based on the PLIC interface reconstruction (right). The VOF fluxes are: $F_L = F_{x(i-1/2,j)}$, $F_R = F_{x(i+1/2,j)}$, $F_B = F_{y(i,j-1/2)}$, and $F_T = F_{y(i,j+1/2)}$.

is entirely donated to a neighbouring one, and that the dilation terms sum up to null divergence. The value of the Heaviside function in the integrals on the RHS is constant during the one-dimensional advections (both in x- and y- directions) and is set to:

$$H^{n-1/2}_{(i,j)} = \begin{cases} 1 & \text{if } f^{n-1/2}_{(i,j)} > 0.5 \\ 0 & \text{Otherwise} \end{cases} \tag{4.28}$$

In order to ensure that the volume fraction is bounded in the set $f \in [0,1]$, a restriction on the CFL number is enforced: CFL < 0.5.

Finally, the Weymouth and Yue, 2010 scheme for a 2D case reads:

$$\begin{aligned} f^{*}_{(i,j)} = f^{n-1/2}_{(i,j)} &- \frac{\Delta t}{V}\left(F_{x(i+1/2,j)} - F_{x(i-1/2,j)}\right) \\ &+ \frac{\Delta t H^{n-1/2}_{(i,j)}}{\Delta}\left(u^{n}_{f(i+1/2,j)} - u^{n}_{f(i-1/2,j)}\right) \end{aligned} \tag{4.29}$$

$$f_{(i,j)}^{n+1/2} = f_{(i,j)}^{*} - \frac{\Delta t}{V}\left(F_{y(i,j+1/2)} - F_{y(i,j-1/2)}\right) + \frac{\Delta t H_{(i,j)}^{n-1/2}}{\Delta}\left(v_{f(i,j+1/2)}^{n} - v_{f(i,j-1/2)}^{n}\right) \tag{4.30}$$

This method ensures that the fluid mass is conserved, provided the face-velocity field $\mathbf{u}_f$ used to transport the volume fraction is divergence-free. However, when phase-change occurs, the divergence of the velocity field is expected to be non null at the interface, according to the balance of mass (equation 3.22). Therefore, the advection scheme of Weymouth and Yue, 2010 cannot ensure mass conservation for this type of flows. The scope of the present thesis is to develop a numerical phase-change model to make geometric VOF schemes, which rely on a divergence-free velocity field, compatible with phase-change flows. The proposed methodology is presented in chapter 5.

4.3 The Navier-Stokes solver

The Navier-Stokes (NS) solver implemented in Basilisk for the solution of the governing equations (3.22 - 3.23) is based on a time-splitting pressure-correction method, which is second order accurate for time and space discretizations. For a general description of the algorithm, the reader is referred to Sharaborin et al., 2021; more details on similar schemes can be found in Popinet, 2003 and Popinet, 2009. The primary variables are the cell-centred pressure (p), velocity ($\mathbf{u}$) and density (ρ) fields, whilst the viscosity (μ) is computed on the cell faces; an auxiliary face-centred velocity field ($\mathbf{u}_f$) is allocated for the decoupling of pressure and velocity. In the following, examples of numerical schemes are reported for 2D cases; extension to 3D is generally straightforward.

The overall time step integration reads:

$$\mathbf{u}^{n+1} = \mathbf{u}^{n} + \Delta t\left(-\nabla\cdot\left(\mathbf{u}^{n+1/2}\otimes\mathbf{u}^{n+1/2}\right) + \frac{1}{\rho^{n+1/2}}\left[-\nabla p^{n+1} + \nabla\cdot\left(2\mu^{n+1/2}\mathbf{S}^{n+1}\right)\right] + \mathbf{a}^{n+1}\right) \tag{4.31}$$

where the gravitational acceleration and surface tension terms have been included in the generic acceleration field $\mathbf{a}$.

After the update of the volume fraction field to time $t^{n+1/2}$ (which is transported by the face velocity field $\mathbf{u}_f^n$), the properties of the fluid are computed accordingly. The density in cell (i, j) is (equation 3.12):

$$\rho_{(i,j)}^{n+1/2} = f_{(i,j)}^{n+1/2}\rho_c + \left(1 - f_{(i,j)}^{n+1/2}\right)\rho_d \tag{4.32}$$

and the viscosity on the cell edge $(i - 1/2, j)$ reads (equation 3.13):

$$\mu_{(i-1/2,j)}^{n+1/2} = f_{(i-1/2,j)}^{n+1/2}\mu_c + \left(1 - f_{(i-1/2,j)}^{n+1/2}\right)\mu_d \tag{4.33}$$

where $f_{(i-1/2,j)}^{n+1/2} = \frac{1}{2}\left(f_{(i,j)}^{n+1/2} + f_{(i-1,j)}^{n+1/2}\right)$. Other averaging formula could be used here (e.g. the harmonic mean) and smearing functions can be introduced to smooth the change of properties across the interface.

Once the fluid properties are updated, the advection term is integrated explicitly:

$$\mathbf{u}_a^{n+1} = \mathbf{u}^n - \Delta t \nabla \cdot \left(\mathbf{u}^{n+1/2} \otimes \mathbf{u}^{n+1/2}\right) \tag{4.34}$$

This operation is performed by advecting the cell-centred velocity field $\mathbf{u}^n$ with the (unknown) face velocity $\mathbf{u}_f^{n+1/2}$, from time t^n to t^{n+1}. The face-centred velocity field at time $t^{n+1/2}$ is extrapolated from $\mathbf{u}^n$ with the unsplit, upwind second order scheme of Bell et al., 1989, performing an interpolation in space (from cell-centres to cell faces) and in time (from t^n to $t^{n+1/2}$). The contribution of the pressure gradient and acceleration terms is taken into account and an example of face velocity extrapolation is reported here for the 2D horizontal component, where the upwind cells are assumed to be on the left side for the x-velocity and on the bottom side for the y-velocity:

$$\begin{aligned} u_{f(i-1/2,j)}^{n+1/2} = u_{(i-1,j)}^n &+ \left(1 - \frac{\Delta t}{\Delta}\overline{u}_{f(i-1/2,j)}^n\right)\frac{\partial u^n}{\partial x}\frac{\Delta}{2} \\ &+ G_{xf(i-1/2,j)}^n\frac{\Delta t}{2} - v_{(i-1,j)}^n\frac{\partial u^n}{\partial y}\frac{\Delta t}{2} \end{aligned} \tag{4.35}$$

The second term on the RHS of equation 4.35 represents the extrapolation in space (from cell $(i-1,j)$ to the cell boundary $(i-1/2,j)$) and in time (from t^n to $t^{n+1/2}$) (see Figure 4.8a) and the average face velocity is computed from the neighbouring cell-centred values, i.e. $\overline{u}^n_{f(i-1/2,j)} = \frac{1}{2}\left(u^n_{(i-1,j)} + u^n_{(i,j)}\right)$. The following term is the contribution of pressure and accelerations, i.e. $G^n_{xf(i-1/2,j)} = -\frac{1}{\rho}\frac{\partial p^n}{\partial x} + a^n_x$ and the last one represents the effect of the cross flow, i.e. the velocity along the y- direction (see Figure 4.8b). However, the face velocity field obtained with the scheme of equation

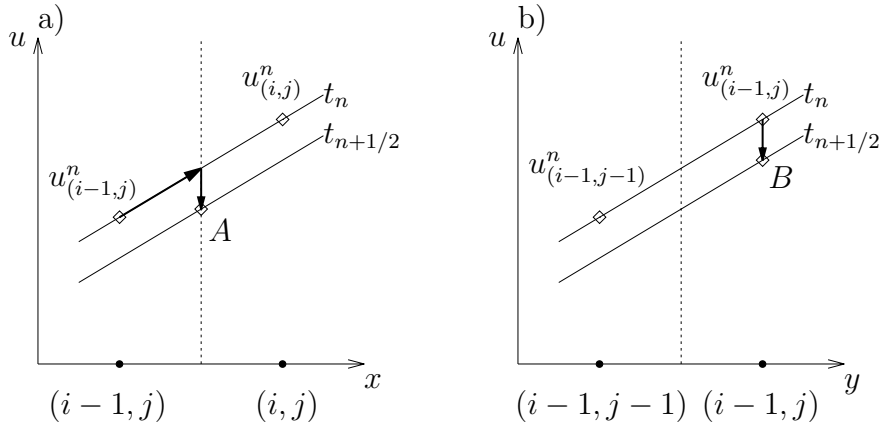

Figure 4.8: Prediction of face velocity field at time $t^{n+1/2}$. The velocity on the cell boundary $(i-1/2,j)$ is obtained through extrapolation (in space and time) from the upwind cell to point A (left). The velocity in the upwind cell is advanced to point B to take into account the effect of the cross flow velocity (right).

4.35 is generally not consistent with the continuity equation and a projection step is performed to correct $\mathbf{u}_f^{n+1/2}$ (more details about the projection operator are given below). Finally, the explicit advection scheme of Bell et al., 1989, with the corrected face velocity field, is used to obtain $\mathbf{u}_a^{n+1}$.

Before taking into account the effect of viscosity, the contribution of pressure and acceleration terms at time t^n is included:

$$\mathbf{u}^{n+1}_{corr(\Delta t)} = \mathbf{u}^n_a + \Delta t\left(-\frac{\nabla p^n}{\rho^{n+1/2}} + \mathbf{a}^n\right) \tag{4.36}$$

and then the viscous term is integrated implicitly:

$$\mathbf{u}_v^{n+1} = \mathbf{u}_{corr(\Delta t)}^{n+1} + \frac{\Delta t}{\rho^{n+1/2}} \nabla \cdot \left(2\mu^{n+1/2}\mathbf{S}^{n+1}\right) \tag{4.37}$$

The integration of equation 4.37 is performed with an implicit multigrid solver, which uses multiple grids (at different levels of refinement) to efficiently resolve Poisson-Helmholtz equations; more details about this solver can be found in Popinet, 2015. The viscous term is integrated with a second order central differential scheme, that for a 2D case (horizontal component) reads:

$$\begin{aligned} u_{v(i,j)}^{k} = \Bigg\{ & u_{(i,j)}^{k-1}\Delta^2 + \frac{\Delta t}{\rho}\Bigg[2\mu_{(i+1/2,j)}u_{(i+1,j)}^{k-1} + 2\mu_{(i-1/2,j)}u_{(i-1,j)}^{k-1} \\ & + \mu_{(i,j+1/2)}\Bigg(u_{(i,j+1)}^{k-1} \\ & + \frac{1}{4}\left(v_{(i+1,j)}^{k-1} + v_{(i+1,j+1)}^{k-1} - v_{(i-1,j)}^{k-1} - v_{(i-1,j+1)}^{k-1}\right)\Bigg) \\ & + \mu_{(i,j-1/2)}\Bigg(u_{(i,j+1)}^{k-1} \\ & - \frac{1}{4}\left(v_{(i+1,j)}^{k-1} + v_{(i+1,j-1)}^{k-1} - v_{(i-1,j)}^{k-1} - v_{(i-1,j-1)}^{k-1}\right)\Bigg)\Bigg]\Bigg\} \\ & / \left[\Delta^2 + \frac{\Delta t}{\rho}\left(2\mu_{(i-1/2,j)} + 2\mu_{(i+1/2,j)} + \mu_{(i,j+1/2)} + \mu_{(i,j-1/2)}\right)\right] \end{aligned} \tag{4.38}$$

where the superscript k refers to the k-th iteration of the multigrid solver. The viscous solver 4.38 is iterated until the maximum residual is smaller than a threshold value; then the contribution of pressure and acceleration terms at time t^n is removed:

$$\mathbf{u}_{corr(-\Delta t)}^{n+1} = \mathbf{u}_v^{n+1} - \Delta t\left(-\frac{\nabla p^n}{\rho^{n+1/2}} + \mathbf{a}^n\right) \tag{4.39}$$

Before the computation of pressure at t^{n+1}, the face velocity field ($\mathbf{u}_f^*$) is updated

with the acceleration term:

$$\begin{aligned} u^*_{f(i-1/2,j)} &= \frac{1}{2}\left(u^{n+1}_{corr(-\Delta t)(i,j)} + u^{n+1}_{corr(-\Delta t)(i-1,j)}\right) + \Delta t a^{n+1}_{x(i-1/2,j)} \\ v^*_{f(i,j-1/2)} &= \frac{1}{2}\left(v^{n+1}_{corr(-\Delta t)(i,j)} + v^{n+1}_{corr(-\Delta t)(i,j-1)}\right) + \Delta t a^{n+1}_{y(i,j-1/2)} \end{aligned} \tag{4.40}$$

Many equilibrium solutions depend on the balance between acceleration terms and pressure, e.g. Laplace equation for the equilibrium between pressure and surface tension across the interface of a stationary spherical bubble/droplet. In order to ensure a consistent spatial discretization, both pressure gradient (∇p) and acceleration term ($\mathbf{a}$) are discretized on the same locations, i.e. the cell faces. When surface tension is considered, the corresponding acceleration term is discretized using the approach of Brackbill et al., 1992:

$$\frac{\sigma\kappa\mathbf{n}_\Sigma}{\rho}\delta_\Sigma = \frac{\sigma\kappa\nabla f}{\rho} \tag{4.41}$$

where the gradient of volume fraction is computed on the cell boundaries, by using the following scheme $\frac{\partial f}{\partial x}_{(i-1/2,j)} = \frac{1}{\Delta}\left(f_{(i,j)} - f_{(i-1,j)}\right)$. In this thesis, the surface tension coefficient is assumed uniform (see section 3.1). However, it is worth reminding here that σ generally depends on several factors, which include temperature, chemical reactions and electric fields. The presence of surfactants also affects σ, as it induces a gradient of surface tension and generates the well-known Marangoni effect (see section 2.1). The above-mentioned effects are neglected in this work and some of the simulations presented in chapters 6 and 7 adopt two-dimensional axisymmetric models to reduce the computational cost. This introduces a further approximation, since surface tension is typically a three-dimensional force. However, the results presented in the following show that the above assumptions provide sufficiently accurate results for the applications considered in this thesis.

A method where the discretization of the acceleration terms are consistent with the gradient of pressure is defined as a well-balanced method and, in the case of flows with surface tension, this is a fundamental feature to reduce the magnitude of spurious currents (see Popinet, 2018 for a review about numerical methods for surface tension problems). The term in equation 4.41 requires the computation of the

interface curvature k, which is generally a challenging task for VOF methods. Basilisk implements a height function (HF) approach where the location of the interface (height) is first obtained from the summation of the volume fraction field over few cells and then is differentiated in order to compute the curvature. For a 2D case (see Figure 4.9), the interface is obtained as:

$$\kappa_{(i,j)} = \frac{\partial_{xx} h}{(1 + \partial_x^2 h)^{3/2}} \tag{4.42}$$

where h is the interface height and the derivatives are computed with central finite difference schemes:

$$\begin{aligned} \partial_{xx} h_{(i,j)} &= \frac{h_{(i+1,j)} + h_{(i-1,j)} - 2h_{(i,j)}}{\Delta^2} \\ \partial_x h_{(i,j)} &= \frac{h_{(i+1,j)} - h_{(i-1,j)}}{2\Delta} \end{aligned} \tag{4.43}$$

In the case of low mesh resolution or highly curved interfaces, the HF method could fail to find a suitable interfacial height; in this case a parabolic function is fitted through the interface and the curvature is obtained by differentiating the resulting formula. The reader is referred to Popinet, 2009 for the details of the HF algorithm.

To get the face velocity at time t^{n+1}, the contribution of pressure is taken into account:

$$\mathbf{u}_f^{n+1} = \mathbf{u}_f^* - \frac{\Delta t}{\rho^{n+1/2}} \nabla p^{n+1} \tag{4.44}$$

By applying the conservation of mass (equation 3.22), the following Poisson equation for the pressure is obtained:

$$\nabla \cdot \left(\frac{\Delta t}{\rho^{n+1/2}} \nabla p^{n+1} \right) = \nabla \cdot \mathbf{u}_f^* - \dot{m}^{n+1/2} \left(\frac{1}{\rho_d} - \frac{1}{\rho_c} \right) \delta_\Sigma \tag{4.45}$$

where the last term on the RHS represents the contribution of the mass transfer at the interface; details on the numerical discretization of this term are given in chapter 5. Equation 4.45, also referred to as the projection step, is solved implicitly with the

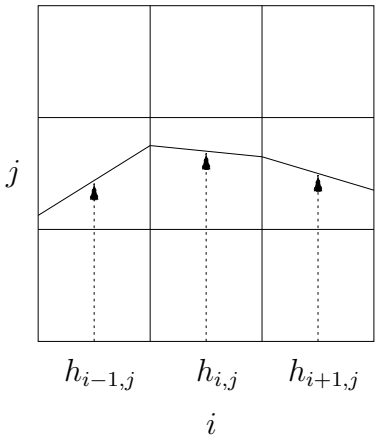

Figure 4.9: Curvature estimation with the HF method.

multigrid solver. After the pressure at time t^{n+1} is obtained, the final face-centred velocity field $\mathbf{u}_f^{n+1}$ is obtained from equation 4.44. The projection step performed here is the same used for the correction of the face velocity at time $t^{n+1/2}$, but a time step of $\Delta t/2$ is used there instead of Δt.

Finally, the cell-centred velocity $\mathbf{u}^{n+1}$ is obtained from $\mathbf{u}^{n+1}_{corr(-\Delta t)}$ (equation 4.39):

$$\mathbf{u}^{n+1} = \mathbf{u}^{n+1}_{corr(-\Delta t)} + \Delta t \left(-\frac{\nabla p^{n+1}}{\rho^{n+1/2}} + \mathbf{a}^{n+1} \right) \tag{4.46}$$

The time step integration is concluded with the adaption of the grid, according to the criteria presented in section 4.1.

4.4 Overview of the time step integration

In this section, an overview of the main steps of the combined Volume of Fluid and Navier-Stokes solver (VOF-NS) is provided.

1. Set the time step Δt according to the CFL constraint. When the VOF solver is used, the CFL limit is CFL = 0.5; this condition is relaxed to CFL = 0.8 for

single-phase flows. The maximum allowed time step is:

$$\Delta t_{\max} = \min\left(\min\left(\frac{\Delta}{|u_f|}, \frac{\Delta}{|v_f|}\right)\mathrm{CFL}, \sqrt{\frac{(\rho_c + \rho_d)\,\Delta^3}{2\pi\sigma}}\right) \tag{4.47}$$

where the second term in the brackets is the time step constraint for the (explicit) surface tension scheme. The CFL criterion is sufficient to ensure the stability of the solver, since diffusive terms (e.g. viscous effects) are solved implicitly. Other phenomena, such as chemical reactions or mass transfer, introduce additional time scales that need to be taken into account when setting $\Delta t_{\max}$. Reactions are not considered in this work, whilst mass transfer is discussed in chapter 5. The maximum time step in case of volume change due to the transport of mass across the gas-liquid interface is set in a way to ensure $\mathrm{CFL} = 0.5$, as required by the stability properties of the VOF solver.

2. Update the volume fraction field to time $t^{n+1/2}$ ($f^{n+1/2}$), using the face velocity field $\mathbf{u}_f^n$.

3. Update the fluid properties $\rho^{n+1/2}, \mu^{n+1/2}$.

4. Solve the advection term with the explicit scheme of Bell et al., 1989:

$$\mathbf{u}_a^{n+1} = \mathbf{u}^n - \Delta t \nabla \cdot \left(\mathbf{u}^{n+1/2} \otimes \mathbf{u}^{n+1/2}\right) \tag{4.48}$$

This operation requires the prediction (and correction) of the face velocity field at time $t^{n+1/2}$ ($\mathbf{u}_f^{n+1/2}$).

5. Add the contribution of pressure gradient and acceleration terms at time t^n:

$$\mathbf{u}_{corr(\Delta t)}^{n+1} = \mathbf{u}_a^n + \Delta t\left(-\frac{\nabla p^n}{\rho^{n+1/2}} + \mathbf{a}^n\right) \tag{4.49}$$

6. Integrate the viscous term with the implicit multigrid solver:

$$\mathbf{u}_v^{n+1} = \mathbf{u}_{corr(\Delta t)}^{n+1} + \frac{\Delta t}{\rho^{n+1/2}} \nabla \cdot \left(2\mu^{n+1/2}\mathbf{S}^{n+1}\right) \tag{4.50}$$

7. Remove the correction:

$$\mathbf{u}^{n+1}_{corr(-\Delta t)} = \mathbf{u}^{n+1}_{v} - \Delta t \left(-\frac{\nabla p^{n}}{\rho^{n+1/2}} + \mathbf{a}^{n} \right) \tag{4.51}$$

8. Get the temporary face velocity field $\mathbf{u}^{*}_{f}$ by taking into account the acceleration term $\mathbf{a}^{n+1}$:

$$\begin{aligned} u^{*}_{f(i-1/2,j)} &= \frac{1}{2}\left(u^{n+1}_{corr(-\Delta t)(i,j)} + u^{n+1}_{corr(-\Delta t)(i-1,j)} \right) + \Delta t a^{n+1}_{x(i-1/2,j)} \\ v^{*}_{f(i,j-1/2)} &= \frac{1}{2}\left(v^{n+1}_{corr(-\Delta t)(i,j)} + v^{n+1}_{corr(-\Delta t)(i,j-1)} \right) + \Delta t a^{n+1}_{y(i,j-1/2)} \end{aligned} \tag{4.52}$$

9. Apply the projection step and get the pressure at time t^{n+1} with the multigrid solver:

$$\nabla \cdot \left(\frac{\Delta t}{\rho^{n+1/2}} \nabla p^{n+1} \right) = \nabla \cdot \mathbf{u}^{*}_{f} - \dot{m}^{n+1/2} \left(\frac{1}{\rho_d} - \frac{1}{\rho_c} \right) \delta_{\Sigma} \tag{4.53}$$

10. Update the face velocity field to time t^{n+1}:

$$\mathbf{u}^{n+1}_{f} = \mathbf{u}^{*}_{f} - \frac{\Delta t}{\rho^{n+1/2}} \nabla p^{n+1} \tag{4.54}$$

11. Update the centred velocity field to time t^{n+1}:

$$\mathbf{u}^{n+1} = \mathbf{u}^{n+1}_{corr(-\Delta t)} + \Delta t \left(-\frac{\nabla p^{n+1}}{\rho^{n+1/2}} + \mathbf{a}^{n+1} \right) \tag{4.55}$$

12. Adapt the grid.

In this chapter, the VOF method and Navier-Stokes solver implemented in Basilisk have been introduced. In the description of the Volume of Fluid method, the flow was assumed without any mass transfer between the phases. In case of phase-change flows, the source term in the transport of the Heaviside function (equation 3.21) must be taken into account and the volume fraction updated accordingly. The accuracy of the solution for phase-change flows relies on the prediction of the mass

transfer rate $\dot{m}$, that appears in the governing equations 3.21 - 3.22 and requires a careful treatment. In the next chapter, the phase-change model developed within the present thesis is introduced and its implementation in the combined VOF-NS solver is discussed.

Chapter 5

The phase-change model

In this chapter, the phase-change model developed within the present thesis and its implementation in the Basilisk code are discussed. The main objective of this work is the development of a numerical framework for the modelling of two-phase incompressible flows with phase-change, based on a geometric VOF method. As discussed in chapter 4, such methods are generally developed for incompressible flows without mass transfer and rely on the divergence-free kinematic constraint for the velocity field. However, in the case of mass exchange between the phases, the velocity field is generally not divergence-free at the interface, due to the continuity of mass (equation 3.22), and incompressible VOF methods do not guarantee mass conservation under this circumstance. This issue is addressed in the present work by developing an original approach, which is based on the extension of the velocity field of the primary phase (i.e. where $H = 1$) across the interface, in a way that the divergence-free condition applies to the interface as well. This is the most significant contribution of the present thesis to the numerical methodology.

The chapter is organized as follows. The transport equation for the volume fraction field with mass transfer and its integration are presented in section 5.1, whilst the proposed velocity extension algorithm is discussed in section 5.2. The two-scalar method for the transport of species is introduced in section 5.3 and the numerical scheme used for the prediction of the mass transfer rate is presented in section 5.4. Finally, an overview of the proposed phase-change model and its implementation in

the Basilisk code is given in section 5.5.

5.1 The VOF method with phase-change

The transport equation for the Heaviside function in the general case of flows with phase-change was introduced in section 3.2 (equation 3.21) and is reported here for the reader convenience:

$$\partial_t H + \nabla \cdot (H\mathbf{u}) = -\frac{\dot{m}}{\rho_c}\delta_\Sigma \tag{5.1}$$

The integration of equation 5.1 in the control volume V defined by the generic cell (i, j) leads to the FV formulation:

$$\frac{\partial f_{(i,j)}}{\partial t} \approx \frac{f^{n+1/2}_{(i,j)} - f^{n-1/2}_{(i,j)}}{\Delta t} = -\frac{1}{V}\oint_{\partial V} H\mathbf{u}_c \cdot \mathbf{n}\, dS \; - \frac{1}{V}\int_V \frac{\dot{m}}{\rho_c}\delta_\Sigma\, dS \tag{5.2}$$

where the liquid volume fraction f is advanced from time $t^{n-1/2}$ to $t^{n+1/2}$, coherently with the VOF-NS solver (see section 4.3). The velocity in the advection term of equation 5.2 has been replaced by $\mathbf{u}_c$ to emphasize the point that the Heaviside function is transported by the respective phase velocity only (the continuous phase velocity, in this case), since $H = 0$ in Ω_d.

The integration of equation 5.2 is performed in two steps. First, f is advected by the continuous phase velocity field:

$$\frac{\tilde{f}_{(i,j)} - f^{n-1/2}_{(i,j)}}{\Delta t} = -\frac{1}{V}\oint_{\partial V} H\mathbf{u}_c \cdot \mathbf{n}\, dS \tag{5.3}$$

Then, the source term due to the mass transfer is taken into account:

$$\frac{f^{n+1/2}_{(i,j)} - \tilde{f}_{(i,j)}}{\Delta t} = -\frac{1}{V}\int_V \frac{\dot{m}}{\rho_c}\delta_\Sigma\, dS \tag{5.4}$$

The geometric VOF scheme implemented in Basilisk (equations 4.29 - 4.30), uses the one-fluid face-centred velocity $\mathbf{u}^n_f$ to advect the interface and requires $\mathbf{u}^n_f$ to

be divergence-free to ensure mass conservation during the transport of the volume fraction, which is always the case for incompressible flows without mass transfer. At this point a remark is in order. The kinematic constrain on the divergence of the velocity field applies only to the faces of the cells that contain liquid (either pure liquid or interfacial cells), so that the dilation terms from equations 4.29 - 4.30 sum up to zero:

$$\frac{\Delta t H^{n-1/2}_{(i,j)}}{\Delta}\left(u^n_{f(i+1/2,j)} - u^n_{f(i-1/2,j)} + v^n_{f(i,j+1/2)} - v^n_{f(i,j-1/2)}\right) = 0 \tag{5.5}$$

where the divergence of the velocity field in cell (i, j) is computed as:

$$\left[\nabla \cdot \mathbf{u}^n_f\right]_{(i,j)} = \frac{u^n_{f(i+1/2,j)} - u^n_{f(i-1/2,j)} + v^n_{f(i,j+1/2)} - v^n_{f(i,j-1/2)}}{\Delta} \tag{5.6}$$

However, for pure gas cells, condition 5.5 is always met even if $\left[\nabla \cdot \mathbf{u}^n_f\right]_{(i,j)} \neq 0$, since $H^{n-1/2}_{(i,j)} = 0$ (see equation 4.28). Therefore, the way to make the incompressible VOF scheme of Weymouth and Yue, 2010 compatible with phase-change flows is to ensure that condition 5.5 is always satisfied in interfacial cells, even when mass transfer occurs (the condition is automatically true for pure liquid/gas cells, due to the incompressibility of the phases). This is achieved by extending the liquid velocity field across the gas-liquid interface, so that for each cell where $f > \epsilon$, the divergence of the velocity field is null (ϵ is a threshold value used to identify the cells that contain liquid). Such velocity correction should be able to preserve the velocity field in pure liquid/gas cells (where $\mathbf{u}^n_f$ is already divergence-free) and modify $\mathbf{u}^n_f$ in interfacial cells only. However, a solenoidal extension requires a velocity correction in a few neighbouring (pure) cells too; these cells must be pure gas ones, as we need to preserve the face-centred velocity in liquid cells, since this is the phase velocity used for the transport of the Heaviside function (equation 5.1). After the correction of the face-centred velocity, the advection step (equation 5.3) is integrated with the available scheme of Weymouth and Yue, 2010. The details of the proposed velocity extension algorithm to correct the velocity field are given in section 5.2.

After the advection of the interface, the volume fraction field is updated with the

contribution of the mass transfer. The source term in equation 5.4 is integrated in a geometric way, based on the PLIC reconstruction of the interface (see Malan et al., 2021), and consists of a rigid displacement of the interface along the normal direction $\mathbf{n}_\Sigma$:

$$\mathbf{h}_\Sigma = -\frac{\dot{m}}{\rho_c}\frac{\Delta t}{\Delta}\mathbf{n}_\Sigma \tag{5.7}$$

To get the volume fraction field $f^{n+1/2}$ after the displacement $\mathbf{h}_\Sigma$, the intercept α is first updated from the advetcion step (which occurs at time $\tilde{t}$) and, for the 2D example reported in Figure 5.1, reads:

$$\alpha^{n+1/2} = \tilde{\alpha} - \frac{\dot{m}}{\rho_c}\frac{\Delta t}{\Delta}\sqrt{[(\tilde{n}_{\Sigma x})^2 + (\tilde{n}_{\Sigma y})^2]} \tag{5.8}$$

and for a 3D case, the intercept is simply:

$$\alpha^{n+1/2} = \tilde{\alpha} - \frac{\dot{m}}{\rho_c}\frac{\Delta t}{\Delta}\sqrt{[(\tilde{n}_{\Sigma x})^2 + (\tilde{n}_{\Sigma y})^2 + (\tilde{n}_{\Sigma z})^2]} \tag{5.9}$$

where the interface normal is such that $|n_{\Sigma x}| + |n_{\Sigma y}| + |n_{\Sigma z}| = 1$ (see section 4.2.1). Then, the value of $f^{n+1/2}$ is uniquely determined from the intercept $\alpha^{n+1/2}$ and the normal $\mathbf{n}_\Sigma^{n+1/2}$, which is not changed between $\tilde{t}$ and $t^{n+1/2}$. The function used to update the volume fraction automatically limits f in the set $[0, 1]$, since it takes into account only the volume occupied by the primary phase within the cell. However, when a cell is either almost filled or empty, the interface displacement $\mathbf{h}_\Sigma$ can be large enough to move the interface completely beyond the cell boundaries. In this case, the extra amount (either positive or negative) of volume fraction needs to be redistributed in the neighbouring cells to preserve mass.

5.2 The velocity extension algorithm: a novel approach

In this section, a novel method to extend the primary phase velocity field (the liquid one in this work) in such a way to make it divergence-free in interfacial cells is

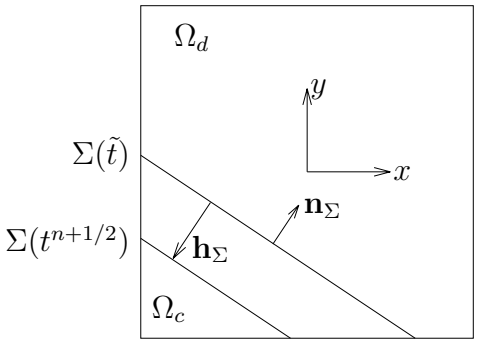

Figure 5.1: Normal displacement ($\mathbf{h}_\Sigma$) of the interface due to a (positive) global mass transfer rate $\dot{m}$.

presented. As explained in section 5.1, this step is necessary to use the geometric VOF scheme of Weymouth and Yue, 2010 for the advection of the Heaviside function (equation 5.3). Although developed for different reasons, several approaches exist to extend phase velocity fields in multiphase flows. The Ghost Fluid method (Fedkiw et al., 1999) is the basis for the development of the algorithms proposed in Nguyen et al., 2001, Sussman, 2003 and Tanguy et al., 2007. More recently, Malan et al., 2021 proposed a different approach for evaporating flows which serves the same purpose as required by the present work, i.e. make incompressible VOF schemes compatible with phase-change flows. All these methods require the solution of at least one additional Poisson equation to make the final extended velocity field divergence-free. The algorithm proposed here doesn't require the solution of additional partial differential equations and can be readily implemented in existing codes, with minimum computational effort. The fundamental idea of the proposed method consists of redistributing the original mass transfer rate field ($\dot{m}$) from the interfacial cells to the neighbouring pure gas cells and store the redistributed term into a new scalar field $\dot{m}'$. This algorithm is based on a two step procedure that is illustrated in the following for a 2D case; extension to 3D is straightforward.

The first step is the computation of the (volume-average) mass transfer rate term $\dot{m}$ (see section 5.4) for each interfacial cell; a cell is marked as interfacial if the value

of the volume fraction field is in the set $f \in]\epsilon, 1-\epsilon[$, where the threshold ϵ is set to $\epsilon = 10^{-6}$. For each interfacial cell (i, j), the number of pure gas cells (i.e. where $f < \epsilon$) that are inside the 3×3 stencil centred on cell (i, j) is stored in the newly allocated cell-centred scalar field $avg_{(i,j)}$ (see Figure 5.2a). These pure gas cells are marked as "acceptors" of the central "donor" cell (i, j) and an acceptor (donor) cell may have multiple related acceptors (donors). The field avg is set to null in all the cells that do not contain the interface.

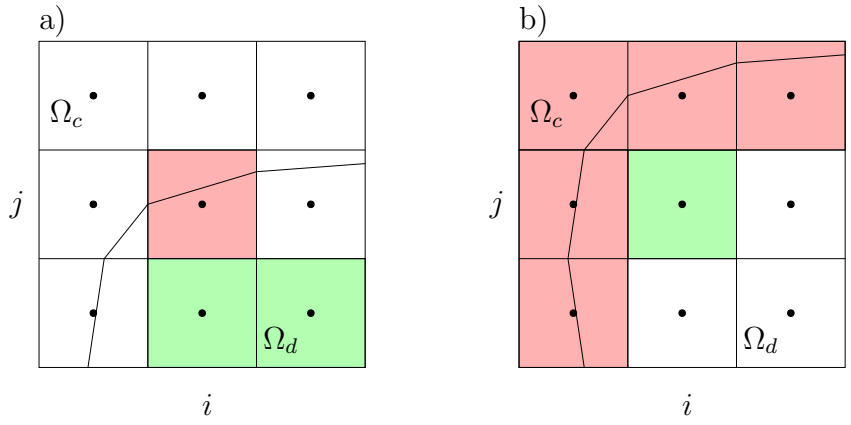

Figure 5.2: a) Computation of the field avg for the donor cell (i, j) (red cell). The number of acceptors (green cells) is computed inside the 3×3 stencil and, in this case, $avg_{(i,j)} = 2$. b) Computation of the redistributed mass transfer term $\dot{m}'$ for the acceptor cell (i, j) (green cell). For this cells, the donors are the interfacial cells within the 3×3 stencil (red cells).

The second step is the redistribution of the mass transfer rate term $\dot{m}$ from donor cells to acceptor ones. For each acceptor, the contribution from all the relative donors is computed and stored in the newly allocated cell-centred scalar field $\dot{m}'$; this field is set to null for all the other cells. Donor cells contain two type of information, i.e. the mass transfer rate $\dot{m}$ and the interface area A_Σ. In order to pass both information to acceptors, the redistributed field $\dot{m}'$ in the generic acceptor cell (i, j) is computed

in the following way (see Figure 5.2b):

$$\dot{m}'_{(i,j)} = \sum_{\text{donor}(l,k)} \frac{\dot{m}_{(l,k)}}{avg_{(l,k)}} A_{\Sigma(l,k)} \tag{5.10}$$

where the summation in equation 5.10 is performed for all the donors (l,k) related to the acceptor (i,j), i.e. the interfacial cells within the 3×3 stencil centred on cell (i,j). It is remarked here that the terms acceptor and donor refer to the redistribution of the mass source term from the interfacial cells (i.e. donors) to the neighbouring pure gas cells (i.e. acceptors), irrespective of the direction of the mass exchange (e.g from liquid to gas or vice versa). The formula of equation 5.10 ensures that once $\dot{m}$ is replaced by $\dot{m}'$, the overall mass per time unit that is exchanged across the interface is conserved, i.e.:

$$\sum_{\Omega} \dot{m} A_{\Sigma} = \sum_{\Omega} \dot{m}' \tag{5.11}$$

To obtain the extended liquid velocity field across the interface, the mass transfer term in the projection step of the Navier-Stokes solver (equation 4.45) is replaced by the redistributed term $\dot{m}'$. The projection step is used to get the pressure field at time t^{n+1} by enforcing the continuity equation and is reported here for the reader convenience:

$$\nabla \cdot \left(\frac{\Delta t}{\rho^{n+1/2}} \nabla p^{n+1} \right) = \nabla \cdot \mathbf{u}_f^* - \dot{m}^{n+1/2} \left(\frac{1}{\rho_d} - \frac{1}{\rho_c} \right) \delta_{\Sigma} \tag{5.12}$$

After the integration of equation 5.12 in the control volume V defined by cell (i,j) and substitution of $\dot{m}$ with $\dot{m}'$, the new projection step (in its FV formulation) for the computation of p^{n+1} reads:

$$\left[\nabla_{\Delta} \cdot \left(\frac{\Delta t}{\rho^{n+1/2}} \nabla_{\Delta} p^{n+1} \right) \right]_{(i,j)} = \left[\nabla_{\Delta} \cdot \mathbf{u}_f^* \right]_{(i,j)} - \dot{m}'^{n+1/2}_{(i,j)} \left(\frac{1}{\rho_d} - \frac{1}{\rho_c} \right) \frac{1}{V} \tag{5.13}$$

where ∇_{Δ} is the numerical (discretized) gradient operator and the Dirac function has been replaced by $\delta_{\Sigma} = A_{\Sigma}/V$ (see Fleckenstein and Bothe, 2015). The new projection step ensures that the face-centred velocity field $\mathbf{u}_f^{n+1}$ obtained from p^{n+1}

through equation 4.44 is divergence-free in all the cells where $\dot{m}' = 0$, which is always true for pure liquid and interfacial cells. This provides a natural extension of the continuous phase velocity across the interface, and an example of the velocity field obtained with the proposed algorithm, for the flow around a gas bubble exchanging mass with the liquid, is reported in Figure 5.3 (this example is discussed in detail in chapter 6).

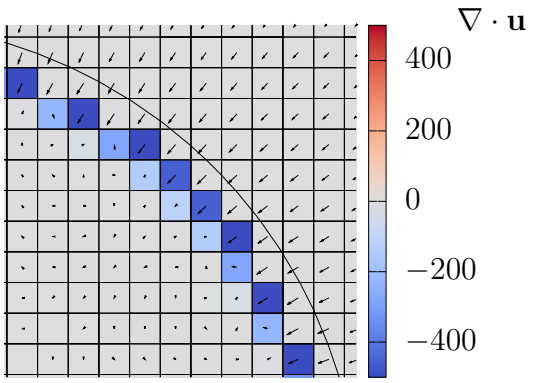

Figure 5.3: Contours of the divergence of the velocity field around a dissolving bubble. The redistributed mass transfer term ensures that the velocity field is divergence-free in pure liquid and interfacial cells and results in a smooth extension of the liquid velocity field across Σ. Variables are non-dimensional.

A drawback of the proposed methodology is given by the possibility that no acceptors exist for one or more donors. This can happen for highly curved interfaces and/or low mesh resolution; however, the present thesis aims at direct numerical simulations, where a fine mesh is always required to capture all the flow features around the interface and the grid is assumed fine enough to provide at least one acceptor for each donor.

At this point, it is important to note that the idea of redistributing the mass transfer term has already been proposed in the literature by Hardt and Wondra, 2008 and successfully used for diffusion-driven phase change flows (see Vachaparambil and Einarsrud, 2020). However, the methodology of Hardt and Wondra, 2008 was developed to reduce numerical instabilities that occur when the source term is dis-

tributed in a narrow layer of cells and does not provide a (corrected) divergence-free velocity field near the interface. On the other hand, the velocity extension algorithm proposed in the present thesis does not require the solution of an additional inhomogeneous Helmholtz equation for the redistribution process and completely removes $\dot{m}$ from the interfacial cells.

5.3 Species transport: the two-scalar method

In this section, the numerical approach for the transport of soluble species in two-phase flows is illustrated. The starting point for the derivation of the discretization schemes is the transport equation for the molar concentration of the generic k-th species (equation 3.35), which is reported here for the reader convenience:

$$\partial_t c^k + \mathbf{u} \cdot \nabla c^k - \nabla \cdot \left(D^k \nabla c^k \right) = 0 \quad \text{in } \Omega \setminus \Sigma \tag{5.14}$$

Equation 5.14 is not valid at the interface and needs to be coupled with the jump conditions for the continuity of mass (equation 3.25) and chemical partitioning of the concentrations (equation 3.37) at Σ. The discontinuity in the concentration profile across the (saturated) interface (handled by Henry's Law, see section 3.3), makes the integration of the species transport equation a challenging task for numerical methods, which have the requirements to preserve such discontinuity and prevent any artificial transfer of species between the phases. This problem is indeed very similar to the advection of the Heaviside function and this suggests that the choice of the right approach must rely on the method used for the transport of the volume fraction field (see Deising et al., 2016). As was introduced in section 2.3.3, there exist two main approaches for the transport of soluble species, i.e. one-scalar and two-scalar methods. Since Basilisk adopts a geometric VOF scheme, the most appropriate choice is the two-scalar method, where the same (geometric) fluxes computed for the advection of the volume fraction field are used for the (convective) transport of

species. This implies that two concentration fields need to be transported separately for each species: one is carried by the continuous phase (c_c^k), and the second one is associated to the disperse phase (c_d^k).

In this thesis, the two-scalar method of Bothe and Fleckenstein, 2013 and Fleckenstein and Bothe, 2015 is implemented in the Basilisk code. The starting point for the derivation of the method is the integration of the species transport equation (5.14) in the control volume V_c, i.e. the region occupied by the continuous phase within the cell boundaries (see Figure 5.4):

$$\int_{V_c} \partial_t c_c^k \, dV \; + \oint_{\partial V_c} c_c^k \, (\mathbf{u}_c - \mathbf{u}_\Sigma) \cdot \mathbf{n} \, dS \; - \oint_{\partial V_c} D_c^k \nabla c_c^k \cdot \mathbf{n} \, dS \; = 0 \tag{5.15}$$

where the subscript c has been included to remind that this integral balance is performed in the continuous phase only. Since the interface is moving with $\mathbf{u}_\Sigma$, the

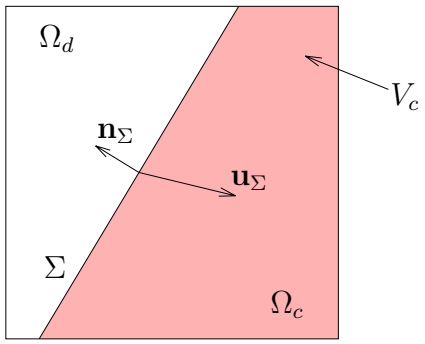

Figure 5.4: Integration volume (red area) for the species transport equation in Ω_c. Since the integral balance is performed in V_c, the velocity of the interface $\mathbf{u}_\Sigma$ needs to be taken into account.

velocity at which the molar concentration is advected at Σ is given by the difference $\mathbf{u}_c - \mathbf{u}_\Sigma$; for the other (fixed) boundaries (where $\mathbf{u}_\Sigma = 0$) it reduces to $\mathbf{u}_c$. Equation

5.15 can be reformulated as:

$$\begin{aligned}&\int_{V_c} \partial_t c_c^k \, dV \; + \oint_{\partial V_c \setminus \Sigma} c_c^k \mathbf{u}_c \cdot \mathbf{n} \, dS \; - \oint_{\partial V_c \setminus \Sigma} D_c^k \nabla c_c^k \cdot \mathbf{n} \, dS \\ &+ \oint_{\Sigma} \left(c_c^k \left(\mathbf{u}_c - \mathbf{u}_\Sigma \right) - D_c^k \nabla c_c^k \right) \cdot \mathbf{n}_\Sigma \, dS \; = 0\end{aligned} \tag{5.16}$$

and substituting equation 3.30 for the species mass transfer into equation 5.16 gives:

$$\begin{aligned}\frac{\phi_{c(i,j)}^{k,n+1/2} - \phi_{c(i,j)}^{k,n-1/2}}{\Delta t} V + \oint_{\partial V_c \setminus \Sigma} c_c^k \mathbf{u}_c \cdot \mathbf{n} \, dS \; - \oint_{\partial V_c \setminus \Sigma} D_c^k \nabla c_c^k \cdot \mathbf{n} \, dS \\ = - \oint_{\Sigma} \frac{\dot{m}^k}{M^k} \, dS\end{aligned} \tag{5.17}$$

where the cell volume-average quantity ϕ^k has been introduced, coherently with the treatment of variables in FV methods, and the species mass transfer term appears explicitly. The integration in time of equation 5.17 is performed between $t^{n-1/2}$ and $t^{n+1/2}$, consistently with the advancement of the interface. The relation between volume-average and phase-average variables is given by the following relationship:

$$\phi_{p(i,j)}^k = f_{p(i,j)} \frac{1}{V_p} \int_{V_p} c_p^k \, dV \; = f_{p(i,j)} c_{p(i,j)}^k \quad \text{for } p = c, d \tag{5.18}$$

In an analogous way, the integral balance for the molar concentration in the disperse phase reads:

$$\begin{aligned}\frac{\phi_{d(i,j)}^{k,n+1/2} - \phi_{d(i,j)}^{k,n-1/2}}{\Delta t} V + \oint_{\partial V_d \setminus \Sigma} c_d^k \mathbf{u}_d \cdot \mathbf{n} \, dS \; - \oint_{\partial V_d \setminus \Sigma} D_d^k \nabla c_d^k \cdot \mathbf{n} \, dS \\ = \oint_{\Sigma} \frac{\dot{m}^k}{M^k} \, dS\end{aligned} \tag{5.19}$$

Equations 5.17 - 5.19 clearly show the reason why the two-scalar method is the appropriate choice for the transport of species when a geometric VOF scheme is used. During the advection and diffusion steps, the concentration fields c_c^k, c_d^k must be confined to their respective side of the interface, i.e. no transfer of species can

occur between the phases, since the relative surface integrals are computed on $\partial V_c \setminus \Sigma$ and $\partial V_d \setminus \Sigma$ respectively, and the mass transfer across the interface is entirely given by the term on the RHS. A geometric VOF formulation ensures that both concentration fields are advected only within their respective phase, since the fluxes for the volume fraction of both phases are computed separately and are used for the advection of the respective species fields (see section 5.3.1). On the other hand, if a one-scalar formulation is used, only one transport equation for each species is solved and the advection term cannot be related consistently with the geometric phase fluxes. Hybrid methods that combine the two-scalar approach for the advection term and the one-scalar formulation for the diffusive step have been proposed in the literature, but in this case the contribution of the mass transfer is included in the integration of the diffusive term (see Farsoiya et al., 2021).

A special treatment, based on the geometric reconstruction of the interface, is also reserved for the diffusive term in order to prevent artificial diffusion of concentration across the interface, and the relative details are presented in section 5.3.2.

5.3.1 Species advection

The integration of the advection term is performed at the same time as the advection of the Heaviside function (equation 5.3) (see López-Herrera et al., 2015) and, for the generic phase p, it reads:

$$\frac{\tilde{\phi}^k_{p(i,j)} - \phi^{k,n-1/2}_{p(i,j)}}{\Delta t} = -\frac{1}{V} \oint_{\partial V_p \setminus \Sigma} c^k_p \mathbf{u}_p \cdot \mathbf{n} \, dS \quad \text{for } p = c, d \tag{5.20}$$

To make the advection of molar concentrations consistent with the advancement of the interface, the same operator-split scheme from the VOF method is used here and, for a 2D case, it reads:

$$\begin{aligned} \phi^{k,*}_{p(i,j)} = \phi^{k,n-1/2}_{p(i,j)} &- \frac{\Delta t}{V} \left(F^k_{p,x(i+1/2,j)} - F^k_{p,x(i-1/2,j)} \right) \\ &+ \frac{\Delta t C^{k,n-1/2}_{p(i,j)}}{\Delta} \left(u^n_{f(i+1/2,j)} - u^n_{f(i-1/2,j)} \right) \end{aligned} \tag{5.21}$$

$$\begin{aligned}\tilde{\phi}^k_{p(i,j)} = \phi^{k,*}_{p(i,j)} - \frac{\Delta t}{V}\left(F^k_{p,y(i,j+1/2)} - F^k_{p,y(i,j-1/2)}\right) \\ + \frac{\Delta t C^{k,n-1/2}_{p(i,j)}}{\Delta}\left(v^n_{f(i,j+1/2)} - v^n_{f(i,j-1/2)}\right)\end{aligned} \tag{5.22}$$

where the concentration for the dilatation term is computed with a criterion similar to the one used for the Heaviside function (equation 4.28):

$$C^{k,n-1/2}_{p(i,j)} = \begin{cases} \phi^{k,n-1/2}_{p(i,j)} / f^{n-1/2}_{p(i,j)} & \text{if } f^{n-1/2}_{p(i,j)} > 0.5 \\ 0 & \text{Otherwise} \end{cases} \tag{5.23}$$

The fluxes F^k_p are computed based on the PLIC ones used for the advection of the volume fraction field (equation 4.27) and, for the transport across the boundary $(i-1/2, j)$, the fluxes read (see Figure 5.5):

$$F^k_{p,x(i-1/2,j)} = \frac{\Delta V_p}{\Delta t} c^k_{p(i-1/2,j)} \quad \text{for } p = c, d \tag{5.24}$$

where ΔV_p is the exact (in the sense of the PLIC reconstruction of the interface) amount of volume of phase p that crosses the cell edge. The molar concentration

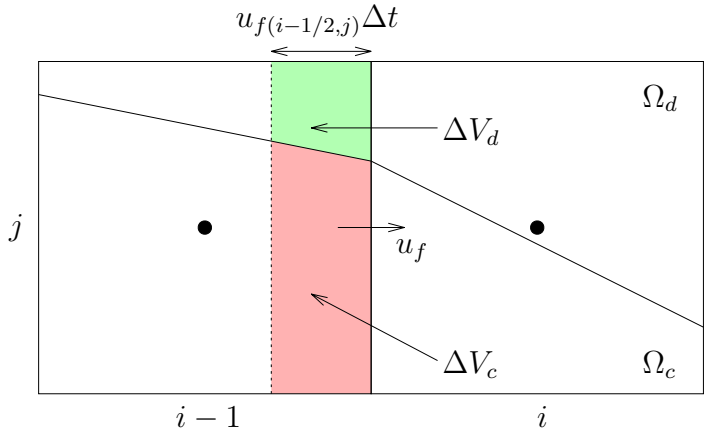

Figure 5.5: Advection of species concentrations confined within the respective phases. The transport fluxes across the cell boundary are based on the PLIC advection of the respective volume of fluids (red and green volumes for the liquid and gaseous phases, respectively).

on the face is predicted using the upwind scheme of Bell et al., 1989 (see section 4.3), which performs an extrapolation in time (half time step) and in space (from the upwind cell centre to the cell boundary):

$$c^k_{p(i-1/2,j)} = \frac{\phi^k_{p(i-1,j)}}{f_{p(i-1,j)}} + \left(1 - \frac{\Delta t}{\Delta} u^n_{f(i-1/2,j)}\right) \frac{\partial c^k_p}{\partial x} \frac{\Delta}{2} \tag{5.25}$$

where cell $(i-1, j)$ is assumed to be the upwind cell (i.e. $u_{f(i-1/2,j)} > 0$) and the concentration gradient is computed either with a standard central finite difference scheme or with a shifted two-point scheme when the boundary is close to the interface.

At this point it is important to note that, in the case of phase-change flows, a correction is needed for the advection of the concentrations in Ω_d. This is due to the fact that, after the redistribution of the mass transfer term (see section 5.2), the velocity field is generally no longer divergence-free in a layer of pure gas cells next to the interface (see Figure 5.3). Therefore, the requirement for the dilation terms to sum up to zero in equations 5.21 - 5.22 (see section 5.1) is no longer satisfied and mass conservation cannot be ensured anymore. This happens in the disperse phase only, since the velocity field is divergence-free everywhere in pure liquid and mixed cells; therefore, the correction must be applied to the transport of ϕ^k_d only. A simple way to implement such correction (see Fleckenstein and Bothe, 2015) is to subtract the global dilation term after all the one-dimensional advection operations are performed, i.e.:

$$\tilde{\phi}^{k,corr}_{d(i,j)} = \tilde{\phi}^k_{d(i,j)} - \frac{\Delta t C^{k,n-1/2}_{d(i,j)}}{\Delta} \left(u^n_{f(i+1/2,j)} - u^n_{f(i-1/2,j)} + v^n_{f(i,j+1/2)} - v^n_{f(i,j-1/2)}\right) \tag{5.26}$$

This correction does not affect the solution in pure gas cells far from the interface, since in these cells the velocity field is divergence-free and the last term on the RHS of equation 5.26 reduces to $\Delta t C^{k,n-1/2}_{d(i,j)} \left[\nabla_\Delta \cdot \mathbf{u}^n_f\right]_{(i,j)} = 0$. For the same reason, the correction can be safely applied also to incompressible two-phase flows without mass transfer, where $\nabla \cdot \mathbf{u} = 0$ everywhere. Finally, it is reminded that such correction is not necessary for the transport of the volume fraction field, since, in this case, the

dilation terms always sum up to zero (see section 5.1).

After the advection step, the mass source terms are integrated:

$$\frac{\tilde{\tilde{\phi}}^k_{c(i,j)} - \tilde{\phi}^k_{c(i,j)}}{\Delta t} = -\frac{\dot{m}^k_{(i,j)}}{M^k}\frac{A_\Sigma}{V} \tag{5.27}$$

$$\frac{\tilde{\tilde{\phi}}^k_{d(i,j)} - \tilde{\phi}^k_{d(i,j)}}{\Delta t} = \frac{\dot{m}^k_{(i,j)}}{M^k}\frac{A_\Sigma}{V} \tag{5.28}$$

Equations 5.27 - 5.28 show that the two scalar method is naturally mass conservative, since the same amount of mass that is subtracted (added) from the continuous domain is added (subtracted) to the disperse phase.

The species mass transfer must occur at the same time as the phase volume change (equation 5.4), since these two terms are related, i.e. the interface is shifted because some transfer of species occurs. If, for example, diffusion (see section 5.3.2) occurs after the phase volume change but before the transfer of species between the phases, some nonphysical concentration values can appear next to the interface, due to the inconsistency in the order of the transport steps (see Fleckenstein and Bothe, 2015). An overview of the integration steps and their order is presented in section 5.5.

5.3.2 Species diffusion

The last step is the integration of the diffusive term:

$$\frac{\phi^{k,n+1/2}_{p(i,j)} - \tilde{\tilde{\phi}}^k_{p(i,j)}}{\Delta t} = \frac{1}{V}\oint_{\partial V_p \setminus \Sigma} D^k_p \nabla c^k_p \cdot \mathbf{n}\, dS \quad \text{for } p = c, d \tag{5.29}$$

Analogously to the advection step, no mass transfer can occur at this stage, since the whole exchange of species moles between the phases has already been taken into account in the source term in equations 5.27 - 5.28. To put the integral in equation 5.29 in a convenient way for standard FV discretization schemes, where the transport fluxes are computed across the cell boundaries rather than the phase volume (V_p) borders, the approach presented in López-Herrera et al., 2015 and Magdelaine-Guillot

de Suduiraut, 2019 is adopted in the present thesis. The derivation of this method is presented here for a 2D case; extension to 3D is straightforward. The numerical discretization of equation 5.29 in Ω_c (an analogous formulation applies for Ω_d) for the case shown in Figure 5.6 reads:

$$\frac{\phi^{k,n+1/2}_{c(i,j)} - \tilde{\tilde{\phi}}^{k}_{c(i,j)}}{\Delta t} = \frac{D^k_c}{V}\left[\left(\frac{\partial c^k_c}{\partial x}A_c\right)_{(i+1/2,j)} - \left(\frac{\partial c^k_c}{\partial x}A_c\right)_{(i-1/2,j)} - \left(\frac{\partial c^k_c}{\partial y}A_c\right)_{(i,j-1/2)}\right] \tag{5.30}$$

where A_c is the (variable) face area of the boundaries of the control volume V_c and the diffusion coefficient is assumed constant. The diffusive flux across the interface,

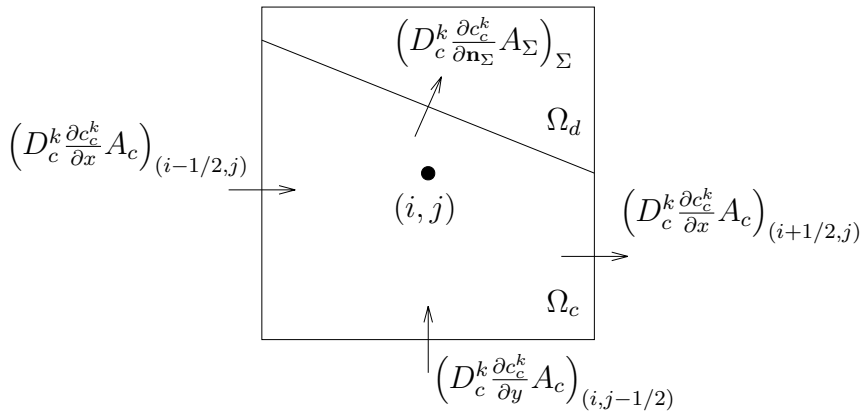

Figure 5.6: Diffusion of the species concentration confined within the continuous domain Ω_c. The diffusive flux across the interface is set to zero, since no mass transfer can occur at this stage.

i.e. $\left(D^k_c A_\Sigma \partial c^k_c / \partial \mathbf{n}_\Sigma\right)$, has been set to zero to prevent any diffusive mass transfer between the phases. Equation 5.30 can be easily generalized as:

$$\frac{\phi^{k,n+1/2}_{p(i,j)} - \tilde{\tilde{\phi}}^{k}_{p(i,j)}}{\Delta t} = \frac{1}{V}\sum_{\text{cell faces}} \frac{\partial c^k_p}{\partial \mathbf{n}}\left(D^k_p f_{f,p}\right) A \quad \text{for } p = c, d \tag{5.31}$$

where $f_{f,p}$ is the face fraction (based on the PLIC reconstruction) on the cell boundary of phase p, i.e. $f_{f,p} = A_p/A$. The formulation of equation 5.31 is equivalent to a standard FV scheme, where the fluxes across the boundaries are computed on all the cell faces and the diffusion coefficient is multiplied by the face fraction. The gradients along the Cartesian axes in equation 5.31 are computed with a central finite difference scheme applied to the phase-average variables $c^k_{p(i,j)}$, which are obtained from their respective volume-average quantities $\phi^k_{p(i,j)}$ through equation 5.18.

The diffusion step is solved implicitly with the multigrid solver as a standard diffusion equation, where the face-centred diffusion coefficient D^k_p is first multiplied by the face fraction $f_{f,p}$.

5.4 Mass transfer scheme

To close the system for the numerical solution of the governing equations, the species mass transfer rate $\dot{m}^k$ needs to be computed. This term appears in the transport equation for the volume fraction field (equation 5.2, as the global mass transfer rate $\dot{m}$), in the projection step (equation 5.13, in the form of the redistributed term $\dot{m}'$), and finally in the species equations 5.17 and 5.19. Therefore, it is fundamental to accurately predict the individual mass transfer rates, since the global solution is strongly affected by these fields. In this section, the numerical scheme used for the prediction of $\dot{m}^k$ is illustrated for a 2D geometry; extension to 3D is straightforward.

The formula for the mass transfer rate was derived in section 3.3 and is reported here for the reader convenience:

$$\dot{m}^k_p = \frac{\rho^k_p}{\rho_p} \sum_{l=1}^{n-1} \dot{m}^l_p - M^k D^k_p \nabla c^k_p \cdot \mathbf{n}_\Sigma \quad \text{for } p = c, d \tag{5.32}$$

Equation 5.32 can be computed from both side of the interface, but the result must be the same due to the jump condition for the continuity of mass (equation 3.25), i.e. $\dot{m}^k_c = \dot{m}^k_d$. In the present thesis, only liquid dilute solutions are considered (see

section 3.3) and the following assumption is generally true:

$$\frac{\rho_c^k}{\rho_c} \approx 0 \tag{5.33}$$

Therefore, equation 5.32 can be simplified to (when computed from the continuous side of the interface):

$$\dot{m}_c^k = -M^k D_c^k \nabla c_c^k \cdot \mathbf{n}_\Sigma \tag{5.34}$$

Equation 5.34 is used in the present work to compute the individual mass transfer rates and the gradient of concentration at the interface is evaluated using the unsplit geometric method proposed by Bothe and Fleckenstein, 2013. The scheme is presented in Figure 5.7 for a 2D case, where P is the centroid of the interface in the mixed cell (i, j) and the values of concentration in points P_1 and P_2 are obtained from quadratic (bi-quadratic in 3D) interpolation; the values used for the interpolation are the closest cell-centred one and the values in the top and bottom cells, if $|n_{\Sigma x}| > |n_{\Sigma y}|$, or right and left cells, when $|n_{\Sigma y}| > |n_{\Sigma x}|$. For the case of Figure 5.7,

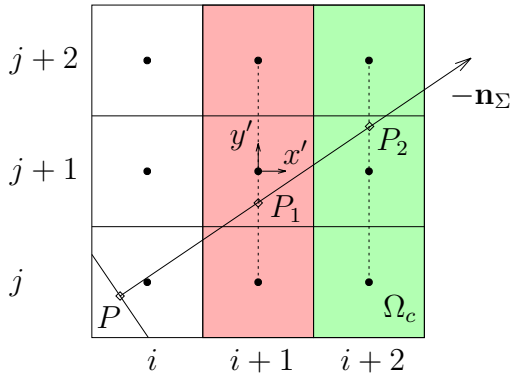

Figure 5.7: Geometric mass transfer scheme. The extrapolated value in P_1 is obtained from the concentrations inside the red cells, whilst the value in P_2 is extrapolated from the green ones.

$|n_{\Sigma x}| > |n_{\Sigma y}|$ and the concentration in P_1 is given by (a similar formula applies to

P_2):

$$c_c^k(P_1) = \left[c^k_{c(i+1,j)}\left(y'_{P_1} - 1\right) + c^k_{c(i+1,j+2)}\left(y'_{P_1} + 1\right)\right]\frac{y'_{P_1}}{2} - c^k_{c(i+1,j+1)}\left(y'^2_{P_1} - 1\right) \quad (5.35)$$

where $x'y'$ is a local reference system centred on cell $(i+1, j+1)$, made non-dimensional with the cell size Δ. The gradient is then computed by weighting the two first-order derivatives:

$$-\frac{\partial c^k_{c(i,j)}}{\partial \mathbf{n}_\Sigma} = f_c\frac{c_c^k(P_1) - c_c^k(P)}{\overline{PP_1}} + (1 - f_c)\frac{c_c^k(P_2) - c_c^k(P)}{\overline{PP_2}} \quad (5.36)$$

The value at the centroid of the interface $c_c^k(P)$ is computed by applying Henry's Law (equation 3.37), i.e. $c_c^k(P) = c_d^k(P)/H_e^k$, where the concentration on the disperse side of the interface $c_d^k(P)$ is extrapolated from the cell-centred values in Ω_d along the normal $\mathbf{n}_\Sigma$. Finally, after all the individual mass transfer rates are computed, the overall mass transfer rate in the mixed cell (i, j) is obtained as $\dot{m}_{(i,j)} = \sum_{l=1}^{n-1} \dot{m}^l_{c(i,j)}$, where the n-th component is the (non-transferable) solvent. The weighting factor in equation 5.36 makes the computation of the gradient less sensitive to the position of the centroid P. Indeed, a heavier weight is attributed to the first derivative when the cell is mainly composed of liquid (i.e. P is sufficiently far from $P1$), but, in the case that P and $P1$ are too close, the scheme automatically assigns more importance to the second term. The scheme of equation 5.36 is expected to be first order accurate and a grid convergence analysis is reported in Appendix A.

At this point, it is important to remark that the redistributed mass transfer term $\dot{m}'$ is used only in the projection step of the NS solver (equation 5.13), whilst the original mass transfer rate $\dot{m}$ and the individual ones $\dot{m}^k$ are left unchanged in the transport of the volume fraction (equation 5.2) and molar concentrations (equations 5.17 and 5.19). It is worth noting that, although the Poisson equation for pressure (projection step) and the transport of the Heaviside function have different source terms ($\dot{m}'$ and $\dot{m}$ respectively), the advection of momentum and volume fraction are consistent, since the face-centred velocity field $\mathbf{u}_f$ used for the advection of both quantities is obtained from the same projection step. The reader is referred to

Appendix B for more information.

5.5 Overview of the phase-change model

In this section, an overview of the proposed methodology and its implementation in the Basilisk VOF-NS solver is presented; the main steps are summarized in the following diagram (Figure 5.8).

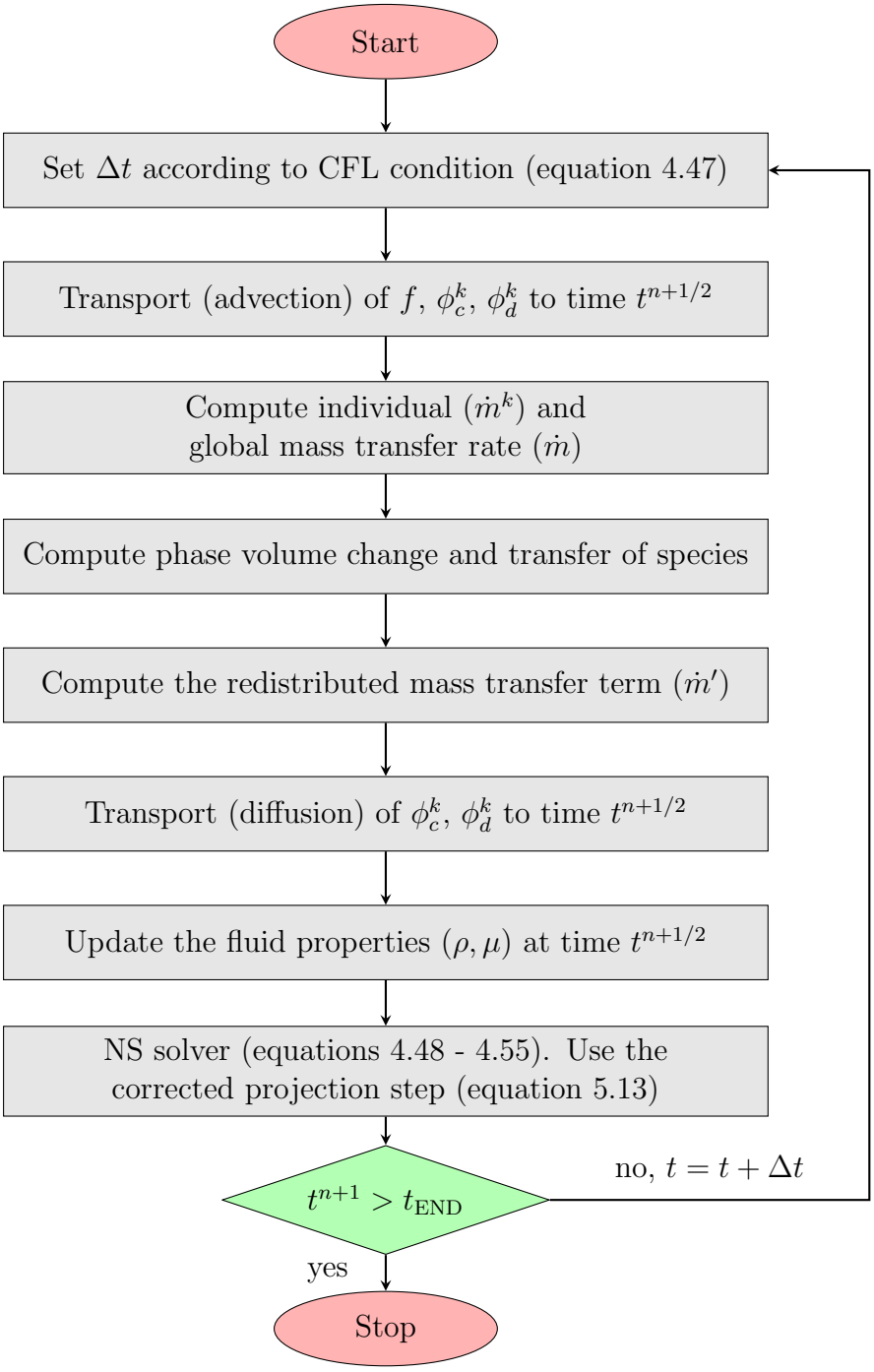

Figure 5.8: Overview of the phase-change solver.

Chapter 6

Validation of the numerical framework

In this chapter, the numerical methodology developed within the present thesis is validated against several benchmarks, which include analytical and semi-analytical solutions, experimental data and numerical studies. All the cases presented here are solved in a non-dimensional form and the related reference parameters (identified by the subscript $_{\text{ref}}$) are introduced in each of the following sections, where the non-dimensional variables are distinguished with the superscript *, e.g. $\mathbf{x}^* = \mathbf{x}/L_{\text{ref}}$, $t^* = t/t_{\text{ref}}$, $\mathbf{u}^* = \mathbf{u}/U_{\text{ref}}$, etc. The relevant non-dimensional numbers for the study of mass transfer in two-phase (bubbly) flows are recalled in section 6.1. The rest of the chapter is divided into two main sections: the test cases for pure soluble species are presented in section 6.2, whilst the competing mass transfer in mixtures of species is discussed in section 6.3.

Finally, it is reminded that in the present work the gaseous and liquid phases are referred to as the disperse and continuous phases respectively and that these terms will be used interchangeably in the following.

6.1 Non-dimensional groups

The non-dimensional numbers that describe the dynamics of bubbles exchanging mass in two-phase systems have been already introduced in chapter 2. Here, they are reported for the reader convenience and some definitions are extended to multi-component mass transfer problems (i.e. mixtures of different species).

The dynamics of a bubble immersed in a liquid and driven by the gravitational field $\mathbf{g}$ can be described by the Galilei and Bond numbers. The Galilei number compares the gravitational and viscous forces and is defined as:

$$Ga = \sqrt{\frac{gD_b^3}{\nu_c^2}} \tag{6.1}$$

where D_b is the bubble diameter and ν_c is the kinematic viscosity of the continuous phase. The ratio between gravitational and capillary forces is evaluated by the Bond number:

$$Bo = \frac{\rho_c g D_b^2}{\sigma} \tag{6.2}$$

For a moving bubble, the Reynolds number is defined as:

$$Re_b = \frac{\rho_c U_b D_b}{\mu_c} \tag{6.3}$$

where U_b is the velocity magnitude of the bubble centre of mass.

In diffusion-driven phase-change problems, the Schmidt number compares the rates of diffusion between the phase momentum and species concentration in the liquid phase. For the k-th species, it reads:

$$Sc^k = \frac{\nu_c}{D_c^k} \tag{6.4}$$

A measure of the relative importance of the advection transport of the k-th species against the diffusive transport of the same species is given by the Péclet number:

$$Pe^k = Re_b Sc^k \tag{6.5}$$

For many applications involving mass transfer in two-phase systems, the amount of soluble species initially dissolved in the solvent is a relevant technical parameter that can be controlled during the operation of the system. The difference between the concentrations at the (saturated) interface and in the bulk liquid, i.e. $\Delta c^k = \left(\left(c_c^k\right)_\Sigma - c_{\text{bulk}}^k\right)$, provides a reference driving force for the mass transfer process, since $\dot{m}^k \propto -\Delta c^k$. The saturation ratio ζ^k compares the two concentration values for the k-th species:

$$\zeta^k = \frac{c_{\text{bulk}}^k}{\left(c_c^k\right)_\Sigma} \tag{6.6}$$

Depending on the value of ζ^k, the solution can be classified as (with respect to the k-th species):

- saturated, if $\zeta^k = 1$
- super-saturated, if $\zeta^k > 1$
- under-saturated, if $\zeta^k < 1$

When the solution is super-saturated, an excess of species concentration (with respect to the saturation value) exists in the liquid region around the interface and the system is not balanced. A diffusive process will then transfer moles of the k-th species from the continuous phase to the disperse one, in order to bring the system at the equilibrium point $\zeta^k = 1$. For the same reason, moles are transported out of the disperse phase when the solution is under-saturated. Although the saturation ratio is a convenient parameter for technical applications to globally classify the concentration in a solution, the transport of moles across the interface is rather a local process and depends on the local concentration around the interface. The rate of mass transfer is generally not constant at the interface (see section 6.2.4) and different regions with opposite values of $\dot{m}^k$ can occur simultaneously. Finally, when the system contains a mixture of different species, the solution can be classified as super-saturated with respect to some of the species and under-saturated (or saturated) with respect to the others.

Based on the reference concentration difference Δc^k, the mass transfer coefficient for the k-th species is defined as:

$$k_m^k = -\frac{\int_\Sigma \dot{m}^k \, dS}{A_\Sigma M^k \Delta c^k} \tag{6.7}$$

where A_Σ is the global area of the interface. The rate of mass transfer is compared to the diffusion velocity in the non-dimensional Sherwood number for the k-th species:

$$Sh^k = \frac{k_m^k L_{\text{ref}}}{D_c^k} \tag{6.8}$$

where the reference length is generally set to $L_{\text{ref}} = D_b$ for bubbles. The Sherwood number offers a convenient description of the mass transfer process and much research effort has been put to derive predictive formula for this parameter for bubbly flows (see Deising et al., 2018 for a review). However, owing to the complexity of the problem, no universal laws can be derived for the Sherwood number and its prediction for many applications rely on experiments and/or numerical simulations.

6.2 Pure species

In this section, several benchmarks for phase-change of pure soluble species are presented and discussed in detail. In the following, the species indicator k is omitted since only one transferable species exists when pure gaseous phases are considered, i.e. $c_{c,d}^k = c_{c,d}$. As explained in chapter 3, in the case of pure species the concentration in the disperse domain c_d is constant due to the incompressibility assumption and is directly related to the phase density, i.e. $c_d = \rho_d / M$. This assumption has a significant effect on the numerical solution of this type of flows when two-scalar methods are used (see chapter 5.3), since only the species transport in the continuous phase (equation 5.17) is solved (being the concentration in Ω_d uniform known a priori). The interface is always assumed saturated and the interfacial concentration on the liquid side is constant and equal to $(c_c)_\Sigma = c_d / H_e$ (Henry's law). Adaptive mesh refinement is used to reach the required grid resolution for fully resolved sim-

ulations in regions where strong gradients appear, whilst keeping the computational cost relatively low (compared to the equivalent simulations with static meshes). As was discussed in section 4.1, the mesh is adapted based on a wavelet estimation of the spatial discretization error for some specific fields and the corresponding threshold values are reported in Table 6.1.

Field	Threshold error (ξ)
Velocity (u, v, w)	10^{-2}
Liquid volume fraction	10^{-3}
Solid volume fraction	10^{-3}
Soluble species ($c_{c,d}$)	10^{-3}

Table 6.1: Threshold values of the selected fields for the adaptive mesh refinement algorithm (see criterion 4.6). The value for c_d is reported here for the reader's convenience, but is used in section 6.3 only, where mixtures of species are modelled. The solid volume fraction field refers to the modelling of complex geometries via immersed boundaries (see section 7.2.2). Values of ξ are non-dimensional, consistently with the following simulations.

The novelty of the proposed phase-change model illustrated in chapter 5 is the velocity extension algorithm (see section 5.2) used to extend the primary phase velocity field across the interface in a divergence-free way. This part of the model needs to be carefully assessed, since the accuracy and the mass conservation properties of the method rely on this step. Therefore, a specific benchmark to validate the correctness of the extended velocity field is proposed in section 6.2.1 for a pure gaseous bubble with constant mass transfer rates. The rest of the section is organized as follows. The classic benchmark for phase-change flows - the Stefan problem - is tested in section 6.2.2, whilst the cases of suspended bubbles in super- and under-saturated solutions are discussed in section 6.2.3. Finally, rising bubbles at different Péclet numbers and in a very viscous flow (creeping flow) are presented in section 6.2.4.

6.2.1 Bubbles with fixed mass transfer rates

The purpose of this benchmark is to assess the correctness of the velocity extension algorithm and to compare the solution with the case where no correction is applied. The test consists of a single 3D spherical bubble exchanging mass with the surrounding liquid at a constant rate. Gravity is neglected and, since the mass transfer rate is set a priori, the problem is decoupled from the transport of species and no equation is solved for the molar concentration. In this way, no additional numerical errors related to the discretization schemes used for the mass transfer rate and the transport of species are introduced in the solution, and the effectiveness of the velocity extension algorithm can be tested properly.

The properties of the gas-liquid system used for this benchmark are reported in Table 6.2 and correspond to a CO_2 - water system.

Phase	Density ($\mathrm{kg\,m^{-3}}$)	Viscosity ($\mathrm{N\,s\,m^{-2}}$)	Surface tension ($\mathrm{N\,m^{-1}}$)
Liquid	998	1.05×10^{-3}	0.072
Gas	1.8	1.46×10^{-5}	

Table 6.2: Gas-liquid properties for the bubble with fixed mass transfer rates.

For each simulation, the initial bubble diameter is set to $D_b^{t=0} = 0.01\,\mathrm{m}$ and the computational domain is a cube with dimension $L0 = 0.5\,\mathrm{m}$. Results are made non-dimensional with the reference length $L_{\mathrm{ref}} = D_b^{t=0}$ and time $t_{\mathrm{ref}} = \rho_c \left(D_b^{t=0}\right)^2 / \mu_c$, whilst the reference velocity follows from $U_{\mathrm{ref}} = L_{\mathrm{ref}}/t_{\mathrm{ref}}$; these parameters are reported in Table 6.3. The adaptive mesh refinement technique is used to keep the

L_{ref} (m)	t_{ref} (s)	U_{ref} ($\mathrm{m\,s^{-1}}$)
0.01	95	1.05×10^{-4}

Table 6.3: Reference dimensions for the bubble with fixed mass transfer rates.

mesh resolution at the finest level (set to $l^{\max} = 11$ for this test) around the inter-

face, where the strongest velocity gradients occur. The minimum mesh size is then $\Delta(l^{\max}) = L0/2^{11} \approx 2.44 \times 10^{-4}\,\mathrm{m}$, which corresponds to approximately 41 cells per diameter (at $t = 0$). As the bubble dissolves or expands, the liquid is pulled inside or pushed outside the domain, respectively. To allow the flow field to freely enter or leave the domain, outflow boundary conditions (i.e. fixed pressure and null gradient for the velocity) are assigned to all the external boundaries. A summary of the simulated cases with their relative setup is summarised in Table 6.4. Cases A and B represent a dissolving bubble (negative mass transfer rates) and compare the effect of the velocity extension algorithm. Case C is analogous to Case A, but for an expanding bubble ($\dot{m} > 0$).

Case	$L0$ (m)	$D_b^{t=0}$ (m)	$\dot{m}$ ($\mathrm{kg\,m^{-2}\,s^{-1}}$)	$l^{\max}$	Extended $\mathbf{u}$	$\mathbf{g}$ ($\mathrm{m\,s^{-2}}$)
A	0.5	0.01	-1.8×10^{-3}	11	yes	0
B	0.5	0.01	-1.8×10^{-3}	11	no	0
C	0.5	0.01	1.8×10^{-3}	11	yes	0

Table 6.4: List of cases for the bubble with fixed mass transfer rates.

The analytical solution for this problem is readily obtained from the following balance for an infinitesimal element of the interface surface dA_Σ (see Figure 6.1):

$$dr\, dA_\Sigma = dV = \frac{\dot{m}}{\rho_d} dt\, dA_\Sigma \tag{6.9}$$

and the formula for the bubble radius (R_b) follows by integration over the whole surface:

$$R_b(t) = R_b^{t=0} + \frac{\dot{m}}{\rho_d} t \tag{6.10}$$

Results are compared in Figure 6.2 for cases A and B against the analytical solution of equation 6.10. The numerical solution obtained with the correction algorithm (Case A) shows a good agreement with the reference solution until $t^* \approx 0.04$, whilst a small deviation is observed for $t^* > 0.04$. This discrepancy is due to the mesh reso-

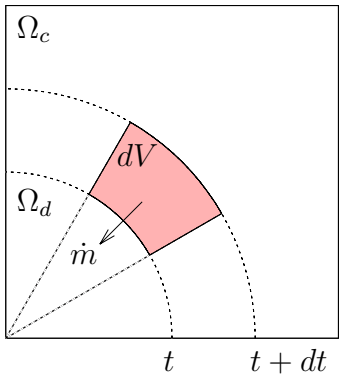

Figure 6.1: Radial displacement of an infinitesimal element of the interface from time t to $t + dt$. The red volume dV represents the volume phase change between the phases (in this case $\dot{m}$ is assumed positive).

lution that is not fine enough to accurately resolve the interface after this time, since the number of cells per diameter is lower than 10 for $t^* > 0.04$. However, this is not a limitation of the proposed numerical method, but is rather an intrinsic feature of dissolving bubbles, where $R(t) \to 0$ and no mesh can be fine enough to solve the flow field until complete dissolution. On the other hand, the solution of Case B is far off from the analytical one, as a consequence of the incompatibility between the velocity field and the (geometric) VOF method and results in a significantly slower dissolution rate. In this case, the advection of the interface is no longer mass-conservative and generates a non-physical behaviour. The velocity fields around the interface and their divergence are reported in Figure 6.3a and Figure 6.3b for cases A and B, respectively. In the first case, the velocity field is divergence-free in all the cells that contain liquid (both pure and mixed cells) and the dilation effect that comes from the continuity of mass in phase-change flows is distributed in the pure gas cells next to the interface (through the mass transfer redistribution process, see section 5.2). The resulting velocity field in the liquid region is smoothly extended across the interface and satisfies the criterion of equation 5.5 for the (mass-conservative) transport of the interface. On the other hand, the original mass transfer term is used in Case B to enforce the continuity equation and produces a non divergence-free velocity field in

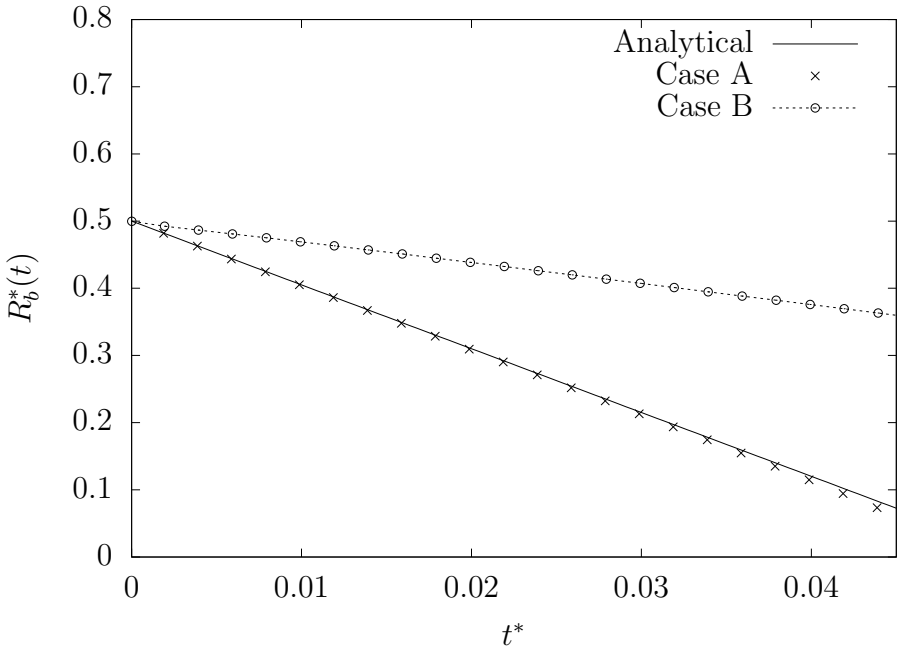

Figure 6.2: Radius Vs time for the dissolving bubble cases. When the velocity field is not extended across the interface (Case B), the numerical solution deviates significantly from the analytical one.

the mixed cells, which results in an strong discontinuity at the interface. The transport of the interface is therefore no longer mass conservative and does not preserve the axisymmetric shape of the bubble.

The solution of Case C is compared in Figure 6.4 against the relative analytical solution and excellent agreement is found for the prediction of the radius growth. In the case of expanding bubbles, the mesh refinement ensures that more than 40 cells per diameter always exist for $t > 0$ and the solution is accurate at every time step. Finally, the horizontal velocity fields around the interface are compared for cases A and C in Figure 6.5 at $t^* = 0.01$. In the first case (Figure 6.5a), the velocity field is compressing the bubble and some liquid material enters the domain from the external boundaries. The opposite scenario is represented in Figure 6.5b, where the expanding bubble forces the liquid phase to leave the domain. In both cases, the velocity fields (vectors) are axisymmetric and preserve the spherical shape of the

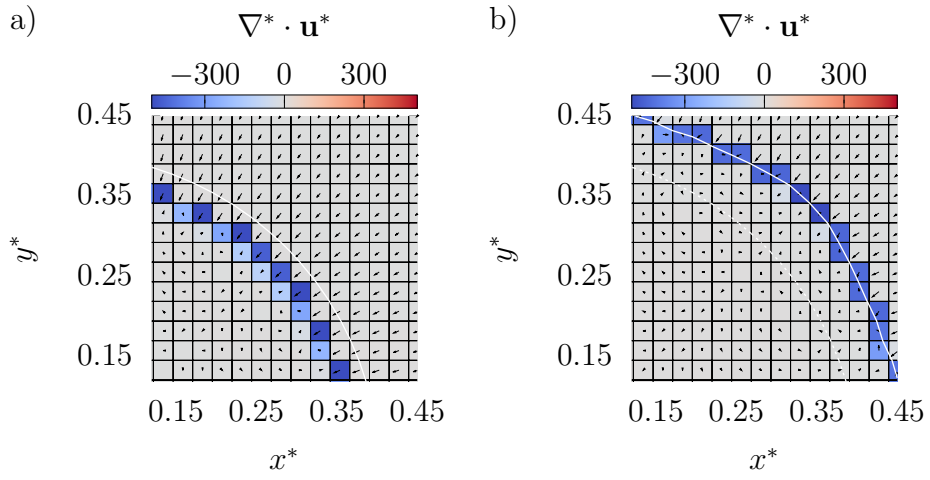

Figure 6.3: Velocity field (vectors) and contours of the velocity divergence for cases A (a) and B (b) at $t^* = 0.01$. In Case A, the liquid velocity is smoothly extended across the interface (white line) and preserves the axisymmetric shape of the bubble. In Case B, the flow field is not compatible with the VOF method and produces a significant deviation from the reference solution (dotted line).

bubbles.

The benchmarks presented in this section demonstrate the importance of the mass transfer redistribution process and the accuracy of the corrected velocity field, which results in a smooth extension across the interface and is necessary for the conservation of mass during the advection of the interface. On the other hand, if the velocity is not corrected, a strong deviation from the correct solution is expected.

6.2.2 The Stefan problem

In this section, the first test for a fully coupled solution (i.e. phase volume change and transport of species) is proposed. The Stefan problem is a classic benchmark for phase-change flows and consists of a planar interface that separates the gaseous and liquid regions. The liquid phase is initially under-saturated (no species are dissolved into the liquid, i.e. $\zeta = 0$) and the diffusion of the soluble species into the continuous region drives the displacement of the interface, which forces the liquid to cross the

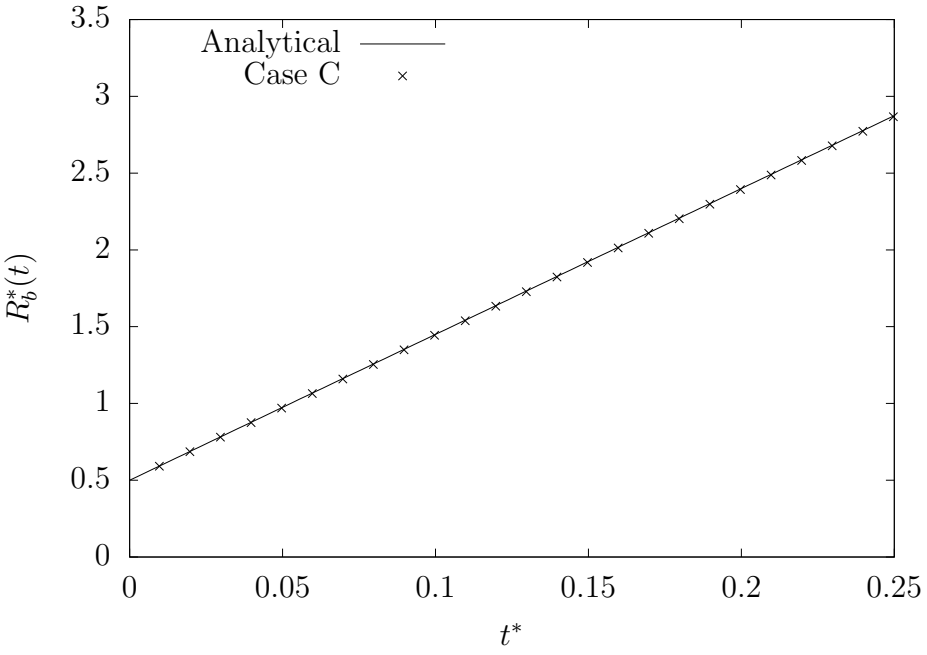

Figure 6.4: Radius Vs time for the growing bubble case.

boundaries and enter the domain.

The properties of the gas-liquid system are summarised in Table 6.5, where two gas species with a different diffusivity are reported. Gas A represents a large diffusivity case, whilst Gas B corresponds to the diffusivity of CO_2 in water. The Schmidt numbers are $Sc = 5.26$ and $Sc = 526$ for Gas A and B respectively, whilst the Henry's law coefficient is set to $H_e = 1.203$ for both cases. Results are made

Phase	Density ($\mathrm{kg\,m^{-3}}$)	Viscosity ($\mathrm{N\,s\,m^{-2}}$)	Diffusivity ($\mathrm{m^2\,s^{-1}}$)	M ($\mathrm{kg\,mol^{-1}}$)	Sc	H_e
Liquid	998	1.05×10^{-3}				
Gas A	1.8	1.46×10^{-5}	2×10^{-7}	0.044	5.26	1.203
Gas B	1.8	1.46×10^{-5}	2×10^{-9}	0.044	526	1.203

Table 6.5: Gas-liquid properties for the Stefan problem.

non-dimensional with the reference length $L_{\mathrm{ref}} = 0.01\,\mathrm{m}$, time $t_{\mathrm{ref}} = \rho_c L_{\mathrm{ref}}^2/\mu_c$ and

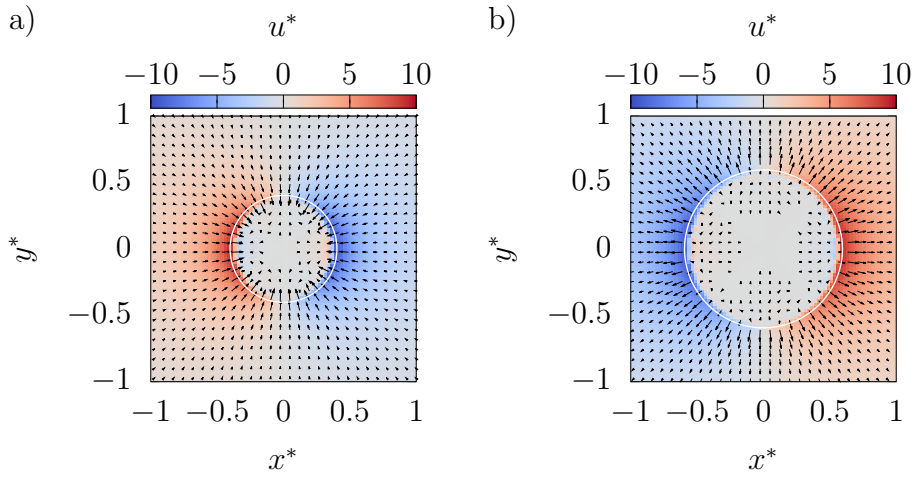

Figure 6.5: Velocity field (vectors) and contours of horizontal velocity for Case A (a) and Case B (b) at $t^* = 0.01$.

the gaseous concentration, i.e. $c_{\text{ref}} = \rho_d/M$; a summary of the reference values is reported in Table 6.6.

L_{ref} (m)	t_{ref} (s)	U_{ref} (m s^{-1})	c_{ref} (mol m^{-3})
0.01	95	1.05×10^{-4}	40.9

Table 6.6: Reference dimensions for the Stefan problem.

Here a 2D problem is modelled, where the interface is represented by an horizontal line that separates the liquid region (top) from the gaseous one (bottom). The problem is symmetric along the $x-$direction and to allow the liquid to freely enter the domain as the interface moves, an outflow boundary conditions is set on the top boundary, whilst symmetry boundary conditions are applied at the other boundaries. Gravity and surface tension are not taken into account and a sketch of the numerical setup is shown in Figure 6.6.

The Stefan problem can be solved analytically (see Crank, 1975), and the velocity field is characterized by a null value in the gaseous region ($\mathbf{u}_d = 0$), whilst in the

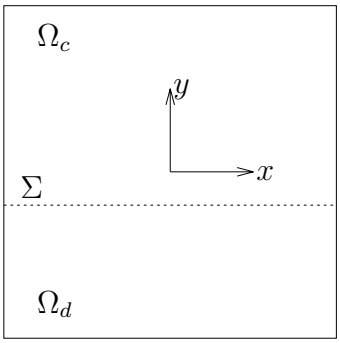

Figure 6.6: Numerical domain for the Stefan problem.

liquid domain it assumes the uniform value:

$$\mathbf{u}_c = \left(\frac{\rho_c - \rho_d}{\rho_c} \right) \mathbf{u}_\Sigma \tag{6.11}$$

The magnitude of the interface velocity is proportional to $\sqrt{D}$ and inversely proportional to the solubility (Henry's law coefficient) and is given by:

$$|\mathbf{u}_\Sigma| = \frac{D_c}{H_e \sqrt{\pi D_c t}} \tag{6.12}$$

The displacement of the interface (L_Σ) follows from the integration in time of equation 6.12:

$$L_\Sigma(t) = \frac{2}{H_e} \sqrt{\frac{D_c t}{\pi}} \tag{6.13}$$

Finally, the concentration in the liquid domain at a point with distance from the interface equal to $y - y_\Sigma(t)$ (the problem is symmetric along the x-direction) is given by:

$$c_c(y,t) = (c_c)_\Sigma \left(1 - \text{erf} \left(\frac{y - y_\Sigma(t)}{2\sqrt{D_c t}} \right) \right) \tag{6.14}$$

A grid convergence study is performed for both the soluble species (Gas A and Gas B), and a summary of the cases is shown in Table 6.7. For each case, the maximum

level of refinement is reported, along with the corresponding mesh size $\Delta(l^{\max})$ and the relative error on the interface displacement (at time $t = 76\,\mathrm{s}$), computed as:

$$\mathrm{err}(L_\Sigma) = \left| \frac{L_\Sigma^{\mathrm{Analyt.}} - L_\Sigma^{\mathrm{Num.}}(\Delta)}{L_\Sigma^{\mathrm{Analyt.}}} \right| \tag{6.15}$$

where $L_\Sigma^{\mathrm{Analyt.}}$ is the exact interface displacement computed with equation 6.13 and $L_\Sigma^{\mathrm{Num.}}$ is the numerical solution, which depends on the grid size Δ. The convergence

Case	Gas	Sc	$L0$ (m)	$l^{\max}$	$\Delta(l^{\max})$ (m)	$\mathrm{err}(L_\Sigma)$
A.1	A	5.26	0.1	6	1.56×10^{-3}	8.18×10^{-2}
A.2	A	5.26	0.1	8	3.91×10^{-4}	4.00×10^{-3}
A.3	A	5.26	0.1	9	1.95×10^{-4}	6.17×10^{-4}
B.1	B	526	0.01	6	1.56×10^{-4}	8.07×10^{-2}
B.2	B	526	0.01	7	7.81×10^{-5}	1.67×10^{-2}
B.3	B	526	0.01	8	3.91×10^{-5}	2.50×10^{-3}

Table 6.7: List of cases for the grid convergence analysis of the Stefan problem.

of the solution with the grid refinement is shown in Figure 6.7a and Figure 6.7b for Gas A and Gas B respectively. From the mesh convergence analysis, it is clear that the requirement in terms of grid refinement around the interface depends on the Schmidt number of the problem. To reach a similar order of accuracy in both cases (Gas A and Gas B) a finer mesh is required for the low diffusivity case ($Sc = 526$) than the one used for the large diffusivity case ($Sc = 5.26$). The reason is due to the thickness of the concentration boundary layer that develops on top of the interface from the liquid side (δ_c), which increases as the diffusivity increases, since the mass transfer is proportional to $\dot{m} \propto D_c$. A qualitative representation of the concentration distribution in the liquid domain is reported in Figure 6.8a and Figure 6.8b for Gas A (Case A.3) and Gas B (Case B.3) respectively, at two different times; the interface is represented by the white horizontal line and the liquid region is on top of it. The large diffusivity gas releases more species into the liquid and results

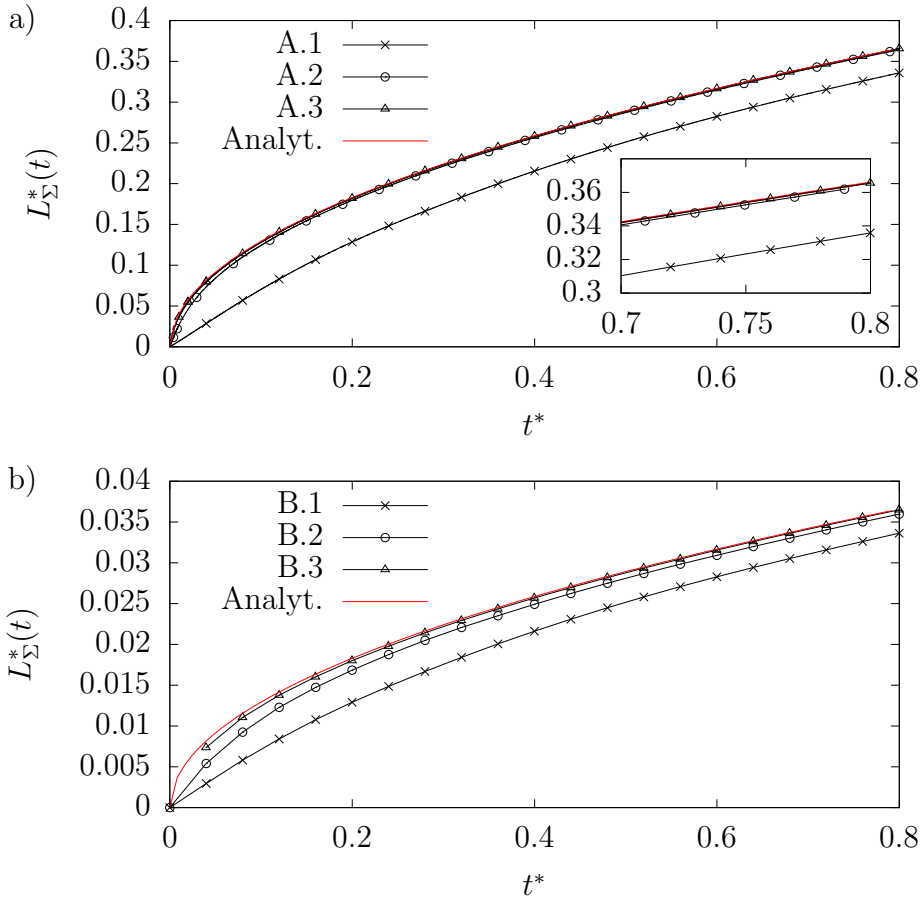

Figure 6.7: Grid convergence analysis for the Stefan problem. Plot of interface displacement Vs time for Gas A (a) and Gas B (b).

in a larger displacement of the interface compared to the low diffusivity case, where the concentration of species in the liquid domain is confined into a thin region on top of the interface.

Finally, velocity and concentration profiles along the vertical line $x = 0$ are plotted in Figure 6.9a and Figure 6.9b for Gas A and Gas B, respectively. Both profiles have analytical solutions (equation 6.11 for the velocity and equation 6.14 for the concentration) and are characterized by discontinuities at the interface. The numerical solutions reproduce the jumps across the interface and are in excellent

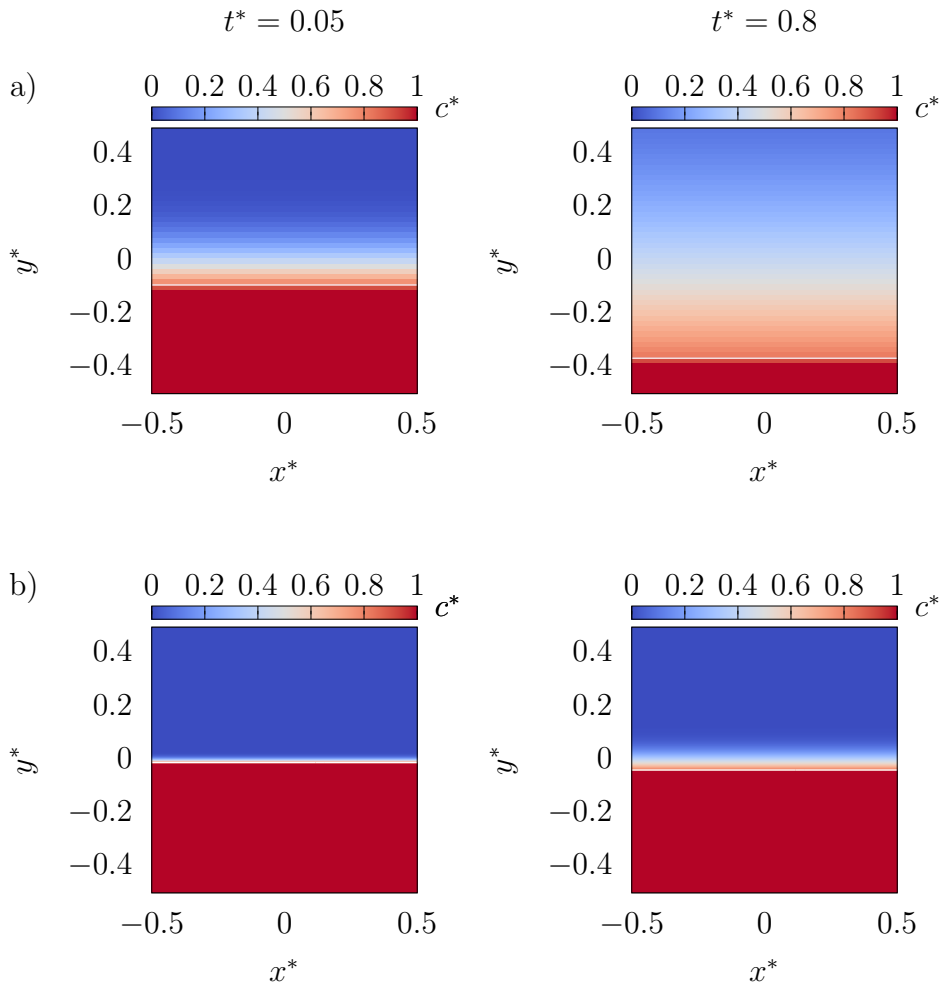

Figure 6.8: Contours of species concentration for Case A.3 (a) and Case B.3 (b) at $t^* = 0.05$ (left) and $t^* = 0.8$ (right).

agreement for the concentration profiles at both times $t^* = 0.05$ and $t^* = 0.8$. The velocity profiles at $t^* = 0.05$ show a deviation from the analytical solution for both gas diffusivities. This behaviour is probably due to the initialization of the numerical computation that assumes a saturated interface whilst no gas is yet dissolved into the liquid. Such nonphysical initial condition is then adsorbed as soon as the concentration boundary layer develops on top of the interface, and no significant deviations are reported for the velocity profiles at later times.

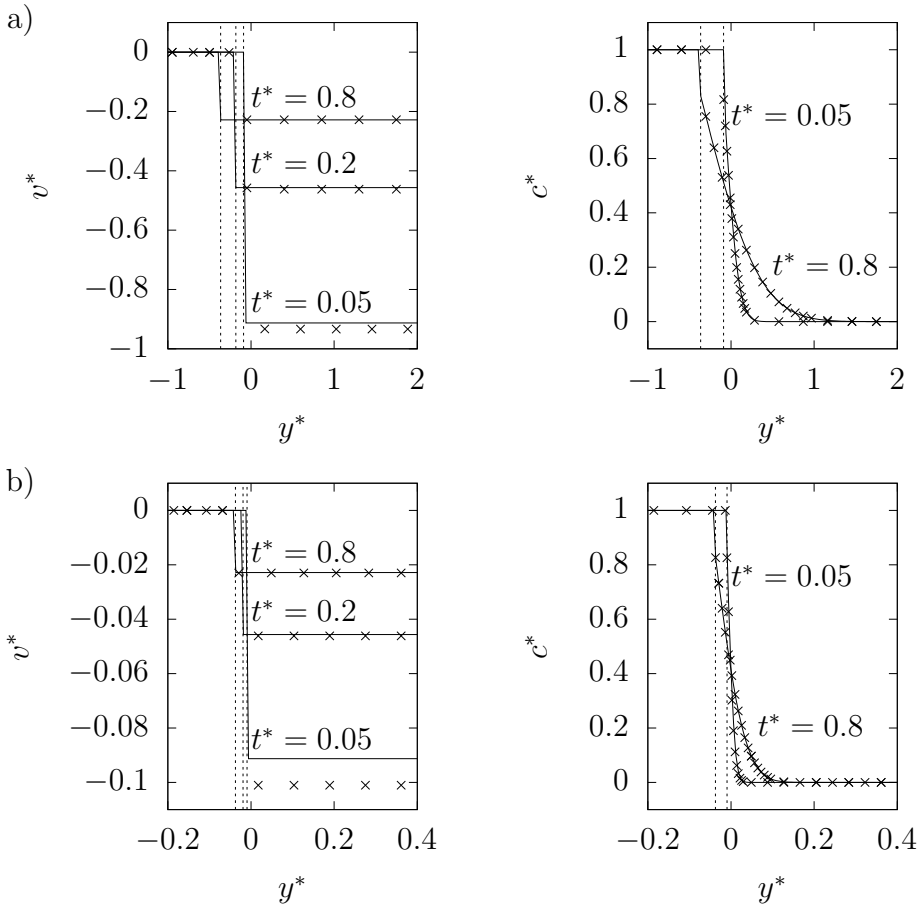

Figure 6.9: Velocity (left) and concentration (right) profiles for Case A.3 (a) and Case B.3 (b). The continuous lines represent the analytical curves, whilst the symbols (×) are the numerical solutions. The interface locations are identified by the vertical dotted lines.

6.2.3 Suspended bubbles

In this section, the problem of mass transfer for suspended bubbles in solutions with different concentrations is discussed. Both cases of growing and dissolving bubbles are considered and the properties of the gas-liquid system are reported in Table 6.8. The diffusivity has been increased significantly with respect to the typical values for soluble gaseous species in liquids (which are typically around $D_c \propto 10^{-9}\,\mathrm{m^2\,s^{-1}}$)

Phase	Density ($\mathrm{kg\,m^{-3}}$)	Viscosity ($\mathrm{N\,s\,m^{-2}}$)	Diffusivity ($\mathrm{m^2\,s^{-1}}$)	M ($\mathrm{kg\,mol^{-1}}$)	σ ($\mathrm{N\,m^{-1}}$)	H_e
Liquid	998	1.05×10^{-3}			0.072	
Gas	1.8	1.46×10^{-5}	2×10^{-5}	0.044		5

Table 6.8: Gas-liquid properties for the suspended bubbles.

in order to speed up the mass transfer process (since $\dot{m} \propto D_c$), and reduce the computational cost of the simulations; the resulting Schmidt number is $Sc = 0.0526$. The bubble centre of mass is fixed since no gravity is taken into account, and the initial diameter is set to $D_b^{t=0} = 0.01\,\mathrm{m}$. Results are made non-dimensional with the reference length $L_{\mathrm{ref}} = D_b^{t=0}$, time $t_{\mathrm{ref}} = \rho_c L_{\mathrm{ref}}^2/\mu_c$ and the gaseous concentration, i.e. $c_{\mathrm{ref}} = \rho_d/M$; a summary of the reference values is reported in Table 6.9.

L_{ref} (m)	t_{ref} (s)	U_{ref} ($\mathrm{m\,s^{-1}}$)	c_{ref} ($\mathrm{mol\,m^{-3}}$)
0.01	95	1.05×10^{-4}	40.9

Table 6.9: Reference dimensions for the suspended bubble cases.

Bubbles growing in super-saturated solutions

When a bubble is immersed in a super-saturated solution ($\zeta > 1$), the concentration around the interface (on the liquid side) exceeds the saturated value predicted by Henry's law, which depends on the pressure of gas on the liquid phase. The excess of concentration in the liquid is then redistributed by a diffusive process, until the concentration of the solution reaches the saturation value and the gas-liquid system is at the equilibrium. The diffusive process consists of the transport (across the interface) of species moles from the liquid region to the gaseous one, and the volume of the bubble expands accordingly.

The problem of a single bubble immersed in an infinite liquid medium with a uniform super-saturated concentration (and no gravitational effects) was solved ana-

lytically by Scriven, 1959 and the resulting equation for the bubble radius evolution is:

$$R_b(t) = 2\beta\sqrt{D_c t} \tag{6.16}$$

where β is a non-dimensional growth factor that depends on the liquid and gas densities (ρ_c, ρ_d), initial solution concentration (c_{bulk}) and interfacial concentration on the liquid side $(c_c)_\Sigma$. The factor β comes from the solution of the following equation:

$$\Phi = 2\beta^3 \exp\left(\beta^2 + 2\epsilon\beta^2\right) \int_\beta^\infty x^{-2} \exp\left(x^2 - 2\epsilon\beta^3 x^{-1}\right) dx \tag{6.17}$$

where Φ and ϵ are:

$$\Phi = \frac{\rho_c}{\rho_d} \frac{M\left(c_{\text{bulk}} - (c_c)_\Sigma\right)}{\rho_c - M(c_c)_\Sigma} \tag{6.18}$$

and

$$\epsilon = \frac{\rho_c - \rho_d}{\rho_c} \tag{6.19}$$

Here, a single 3D bubble with initial diameter $D_b^{t=0} = 0.01\,\text{m}$ is modelled and the size of the computational domain is set to $L0 = 0.5\,\text{m}$; gravity is not taken into account and outflow boundary conditions are applied at the external boundaries to allow the liquid to exit the domain as the bubble expands. Scriven's solution (equation 6.16) assumes that no bubble exists at $t = 0$ (i.e. $R_b^{t=0} = 0$); however, within the VOF modelling approach, the volume fraction of gas must be initialized to $f_d = 1$ in a few cells so that a finite-size bubble can be generated accordingly. To make the numerical solution comparable with the analytical one, the computation is first initalized with a bubble with radius $R_b = 0.005\,\text{m}$ and the size of the bubble is kept constant until $t = \bar{t}$, where $\bar{t}$ is the time required for the bubble to grow from $R_b = 0\,\text{m}$ to $R_b = 0.005\,\text{m}$, according to equation 6.16. In the first part of the simulation (i.e. until $t = \bar{t}$), the redistributed mass transfer term $\dot{m}'$ is set to null everywhere, so that the phase volume change effect is neglected and the bubble size remains constant (no velocity field develops at this stage). However, the interfacial mass transfer term $\dot{m}$ is applied in the species transport (equation 5.17) so that a realistic boundary layer concentration develops around the interface. The purpose of

this initialization strategy is to obtain a concentration field at time $t = \bar{t}$ as close as possible to the analytical one, where a variable concentration distribution develops around the interface right after the nucleation stage ($t = 0\,\mathrm{s}$). If the bubble volume change is taken into account in the VOF model as the simulation starts, the mass transfer would be significantly over predicted, due to the initial discontinuity of the concentration field, which turns into a numerically (and mesh dependent) very high concentration gradient (it is reminded here that $\dot{m} \propto -\partial c/\partial \mathbf{n}_\Sigma$). For $t > \bar{t}$, the full phase-change model (i.e. phase volume change and transfer of species) is solved and the mass transfer activates the liquid velocity field; the volume of the bubble is free to evolve accordingly.

Three levels of super-saturation are considered in this section, and the relative growth factors (β) and initialization times ($\bar{t}$) are reported in Table 6.10.

ζ	β	$\bar{t}$ (s)
2	0.421	1.7670
3	0.669	0.6935
4	0.895	0.3895

Table 6.10: Growth factors (β) and times ($\bar{t}$) to reach the bubble size $R_b^{t=\bar{t}} = 0.005\,\mathrm{m}$ for different super-saturation levels.

First, a mesh sensitivity study is performed for the case $\zeta = 2$. The corresponding cases with increasing mesh refinement are summarised in Table 6.11. For each case,

Case	ζ	$L0$ (m)	$D_b^{t=0}$ (m)	$l^{\max}$	$\Delta(l^{\max})$ (m)	cells/$D_b^{t=0}$	err(R_b)
A.1	2	0.5	0.01	8	1.95×10^{-3}	≈ 5	8.34×10^{-2}
A.2	2	0.5	0.01	9	9.77×10^{-4}	≈ 10	2.56×10^{-2}
A.3	2	0.5	0.01	10	4.88×10^{-4}	≈ 20	1.20×10^{-2}
A.4	2	0.5	0.01	11	2.44×10^{-4}	≈ 41	8.90×10^{-3}

Table 6.11: List of cases for the grid convergence analysis of the Scriven problem with $\zeta = 2$.

the maximum level of refinement is reported, along with the corresponding mesh size $\Delta(l^{\max})$, the number of cells per initial diameter and the relative error of the bubble radius (at time $t = 28.5\,\mathrm{s}$), computed as:

$$\mathrm{err}(R_b) = \left| \frac{R_b^{\mathrm{Analyt.}} - R_b^{\mathrm{Num.}}(\Delta)}{R_b^{\mathrm{Analyt.}}} \right| \tag{6.20}$$

where $R_b^{\mathrm{Analyt.}}$ is the exact interface displacement computed with equation 6.16 and $R_b^{\mathrm{Num.}}$ is the numerical solution, which depends on the grid size Δ. The plot of the bubble radius against time and the comparison with the analytical solution is reported in Figure 6.10. As it was explained above, the numerical solutions start

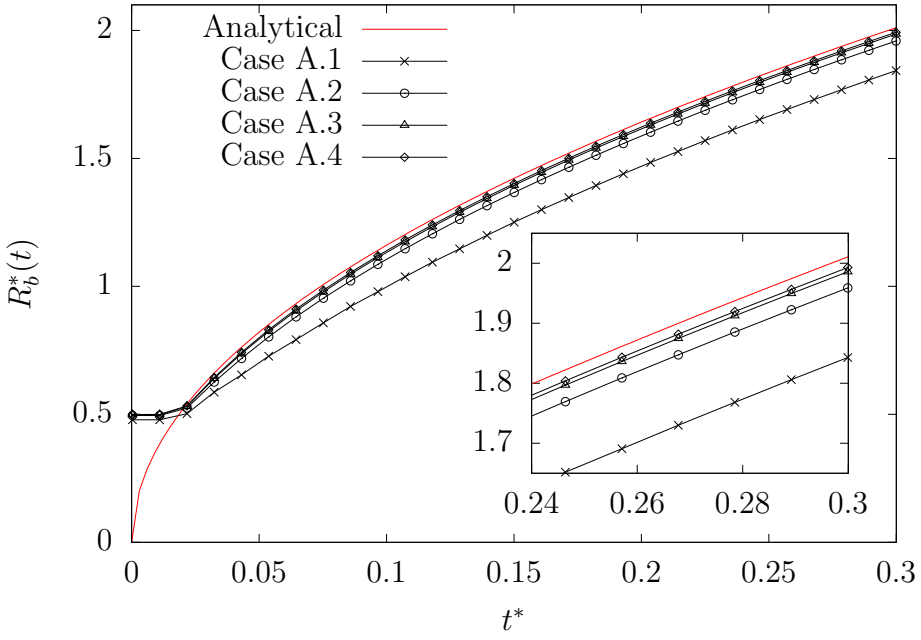

Figure 6.10: Grid convergence for the Scriven problem with $\zeta = 2$. Plot of bubble radius Vs time.

from a bubble with radius $R_b^* = 0.5$ ($R_b = 0.005\,\mathrm{m}$) and the size is kept constant until $t = \bar{t}$. At time $t = \bar{t}$, a concentration boundary layer is developed around the interface, but the liquid velocity is still null everywhere. Therefore, when the

full phase-change solver is turned on there is a (small) delay in the volume change since the liquid velocity must be activated and propagate through the continuous medium. This effect can be visible at $t = \bar{t}$, where the slope of the numerical plots is smaller than the analytical one. However, after a transient period, the radius growth rate approaches the reference one and the grid A.3 represents a good compromise between accuracy and computational cost; this mesh density is also used for the other saturation levels (i.e. $\zeta = 3$ and $\zeta = 4$). It is finally noted that, due to the delay in the activation of the volume change, there is no benefit in further refining the mesh since all the numerical plots are slightly shifted down (for the reduced slope at $t = \bar{t}$) from the analytical one.

A summary of the cases for the different saturation levels is reported in Table 6.12. Results in terms of radius growth for the various saturation levels are reported

Case	ζ	$L0$ (m)	$D_b^{t=0}$ (m)	$l^{\max}$	β	$\bar{t}$ (s)
A	2	0.5	0.01	10	0.421	1.7670
B	3	0.5	0.01	10	0.669	0.6935
C	4	0.5	0.01	10	0.895	0.3895

Table 6.12: List of cases for the Scriven problem with different saturation levels.

in Figure 6.11, where good agreement is found for all the simulated cases.

Finally, a qualitative representation of the species concentration around the interface and the effect of the saturation level on the growth rate is shown in Figure 6.12, where the contours of concentration are plotted on the XY plane at time $t^* = 0.3$, for $\zeta = 2$ (Figure 6.12a), $\zeta = 3$ (Figure 6.12b) and $\zeta = 4$ (Figure 6.12c). The concentration is discontinuous across the interface, since $c^* = 1$ inside the bubble whilst the value in the liquid region depends on the level of supersaturation. It is reminded here that the Henry's law coefficient for these simulations is set to $H_e = 5$, which means that the interfacial (liquid) concentration is equal to $(c_c^*)_\Sigma = 0.2$.

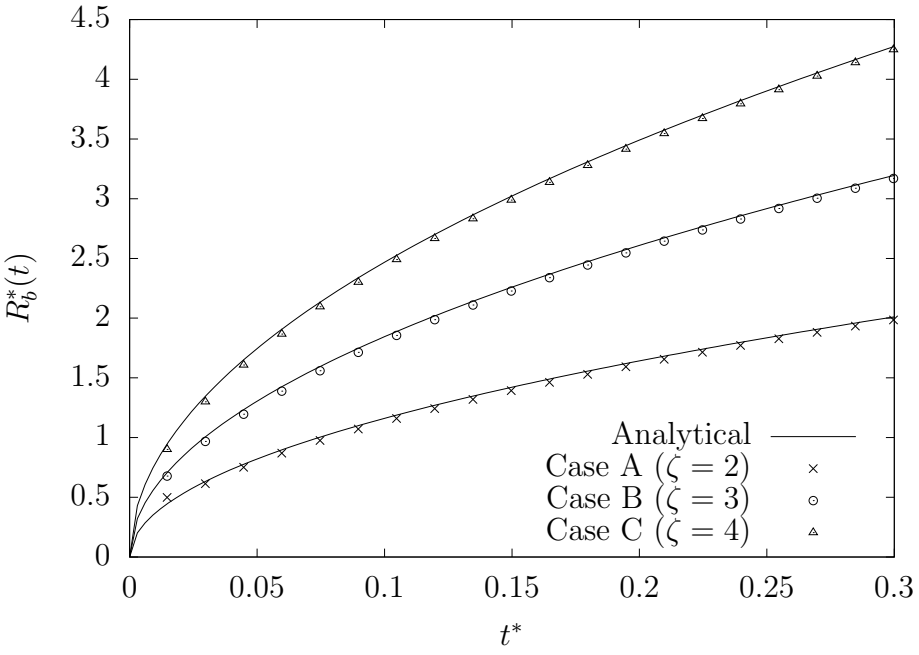

Figure 6.11: Radius Vs time for growing bubbles in super-saturated solutions at different saturation levels.

Bubbles dissolving in under-saturated solutions

In this section, the case of a bubble dissolving in an under-saturated solution with no initial concentration of dissolved gas ($\zeta = 0$) is modelled. A simplified version of this problem, where the advection of species is neglected, was solved analytically by Epstein and Plesset, 1950 for an infinite domain internally bounded by a sphere with a constant radius $\bar{R}$ and uniform concentration in the liquid c_{bulk}. The mathematical formulation of the problem reads:

$$\begin{aligned} \partial_t c_c &= \nabla \cdot (D_c \nabla c_c) \\ c_c(r,0) &= c_{\text{bulk}} \qquad \text{for} \quad r > \bar{R} \\ c_c(\bar{R},t) &= (c_c)_\Sigma \qquad \text{for} \quad t > 0 \\ \lim_{r\to\infty} c_c(r,t) &= c_{\text{bulk}} \qquad \text{for} \quad t > 0 \end{aligned} \tag{6.21}$$

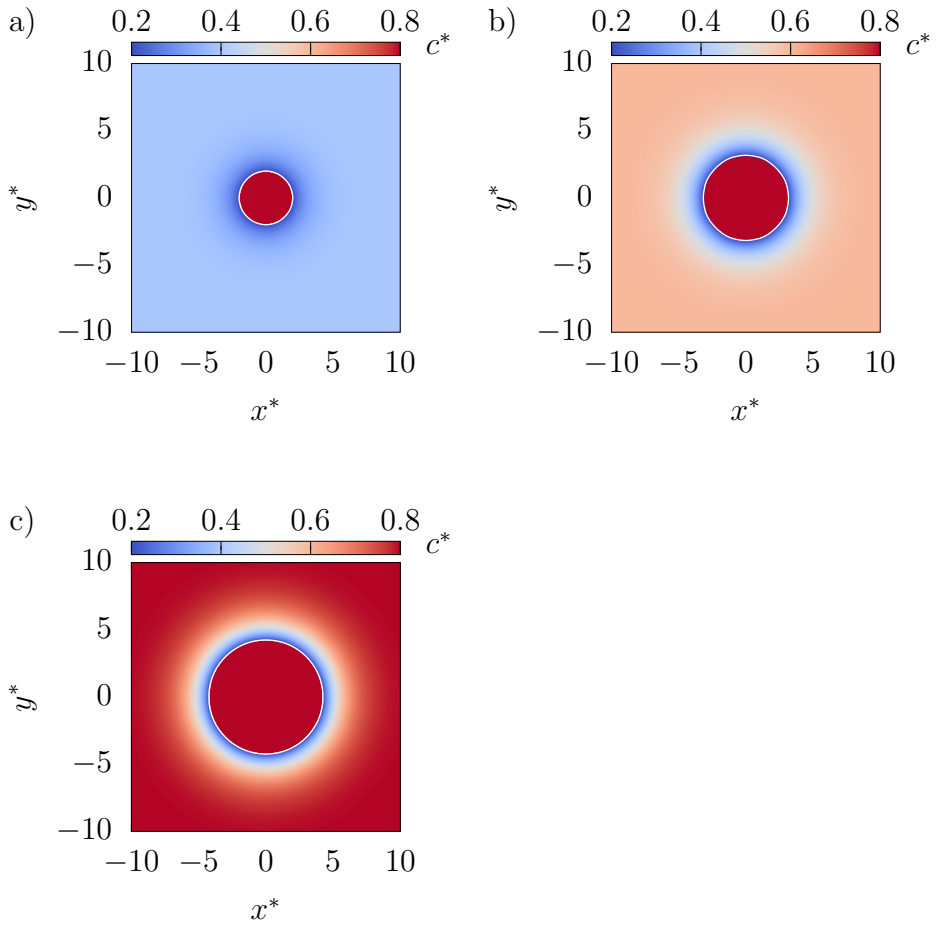

Figure 6.12: Interface (white line) and contours of species concentration on the XY plane at $t^* = 0.3$, for $\zeta = 2$ (a), $\zeta = 3$ (b) and $\zeta = 4$ (c).

In this case, the mass transfer is entirely dominated by the diffusive process and, given the spherical symmetry of the problem, the mass contained within the bubble (m_b) with radius $\bar{R}$ is:

$$\frac{dm_b}{dt} = 4\pi\bar{R}^2 \left(MD_c \frac{\partial c_c}{\partial r} \right) \tag{6.22}$$

The analytical solution of Epstein and Plesset, 1950 to the problem defined by equations 6.21 - 6.22 is given by:

$$\frac{dm_b}{dt} = 4\pi \bar{R}^2 M D_c \left(c_{\text{bulk}} - (c_c)_\Sigma\right) \left(\frac{1}{\bar{R}} + \frac{1}{\sqrt{\pi D_c t}}\right) \tag{6.23}$$

which is valid for the mass flow out from a bubble with constant size $\bar{R}$. The concentration field in the liquid domain is (see Crank, 1975):

$$c_c(r,t) = c_{\text{bulk}} + ((c_c)_\Sigma - c_{\text{bulk}}) \frac{\bar{R}}{r} \text{erfc}\left(\frac{r - \bar{R}}{2\sqrt{D_c t}}\right) \tag{6.24}$$

Equation 6.23 can be used to approximate a bubble that changes in time by replacing $\bar{R}$ with $R_b(t)$ and, using the relation between mass and radius (i.e. $dm_b/dt = 4\pi R_b^2 \rho_d \left(dR_b/dt\right)$), the following formula for the prediction of the time evolving radius is obtained:

$$\frac{dR_b}{dt} = \frac{M D_c \left(c_{\text{bulk}} - (c_c)_\Sigma\right)}{\rho_d} \left(\frac{1}{R_b(t)} + \frac{1}{\sqrt{\pi D_c t}}\right) \tag{6.25}$$

Equation 6.25 (also referred to as EP model) provides an approximation for a bubble that exchanges mass with the surrounding liquid. Such (quasi-stationary) approximation is as accurate as the mass transfer process is slow (i.e. the effect of the species advection is negligible compared to diffusion), and the growth rate of the concentration boundary layer is fast compared to the rate of dissolution (see Duda and Vrentas, 1971). This is usually the case of gas bubbles dissolving in liquids, since diffusion coefficients are typically small (e.g. $D_c \propto 10^{-9}\,\text{m}^2\,\text{s}^{-1}$). However, the EP model is no longer valid when the bubble is almost completely dissolved since, at that stage, the rate of radius change prevails on the evolution of the concentration boundary layer and the quasi-stationary approximation does not hold anymore.

Here, a single 3D bubble with initial diameter $D_b^{t=0} = 0.01\,\text{m}$ is modelled and the size of the computational domain is set to $L0 = 0.2\,\text{m}$; gravity is not taken into account and outflow boundary conditions are applied at the external boundaries to allow the liquid to enter the domain as the bubble dissolves. A mesh with approximately 102 cells per (initial) diameter is used (which corresponds to $l^{\max} = 11$); the

choice of a finer mesh with respect to the case of a growing bubble is justified by the fact that more cells are needed to properly resolve the flow around the interface as the bubble dissolves. The first test consists of modelling the exact EP solution (equations 6.23 - 6.24), where the bubble is kept at a constant size and the species is allowed to flow freely into the liquid region. In this model, the redistributed mass transfer term $\dot{m}'$ is set to zero everywhere, so that no phase volume change occurs and the velocity field is null everywhere; the interfacial mass transfer term $\dot{m}$ is applied to the species transport equation to compute the transfer of moles between the phases. In this way, the numerical model replicates exactly the assumptions behind the analytical solution. The methodology is then tested against the approximate solution for a bubble changing with time and, for this case, the effect of the advection term in the transport of species is discussed. A summary of the presented cases is summarised in Table 6.13.

Case	$L0$ (m)	$D_b^{t=0}$ (m)	ζ	$l^{\max}$	Volume change	Species advection
A	0.2	0.01	0	11	no	no
B	0.2	0.01	0	11	yes	no
C	0.2	0.01	0	11	yes	yes

Table 6.13: List of cases for the Epstein-Plesset model.

For Case A, where the bubble boundary is kept fixed, an equivalent time evolving volume is computed based on the species mass flux across the interface:

$$V_b(t) = V_b^{t=0} + \frac{1}{\rho_d} \int_0^t \int_\Sigma \dot{m}\, ds\, dt' \tag{6.26}$$

The corresponding (time evolving) radius and the concentration values at three points in the liquid domain are plotted in Figure 6.13a and Figure 6.13b respectively, and compared against the analytical solutions (equations 6.23 - 6.24), where in equation 6.23 the mass transfer has been replaced by $dm_b/dt = 4\pi R_b^2 \rho_d \, (dR_b/dt)$; excellent agreement is found between the analytical and numerical solutions.

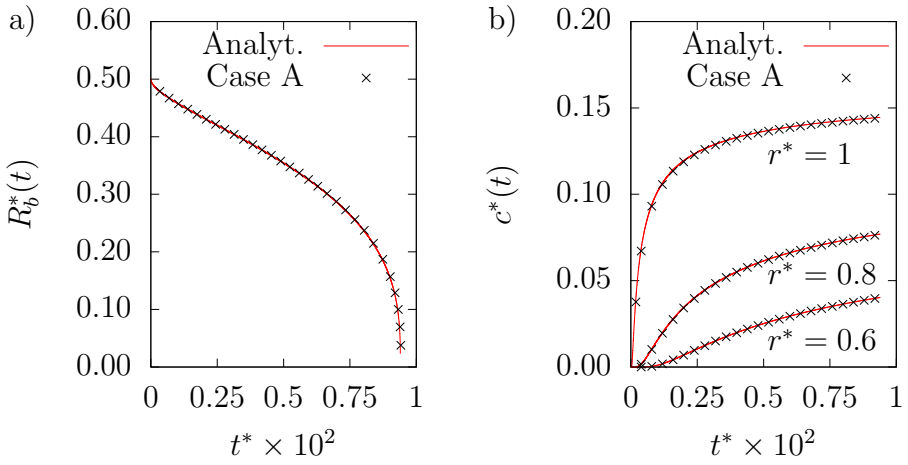

Figure 6.13: Predicted radius (a) and concentration values (b) at three points with different radial distances from the centre of the bubble. The bubble size is kept fixed and the radius prediction is based on the species flux across the interface. Numerical simulations are compared against the exact EP model.

Cases B and C model the actual bubble volume change and show the effect of the advection term in the transport of species. When the advection term is taken into account (Case C), the concentration field is transported also by the liquid velocity field (and not only by diffusion). Therefore, the region where the concentration is variable but larger than the bulk value (i.e. the concentration boundary layer around the interface) is transported with a velocity close to the interfacial one ($\mathbf{u}_\Sigma$) and is kept "attached" to the interface; the difference in the concentration values between the interface $(c_c)_\Sigma$ and the adjacent liquid region is then smaller compared to the case where no advection occurs. As a result, the concentration gradient at the interface ($\partial c_c/\partial r$) is steeper in the case without advection (Case B) and the resulting dissolution rate is faster than the one in Case C. These cases are compared against the EP model for a bubble changing with time (equation 6.25), and the results are shown in Figure 6.14. The plot confirms that the bubble dissolves slower in Case C and, since the EP model neglects the advection term (equation 6.21), Case B is in better agreement with the analytical model than Case C. The numerical solution of Case B matches with good accuracy the EP model until $t^* \approx 0.015$, when the radius

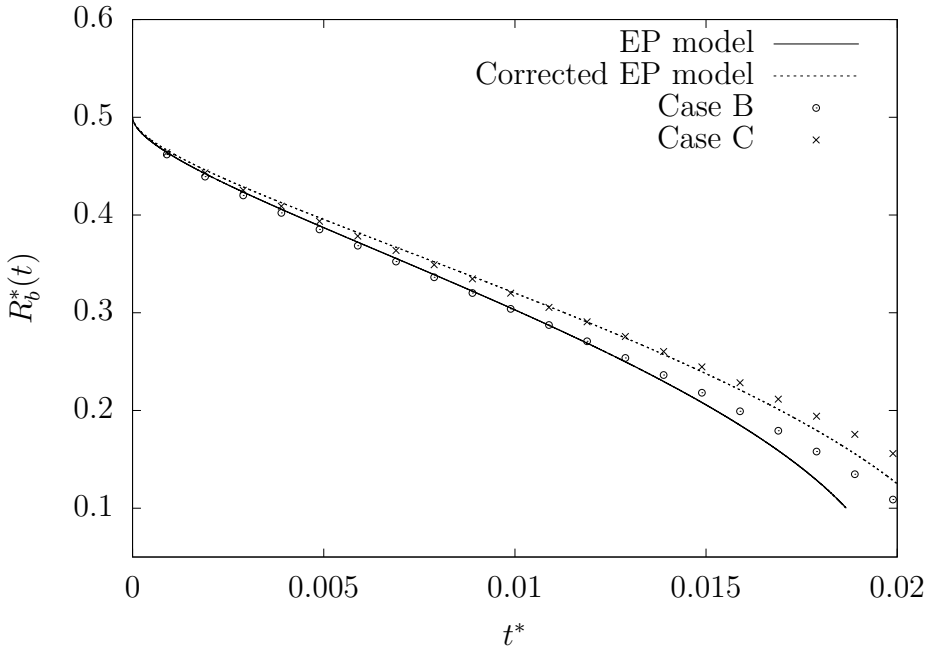

Figure 6.14: Radius Vs time for a dissolving bubble in an under-saturated solution. The full species transport (advection + diffusion) is solved in Case C, whilst only diffusion is taken into account in Case B. A corrected version of the EP model (see text) is derived, based on experimental findings.

change rate is no longer negligible for the quasi-stationary approximation and the EP model is not valid anymore.

The dissolution time predicted by the EP model (t_{diss}^{EP}) underestimates the actual value, due to the missing advection effect in the model. A detailed experimental study on the validity of the EP model was performed by Duncan and Needham, 2004, where the authors compare the time required for a bubble to dissolve (based on experiments) against the predictions of the EP model. The authors use a simplified version of the EP model, where the last term on the RHS of equation 6.25 is neglected and the corresponding dissolution time is given by:

$$\tilde{t}_{\text{diss}}^{EP} = \frac{\rho_d \left(R_b^{t=0}\right)^2}{2D_c \left(c_c\right)_\Sigma M(1-\zeta)} \tag{6.27}$$

The conclusion of the experimental investigation is that the simplified EP model (equation 6.27) overpredicts the dissolution time of a bubble in an under-saturated solution by approximately 8.2%. However, for an air-water system the results reported in Epstein and Plesset, 1950 show that the (complete) EP model predicts a dissolution rate around $t_{\text{diss}}^{EP} \approx 0.84\tilde{t}_{\text{diss}}^{EP}$. Therefore, the conclusions of Duncan and Needham, 2004 can be reformulated, stating that the EP model underpredicts the dissolution time by approximately 10%. This correction factor is used in Figure 6.14 to plot a corrected curve for the EP model, which shows a better correlation with the numerical Case C, in agreement with the experimental findings.

Finally, it is observed that the bubble dissolution in Case A (Figure 6.13a) is significantly faster than cases B and C, since the surface of the bubble is kept constant during the simulation and a larger area is available for the mass transfer process, whilst in cases B and C the area of the interface reduces over time.

6.2.4 Rising bubbles

In the cases considered so far, bubbles are stationary since neither gravity nor external forces are considered and the concentration distribution has a (spherical) symmetric shape. In this section, the case of rising bubbles under the gravitational force is considered. The computational domain is large compared to the size of the bubbles, so that end wall effects are neglected.

Two different studies are proposed here. The first one consists of a rising bubble in a solution with different diffusivities and the effect of the Péclet number on the mesh requirements for the numerical modelling of mass transfer is discussed. The second test is a bubble rising in a creeping flow, where the volume change rate is compared against a semi-analytical model. In both cases, the liquid solutions are under-saturated and the saturation ratio is set to $\zeta = 0$.

Rising bubbles at different Péclet numbers

The limiting factor for direct numerical simulations of diffusion driven phase-change problems is mainly given by the thickness of the liquid-side concentration boundary

layer δ_c, which must be resolved with enough grid points to accurately predict the mass transfer at the interface. Indications on the thickness of δ_c can be obtained from the Péclet (Pe) number (equation 6.5), which measures the ratio between the transport by convection and diffusion. For convection-dominated cases, the potential flow theory shows that the concentration boundary layer evolves as $\delta_c \propto Pe^{-1/2}$ (see the discussion in section 2.3.1), whilst the ratio between concentration and hydrodynamic boundary layer follows the relation $\delta_c/\delta_h \propto Sc^{-1/2}$ (Bothe and Fleckenstein, 2013). Therefore, the smallest spatial scale is generally given by δ_c and the larger is the Péclet number, the more important is the advection term that tends to keep the boundary layer confined within a thin region around the interface. On the other hand, for low Pe values, diffusion is predominant and the concentration boundary layer expands uniformly in a wider area.

The aim of this section is to provide a detailed (and quantitative) analysis of the mesh resolution (around the interface) required to capture the concentration boundary layer at different Pe numbers. Three different soluble species are tested, with a different diffusivity and the properties of the gas-liquid systems are reported in Table 6.14. Here, 2D axisymmetric simulations of bubbles in a large domain are

Phase	Density ($\mathrm{kg\,m^{-3}}$)	Viscosity ($\mathrm{N\,s\,m^{-2}}$)	Diffusivity ($\mathrm{m^2\,s^{-1}}$)	M ($\mathrm{kg\,mol^{-1}}$)	σ ($\mathrm{N\,m^{-1}}$)	H_e
Liquid	998	0.005			0.06	
Gas A	1.2	1.8×10^{-5}	2×10^{-7}	0.044		5
Gas B	1.2	1.8×10^{-5}	2×10^{-8}	0.044		5
Gas C	1.2	1.8×10^{-5}	2×10^{-9}	0.044		5

Table 6.14: Gas-liquid properties for rising bubbles at different Péclet numbers.

performed. The gravitational acceleration acts along the x-direction (i.e. $\mathbf{g} = -g\mathbf{e}_x$) and so is the rising trajectory of the bubble. The initial diameter is set to $D_b^{t=0} = 0.001\,\mathrm{m}$ and results are made non-dimensional with the reference length $L_{\mathrm{ref}} = D_b^{t=0}$, time $t_{\mathrm{ref}} = \sqrt{L_{\mathrm{ref}}/g}$ and the gaseous concentration, i.e. $c_{\mathrm{ref}} = \rho_d/M$; a summary of the reference values is reported in Table 6.15. The non-dimensional numbers that describe the dynamics of the bubble are $Ga = 19.8$ and $Bo = 0.163$ and, for these

L_{ref} (m)	t_{ref} (s)	U_{ref} (m s^{-1})	g_{ref} (m s^{-2})	c_{ref} (mol m^{-3})
0.001	0.01	0.099	9.81	27.3

Table 6.15: Reference dimensions for rising bubbles at different Péclet numbers.

parameters, the bubble is expected to rise along a straight direction, preserving its spherical shape (see Tripathi et al., 2015). The phase volume change is not taken into account in these simulations and only the species transfer between the phases is computed. The volume of the bubble is then constant and, for all the tested gaseous species, the bubble reaches the same steady state regime (after a short transient period in which it accelerates from rest). The list of cases studied in this section is reported in Table 6.16. Adaptive mesh refinement is used for these simulations and

Case	Gas	ζ	$L0$ (m)	$D_b^{t=0}$ (m)	$l^{\max}$	$\Delta(l^{\max})$ (m)	Sc	Re_b	Pe
A	A	0	0.12	0.001	14	7.32×10^{-6}	25.05	18.56	465
B	B	0	0.06	0.001	15	1.83×10^{-6}	250.5	18.56	4650
C	C	0	0.06	0.001	17	4.58×10^{-7}	2505	18.56	46500

Table 6.16: List of cases for rising bubbles at different Péclet numbers.

the max grid level ($l^{\max}$) reported for each of the cases represents the necessary grid discretization to get a mesh independent solution. As explained earlier, the limiting factor for the mesh resolution is given by the mass transfer process, which requires a certain amount of grid points within δ_c to capture the gradient of concentration at the interface. In terms of bubble trajectory, acceleration and velocity, a grid with level 14 is sufficient to get mesh independent results; by further refining the grid up to level 17, no significant difference in the bubble velocity is found. Since the phase volume change is not taken into account, the behaviour of the bubble is the same for all the cases (i.e. the mass transfer is decoupled from the dynamics) and the terminal (steady) rising velocity for each of them is $U_b \approx 0.093\,\text{m s}^{-1}$, which corresponds to $Re_b = 18.56$. The plot of the bubble Reynolds number against time is reported in

Figure 6.15 for Case A, where it is shown that, after a transient period, a steady state regime with constant velocity is reached at $t^* \approx 3$.

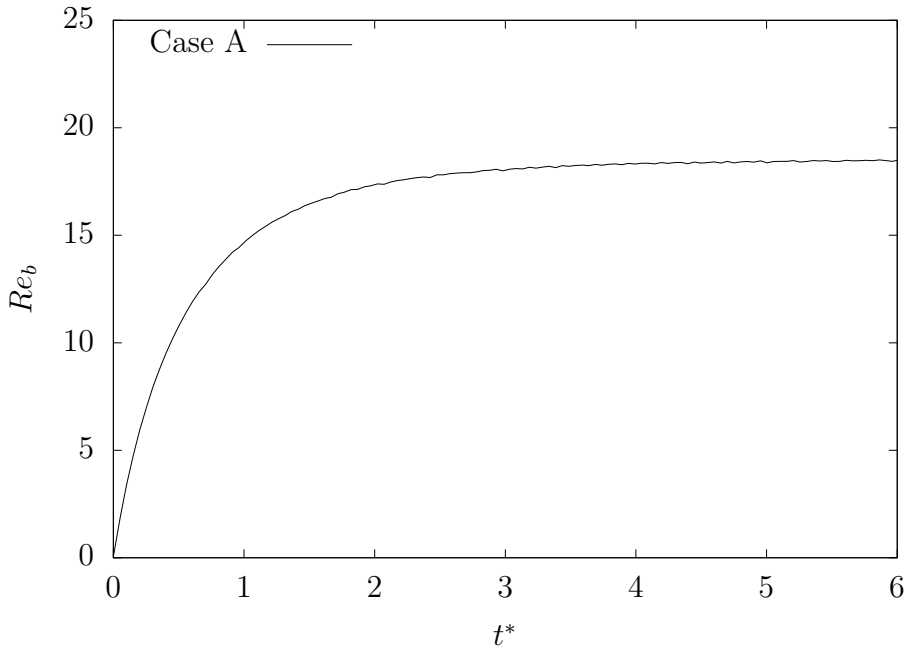

Figure 6.15: Reynolds number Vs time for the rising bubble of Case A. After a transient period where the bubble accelerates from rest, a steady state regime is approached.

The mass transfer of the bubble is compared, in terms of Sherwood numbers, against the formula proposed in the experimental work of Takemura and Yabe, 1998. This correlation formula is valid for the range $Re_b < 100$ and $Pe > 1$ (and therefore applicable to cases A, B and C) and reads:

$$Sh = \frac{2}{\sqrt{\pi}} \left[1 - \frac{2}{3} \frac{1}{\left(1 + 0.09 Re_b^{2/3}\right)^{3/4}} \right]^{1/2} \left(2.5 + \sqrt{Pe}\right) \tag{6.28}$$

Results are shown in Figure 6.16 where, for all the simulated cases, the corresponding Sherwood number predicted by equation 6.28 is computed with the terminal

(steady-state) Reynolds and Péclet numbers. The simulations are initialized with

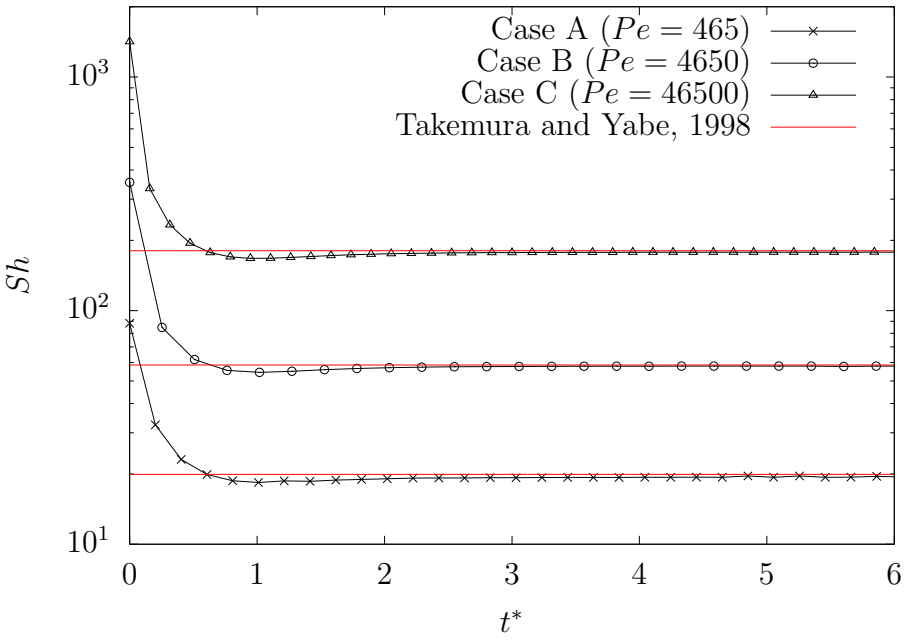

Figure 6.16: Sherwood number Vs time for rising bubbles at different Péclet numbers. After a transient regime, the numerical simulations approach the value predicted by Takemura and Yabe, 1998 (equation 6.28).

a discontinuous concentration field (i.e. $c^* = 1$ in Ω_d and $c^* = 0$ in Ω_c) and the mass transfer in the first part of the numerical computation assumes large values due to the extremely thin concentration boundary layer ($\delta_c \to 0$ for $t^* = 0$) and, therefore, strong concentration gradient. After a transient regime, where the species that is released into the liquid forms a concentration boundary layer around the bubble, a steady solution for the Sherwood number is reached and the terminal values approach the predictions of Takemura and Yabe, 1998, with a relative error below 2%. Such a steady-state regime for the Sherwood number is clearly related to the (steady-state) dynamics of the bubble, that is characterized by a constant terminal velocity that allows for a time independent (in a reference frame moving with the bubble) concentration boundary layer to develop around the interface.

Concentration profiles at the equatorial line of the bubble (i.e. $x = x_b$, where

x_b is the x-coordinate of the center of the bubble) are compared in Figure 6.17 for the various Péclet numbers at time $t^* = 6$. As is expected, for large Pe numbers

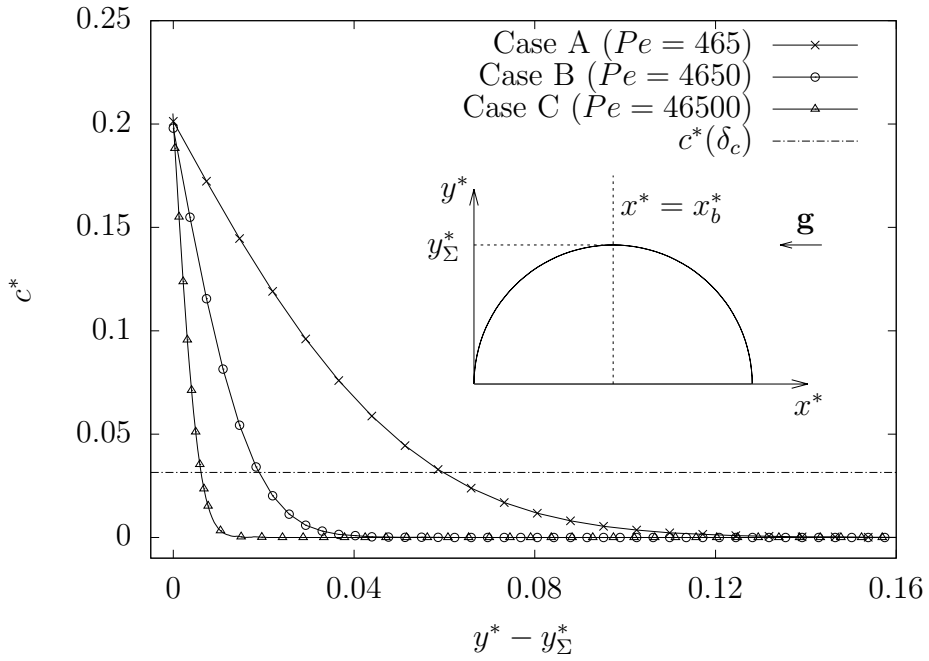

Figure 6.17: Equatorial concentration profiles at $t^* = 6$ for different Péclet numbers.

the concentration profile is steeper than for low Pe values, where the diffusive term becomes more relevant and the species concentration diffuses more rapidly into the liquid region. In order to provide a quantitative measure of the boundary layer thickness δ_c, the definition proposed by Bothe and Fleckenstein, 2013 is used here, where δ_c is assumed to be the distance from the interface at which the concentration field reaches the value:

$$c(\delta_c) = (c_c)_\Sigma \, (1 - \mathrm{erf}(1)) \tag{6.29}$$

The horizontal (dotted) line in Figure 6.17 represents the concentration value $c(\delta_c)$ and the distance from the interface where this value occurs reduces significantly with increasing Péclet numbers. A summary of the numerical cases along with the respective boundary layer thicknesses and mesh refinements is presented in Table 6.17, where the more demanding requirements in terms of grid resolution as the Péclet

Case	Pe	$\Delta(l^{\max})$ (m)	δ_c (m)	cells/$D_b^{t=0}$	cells/δ_c
A	465	7.32×10^{-6}	5.98×10^{-5}	137	8
B	4650	1.83×10^{-6}	1.89×10^{-5}	546	10
C	46500	4.58×10^{-7}	6.12×10^{-6}	2185	13

Table 6.17: Grid refinements and concentration boundary layer thicknesses for rising bubbles at different Péclet numbers.

number increases are evident. As expected, given the rectilinear rising trajectory and spherical shape, the thickness of δ_c evolves following the potential flow theory, i.e. $\delta_c \propto Pe^{-1/2}$. It is reminded here that adaptive mesh refinement technique is an extremely useful approach for this class of problems, where the maximum grid density is needed only around the interface.

Finally, a qualitative representation of the species concentration around the interface and the corresponding grid refinement is shown in Figure 6.18, for cases A, B and C at time $t^* = 6$.

Rising bubble in a creeping flow

In this section, the case of a rising bubble in a creeping flow is modelled. Here the same setup proposed in Fleckenstein and Bothe, 2015 is replicated and the properties of the gas-liquid system are reported in Table 6.18. To obtain a low Reynolds flow

Phase	Density ($\mathrm{kg\,m^{-3}}$)	Viscosity ($\mathrm{N\,s\,m^{-2}}$)	Diffusivity ($\mathrm{m^2\,s^{-1}}$)	M ($\mathrm{kg\,mol^{-1}}$)	σ ($\mathrm{N\,m^{-1}}$)	H_e
Liquid	1245	0.46			0.06	
Gas	1.2	1.8×10^{-5}	1.48×10^{-6}	0.044		5

Table 6.18: Gas-liquid properties for a rising bubble in a creeping flow.

(i.e. a creeping flow), the selected liquid viscosity is significantly large (compared to common aqueous solutions) and this limits the magnitude of the rising velocity of the bubble. In the work of Fleckenstein and Bothe, 2015, the authors derive an

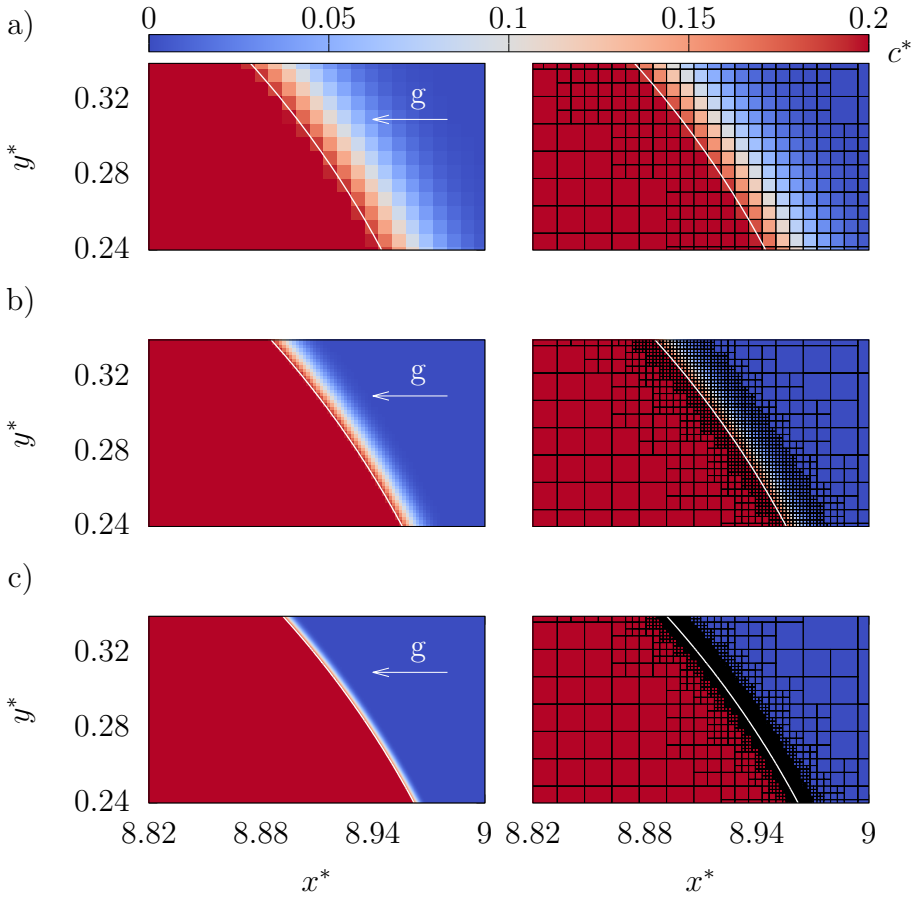

Figure 6.18: Contours of concentration (left) and mesh refinement (right) for Case A (a), Case B (b) and Case C (c), at $t^* = 6$.

analytical model for the mass transfer of a bubble rising in a creeping flow. This model is based on the Hadamard-Rybczynski solution for the steady-state velocity field around a rigid spherical particle moving along a straight line at low speeds (Hadamard, 1911 and Rybczynski, 1911 - see section 2.1.2) and the terminal velocity of a particle with radius R_b in a gravitational field g reads:

$$U_b = \frac{2}{3}\frac{\rho_c - \rho_d}{\mu_c} g R_b^2 \frac{1 + \mu_d/\mu_c}{2 + 3\mu_d/\mu_c} \tag{6.30}$$

The terminal velocity predicted by equation 6.30 for the gas-liquid properties reported in Table 6.18 is $U_b = 0.035\,\mathrm{m\,s^{-1}}$. However, in the simulation of Fleckenstein and Bothe, 2015 the resulting rising velocity is found to be $U_b = 0.03\,\mathrm{m\,s^{-1}}$, which underestimates the theoretical value. To reproduce the results reported in Fleckenstein and Bothe, 2015 and validate the numerical methodology, the gravitational acceleration in the present work is set to $g = 8.92\,\mathrm{m\,s^{-2}}$, so that the resulting terminal velocity of the bubble matches the value $U_b = 0.03\,\mathrm{m\,s^{-1}}$. Here a single 3D bubble, with initial diameter $D_b^{t=0} = 0.004\,\mathrm{m}$ is confined in a large domain and surrounded by an under-saturated solution with $\zeta = 0$. The corresponding non-dimensional numbers are $Ga = 2.04$, $Bo = 2.96$ and $Sc = 250$. According to the results reported in the work of Tripathi et al., 2015, a bubble characterised by these Galilei and Bond numbers is expected to rise vertically and retain its spherical shape; the assumptions of the Hadamard-Rybczynski model are then fulfilled and their solution can be applied to the present case. A summary of the numerical setup is reported in Table 6.19, where the mesh refinement corresponds to approximately 68 cells per (initial) diameter. An outflow boundary condition is set on the top face of the cubic

Case	ζ	$L0$ (m)	$D_b^{t=0}$ (m)	$l^{\max}$	$\Delta(l^{\max})$ (m)	g ($\mathrm{m\,s^{-2}}$)	Sc
A	0	0.48	0.004	13	5.86×10^{-5}	8.92	250

Table 6.19: Numerical setup for a rising bubble in a creeping flow.

domain to allow the liquid flow across the boundary as the bubble shrinks; symmetric boundary conditions are applied to the other boundaries. Results are made non-dimensional with the reference length $L_{\mathrm{ref}} = D_b^{t=0}$, time $t_{\mathrm{ref}} = \sqrt{L_{\mathrm{ref}}/g}$ and the gaseous concentration, i.e. $c_{\mathrm{ref}} = \rho_d/M$; a summary of the reference values is reported in Table 6.20.

To reproduce the regime where the analytical model is valid, the bubble needs to reach a steady state regime where the rising velocity is constant and the concentration field around the bubble is time independent. The numerical simulation is first run without taking into account the phase volume change (i.e. $\dot{m}'$ is set to null ev-

L_{ref} (m)	t_{ref} (s)	U_{ref} (m s^{-1})	g_{ref} (m s^{-2})	c_{ref} (mol m^{-3})	$\dot{m}_{\text{ref}}$ ($\text{kg m}^{-2}\,\text{s}^{-1}$)
0.004	0.021	0.189	8.92	27.3	235.2

Table 6.20: Reference dimensions for a rising bubble in a creeping flow.

erywhere) until the bubble reaches its (steady) terminal velocity. During this stage, the mass transfer term ($\dot{m}$) is taken into account in the transport of species and a concentration field develops around the interface until it becomes locally time independent in a reference frame moving with the bubble velocity. The transient regime of the bubble is characterized by an acceleration from rest and the time dependent rising velocity is shown in Figure 6.19; the steady state regime is reached at $\bar{t}^* \approx 25$, where $U_b^* = 0.159$ (i.e. $U_b = 0.03\,\text{m s}^{-1}$). After the bubble reaches the steady state regime, the phase volume change is activated and the volume of the bubble shrinks as some of the gas is released into the liquid. As a result of the volume reduction, the buoyancy force becomes less relevant and the bubble decelerates. This effect is clearly visible in Figure 6.19 for $t^* > \bar{t}^*$, where the rising velocity decreases over time.

The volume reduction of the bubble is shown in Figure 6.20 where it is compared against the analytical solution of Fleckenstein and Bothe, 2015. The phase change process is simulated for a time interval of $\Delta t^* = 15$ (i.e. $\Delta t = 0.315\,\text{s}$) and the numerical solution shows good accuracy, with a relative error on the volume ratio after $\Delta t = 0.25\,\text{s}$ (from the start of the volume phase change) of $\text{err}\,(V_b/V_b^{t=0}) \approx 0.43\%$.

A qualitative representation of the dissolution process is shown in Figure 6.21 at three different times. The plot shows the contours of gas concentration on the XZ plane and the interface of the bubble. As expected, given the Galilei and Bond numbers for this specific problem, the bubble rises vertically and retains its spherical shape. The first two snapshots (Figure 6.21a and Figure 6.21b) are taken at time $t^* = 0$ and $t^* = 20$ respectively. The volume is kept constant at this stage, but the concentration field in the liquid is free to evolve as part of the gas is released from the bubble. The last picture (Figure 6.21c) is taken at $t^* = 40$ and shows the

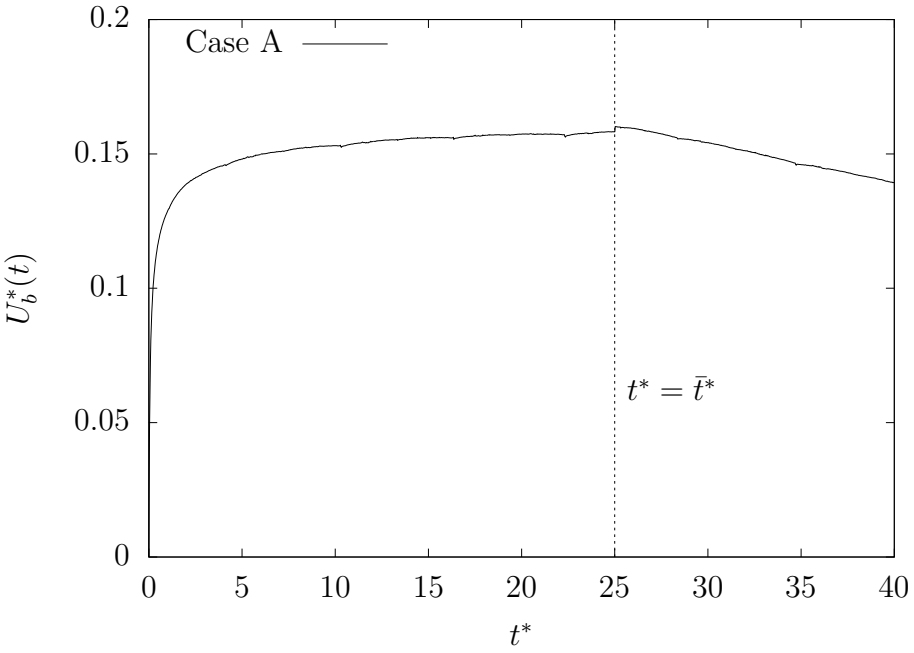

Figure 6.19: Rising velocity profile for a bubble in a creeping flow. The bubble accelerates from rest until the steady state regime is reached (vertical dotted line). For $t^* > 25$, the volume of the bubble reduces and the rising velocity decreases accordingly.

shrinking of the bubble. From these visualizations, it is possible to observe that the thickness of the concentration boundary layer is not constant around the interface and depends on which transport mechanism prevails locally. On top of the bubble, diffusion and advection are in contrast with each other, since diffusion tends to increase the concentration boundary layer thickness uniformly along the radial direction, whilst advection constraints the concentration profile within a thin region. Moving towards the equatorial region, the two transport mechanisms act in different directions: advection occurs mainly along the rising trajectory, whilst diffusion operates always along the radial direction and the thickness of the concentration profile grows accordingly. The wake close to the bottom of the bubble is characterised by a region where the velocity is stagnant. Here, diffusion prevails over advection and makes the concentration field almost uniform.

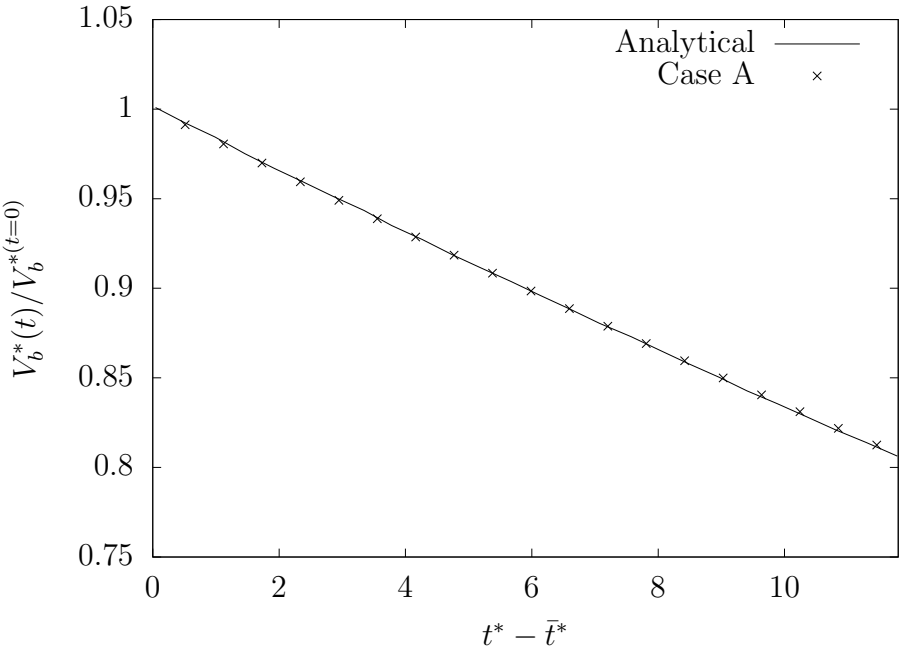

Figure 6.20: Volume ratio Vs time for a rising bubble in a creeping flow. The volume of the bubble is let free to evolve for $t > \bar{t}$.

One of the advantages of numerical modelling is that simulations easily provide access to local information that are difficult to obtain experimentally. An example is shown in Figure 6.22a, where the contour of the mass transfer rate is plotted on the XZ plane at $t^* = 20$. The mass transfer is a local quantity that depends on the gradient of concentration profile at the interface ($\dot{m} \propto -\partial c/\partial \mathbf{n}_\Sigma$) and is directly related to the thickness of the concentration boundary layer. As it was discussed above, the thickness of the concentration profile is minimum on the top of the bubble; as a consequence the gradient is steeper and the mass transfer reaches its maximum (absolute) value (Figure 6.22b). The magnitude of the mass transfer progressively decreases towards the equatorial region (Figure 6.22c) and becomes almost null in the stagnation region at the bottom of the bubble (6.22d), where the concentration is locally uniform.

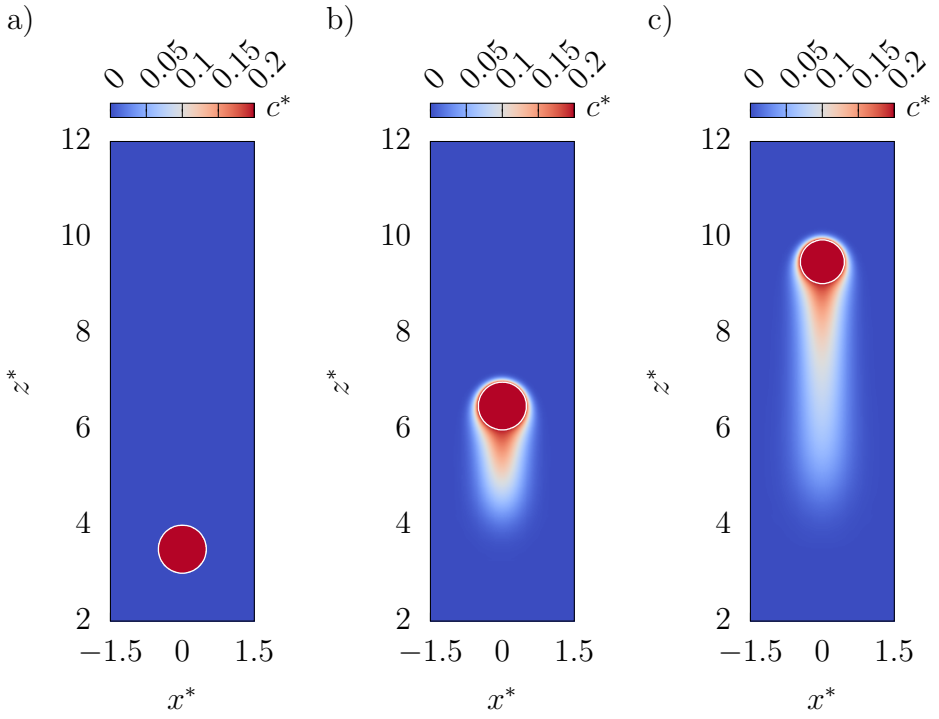

Figure 6.21: Bubble positions and contours of concentration at $t^* = 0$ (a), $t^* = 20$ (b) and $t^* = 40$ (c).

6.3 Mixtures

In the previous section, only pure soluble species were considered. In this particular case, even when a two-scalar approach for the transport of species is employed, only one scalar equation for the concentration field needs to be solved for the prediction of species distribution in the liquid domain, since the concentration in the gaseous region is uniform and equal to $c_d = \rho_d/M$. In this section, the general scenario of gaseous soluble mixtures is considered and two transport equations (one for each phase) are solved for each species, since the concentration field is generally not uniform in both the liquid and gaseous domains.

Here two benchmarks are proposed for the competing mass transfer of multiple soluble species. The first one consists of the modelling of a binary gas surrounded

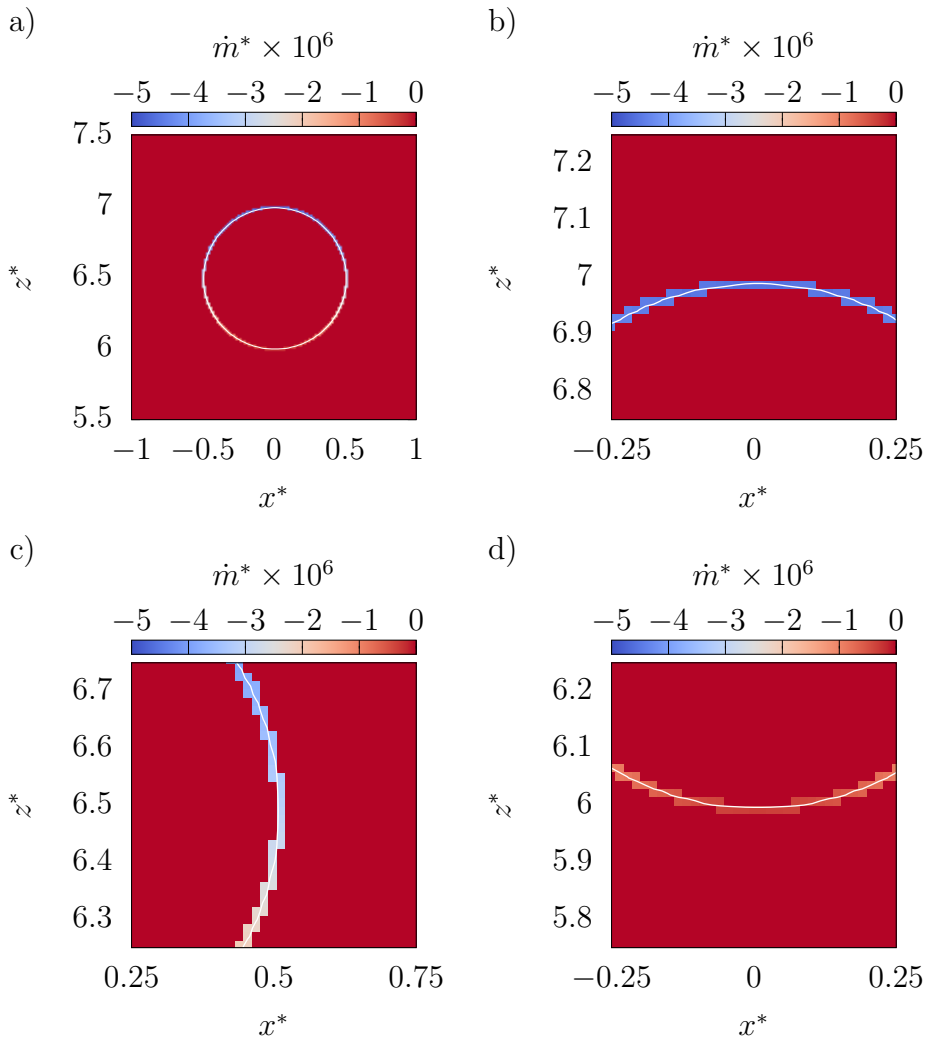

Figure 6.22: Mass transfer rate on the XZ plane at $t^* = 20$. Overview of the field distribution (a) and details for the top (b), equatorial (c) and bottom (d) regions.

by a liquid annulus, whilst the second one is a study of the mass transfer for a rising bubble in a mixed super/under-saturated solution.

6.3.1 Competing mass transfer in an infinite cylinder

In this test case, a binary gaseous mixture made of two soluble components (species A and B) is confined by a liquid annulus where R_{in} and R_{ext} are the inner and outer radius respectively. The liquid phase is therefore confined within the region $R_{\text{in}} < r < R_{\text{ext}}$, whilst the gaseous one exists for $r < R_{\text{in}}$. The axial length of the cylinder (L_z) is infinite and the external radius is set to $R_{\text{ext}} = 1\,\text{mm}$. The inner radius of the liquid annulus, which represents the interface between the phases, is free to move as some of the species crosses the interface and is initially set to $R_{\text{in}}^{t=0} = 0.5\,\text{mm}$. Due to the infinite axial extension, the problem is independent of the axial coordinate and can be represented by a 2D model; a sketch of the computational domain is shown in Figure 6.23.

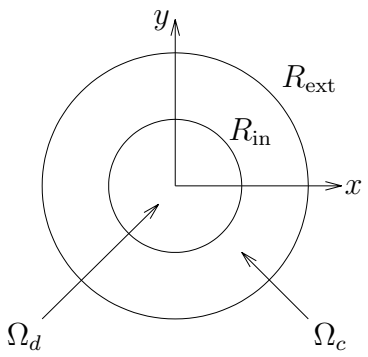

Figure 6.23: Computational domain for an infinite gaseous cylinder (Ω_d) confined by a liquid annulus (Ω_c).

The properties of the gas-liquid system are reported in Table 6.21 and approximate an air-water system.

The cases simulated in this section replicate the setups proposed in Maes and Soulaine, 2020 and, for the first benchmark (referred to as Case A), the gaseous (disperse) phase is initially composed of species B only, i.e. $c_d^{B(t=0)} = \rho_d / M^B$. Species A is assumed to be weakly soluble in the liquid solvent, whilst species B is not soluble and the respective Henry's law coefficients are $H_e^A = 100$ and $H_e^B \to \infty$. By setting Henry's law coefficient to $H_e^B \to \infty$ for species B, the equilibrium value on the liquid

Phase	Density ($\mathrm{kg\,m^{-3}}$)	Viscosity ($\mathrm{N\,s\,m^{-2}}$)	σ ($\mathrm{N\,m^{-1}}$)
Liquid	1000	1×10^{-3}	0.06
Gas	1	1.8×10^{-5}	

Table 6.21: Gas-liquid properties for competing mass transfer in an infinite cylinder.

side of the interface is $\left(c_c^B\right)_\Sigma = 0$, regardless of the amount of species within the gaseous domain. Since no species B exists initially in the liquid domain, the mass transfer of B across the interface is prevented (i.e. the solution is saturated with respect to species B, $\zeta^B = 1$) and the species is confined within the gaseous region. The liquid domain is therefore composed of the solvent (not soluble in the disperse phase) and species A, which has a relatively (compared to a typical gas solubility) large Henry's law coefficient and, therefore, is weakly soluble in the liquid solvent; the concentration of A is kept constant at the external boundary ($r = R_{\mathrm{ext}}$) and set to $c_c^A(R_{\mathrm{ext}}, t) = \rho_d / \left(M^A H_e^A\right)$. Diffusivity is the same for both species and is set to $D_c^A = D_c^B = 10^{-6}\,\mathrm{m^2\,s^{-1}}$ and $D_d^A = D_d^B = 10^{-4}\,\mathrm{m^2\,s^{-1}}$ in the continuous and disperse phases respectively.

Due to the symmetry of the problem, the velocity and concentration fields depend only on the radial distance (and time), and the liquid moves along the radial direction only:

$$\mathbf{u}_c = u_c(r, t)\mathbf{e}_r \tag{6.31}$$

Since the gaseous density is much smaller than the liquid one, the interface moves approximately with the liquid velocity at $r = R_{\mathrm{in}}$ (see the jump condition 3.5):

$$\mathbf{u}_\Sigma(t) = \mathbf{u}_c(R_{\mathrm{in}}, t) \tag{6.32}$$

The mass fraction of the generic k-th species within the disperse region is computed as:

$$m_d^k = \frac{\int_{\Omega_d} c_d^k M^k \, dV}{\int_{\Omega_d} \rho_d \, dV} \tag{6.33}$$

and, for the conservation of mass, the sum of the mass fractions must always be equal to one, i.e.:

$$m_d^A + m_d^B = 1 \tag{6.34}$$

Since the diffusive transport of species A within the gaseous region occurs significantly faster than in the liquid domain ($D_d^A = D_c^A \times 10^2$), the concentration field in Ω_d can be reasonably considered as uniform. As some of the species A flows through the liquid domain and crosses the interface, the inner radius R_{in} grows accordingly and the global amount of mass that has crossed the interface at time t (since $t = 0$) is $\pi \left(R_{\text{in}}^2(t) - R_{\text{in}}^{2(t=0)} \right) L_z \rho_d$; the corresponding (uniform) concentration of A reads:

$$c_d^A(t) = \frac{\rho_d}{M^A} \left(1 - \frac{R_{\text{in}}^{2(t=0)}}{R_{\text{in}}^2(t)} \right) \tag{6.35}$$

For the conservation of mass, as the interface expands with velocity $\mathbf{u}_\Sigma = u_\Sigma(t)\mathbf{e}_r$, the velocity of liquid that is pushed across a cylindrical boundary with radius r is:

$$u_c(r,t) = \frac{R_{\text{in}}(t)}{r} u_\Sigma(t) \tag{6.36}$$

The velocity of the interface depends on the mass transfer of species A only (since B is not soluble) and reads:

$$u_\Sigma(t) = \frac{dR_{\text{in}}}{dt} = \frac{D_c^A M^A}{\rho_d} \left(\frac{\partial c_c^A}{\partial r} \right)_{r=R_{\text{in}}} \tag{6.37}$$

The transport equation in Ω_c for species A in cylindrical coordinates (where $c_c^A(r,t)$ depends only on the radial distance and time) is:

$$\frac{\partial c_c^A}{\partial t} + u_c \frac{\partial c_c^A}{\partial r} = \frac{D_c^A}{r} \frac{\partial}{\partial r} \left(r \frac{\partial c_c^A}{\partial r} \right) \quad \text{for } r > R_{\text{in}}(t) \tag{6.38}$$

Finally, the boundary condition on the liquid side of the interface is provided by

Henry's law that, given the concentration $c_d^A(t)$ in Ω_d (equation 6.35)), reads:

$$c_c^A\left(R_{\text{in}}, t\right) = \frac{\rho_d}{M^A H_e^A}\left(1 - \frac{R_{\text{in}}^{2(t=0)}}{R_{\text{in}}^2(t)}\right) \tag{6.39}$$

whilst the value on the outer boundary is set to:

$$c_c^A\left(R_{\text{ext}}, t\right) = \frac{\rho_d}{M^A H_e^A} \tag{6.40}$$

Equations 6.36 - 6.40 represent the mathematical formulation for the problem of an expanding cylinder of gas confined by an infinite liquid annulus. However, for the specific physical properties of Case A, a simplified formulation can be obtained (see Maes and Soulaine, 2020 for more details). The magnitude of the interface velocity can be estimated from equation 6.37 by assuming:

$$u_\Sigma(t) = \frac{D_c^A M^A}{\rho_d}\left(\frac{\partial c_c^A}{\partial r}\right)_{r=R_{(in)}} \approx \frac{D_c^A}{H_e^A\left(R_{\text{ext}} - R_{\text{in}}^{t=0}\right)} \tag{6.41}$$

and for this specific case results in $u_\Sigma \approx 0.02\,\text{mm}\,\text{s}^{-1}$. Due to the low solubility of species A ($H_e^A = 100$) and the characteristic interface velocity, the concentration of A in the liquid can be assumed at a quasi-stationary equilibrium for $t > 0$ and equation 6.38 can be simplified to:

$$\frac{1}{r}\frac{\partial}{\partial r}\left(r\frac{\partial c_c^A}{\partial r}\right) = 0 \quad \text{for } r > R_{\text{in}}(t) \tag{6.42}$$

The analytical solution for the simplified problem reads:

$$c_c^A(r,t) = \frac{\rho_d}{M^A H_e^A}\left(1 - \frac{R_{\text{in}}^{2(t=0)}}{R_{\text{in}}^2(t)}\frac{\ln\left(r/R_{\text{ext}}\right)}{\ln\left(R_{\text{in}}(t)/R_{\text{ext}}\right)}\right) \quad \text{for } r > R_{\text{in}}(t) \tag{6.43}$$

$$\frac{dR_{\text{in}}}{dt} = \frac{D_c^A R_{\text{in}}^{2(t=0)}}{H_e^A R_{\text{in}}^3(t)\ln\left(R_{\text{in}}(t)/R_{\text{ext}}\right)} \quad \text{for } t > 0 \tag{6.44}$$

and equation 6.44 can be easily integrated numerically.

A summary of the numerical setup for Case A is shown in Table 6.22; the mesh level is set to $l = 8$, which corresponds to $\Delta(l) = 1.95 \times 10^{-5}\,\mathrm{mm}$, whilst the molar masses are the same for both species and equal to $M^A = M^B = 1\,\mathrm{kg\,mol^{-1}}$. The concentration profile of species A in Ω_c is initialized with equation 6.43 at $t = 0$, coherently with the assumption of solution at equilibrium at every time step. Results

Case	$L0$ (m)	$c_d^{A(t=0)}$ ($\mathrm{mol\,m^{-3}}$)	$c_d^{B(t=0)}$ ($\mathrm{mol\,m^{-3}}$)	$c_c^{A(t=0)}$ ($\mathrm{mol\,m^{-3}}$)	$c_c^{B(t=0)}$ ($\mathrm{mol\,m^{-3}}$)	H_e^A	H_e^B
A	0.005	0	1	Eq. 6.43	0	100	∞

Table 6.22: Numerical setup for a cylinder of gas expanding in an infinite liquid annulus.

are made non-dimensional with the reference length $L_{\mathrm{ref}} = R_{\mathrm{ext}}$, time $t_{\mathrm{ref}} = \rho_c R_{\mathrm{ext}}^2/\mu_c$ and concentration $c_{\mathrm{ref}} = \rho_d/M^A$, whilst the reference velocity follows from $U_{\mathrm{ref}} = L_{\mathrm{ref}}/t_{\mathrm{ref}}$; these parameters are reported in Table 6.23.

L_{ref} (m)	t_{ref} (s)	U_{ref} ($\mathrm{m\,s^{-1}}$)	c_{ref} ($\mathrm{mol\,m^{-3}}$)
0.001	1	0.01	1

Table 6.23: Reference dimensions for a cylinder of gas expanding in an infinite liquid annulus.

The numerical simulation is run for a time of $\Delta t = 5\,\mathrm{s}$ and the result in terms of interface position (R_{in}) is compared against the analytical solution (equation 6.44) in Figure 6.24, where a good accuracy is found. It is noted that the global displacement at the end of the simulation is approximately $\Delta R_{\mathrm{in}}^{t=5\,\mathrm{s}} \approx 0.12\,\mathrm{mm}$, which is reasonably close to the prediction of equation 6.41, i.e. $u_\Sigma \Delta t = 0.1\,\mathrm{mm}$.

The concentration profiles of species A along the radial direction at four different times are reported in Figure 6.25 and compared against the analytical solutions of equation 6.35 and equation 6.43 for $r < R_{\mathrm{in}}$ and $R_{\mathrm{in}} < r < R_{\mathrm{ext}}$, respectively. The distribution is discontinuous at $r = R_{\mathrm{in}}$ (Henry's Law) and the concentration

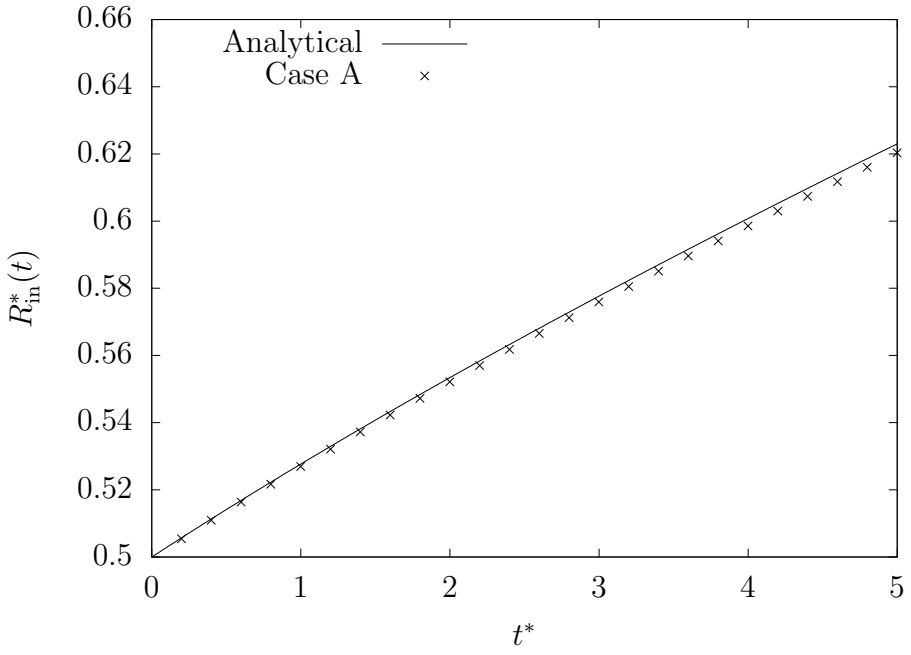

Figure 6.24: Inner radius of the liquid annulus Vs time for Case A.

is uniform in the gaseous phase ($r < R_{\text{in}}$), confirming thus the assumption behind equation 6.35.

Contours of gas concentration for species A and B are presented in Figure 6.26 at two different times and show how the amount of species A increases in Ω_d as the cylinder expands, whilst the concentration of B decreases accordingly. Due to the symmetry of the problem, the interface is always circular at any time $t > 0$.

In the case considered so far (Case A), the only transferable species between the gaseous and liquid phases is species A. In a more general scenario, both species are soluble and can be transported across the interface. In the case of competing mass transfer, the transport of species A and B might occur in opposite directions and the resulting phase volume change takes into account both mass transfers. To test the accuracy of the proposed methodology, four cases of competing mass transfer proposed in Maes and Soulaine, 2020 are tested here. The gaseous region is initially composed of species B only, whilst the liquid phase contains the solvent (not soluble

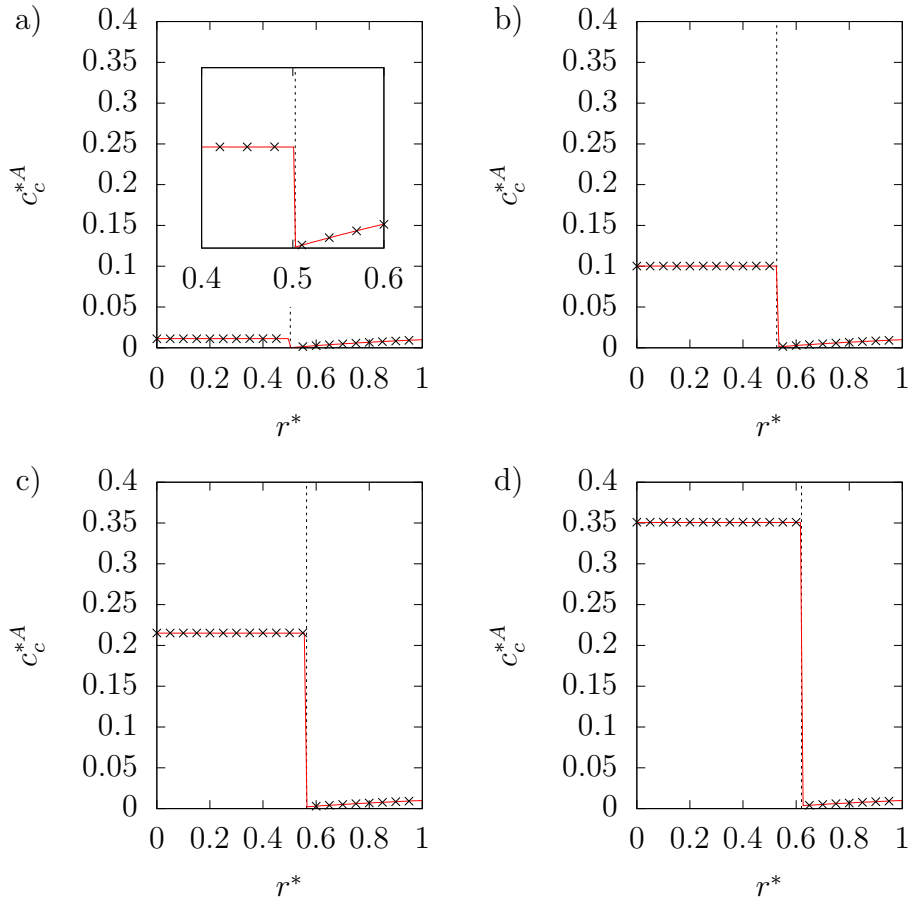

Figure 6.25: Radial concentration profiles of species A at $t^* = 0.1$ (a), $t^* = 1$ (b), $t^* = 2.5$ (c) and $t^* = 5$ (d) for Case A. Crosses represent the numerical solution, whilst the continuous red line is the analytical one. The vertical dotted line shows the interface location, i.e. $r = R_{\text{in}}$.

in Ω_d) and species B at the chemical equilibrium, i.e. $c_c^{B(t=0)} = \rho_d / \left(M^B H_e^B\right)$. The initial concentration of A is set to null everywhere, but the concentration values at the external boundary are $c_c^A(R_{\text{ext}}, t) = \rho_d / \left(M^A H_e^A\right)$ and $c_c^B(R_{\text{ext}}, t) = 0\,\text{mol}\,\text{m}^{-3}$. The system is initially at chemical equilibrium since both saturation ratios are equal to one (i.e. $\zeta^A = \zeta^B = 1$); however, the jump in the concentrations between the liquid phase and the outer border activates an outflow for species B and an inflow for species A (i.e. B diffuses out of the domain, whilst A diffuses into it) that take

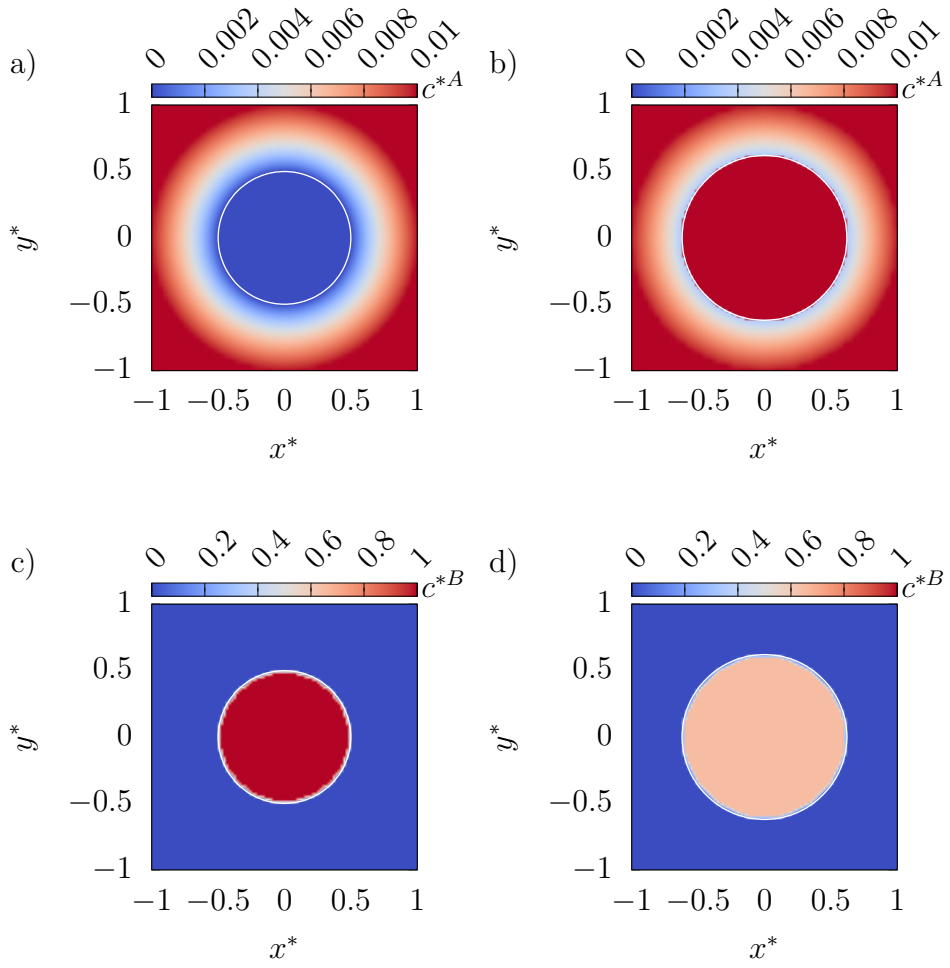

Figure 6.26: Contours of concentration for species A at $t^* = 0$ (a), $t^* = 5$ (b) and species B at $t^* = 0$ (c), $t^* = 5$ (d) for case A. The gaseous region is initially composed of B only, then the concentration of A increases (due to the mass transfer) and B decreases accordingly.

the system far from equilibrium (i.e. $\zeta^A = \zeta^B \neq 1$). At this point, the interface evolves (radially) in order to re-establish the chemical equilibrium. The diffusivity is the same as Case A and so are the geometry of the annulus and the grid refinement. Different solubilities are tested here and a summary of the cases is shown in Table 6.24. It is worth noting that, since the solubility has been increased from Case A and

Case	$L0$ (m)	$c_d^{A(t=0)}$ ($\mathrm{mol\,m^{-3}}$)	$c_d^{B(t=0)}$ ($\mathrm{mol\,m^{-3}}$)	$c_c^{A(t=0)}$ ($\mathrm{mol\,m^{-3}}$)	$c_c^{B(t=0)}$ ($\mathrm{mol\,m^{-3}}$)	H_e^A	H_e^B
B	0.005	0	1	0	1	1	1
C	0.005	0	1	0	1	2	1
D	0.005	0	1	0	0.5	1	2
E	0.005	0	1	0	0.5	2	2

Table 6.24: Numerical setup for a cylinder of gas confined by a liquid annulus.

both species can be transferred across the interface, the analytical model of equations 6.43 - 6.44 is no longer valid for these cases.

The results for cases B, C, D and E are shown in Figure 6.27. For all the cases, the mass fraction of B is initially one $\left(m_d^{B(t=0)} = 1\right)$ whilst the mass fraction of species A is null $\left(m_d^{A(t=0)} = 0\right)$, since B is the only component that exists in Ω_d at $t = 0$. As some of species A flows into the gaseous region and species B is transferred to the liquid domain, the chemical composition of the binary mixture changes and the mass fraction of A increases, whilst the concentration of B in Ω_d decreases. For each plot in Figure 6.27, the total mass fraction for Ω_d (i.e. $m_d^{\mathrm{tot}} = m_d^A + m_d^B$) is reported and is shown that the mass is conserved, i.e. $m_d^{\mathrm{tot}} = 1$ for $t > 0$.

The system evolves towards the equilibrium, where no species B exists in the domain (coherently with the boundary condition at $r = R_{\mathrm{ext}}$, i.e. $c_c^B(R_{\mathrm{ext}}, t) = 0$) and the concentration of A in the liquid is $c_c^{A,\mathrm{eq}} = \rho_d / \left(M^A H_e^A\right)$. In cases B and E (Figure 6.27a and Figure 6.27d respectively), the solubility of the species is the same and the problem is symmetric, since $c_c^{A,\mathrm{eq}} = c_c^{B(t=0)}$. As a result, the mass transfer rate of A across the interface has the same magnitude but opposite direction of species B and the dimension of the gaseous region (R_{in}) remains constant. The only difference between these two cases is the velocity at which the competing mass transfer occurs. In Case E, the diffusive flux that brings B out of the domain (and A into the liquid region) is smaller than Case B, since the initial concentrations in the liquid region are $c_c^{B(t=0)} = 0.5\,\mathrm{mol\,m^{-3}}$ and $c_c^{B(t=0)} = 1\,\mathrm{mol\,m^{-3}}$ for cases E and B respectively, whilst the value at the outer boundary is null for both cases. This is

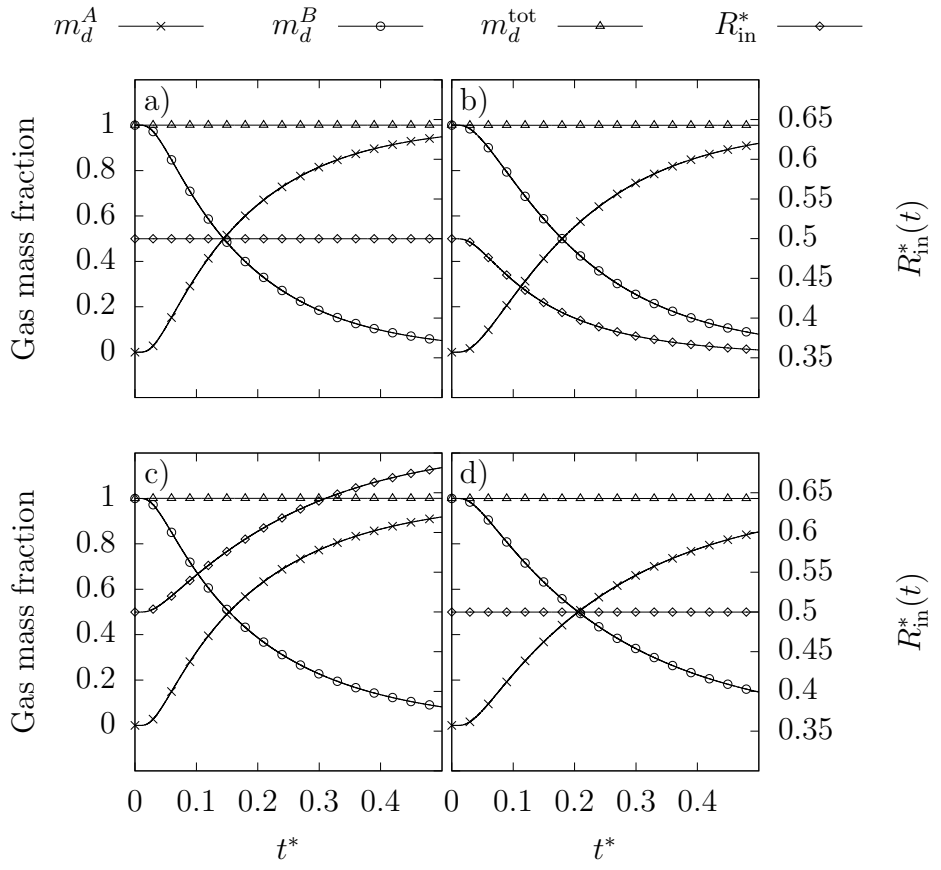

Figure 6.27: Plot of mass fractions in Ω_d and radius R_{in} Vs time for Case B (a), Case C (b), Case D (c) and Case E (d).

evident in Figure 6.27a and Figure 6.27d, where the time required by the system to reach the point $m_d^A = m_d^B = 0.5$ is $t^* = 0.144$ and $t^* = 0.206$ for Case B and Case E respectively.

In Case C (Figure 6.27b), the solubility of the species is different and the concentration of species A in Ω_c at the equilibrium point is $c_c^{A,\text{eq}} = 0.5\,\text{mol}\,\text{m}^{-3} < c_c^{B(t=0)}$. The overall amount of moles of species A that needs to be introduced into the domain is therefore smaller than the number of moles of B that exists at $t = 0$. Therefore, the competing mass transfer results in a net flux of mass out of the domain and the

radius of the gaseous region decreases accordingly. The opposite scenario occurs in Case D (Figure 6.27c), where the net flux of mass is driven by species A and the gaseous cylinder expands.

Finally, a comparison of these cases with the results of Maes and Soulaine, 2020 is reported in Figure 6.28 for the mass fractions in Ω_d and the radius R_{in}. A good comparison is achieved for all the cases, where the trend of the plots matches the reference data for all the plotted variables, although some quantitative differences are visible.

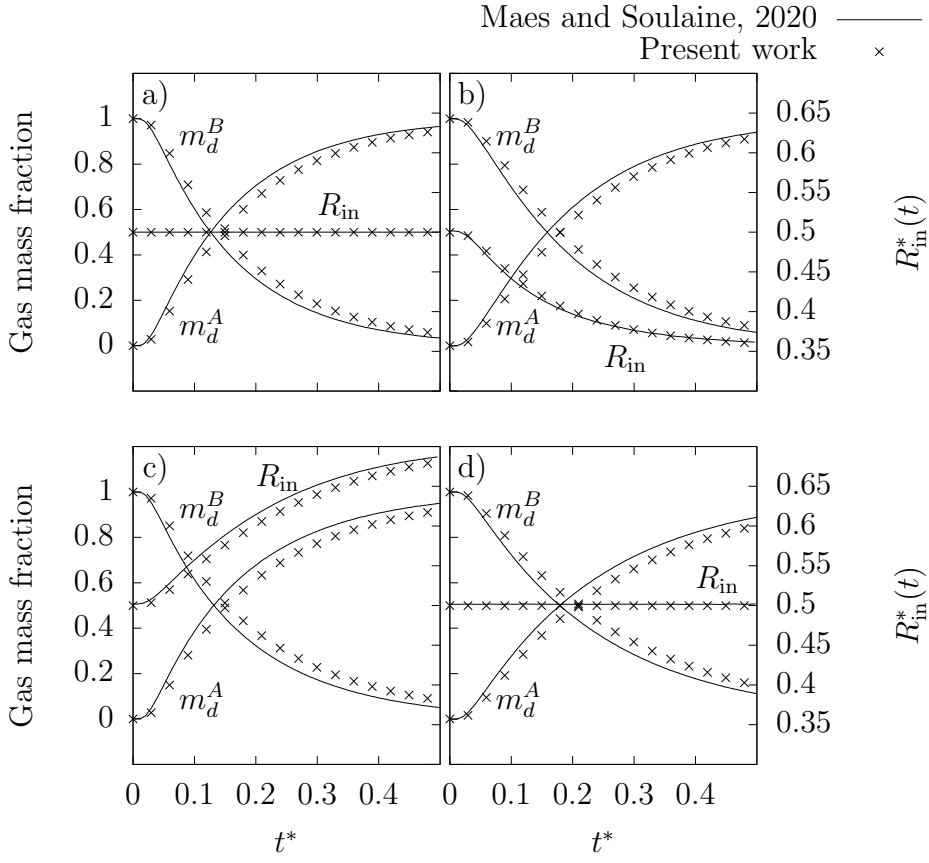

Figure 6.28: Comparison between the present work and the results in Maes and Soulaine, 2020 for Case B (a), Case C (b), Case D (c) and Case E (d).

6.3.2 Competing mass transfer in a rising bubble

In this section, the competing mass transfer amongst multiple soluble species for a rising bubble is considered. This is a common scenario in industrial applications, where several species or contaminants are present in both phases and are transferred in both directions, i.e. from the disperse phase to the continuous one and vice versa. To get an accurate prediction of the phase volume change, all the individual mass transfers need to be taken into account. Here, the test case proposed in the numerical work of Fleckenstein and Bothe, 2015 is reproduced, where a bubble rises in a large domain and three different soluble species are involved into the conjugate mass transfer process. A similar (experimental) investigation, but for bubbles rising in a vertical pipe, is presented in Hosoda et al., 2015.

The properties of the gas-liquid system used for the present test case are reported in Table 6.25. The soluble species that exist in the present model are: CO_2, N_2 and

Phase	Density $(\mathrm{kg\,m^{-3}})$	Viscosity $(\mathrm{N\,s\,m^{-2}})$	σ $(\mathrm{N\,m^{-1}})$
Liquid	997	8.9×10^{-4}	0.072
Gas	1.962	1.445×10^{-5}	

Table 6.25: Gas-liquid properties for the competing mass transfer in a rising bubble.

O_2; the respective properties are reported in Table 6.26. In order to speed up the

Species	Diffusivity in Ω_c $(\mathrm{m^2\,s^{-1}})$	Diffusivity in Ω_d $(\mathrm{m^2\,s^{-1}})$	M $(\mathrm{kg\,mol^{-1}})$	H_e	Sc
CO_2	1.9×10^{-8}	1.9×10^{-6}	0.044	1.20	46.98
N_2	2.0×10^{-8}	2.0×10^{-6}	0.028	67.0	44.63
O_2	2.3×10^{-8}	2.3×10^{-6}	0.032	31.5	38.81

Table 6.26: Gas-liquid properties for the competing mass transfer in a rising bubble.

volume change process and reduce the computational time of the simulation, the diffusivity for all the species in the liquid domain $\left(D_c^k\right)$ has been increased by a

factor of 10 with respect to the real physical property (the same approach is used in the reference case of Fleckenstein and Bothe, 2015); the corresponding diffusivity in the disperse phase $\left(D_d^k\right)$ is assumed to be 100 times larger than the continuous one $\left(\text{i.e. } D_d^k = D_c^k \times 10^2\right)$. The solubility of CO_2 is significantly larger than the solubility of the other species (lower Henry's law coefficient), which means that for the same concentrations in both phases, the mass transfer from the gaseous region to the liquid (under-saturated solutions) occurs faster for CO_2, than N_2 and O_2; the opposite scenario occurs for super-saturated solutions, where the transfer from the continuous phase to the liquid one is quicker for N_2 and O_2 than CO_2. In Table 6.26, the Schmidt numbers are computed with the liquid properties reported in Table 6.25 and are similar for all the species, since the diffusivity of each component doesn't change significantly.

The initial diameter of the bubble is set to $D_b^{t=0} = 0.8\,\text{mm}$ and the bubble is confined in a large domain with $L0 = 48\,\text{mm}$ where it rises under the effect of the gravitational field $g = 9.81\,\text{m}\,\text{s}^{-2}$. Due to the large dimension of the domain compared to the bubble size, end walls effect do not affect the dynamics of the bubble in the present case. The Galilei and Bond numbers are $Ga = 79.39$ and $Bo = 0.0869$ respectively and, for these parameters, the bubble is expected to rise vertically, keeping the original spherical shape. Therefore, a 2D axisymmetric model is used here, where only half of the bubble is considered, and the rising trajectory is the horizontal $x-$axis, i.e. $\mathbf{g} = -g\mathbf{e}_x$. An outflow condition is applied to the right boundary to allow the liquid enter/leave the domain as the bubble volume changes, whilst symmetric conditions are used for the other boundaries; adaptive mesh refinement is used to keep the grid at the finest level around the bubble and save computational cells far from the interface. Results are made non-dimensional with the reference length $L_{\text{ref}} = R_b^{t=0}$, time $t_{\text{ref}} = \sqrt{L_{\text{ref}}/g}$ and the gaseous concentration in Ω_d if the bubble is composed of CO_2 only, i.e. $c_{\text{ref}} = \rho_d / M^{CO_2}$; a summary of the reference values is reported in Table 6.27. To reproduce a competing mass transfer scenario, where the soluble species are transferred across the interface in opposite directions, a mixed under- and super-saturated liquid solution is used. The bubble is initially composed of CO_2 only (i.e. $c_d^{CO_2(t=0)} = 44.59\,\text{mol}\,\text{m}^{-3}$), whilst the liquid

L_{ref} (m)	t_{ref} (s)	U_{ref} (m s^{-1})	c_{ref} (mol m^{-3})
0.0004	0.00639	0.0626	44.59

Table 6.27: Reference dimensions for the competing mass transfer in a rising bubble.

solution is composed by the solvent (not soluble in Ω_d) and species N_2, O_2 with concentrations $c_c^{N_2(t=0)} = 0.51\,\text{mol m}^{-3}$ and $c_c^{O_2(t=0)} = 0.27\,\text{mol m}^{-3}$. The solution is therefore under-saturated for CO_2 $\left(\zeta^{CO_2} = 0\right)$ and super-saturated for the other species $\left(\zeta^{N_2}, \zeta^{O_2} > 0\right)$.

A mesh sensitivity study is first performed to evaluate the level of grid refinement that is necessary to reach a mesh independent solution and a list of the cases with the relative setup is shown in Table 6.28. The simulations are run for a time interval of

	Case A	Case B	Case C	Case D
$D_b^{t=0}$ (m)	0.0008	0.0008	0.0008	0.0008
$L0$ (m)	0.048	0.048	0.048	0.048
$l^{\max}$	13	14	15	16
$\Delta(l^{\max})$ (m)	5.86×10^{-6}	2.93×10^{-6}	1.46×10^{-6}	7.32×10^{-7}
cells/$D_b^{t=0}$	136	273	546	1092
$c_d^{CO_2}$ (mol m^{-3})	44.59	44.59	44.59	44.59
$c_d^{N_2}$ (mol m^{-3})	0	0	0	0
$c_d^{O_2}$ (mol m^{-3})	0	0	0	0
$c_c^{CO_2}$ (mol m^{-3})	0	0	0	0
$c_c^{N_2}$ (mol m^{-3})	0.51	0.51	0.51	0.51
$c_c^{O_2}$ (mol m^{-3})	0.27	0.27	0.27	0.27

Table 6.28: Grid convergence study for the competing mass transfer in a rising bubble. The concentrations in both phases refer to the initial ($t = 0$) chemical composition.

$\Delta t = 0.25\,\text{s}$ and results in terms of phase volume change for the bubble are shown in Figure 6.29. The grid convergence analysis shows that a mesh independent solution is reached for the grid level $l = 15$ (Case C), which corresponds to approximately 546

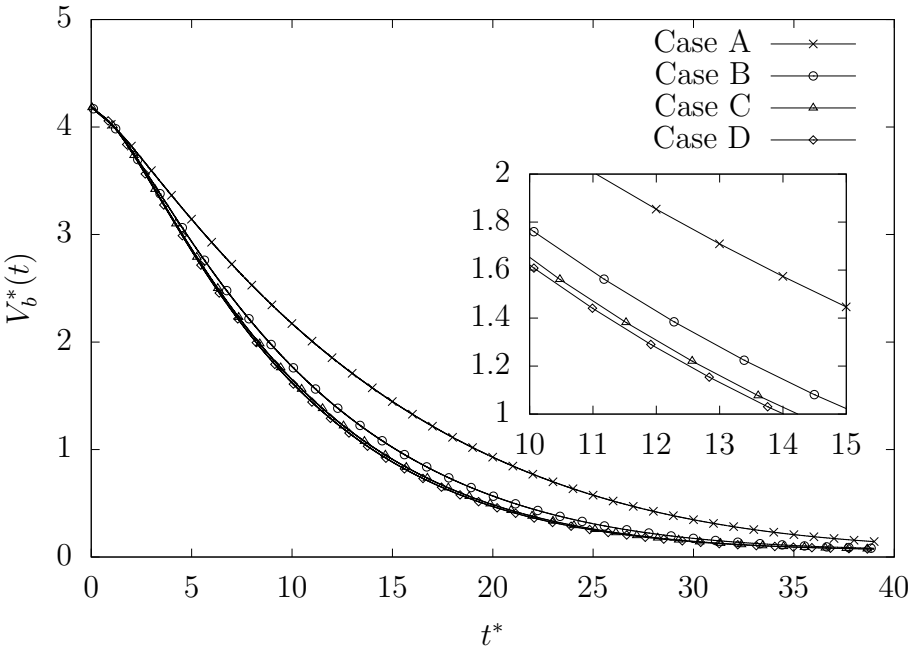

Figure 6.29: Grid convergence for the competing mass transfer in a rising bubble. Plot of bubble volume Vs time.

cells per diameter at $t = 0$. For the selected chemical composition of the liquid and gaseous phases, CO_2 is transferred from the bubble to the liquid (under-saturation), whilst N_2 and O_2 flow in the opposite direction (super-saturation). Due to the larger solubility of CO_2 compared to the other species and the weak super-saturation ratios for N_2 and O_2, the competing mass transfer is dominated by CO_2 and results in a net flow of mass out of the bubble; the phase volume decreases accordingly. The volume reduces almost linearly in the first part of the simulation (until $t^* \approx 10$), where the mass transfer is driven by CO_2 and the concentration of N_2 and O_2 are still marginal. As the chemical composition inside the bubble changes and the mass fractions of N_2 and O_2 become more relevant, the volume change rate decreases and becomes almost negligible for $t^* > 30$. If the simulation was run for $\Delta t^* > 40$, the volume change would have reached a minimum and, after that, started to increase as the mass fraction of CO_2 in Ω_d becomes irrelevant, whilst N_2 and O_2 keep flowing

towards the bubble. Since the solution is mesh independent with $l = 15$, Case C is used in the following part of the analysis.

Due to the phase volume change, the dynamics of the bubble never reaches a steady-state regime. The plot of the bubble rising velocity U_b, along with the Péclet numbers for the soluble species, is shown in Figure 6.30. The bubble accelerates from

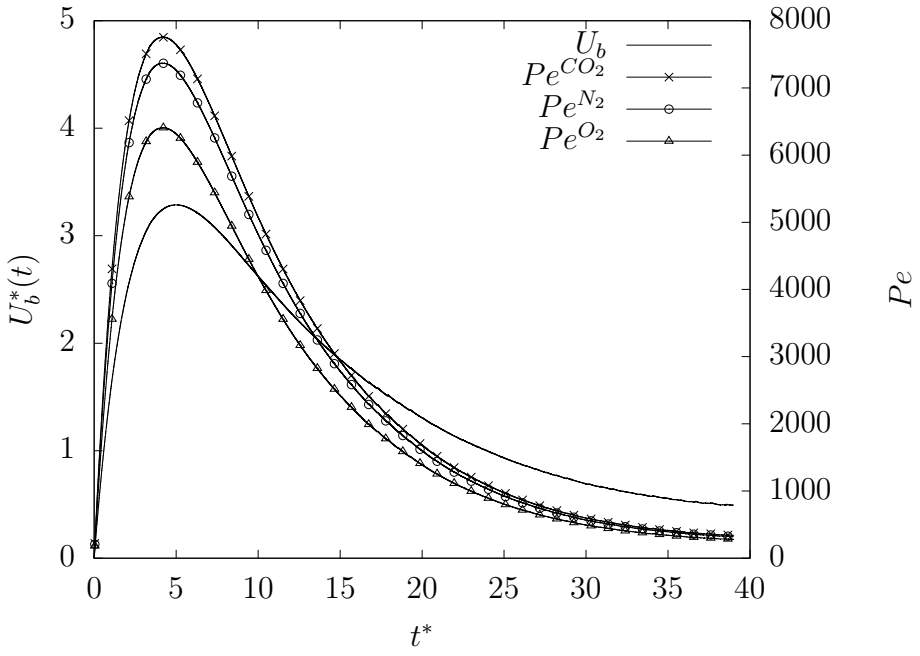

Figure 6.30: Plot of bubble rising velocity and species Péclet numbers Vs time for Case C.

rest until $t^* \approx 6$, where the maximum velocity is reached, and then decelerates as a consequence of the decrease in volume and in the corresponding buoyancy force. The Péclet numbers are computed based on the time dependent bubble diameter $D_b(t)$ and the maximum value is reached for CO_2 at $t^* \approx 6$, where $Pe^{\mathrm{CO_2}} \approx 7800$. The plots of the rising velocity and Péclet numbers have a similar shape, since $Pe^k = Re_b Sc^k$ and the Reynolds number is directly proportional to U_b; however, the curves for Pe are not exactly a scaled version of $U_b(t)$, since the bubble diameter used for the computation of Re_b is time dependent. The results in terms of grid sensitivity are

consistent with the analysis performed in section 6.2.4 for pure bubbles rising at different Péclet numbers in an under-saturated solution ($\zeta = 0$). Although in the present case the competing mass transfer amongst multiple species in a mixed under- and super-saturated solution is considered, the conjugate mass transfer is dominated by CO_2 for which the saturation ratio is null. Therefore, a direct comparison with the previous results for pure bubbles is possible and in that case (where the volume change of the bubble was not taken into account) a mesh independent solution was obtained with 546 cells per bubble diameter at the terminal (steady) $Pe = 4650$ (see Table 6.17). In the present case of competing mass transfer, the maximum Péclet has the same order of magnitude of the steady Pe for the pure species case, and the same mesh resolution with 546 cells per (initial) diameter is needed to reach a grid independent solution (Case C, see Table 6.28). This result suggests that in the case of mixtures where a single species dominates the competing mass transfer (e.g. pure bubbles in slightly contaminated solutions), useful information in terms of grid requirements can be obtained from the equivalent pure species case, without the need to take into account the actual phase volume change.

Results in terms of chemical composition of the bubble are shown in Figure 6.31 for Case C. The bubble is initially composed of CO_2 only, therefore the mass fractions (equation 6.33) are $m_d^{CO_2(t=0)} = 1$ and $m_d^{N_2(t=0)} = m_d^{O_2(t=0)} = 0$. As the phase change process occurs, CO_2 is transferred to the liquid, whilst the other species flow across the interface in opposite directions; the mass fraction of CO_2 decreases, whilst the fractions of the other species increase accordingly. Due to the lower solubility of N_2 compared to O_2 and larger initial concentration in the liquid phase ($c_c^{N_2(t=0)} > c_c^{O_2(t=0)}$ see Table 6.28), the mass fraction of N_2 grows faster than O_2 and reaches the same value of the fraction of CO_2 at $t^* \approx 34.8$ and becomes the most relevant component of the bubble for $t^* > 34.8$. The fraction of O_2 equals CO_2 at $t^* \approx 37.7$ and CO_2 becomes the most marginal species at the end of the simulation. The sum of the mass fractions is reported in Figure 6.31, which shows that the method is mass conservative since the global mass fraction is always $m_d^{CO_2} + m_d^{N_2} + m_d^{O_2} = 1$ for $t > 0$.

To validate the accuracy of the numerical methodology developed within the

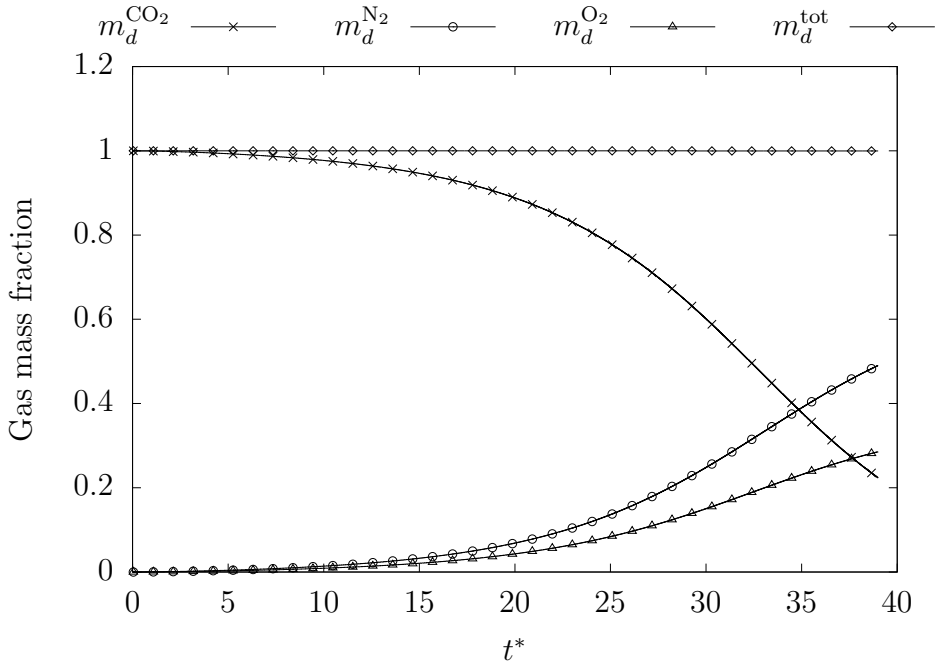

Figure 6.31: Species mass fractions Vs time for Case C.

present thesis, results are compared with the work of Fleckenstein and Bothe, 2015, where the setup for this case was taken from. In the reference of Fleckenstein and Bothe, 2015, the mesh density corresponds to approximately 102 cells per (initial diameter), which is similar to the grid refinement used for Case A in the present work (see Table 6.28). Case A is therefore used for the comparison against the reference case and results in terms of volume and mass fractions of the bubble are reported in Figure 6.32. A good comparison is obtained for all the plotted quantities, which confirms that the proposed methodology is able to deal with the complex case of competing mass transfer in moving bubbles. However, it is worth reminding here that the solution is not mesh independent for Case A and that quantitative differences are clearly visible when Case A is compared against Case C (e.g. in Case A, CO_2 is the major component of the bubble for the whole simulated time, whilst in Case C is the minor one at the end of the simulation).

A qualitative representation of the problem is shown in Figure 6.33, where the

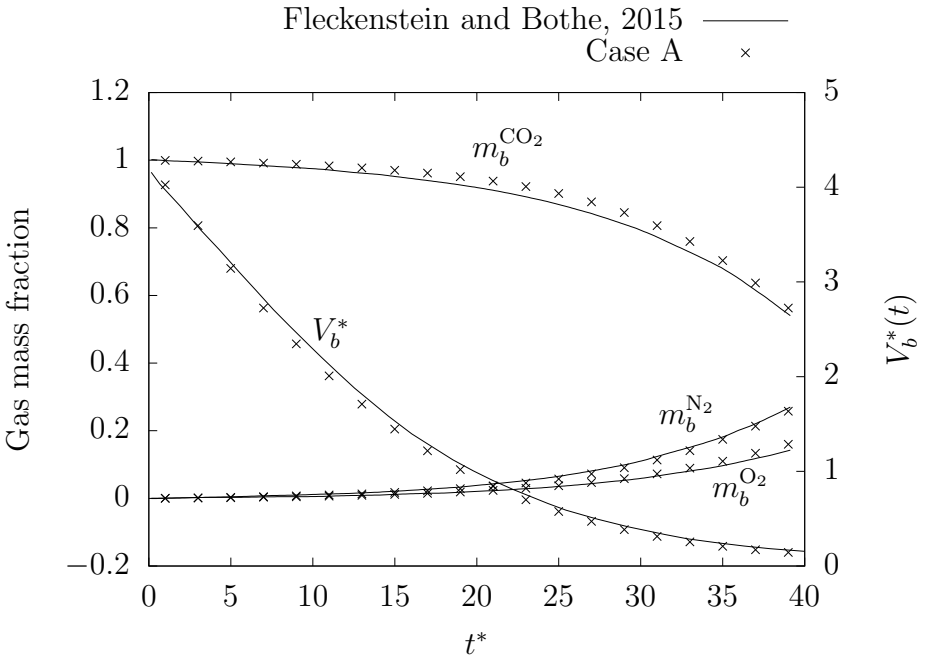

Figure 6.32: Comparison between the work of Fleckenstein and Bothe, 2015 and Case A for the bubble volume and mass fractions.

concentrations of the three soluble species are compared at two different times. At $t^* = 4$, the bubble is mainly composed of CO_2 (Figure 6.33a), whilst the other components have a marginal fraction (Figure 6.33c and Figure 6.33e). The typical distribution of species concentration around a dissolving rising bubble is clearly visible for CO_2: the concentration boundary layer is confined within a thin region on top of the bubble and its thickness increases towards the rear of the bubble, where the transport mechanisms of diffusion and advection occur in different directions. A similar, but symmetric, distribution in the liquid region occurs for N_2 and O_2. In this case, due to the super saturated solution $\left(\zeta^{N_2}, \zeta^{O_2} > 1\right)$, the concentration profiles have their maximum (constant) value in the bulk liquid and reach a minimum at the interface. The near wake of the bubble is therefore characterized by a low concentration region for these species. As the competing mass transfer process develops, the concentration of CO_2 within the bubble reduces (Figure 6.33b), whilst

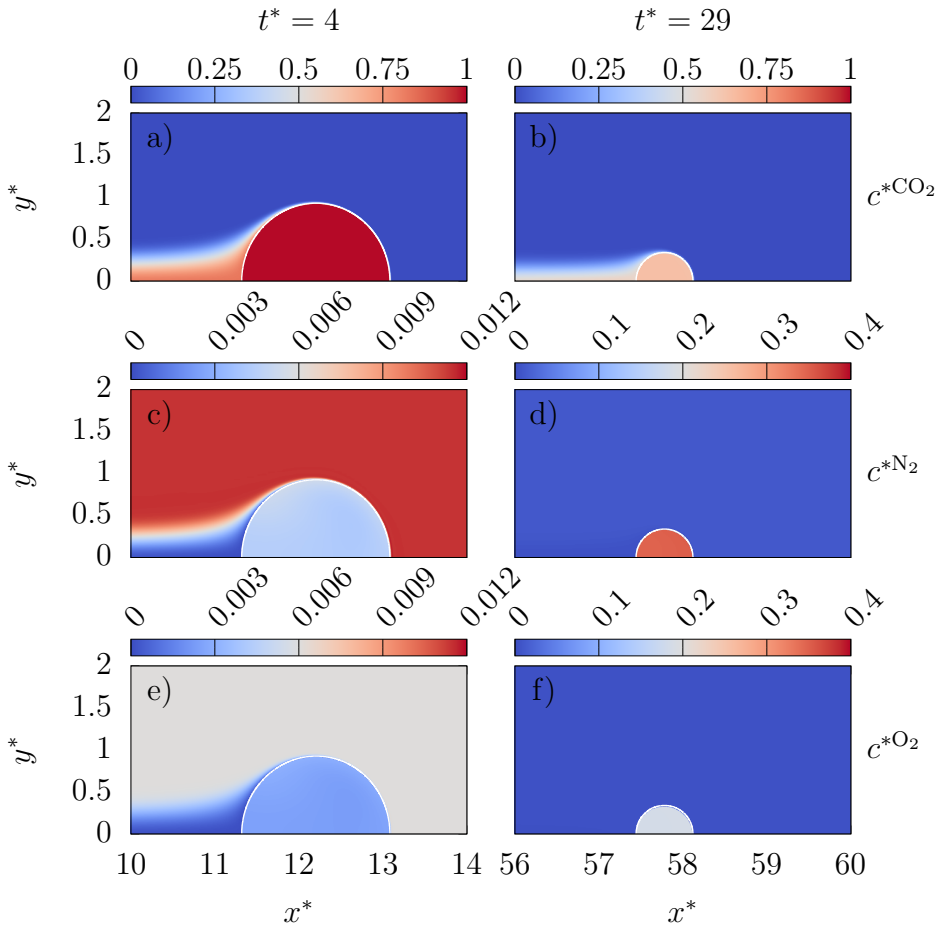

Figure 6.33: Contours of concentration at $t^* = 4$ (left) and $t^* = 29$ (right) for CO_2 (a, b), N_2 (c, d) and O_2 (e, f).

the other components increase their fractions (Figure 6.33d and Figure 6.33f). Consistently with the Galilei and Bond numbers for this specific case, the bubble retains its spherical shape and, due to the larger diffusivity in the gaseous phase than the liquid one, the concentrations in Ω_d can be reasonably assumed constant at every time $t > 0$.

Finally, the profiles along the equatorial line are plotted in Figure 6.34 at $t^* = 4$ and $t^* = 29$, where the typical interfacial concentration profiles for soluble species in under- (CO_2) and super- (N_2, O_2) saturated solutions can be easily recognised. For

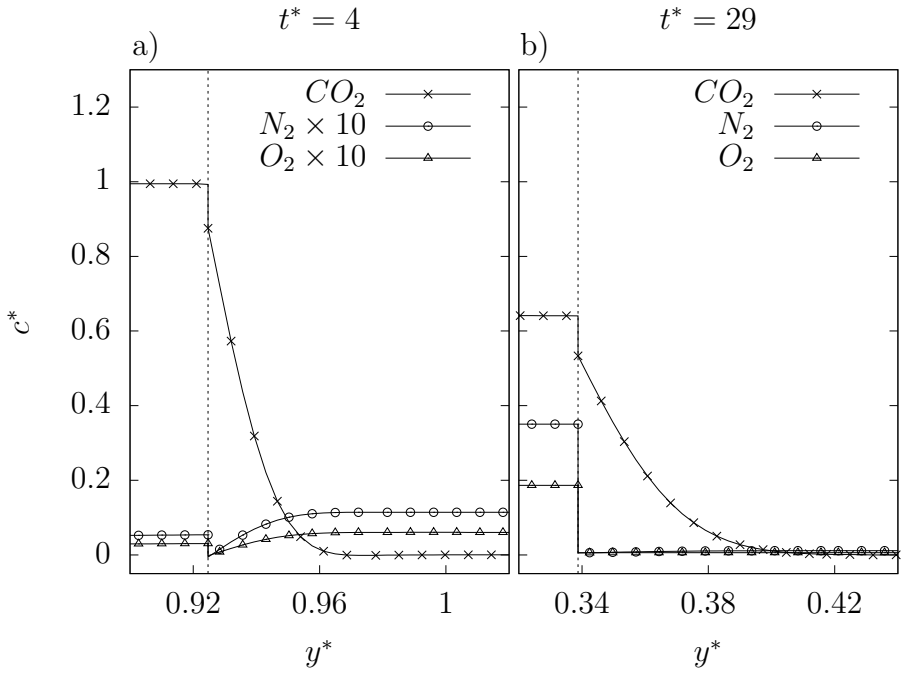

Figure 6.34: Equatorial concentration profiles Vs time for the soluble species at $t^* = 4$ (a) and $t^* = 29$ (b). The vertical dotted lines represent the location of the interface Σ. All the profiles are discontinuous at $y = y_\Sigma$ due to the different solubility of species in the liquid phase.

the first part of the simulation, the concentration of N_2 and O_2 inside the bubble is still marginal and the corresponding profiles have a (constant) bulk value in the liquid phase larger than the gaseous one (Figure 6.34a). As the simulation progresses, the concentrations of N_2 and O_2 in Ω_d get closer to CO_2, and their values become larger than the respective bulk liquid ones (Figure 6.34b). The slope of the profiles at the interface is directly related to the individual mass transfer rates. As the bubble dissolves, the interfacial gradients of concentration decrease due to the increase of the boundary layer thickness (this is evident by comparing Figure 6.34a and Figure 6.34b for CO_2) and the respective species mass transfer rates decrease accordingly.

Finally, it is important to remind here that the present modelling approach is based on the assumption of incompressible (constant) phase densities. However, in case of mixtures and competing mass transfer, the chemical composition of bub-

bles changes over time and the gaseous density should be updated accordingly, since species have different properties. This is currently not performed here and, therefore, a potential improvement to the present numerical method would be the implementation of a compressible disperse phase, where the variable density is related to the composition of the mixture through an equation of state (e.g. ideal gas law for mixtures).

Chapter 7

Applications

In this section, the numerical methodology developed within the present thesis is employed for the modelling of industrially relevant applications. Standard numerical tools used for the design of complex systems are generally based on average models (e.g. RANS) due to the large cost of high-fidelity computations. The goal of this section is to show how Direct Numerical Simulations can be used to inform the development of industrial systems. The focus is on the design of chemical reactors where diffusion-driven mass transfer processes occur. The section is organized as follows: the case of hydrogen bubbles growing in electrochemical cells is studied in section 7.1, whilst mass transfer in two-phase Taylor-Couette reactors is discussed in section 7.2.

7.1 Growing bubbles on planar electrodes

In this section, the growth of electrochemically generated bubbles on planar electrodes is investigated. In electrochemical reactors, the voltage difference between electrodes drives an electric current through the electrolytic solution that activates non-spontaneous chemical reactions. A product of these reactions is typically a gas molecule (e.g. in the electrolysis of water, H_2O is split into oxygen and hydrogen), which is generated next to the electrode wall. As the reaction occurs, a locally

super-saturated solution ($\zeta > 1$) develops near the electrodes and drives the growth of gaseous bubbles on the surface. Bubbles tend to nucleate from microscopic pits on the wall surface (heterogeneous nucleation), where some of the molecules are trapped and form gaseous pockets. As the solution becomes locally super-saturated, the dissolved gas molecules diffuse from the liquid solution to the gaseous sites, and the volume of the pockets increases accordingly, leading eventually to the formation of bubbles. This phenomenon is of great relevance for the design of electrochemical cells, since the presence of bubbles can significantly affect the performance of this type of reactors. When bubbles form on the wall surface, they reduce the active (uncovered) area of the electrodes and induce a non uniform current density in the electrolytic solution. Due to the lower electrical conductivity of the gaseous phase with respect to the liquid one, the presence of bubbles impedes the transport of ions across the reactor cell and the effective resistance of the solution increases. All theses phenomena have a negative effect on the reactor performance and a deep understanding of these processes is fundamental to improve the design of such systems. Due to the complexity of the phenomenon and their multi-physics nature, direct numerical simulation is a valuable tool for the investigation of these processes and can provide detailed information for the improvement of engineering design tools. For a review on the effects of bubbles on electrochemical reactors, the reader is referred to Angulo et al., 2020, whilst a review on bubble generation mechanisms and their management in microfluidic devices can be found in Pereiro et al., 2019.

Here the experimental setup used in the work of Glas and Westwater, 1964 for the study of the growth of hydrogen bubbles on planar electrodes is replicated. In this work, the authors investigate several parameters that can affect the nucleation of bubbles (e.g. current density, electrode dimension and materials, etc) and report a comprehensive study on the growth rates of electrolytic bubbles. The experimental apparatus consists of a wire with a small diameter whose flat end is used as an electrode where bubbles are generated. Different diameters and materials are tested, and the tip of the electrode is immersed into an electrolytic solution. A high speed camera is used to capture images of the growing bubbles and to measure their growth rates and contact angles. A previous numerical study that replicates the same ex-

perimental setup is available in Liu et al., 2016, where the authors combine a VOF method with empirical correlation models for the mass transfer coefficient. In the present work, a direct simulation approach is used and the concentration boundary layer around the interface is fully resolved; the mass transfer follows from the gradient of concentration and no models are used for its prediction.

The properties of the gas-liquid (G-L) systems used in the experiments (Exp) of Glas and Westwater, 1964 and in the present work (Num) are reported in Table 7.1. The large density ratio between the electrolytic solution and hydrogen in the

Phase	Density ($\mathrm{kg\,m^{-3}}$)	Viscosity ($\mathrm{N\,s\,m^{-2}}$)	Diffusivity ($\mathrm{m^2\,s^{-1}}$)	M ($\mathrm{kg\,mol^{-1}}$)	σ ($\mathrm{N\,m^{-1}}$)
L(Exp)	996	8.32×10^{-4}			7.5×10^{-2}
L(Num)	996	8.32×10^{-4}			7.5×10^{-6}
G(Exp)	0.08	8.96×10^{-6}	7.38×10^{-9}	0.002	
G(Num)	0.8	8.96×10^{-6}	7.38×10^{-9}	0.02	

Table 7.1: Gas-liquid properties for a rising bubble in a creeping flow.

experiments ($\rho_c/\rho_d = 12450$) is observed to slow down the implicit solver (multigrid algorithm, see chapter 4.3) of the Navier-Stokes solver; for this reason, the density of the disperse phase has been increased by a factor of 10 in the present simulations. Such change in the density ratio is not expected to affect the dynamics of the bubble, as the present study is limited to the growth stage of bubbles attached to the planar electrode and the movement of the interface is mainly determined by the phase-change process. However, even in the case of rising bubbles, the effect of such change in the density ratio does not affect significantly the general behaviour of the bubbles (e.g. terminal velocity, rising trajectory), as reported in the work of Bunner and Tryggvason, 2002. Since the (uniform) molar concentration and species density in Ω_d are related through the formula $c_d = \rho_d/M$, the molar mass of the soluble species has been increased by the same factor used for the density. In this way, the concentration field from the simulations is directly comparable with the experiments and the corresponding volume change is consistent ($\Delta V_d \propto M/\rho_d$). Due to the small length scales that characterize the experiments, where typical bubble

radius are of the order of $R_b \approx 10^{-1}\,\mathrm{mm}$, the surface tension force prevails over gravity (large interfacial curvature) as long as the bubble is attached to the wall (i.e. the growth stage) and the spherical shape of the interface is preserved. A very fine mesh is then required to resolve the interface dynamics (small bubble radius) and the time step must be small enough to capture the oscillation of the smallest capillary wave. This results in a strong limitation on the maximum time step that can be used to ensure the stability of the numerical (explicit) scheme (see the CFL condition of the Navier-Stokes solver, equation 4.47) and makes the cost of the computations significantly expensive. Therefore, to reduce the computational cost, the surface tension coefficient has been decreased by a factor of 10^{-4} and gravity is neglected. The reduced surface tension, in absence of gravity, is large enough to keep the bubbles in a spherical shape and the simulations are representative of the experimental growth stage, during which the bubbles are still attached to the electrode; the detachment and the following rising regime are not modelled here. The solubility of hydrogen in the electrolytic solution (Henry's law coefficient) is set to $H_e = 53.3$.

The production of dissolved hydrogen (H_2) at the electrode wall is given by Faraday's law:

$$\mathbf{N}^{\mathrm{H_2}} = \frac{I}{2F}\mathbf{n} \tag{7.1}$$

where $\mathbf{N}^{\mathrm{H_2}}$ is the molecular flux of hydrogen ($\mathrm{mol\,m^{-2}\,s^{-1}}$), F is the Faraday constant ($F = 96\,485.3\,\mathrm{A\,s\,mol^{-1}}$), I is the current density ($\mathrm{A\,m^{-2}}$) and $\mathbf{n}$ is the normal vector at the electrode wall. In the present numerical setup, the flat end of the electrode is a circle on the YZ plane centered at the origin of the reference system; the wall normal is therefore $\mathbf{n} = \mathbf{e}_x$ and the flux of hydrogen at the electrode is set through the following Neumann boundary condition for the molar concentration $c_c^{\mathrm{H_2}}$:

$$\begin{aligned} \frac{\partial c_c^{\mathrm{H_2}}}{\partial x} &= \frac{\mathbf{N}^{\mathrm{H_2}} \cdot \mathbf{e}_x}{D_c^{\mathrm{H_2}}} f \quad && \text{for } \sqrt{y^2+z^2} < \frac{D_e}{2} \\ \frac{\partial c_c^{\mathrm{H_2}}}{\partial x} &= 0 && \text{for } \sqrt{y^2+z^2} > \frac{D_e}{2} \end{aligned} \tag{7.2}$$

where $D_e = 0.127\,\mathrm{mm}$ is the electrode diameter. The boundary condition reported in equation 7.2 ensures that the amount of moles introduced by diffusion in the liquid

domain is consistent with Faraday's law (equation 7.1) and that the flux of hydrogen occurs only across the active surface of the electrode (the area adjacent to the liquid solution), i.e. the region where $\sqrt{y^2+z^2} < D_e/2$ and $f > 0$. It is reminded here that the electric field is not modelled in the following simulations. Therefore, its effect on surface tension as well as the presence of electrohydrodynamic stresses in the momentum equation are neglected, consistently with the governing equations discussed in chapter 3.

In the VOF framework, the volume fraction of the disperse phase needs to be initialised with a bubble of finite size (see the discussion in section 6.2.3). In the present simulations, bubbles are initialised with a diameter of $D_b^{t=0} = D_e/10 = 0.0127\,\text{mm}$ and the computational domain has a size of $L0 = 25D_b^{t=0} = 0.3175\,\text{mm}$. Adaptive mesh refinement is used and the maximum grid level is set to $l^{\max} = 10$, which corresponds to a spatial refinement of $\Delta(l^{\max}) = 3.1\times10^{-4}\,\text{mm}$ (approximately 41 cells per diameter at $t = 0$). When a single bubble placed at the centre of the electrode is modelled, the problem is symmetric (the bubble is supposed to expand radially, based on experimental evidence) and the system can be solved with a 2D axisymmetric solver (see Liu et al., 2016). A sketch of the 2D case setup and a representation of the adaptive grid are shown in Figure 7.1a and Figure 7.1b, respectively. The axisymmetric condition is applied to the $x-$axis, whilst an outflow boundary condition is set on the right boundary to allow some of the liquid leave the domain as the bubble grows; the other boundaries are treated as symmetric walls. The electrode surface is then treated as a uniform slip wall, where a prescribed contact angle ϑ can be imposed by setting the corresponding curvature at the wall (see Afkhami and Bussmann, 2009 for details on the numerical implementation). A more appropriate treatment to capture the contact line motion is given by the Navier-slip boundary condition, where the tangential velocity at the wall depends on the shear stress and a characteristic dimension, the slip length, which is generally of a few nanometers. The Navier-slip condition is then coupled with either a static contact angle or a dynamic model. The slip length generally depends on the specific gas-liquid configuration and properties of the surface wall; no universal models exist for its prediction. The derivation of an accurate treatment of the moving contact line

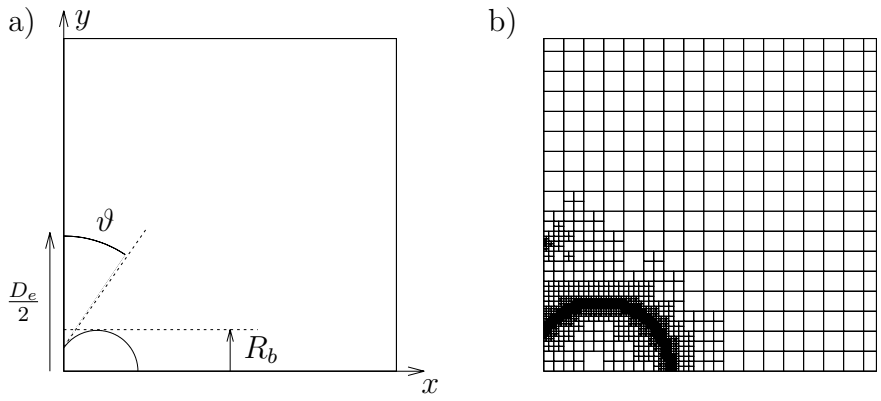

Figure 7.1: 2D Computational domain (a) and adaptive mesh refinement (b) for a growing bubble on a planar wall. The contact angle ϑ is kept constant during the simulation.

is beyond the scope of the present work and the results presented in the following show that, for the prediction of the growth rate of a bubble attached to a solid wall, the use of a standard slip condition provides sufficiently accurate results. The reader interested in a review on the available models for contact lines and their numerical implementation is referred to the work of Sui et al., 2014. When multiple bubbles are considered, the problem is no longer axisymmetric and a 3D model is used. In this case, the electrode is placed at the centre of the left wall and the right boundary is still treated with an outflow condition; all the other walls are symmetric.

The solution is initially saturated (i.e. $\zeta^{\mathrm{H_2}(t=0)} = 1$) and the flux of hydrogen (equation 7.2) starts to increase the concentration in the region adjacent to the electrode for $t > 0$. It is observed in the experiments that, after the current is applied to the electrode, the system requires a waiting time before a bubble can nucleate. During this waiting time (referred to as nucleation time t_n in the present work) the flux of molecules generates a locally super-saturated solution next to the electrode, which then drives the nucleation and the following growth of the bubble. In the present simulations, the nucleation time is set to $t_n = 0.02\,\mathrm{s}$ (which is a realistic value, according to the measurements reported in Glas and Westwater, 1964) and the volume of the bubble is let free to evolve for $t > t_n$.

A relevant parameter for the dynamics of growing bubbles on flat surfaces is the contact angle (ϑ) between the gas-liquid interface and the wall. As the contact angle varies, the interfacial area of a bubble changes accordingly and this, in turn, affects the advection of species as the bubble expands. The contact angle is not a constant property of the systems but rather changes over time as the bubble evolves, as reported by Glas and Westwater, 1964 and, in principle, any model should consider this aspect. Implementing variable contact angle dynamics is out of the scope of the present work and, in these simulations, the effect of the contact angle is tested by comparing two different (but constant over time) values, i.e. $\vartheta = 90\,\text{deg}$ and $\vartheta = 35\,\text{deg}$.

A list of the cases for the modelling of growing bubbles on planar electrodes is reported in Table 7.2. Cases A and B consider the generation of a single bubble,

Case	# bubbles	Solver	I (A m^{-2})	ϑ (deg)	$L0$ (mm)	$\Delta(l^{\max})$ (mm)
A.1	1	2D (Axi)	100	90	0.3175	3.1×10^{-4}
A.2	1	2D (Axi)	300	90	0.3175	3.1×10^{-4}
A.3	1	2D (Axi)	500	90	0.3175	3.1×10^{-4}
A.4	1	2D (Axi)	700	90	0.3175	3.1×10^{-4}
A.5	1	2D (Axi)	1000	90	0.3175	3.1×10^{-4}
B.1	1	2D (Axi)	100	35	0.3175	3.1×10^{-4}
B.2	1	2D (Axi)	300	35	0.3175	3.1×10^{-4}
B.3	1	2D (Axi)	500	35	0.3175	3.1×10^{-4}
B.4	1	2D (Axi)	700	35	0.3175	3.1×10^{-4}
B.5	1	2D (Axi)	1000	35	0.3175	3.1×10^{-4}
C.1	4	3D	100	35	0.635	6.2×10^{-4}
C.2	4	3D	300	35	0.635	6.2×10^{-4}
C.3	4	3D	500	35	0.635	6.2×10^{-4}
C.4	4	3D	700	35	0.635	6.2×10^{-4}
C.5	4	3D	1000	35	0.635	6.2×10^{-4}

Table 7.2: Numerical setup for growing bubbles on planar electrodes.

whilst cases C model the simultaneous growth of multiple (four) bubbles. As it was

introduced earlier, bubbles tend to nucleate from microscopic pits on the electrode surface and, in practical applications, many of these nucleation sites are present in the reactor and, therefore, many bubbles are expected to be generated at the same time. Even in the lab-controlled experiments of Glas and Westwater, 1964, where the electrodes are regularly polished between consecutive runs, small surface defects persist on the wall and multiple bubbles nucleate simultaneously. The choice of modelling four bubbles in cases C is justified by the experimental data, where at least four nucleation sites are generally active at the same time. In the numerical setup of these cases, the bubbles are arranged on a circle at a distance from the center of the electrode of 0.038 mm and are equally spaced. The grid size is coarsened, compared to cases A and B, as this is found not to affect significantly the results but allows for a reduction in the computational cost (which is particularly relevant for 3D simulations). The contact angle for cases C is set to $\vartheta = 35\,\text{deg}$ as this is representative of a time-average contact angle value, as found in the experimental measurements. Finally, it is reminded that gravity is neglected for all the simulated cases and results are presented here in their dimensional form, for a direct comparison against the work of Glas and Westwater, 1964.

The first finding from the experimental campaign is that the growth of bubbles attached to a planar wall follows the same functional relationship of Scriven's solution for suspended bubbles in supersaturated solutions (see section 6.2.3, equation 6.16). The radius of the bubble evolves as $R_b(t) \propto \sqrt{t}$ and the analytical formula is reported here for the reader's convenience:

$$R_b(t) = 2\beta\sqrt{D_c t} \tag{7.3}$$

In the present work, the effect of the current density on the growth of bubbles is investigated for two contact angle values, i.e. $\vartheta = 90\,\text{deg}$ and $\vartheta = 35\,\text{deg}$ (cases A and B, respectively), and results are reported in Figure 7.2. For all the selected current densities and contact angles, the evolution of the radius over time follows with a good approximation the functional law of Scriven and, as expected, the growth rate increases with the current density, as more gas is released into the liquid domain,

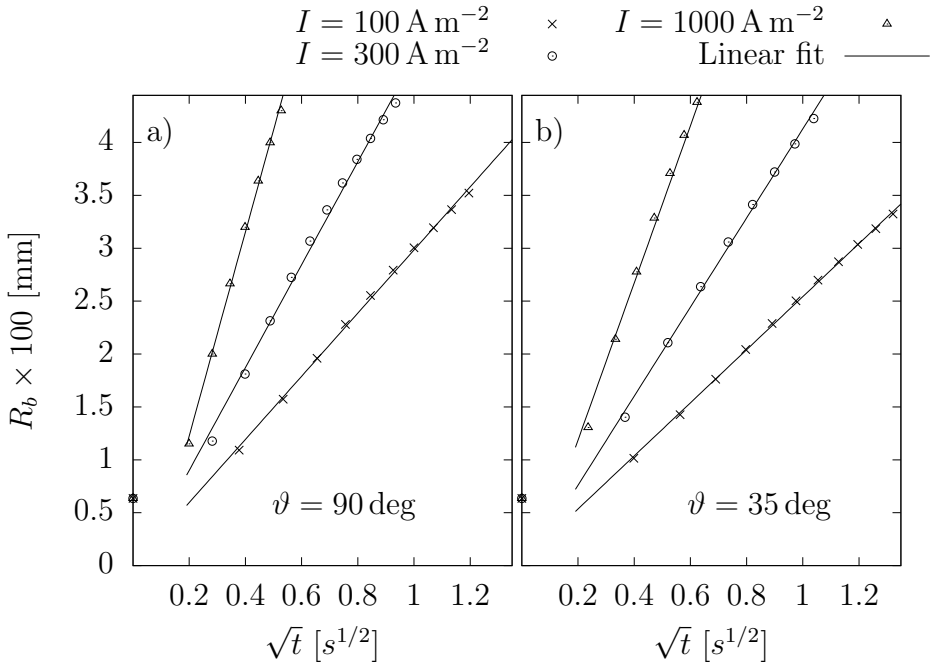

Figure 7.2: Bubble radius evolution for $\vartheta = 90\,\mathrm{deg}$ (a) and $\vartheta = 35\,\mathrm{deg}$ (b) at different current densities. The growth rate follows Scriven's solution, i.e. $R_b \propto \sqrt{t}$.

according to Faraday's Law (equation 7.1).

The growth factor β is derived from the slope of the linear curves that fit to the numerical data and results are compared in Figure 7.3 against the work of Glas and Westwater, 1964 for all the simulated cases (see Table 7.2). The experimental results are characterised by a relevant scattering of the data, especially for large current density values ($I > 600\,\mathrm{A\,m^{-2}}$). This behaviour is due to the variation in the number of nucleation sites, which becomes particularly relevant for large current densities as more sites can be activated simultaneously and less repeatability is observed amongst the experimental measurements. The general behaviour of larger growth factors with increasing current densities is well reproduced by all the numerical simulations (cases A, B and C), regardless of the contact angle between the interface and the wall or the number of growing bubbles. When a single bubble is considered (cases A and B), a significant difference in the growth rate can be observed between $\vartheta = 90\,\mathrm{deg}$

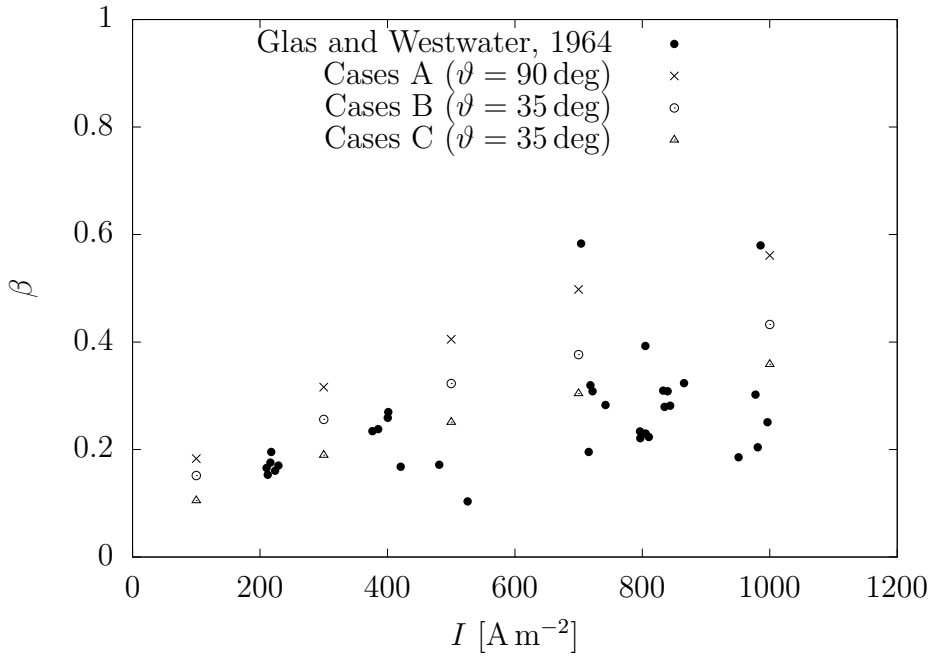

Figure 7.3: Growth factor β Vs current density I. Comparison against the experimental data of Glas and Westwater, 1964.

and $\vartheta = 35\,\mathrm{deg}$. In both cases, the bubble is initialised with the same diameter (i.e. $D_b^{t=0} = 0.0127\,\mathrm{mm}$) but, due the different contact angle, the bubble with $\vartheta = 35\,\mathrm{deg}$ has a more elongated shape along the $x-$axis than the case $\vartheta = 90\,\mathrm{deg}$. This results in two opposite effects since, for $\vartheta = 35\,\mathrm{deg}$, the interfacial area is larger but less exposed to the high concentration region next to the electrode surface. The second effect prevails on the first one and the growth factor β is smaller than the case with $\vartheta = 90\,\mathrm{deg}$; the evolution over time of the bubble interface is compared in Figure 7.4 for cases A.1 and B.1.

When multiple bubbles are considered, the growth factor is smaller than the corresponding single bubble case (see Figure 7.3). This behaviour can be easily explained by considering that the amount of gas produced at the electrode surface is equally shared by the four nucleation sites and, therefore, less gas is available for the growth of each bubble (compared to the single nucleation case). It is observed

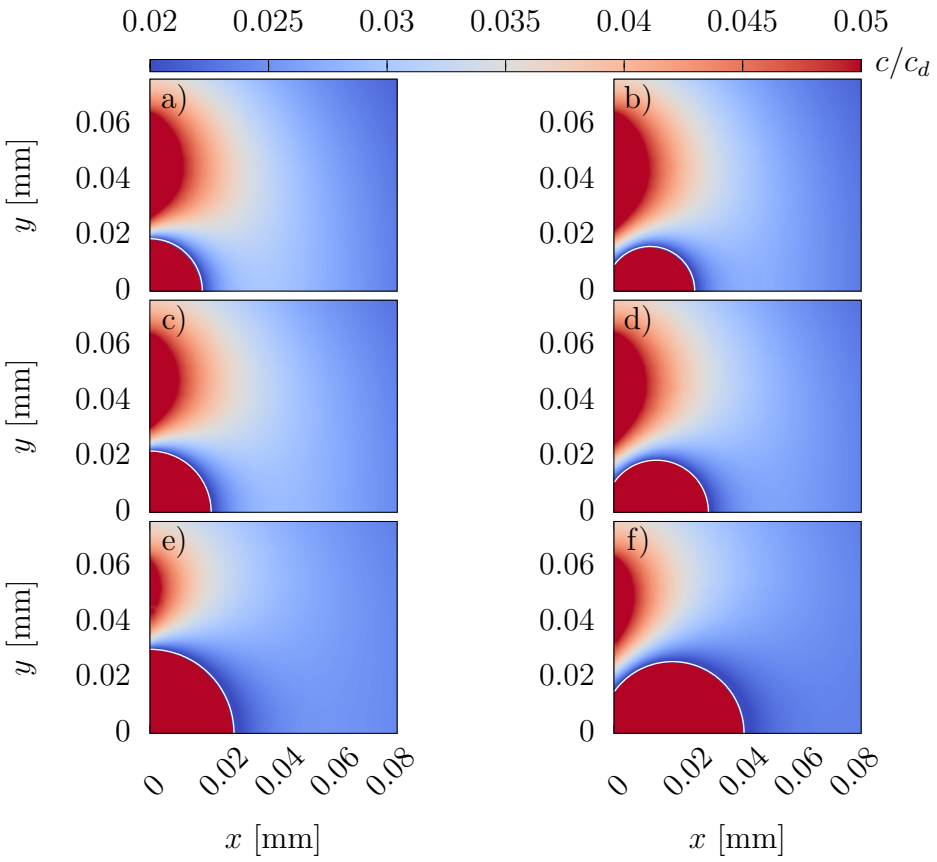

Figure 7.4: Bubble growth and contours of gas concentration for cases A.1 (left) and B.1 (right) at $t = 0.40\,\mathrm{s}$ (a-b), $t = 0.53\,\mathrm{s}$ (c-d) and $t = 1.01\,\mathrm{s}$ (e-f).

here that, due to the symmetric distribution of nucleation sites, all the bubbles are fed with the same amount of dissolved gas and expand at the same rate; however, this is not generally the case in practical applications, where random distribution of bubbles occur and some of them evolve faster than the others. The growth factors for cases C are closer to the experimental values and this confirms the importance of taking into account the variability in the number of nucleation sites when numerical simulations are compared against experiments. The single bubble cases are not very representative of the experiments (where multiple bubbles are generated) and

they generally over predict the growth rate. Finally, it is reminded here that the contact angle between the interface and the wall has a relevant effect on the mass transfer process and that it is generally not constant during the growth stage; a more advanced computational approach should take this into account.

7.2 Mass transfer in two-phase Taylor-Couette reactors

The flow between two rotating coaxial cylinders, known as Taylor-Couette flow, is a well studied configuration that exhibits several complex flow patterns as the rotating speed of the cylinders increases (see the review in section 2.2.2). The generation of counter rotating toroidal vortices within the annulus ensures an efficient mixing of the species in the liquid solution, which is of great advantage to enhance overall reaction rates. This flow configuration has many industrial applications and, in the chemical engineering field, a reactor based on this principle is generally referred to as Taylor-Couette reactor (TCR). The most common configuration of TCRs consists of a rotating inner cylinder, whilst the outer wall is kept fixed. This design has the advantage that the outer cylinder can be easily integrated into external systems like pumps (for the injection/collection of species), or cooling jackets, which are particularly important when the temperature of the solution is a critical parameter (e.g. photochemistry).

In its simplest form, a TCR can be modelled as two coaxial cylinders with top and bottom periodic boundaries (see Figure 7.5). In this way, end geometry effects (which depend on the specific reactor configuration) are neglected and the model is equivalent to a section of two infinite (along the axial direction) cylinders. The main parameters that describe the reactor's configuration are the inner and outer radii (r_{in} and r_{out}, respectively) and the axial length L_z. In terms of non-dimensional numbers, a TCR is generally characterised by the radius ratio:

$$\eta = \frac{r_{\text{in}}}{r_{\text{out}}} \tag{7.4}$$

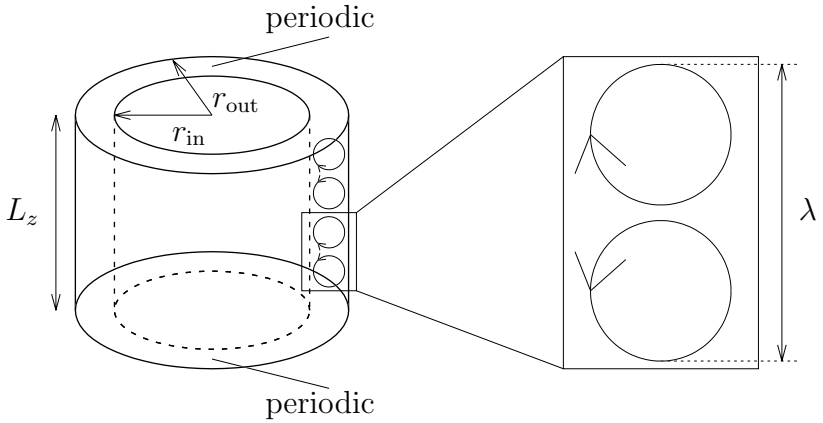

Figure 7.5: Schematic of a TCR with counter-rotating Taylor vortices. Only a section of the reactor is modelled and periodic boundary conditions are applied at the top and bottom faces.

and the aspect ratio:

$$\Gamma = \frac{L_z}{r_{\text{out}} - r_{\text{in}}} \tag{7.5}$$

For a specific configuration (η, Γ), the flow patterns (Taylor-Couette regimes) depend on the Reynolds number:

$$Re = \frac{\rho_c U_{\text{in}} \left(r_{\text{out}} - r_{\text{in}}\right)}{\mu_c} \tag{7.6}$$

where the outer cylinder is assumed fixed (i.e. non rotating) and U_{in} is the tangential velocity of the inner rotor (i.e. $U_{\text{in}} = r_{\text{in}}\omega_{\text{in}}$).

TCRs have successfully been employed for photochemistry (Lee et al., 2017, Lee et al., 2020), electrochemistry (Love et al., 2021, Lee et al., 2022) and many other applications that include polymer synthesis, crystallisation and aggregation processes; for a review on the applications of TCRs, the reader is referred to Schrimpf et al., 2021.

The remaining part of the work is organised as follows. A review on the available theoretical, experimental and computational models currently used to evaluate mass transfer in TCRs is provided in section 7.2.1. The validation of the Basilisk code for the modelling of different flow regimes in a single-phase Taylor-Couette flow is

presented in section 7.2.2, whilst the results of a mass transfer study in a TCR is discussed in section 7.2.3.

7.2.1 Available approaches for quantifying mass transfer in chemical reactors

For reactions that involve multiphase systems, the interphase mass transport is limited by the phase boundary resistance and accurate predictions of mass transfer rates are fundamental to evaluate the overall performance and meet the design targets of the reactor. The mass transfer characteristic of a TCR is typically expressed in terms of Sherwood number (equation 6.8), whose definition is reported here for the reader's convenience:

$$Sh = \frac{k_m L_{\text{ref}}}{D_c} \tag{7.7}$$

The mass transfer coefficient k_m depends on the local concentration of species around the interface and is a non trivial quantity to be measured experimentally. Following its definition, k_m can be written as (see equation 6.7):

$$k_m A_\Sigma \Delta c = \int_\Sigma \frac{\dot{m}}{M}\, ds \tag{7.8}$$

where $\Delta c = (c_\Sigma - \bar{c}(t))$ is the concentration difference between the gas-liquid interface and the average bulk solution that drives the interphase mass transport and $\dot{m}$ is the interfacial mass transfer rate. The (average) molar concentration balance for a generic liquid domain reads:

$$\frac{d\bar{c}}{dt} = k_m \frac{A_\Sigma}{V_c} \Delta c - \frac{R}{M} \tag{7.9}$$

where V_c is the bulk volume of the solution and the last term on the RHS represents a chemical reaction, i.e. $[R] = \mathrm{kg\,m^{-3}\,s^{-1}}$. In the work of Qiao et al., 2018, the authors investigate the oxygen transport in a Taylor-Couette bioreactor and assume the reaction to be of first-order, i.e. $R/M = k\bar{c}(t)$, where k is the (known) reaction rate constant. When the system reaches a steady-state equilibrium, equation 7.9

reduces to:

$$k_m a_\Sigma \left(c_\Sigma - \bar{c}(t)\right) = k\bar{c}(t) \tag{7.10}$$

where the specific interfacial area has been introduced, i.e. $a_\Sigma = A_\Sigma / V_c$. Ramezani et al., 2015 present an experimental measurement of oxygen mass transfer in a semi-batch air-water multiphase TCR, where the gas is continuously supplied through four sparging stones placed at the bottom of the reactor. In this case, no reactions occur and the dissolved concentration in the water solution evolves as:

$$k_m a_\Sigma = \frac{1}{\Delta c} \frac{d\bar{c}}{dt} \tag{7.11}$$

The integration of equation 7.11 gives:

$$\ln\left(1 - \frac{\bar{c}(t)}{c_\Sigma}\right) = -k_m a_\Sigma t \tag{7.12}$$

where the initial bulk concentration is assumed null, i.e. $\bar{c}^{t=0} = 0\,\mathrm{mol\,m^{-3}}$. Equations 7.10 and 7.12 are used in the experimental works of Qiao et al., 2018 and Ramezani et al., 2015, respectively, to quantify the mass transfer coefficient by measuring the dissolved concentration $\bar{c}(t)$ through apposite sensors. These devices must be small enough to reduce perturbations and avoid significant alterations to the flow structure (e.g. Taylor vortices); an accurate prediction of the saturated interfacial concentration c_Σ is also needed and correlation formulae of the type $c_\Sigma = c_\Sigma(T)$, where T is the temperature, are generally used. However, since the measurement of the interfacial area can be extremely difficult to achieve experimentally, the quantity $k_m a_\Sigma$ is generally computed instead. In a TCR, bubbles are generally affected by several operating parameters (e.g. reactor geometry, rotating speed, gas flow rate, etc) and, within the same experiment, they can exhibit different shapes and diameters. Therefore, the choice of a reference length for the Sherwood number is not trivial and a common approach is based on the Sauter mean diameter for a population of bubbles D_s (Grafschafter and Siebenhofer, 2017, Ramezani et al., 2015, Gao, Kong, Ramezani, et al., 2015); the definition of Sherwood number can then be rearranged

as:

$$Sh = \frac{k_m a_\Sigma D_s^2}{D_c} \tag{7.13}$$

Using the experimentally measured values of $k_m a_\Sigma$ and D_s, Sh is obtained from equation 7.13, whilst an estimation of the specific interfacial area can be obtained from:

$$a_\Sigma = \frac{6\varepsilon_d}{D_s} \tag{7.14}$$

where ε_d is the gas holdup, i.e. $\varepsilon_d = V_d/V$ and V is the reactor volume. Following the aforementioned method, experimental correlation formula for Sh numbers in TCRs can be derived. These have typically the following form (see Qiao et al., 2018):

$$Sh = \Phi Re^\lambda Sc^\gamma \tag{7.15}$$

where Re refers to the reactor Reynolds number (equation 7.6) and Sc is the Schmidt number; λ and γ are specific coefficients. Ramezani et al., 2015 derive a different formula of the type:

$$Sh = \Phi Re_a^\lambda \left(Re + \Theta\right)^\gamma \tag{7.16}$$

where Φ and Θ are constants (note that Φ in equation 7.16 is different from equation 7.15) and Re_a refers to the axial Reynolds number, which is related to the supplied gas flow rate through the following relationship:

$$Re_a = \frac{2\rho_c u_d \left(r_{\text{out}} - r_{\text{in}}\right)}{\mu_c} \tag{7.17}$$

where u_d is the superficial gas velocity. It is important to observe that equation 7.16 does not depend on the Sc number (contrary to equation 7.15) and is specific to the air-water system and reactor configuration used in the author's work and cannot be applied to different systems (therefore, the dependency on the gas diffusivity is embedded within the coefficients). Nonetheless, this equation provides valuable information about the physical process of mass transfer in TCRs and can be used to investigate the effects of different operating parameters of the reactor, such as the rotating speed or gas flow rate.

The foregoing experimental procedures for the measurement of the mass transfer coefficient rely on the simplified assumption of a uniform (average) concentration in the bulk liquid solution that drives the interphase mass transport, i.e. $N = k_m \Delta c$ (equivalent to equation 7.11), where N is the molar flux ($\mathrm{mol\,m^{-2}\,s^{-1}}$). This is also the starting point for the derivation of theoretical models for the prediction of mass transfer in multiphase systems. The simplest theory is the two-film theory (TFT) for gas absorption proposed by Whitman, 1923 (see the introduction in section 2.3.2), where the interphase transport of a species from a gas region to the liquid solution is limited by the phases pressure/concentration that develop inside two thin (film) regions across the interface. In this model, the gas and liquid resistances operate in series and produce a global resistance to the mass transfer. However, in many practical applications, the solubility of dissolved species is low and the change in mole fraction within the gas phase can be neglected (Deckwer et al., 1974). Under this assumption, or when the disperse phase is pure (i.e. no mixtures), the concentration in the gas region is assumed constant and the mass transfer resistance is entirely given by the liquid-side film resistance (Levenspiel, 1998); in this case, the model is generally referred to as film theory (FT). The FT assumes a steady linear concentration profile within a liquid film region of thickness x_0 and uses Fick's law of diffusion to compute the mass transfer coefficient as:

$$k_m = \frac{D_c}{x_0} \tag{7.18}$$

In this model, k_m is proportional to the diffusion coefficient and the effect of the fluid velocity field is embedded in the film thickness x_0, which is not know a priori. Therefore, correlation formulae from experiments are generally used to compute the liquid resistance (and eventually the gas contribution, if the TFT is employed) to get the global mass transfer rate for the considered application. The FT (or TFT) is essentially a one-dimensional model that takes into account only the effect of the gas diffusivity and is independent of the fluid motion. The main limitations are given by the assumption that a linear concentration profile exists within the film region and that the corresponding thickness is uniform. An attempt to explicitly include

the effect of the fluid velocity (which affects the thickness x_0) in a two-dimensional model is proposed in the penetration theory of Higbie, 1935, where the liquid film is assumed sufficiently thick and in relative motion with the interface. The resulting mass transfer rate is given by:

$$k_m = \sqrt{\frac{4D_c u_c}{\pi L}} \tag{7.19}$$

where u_c is the fluid velocity and L is the length of the film at the interface. In equation 7.19, the ratio u_c/L represents the exposure time t_e, during which a liquid element of the film is adjacent to the interface and can exchange mass with the gas phase (i.e. $t_e = u_c/L$). Similarly to the FT, t_e is not know a priori and depends on the specific gas-liquid system; therefore, an additional relationship is needed to close the system. With similar results to the penetration approach, Danckwerts, 1951 proposes the surface-renewal theory, where the fundamental interphase mass transfer mechanism still follows the penetration model, but the fluid region next to the interface is continuously refreshed with new elements from the bulk liquid; the corresponding mass transfer coefficient is:

$$k_m = \sqrt{\frac{D_c}{\tau}} \tag{7.20}$$

where τ is a characteristic residence time of a fluid element adjacent to the interface. Equations 7.19 and 7.20 produce similar results in the sense that they predict the same functional dependence on the gas diffusivity (i.e. $k_m \propto \sqrt{D_c}$). In the surface-renewal model (as for the penetration theory) the characteristic time τ is not know a priori and closure models are indeed necessary. For a deeper analysis of these theoretical models, the interested reader is referred to Cussler, 2009 and Levenspiel, 1998. Although the penetration and surface-renewal theories successfully include a more realistic description of the flow field near the interface, none of the aforementioned models provide satisfactory results in terms of mass transfer correlations (C. Wang et al., 2018). The main reason why theoretical models fail is that they assume uniform properties in space. In practical applications, the velocity of the gas/liquid

regions (and their respective properties) can reach different values in different locations of the reactor and the flow regime (e.g. laminar vs turbulent) can affect the distribution of concentration in both phases. In a TCR, the multiplicity of flow regimes adds more complexity to the fluid motion and significantly different mixing properties can be achieved by modifying the operating speed of the reactor. All these variables generate an heterogeneous domain within the reactor vessel, where local super/under saturated regions can coexist and the resulting mass transfer coefficient is highly non-uniform. These features are generally dependent on the reactor characteristics and cannot be predicted by fundamental theoretical models. On the basis of the presented approaches, many application-specific theories have been proposed in the last decades and the interested reader is referred to Huang et al., 2010 for a review on more advanced models.

An attempt to combine theoretical models and CFD methodologies is presented in the work of Gao, Kong, Ramezani, et al., 2015, where the authors develop an adaptive model for mass transfer in a gas-liquid TCR. The proposed approach is based on the penetration theory of Higbie, 1935 (equation 7.19) and the exposure time t_e is adaptively computed based on two different formulations:

$$t_e = \min\left(\frac{1}{F^2}\frac{D_s}{u_{\text{slip}}}, \frac{1}{K^2}\sqrt{\frac{\nu_c}{\varepsilon_c}}\right) \tag{7.21}$$

where F and K are two constants that must be tuned according to the specific application. The first term in equation 7.21 depends on the mean Sauter diameter for a population of bubbles (D_s) and on the slip velocity $u_{\text{slip}} = |\mathbf{u}_d - \mathbf{u}_c|$, whilst the second term comes from the Kolmogorov timescale ($\sqrt{\nu_c/\varepsilon_c}$) for isotropic turbulence, where ε_c is the liquid turbulent dissipation rate. The mass transfer coefficient follows from the computation of the exposure time:

$$k_m = \max\left(F\sqrt{\frac{4D_c}{\pi}\frac{u_{\text{slip}}}{D_s}}, K\sqrt{\frac{4D_c}{\pi}\left(\frac{\varepsilon_c}{\nu_c}\right)^{1/2}}\right) \tag{7.22}$$

In the work of Gao, Kong, Ramezani, et al., 2015, the flow properties needed in

equation 7.22 to calculate k_m are obtained from the solution of an Euler-Euler CFD model, where two sets of governing equations are solved separately (one for each phase) and are coupled through interfacial source terms in the momentum equations. This combined approach overcomes the limiting assumption of uniform flow properties typical of theoretical models, since CFD is used to inform locally the exposure time and the corresponding mass transfer coefficient becomes a non-uniform (interfacial) field variable. However, some limitations in the proposed adaptive model still persist, since coefficients F, K depend on the specific reactor configuration and information on typical bubble sizes are not provided by the model. Gao, Kong, Ramezani, et al., 2015 validate their approach by modelling the same experimental apparatus of Ramezani et al., 2015 and use their correlation formula to obtain the Sauter mean diameter for this specific configuration.

A different approach is presented in C. Wang et al., 2018 for the capture of CO_2 in a wetted wall column reactor, where a VOF method is coupled with the one-scalar approach of Haroun et al., 2010 for the species transport. This method has the advantage of computing the interphase mass transfer based on the local concentration of carbon dioxide and does not rely on the use of models or other correlation data.

Despite their excellent mixing properties, the popularity of TCRs in industry is still limited. This is mainly due to the complex design of these devices that makes them difficult to scale-up and meet the industrial production targets (see Schrimpf et al., 2021, Lee et al., 2020) and to the lack of universal mass transfer correlations for this specific flow configuration. The methodology developed within the present thesis is applied to the study of the fundamental problem of mass transfer of a single bubble in a TCR. The proposed direct numerical approach is suitable for a detailed analysis of the physical processes and the two-scalar method allows for a direct evaluation of the mass transfer rate at the interface. The aim of the following high-fidelity investigation is to provide a numerical tool that can be used to inform reduced order models (see chapter 1) for the design of this class of chemical reactors.

7.2.2 Single-phase Taylor-Couette flow

In this section, the Basilisk code is validated for single-phase Taylor-Couette flows against available experimental and numerical data. Direct numerical simulations of (3D) incompressible flows are performed and wall boundaries are treated with an immersed boundary method, where Dirichlet boundary conditions are enforced with the approach proposed by Schwartz et al., 2006. The tangential velocity $U_{\text{in}} = r_{\text{in}}\omega_{\text{in}}$ is applied at the inner cylinder, whilst the outer one is fixed (i.e. $U_{\text{ext}} = 0$) and periodic boundary conditions are used for the top and bottom ends of the computational domain (see Figure 7.5); the (non-dimensional) rotor speed is set to one, i.e. $U^*_{\text{in}} = 1$ and the viscosity of the liquid is adjusted to reach the desired Reynolds number. The choice of the axial length of the domain (L_z) is particularly relevant when only a section of the reactor is modelled, since periodic boundaries force the flow to adapt to the available space and constrain the number of Taylor vortices that form within the annulus. Results from linear stability analysis for infinite cylinders (see the Appendix by P. H. Roberts in Donnelly et al., 1965) show that the wavelength, i.e. the axial extension of a pair of counter rotating vortices (see Figure 7.5), is expected to be close to $\lambda \approx 2\,(r_{\text{out}} - r_{\text{in}})$. However, the results collected in the work of Chouippe et al., 2014 from different experimental investigations show that a significant dispersion is observed in the measured wavelengths. The main reason is due to the non-uniqueness feature of the Taylor-Couette flow (see section 2.2.2) for which the final observed state of the system depends on the procedure used to reach such state (e.g. acceleration/declaration rates of the rotor, etc) and not only on the geometrical configuration. Therefore, for the validation of the numerical method, it is important to select an axial length that is a multiple of the observed wavelength (i.e. $L_z = n\lambda$), so that a number of n vortex pairs is modelled and a sensible comparison can be made against the reference data. In the present thesis, three configurations are tested, namely $\eta = 0.5, 0.73, 0.91$, at different Reynolds numbers. Details on the main parameters, including the observed wavelength and the critical Reynolds number (Re_{cr}) for the transition from planar Couette flow to TVF, are summarised in Table 7.3 (for a comprehensive summary on the critical

values for a range of radius ratios, the reader is referred to Childs, 2011 and the references therein). The selected choice of configurations allows for a comprehensive

η	$\lambda/(r_{\text{out}} - r_{\text{in}})$	L_z	Re_{cr}	Re	Regime	Reference
0.5	2.09	2λ	55.6	1000	WVF	Dong, 2007
0.5	2.09	2λ	55.6	3000	TTVF	Dong, 2007, Chouippe et al., 2014
0.5	2.09	2λ	55.6	5000	TTVF	Chouippe et al., 2014
0.73	1.716	5λ	84.5	338	TVF	L. Wang, Marchisio, et al., 2005
0.73	1.716	5λ	84.5	1014	WVF	L. Wang, Marchisio, et al., 2005
0.91	3.08	8λ	136.1	5000	TTVF	Chouippe et al., 2014

Table 7.3: Single-phase Taylor-Couette cases.

validation of the single-phase numerical framework, since the main Taylor-Couette regimes are represented (i.e. TVF, WVF and TTVF).

A mesh sensitivity study is first carried out for one of the most demanding cases in terms of mesh resolution (i.e. $\eta = 0.5$ and $Re = 5000$), where the flow regime is fully turbulent and strong velocity fluctuations are expected near the walls. The octree grid structure of Basilisk is used for the discretization of the domain and two cylindrical regions with thickness $\Delta h_{\text{in}} = \Delta h_{\text{out}} = 0.05\,(r_{\text{out}} - r_{\text{in}})$ are used to set different mesh refinements near the walls (see Figure 7.6). Therefore, three different sub-domains can be identified within the annulus, i.e. the inner, outer and bulk regions. Three meshes are tested for the selected configuration and the corresponding parameters are reported in Table 7.4. Mesh M.1 has a uniform resolution within the gap, whilst meshes M.2 and M.3 take advantage of the two refinement regions to increase the grid density near the cylindrical walls (M.2 and M.3 have the same resolution near the walls, but a different mesh density in the bulk region). Numerical modelling of Taylor-Couette flows requires that enough grid points are distributed within the gap between the cylinders, in order to capture the complex flow features that develop as the rotating speed is increased. Meshes M.1 and M.2 have a similar

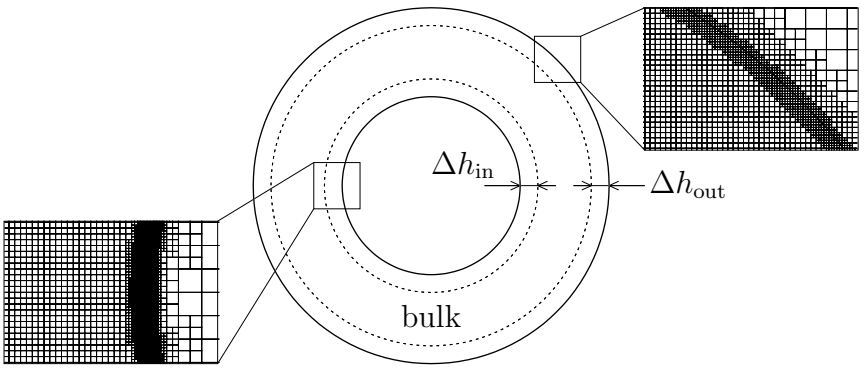

Figure 7.6: Mesh refinements within two cylindrical regions (dashed lines) around the inner and outer walls.

Mesh	N_z^{b}	N_z^{in}	N_z^{out}	N_r^{b}	N_r^{in}	N_r^{out}	$N_\theta^{r_{\text{in}}}$	$N_\theta^{r_{\text{out}}}$	Cells count
M.1	256	256	256	55	3	3	385	770	9.95×10^6
M.2	256	1024	512	55	12	6	1539	1539	5.64×10^7
M.3	512	1024	512	110	12	6	1539	1539	1.13×10^8

Table 7.4: Mesh sensitivity study for the configuration $\eta = 0.5$ and $Re = 5000$. N_z, N_r, N_θ are the number of cells along the axial, radial and azimuthal directions, respectively. The superscripts N^{b}, N^{in}, N^{out} refer to the bulk, inner and outer regions within the domain (see Figure 7.6).

number of radial points (i.e. $N_r = 61$ and $N_r = 73$ respectively), where N_r is computed as $N_r = N_r^{\text{b}} + N_r^{\text{in}} + N_r^{\text{out}}$. However, the cost in terms of total number of cells for this marginal increment of resolution along the radial direction is significantly large (see Table 7.4). This is a limitation of the available Cartesian grid structure, where mesh stretching is not allowed, i.e. the aspect ratio of each cell is fixed to one. Therefore, when the mesh size Δ is refined to fit more points within the gap, more cells are automatically distributed along the other two directions and the size of the overall grid increases significantly. Results from the selected meshes are compared for the average azimuthal velocity $< u_\theta >_{z\theta t}$ (where the operator $<>_{z\theta t}$ refers to the

average in time and along the axial (z) and azimuthal (θ) directions) and for the corresponding fluctuating component:

$$u'_\theta = u_\theta - < u_\theta >_t \tag{7.23}$$

which can be averaged in time in the following way:

$$< u'^2_\theta >_t = < u^2_\theta >_t - < u_\theta >^2_t \tag{7.24}$$

The time interval used for the computation of the average and fluctuating quantities corresponds to 5 revolutions, i.e. $\Delta t = 5t_{\text{rev}}$, where $t_{\text{rev}} = 2\pi r_{\text{in}}/U_{\text{in}}$. Results for $< u_\theta >_{z\theta t}$ and $\sqrt{< u'^2_\theta >_{z\theta t}}$ are plotted in Figure 7.7a and Figure 7.7b, respectively, and compared against the numerical study of Chouippe et al., 2014. The results

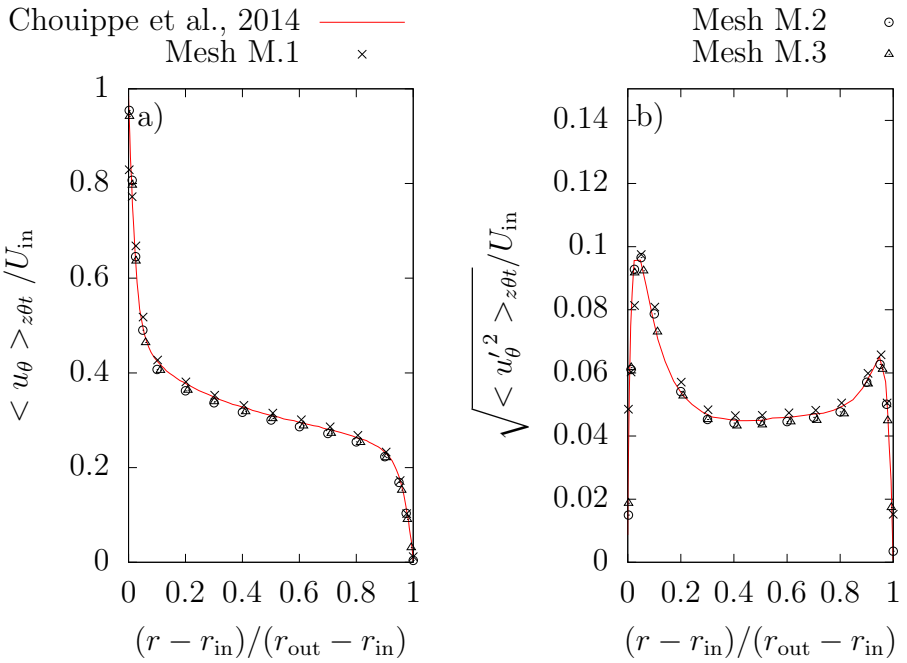

Figure 7.7: Mesh sensitivity study for the configuration with $\eta = 0.5$ and $Re = 5000$. The radial profiles of the average azimuthal velocity (a) and fluctuation (b) are compared against the work of Chouippe et al., 2014.

reported in Figure 7.7 show that the average radial profiles of the plotted quantities are not significantly affected by an increase in the mesh resolution. Mesh M.1 tends to slightly over-predict the velocity fluctuations near the inner wall and the coarser resolution around the cylinders, combined with the immersed boundary method, results in a underestimation of the tangential velocity at the inner rotor; meshes M.2 and M.3 provide almost the same results. The grids are compared in terms of wall unit resolutions in Table 7.5, where the average viscous length scales $\delta^{*,\text{in}}$ and $\delta^{*,\text{out}}$ at the inner and outer cylinders respectively, are computed as:

$$\delta^*_{\text{in,out}} = \frac{\nu_c}{u^*_{\text{in,out}}} \tag{7.25}$$

where the friction velocity u^* is obtained from the shear stress τ_w:

$$u^*_{\text{in,out}} = \sqrt{\frac{|\tau_w^{\text{in,out}}|}{\rho_c}} \tag{7.26}$$

The shear stress in Equation 7.26 is the average value on the cylinders and follows from the integral torque T_w:

$$\tau_w^{\text{in,out}} = \frac{T_w^{\text{in,out}}}{2\pi r^2_{\text{in,out}} L_z} \tag{7.27}$$

The values of $\Delta_{r^+}^{\text{in,out}}$ reported in Table 7.5 are computed with the average wall shear

Mesh	$\Delta_{r^+}^{\text{in}}$	$\Delta_{r^+}^{\text{out}}$	$\text{Cells}_{r^+_{\text{in}}<5}$	$\text{Cells}_{r^+_{\text{out}}<5}$
M.1	2.54	1.31	1	2
M.2	0.598	0.610	4	4
M.3	0.598	0.619	4	4

Table 7.5: Mesh characteristics in terms of wall units and number of cells in the viscous sublayer for the configuration $\eta = 0.5$, $Re = 5000$.

stress (equation 7.27) and, due to the Cartesian structure of the mesh, the non-dimensional quantities $\Delta_{z^+}^{\text{in,out}}$ and $r_{\text{in,out}}\Delta_{\theta^+}$ are the same as $\Delta_{r^+}^{\text{in,out}}$. Meshes M.2

and M.3 have the same refinement near the walls and both have at least four cells within the viscous sublayer region, i.e. $r^+ < 5$. Given the results reported in Figure 7.7 and the requirements in terms of mesh resolution for DNS (i.e. $\Delta_{r^+} < 1$), mesh M.2 is selected as the reference grid for the modelling of Taylor-Couette flows; the grids used for the other configurations have similar characteristics and their details are reported in Table 7.6. All the meshes have the first cell centre within the non-

η	Re	N_r^{b}	N_r^{in}	N_r^{out}	$\Delta_{r^+}^{\mathrm{in}}$	$\Delta_{r^+}^{\mathrm{out}}$	$\mathrm{Cells}_{r_{\mathrm{in}}^+ < 5}$	$\mathrm{Cells}_{r_{\mathrm{out}}^+ < 5}$
0.5	1000	55	3	3	0.733	0.389	3	6
0.5	3000	110	6	6	0.800	0.415	3	6
0.5	5000	55	12	6	0.598	0.610	4	4
0.73	338	26	4	2	0.301	0.464	6	5
0.73	1014	26	4	2	0.965	1.05	3	2
0.91	5000	16	9	9	1.36	1.25	2	2

Table 7.6: Selected mesh characteristics for the single-phase Taylor-Couette cases.

dimensional distance $\Delta_{r^+}^{\mathrm{in,out}} < 1$ from the walls and have at least three cells within the regions $r_{\mathrm{in,out}}^+ < 5$. Exceptions are the configurations with $\eta = 0.73$, $Re = 1014$ and $\eta = 0.91$, $Re = 5000$, where Δ_{r^+} is slightly above one at the wall. In the last case ($\eta = 0.91$), this is due to the small gap within the cylinders, where the maximum number of cells is limited by the Cartesian topology of the grid and a further level of refinement would generate too many cells along the axial and azimuthal directions that cannot be handled with the available computational resources. It is important to remind here that the non-dimensional grid distances are based on the average shear stress (equation 7.27) and that the distance from the first cell centre is assumed to be $\Delta/2$ (this is an approximation, since with the immersed boundary method the grid does not conform to the shape of the solid wall).

The cases reported in Table 7.3 are run until an equilibrium configuration is reached and the flow statistics are stationary. This state occurs when the torque exerted by the fluid on the walls is the same for both the inner and outer cylinders (Chouippe et al., 2014) and an example of the plot of the non-dimensional torque (G_w) for the configuration $\eta = 0.5$, $Re = 5000$ is reported in Figure 7.8. The torque

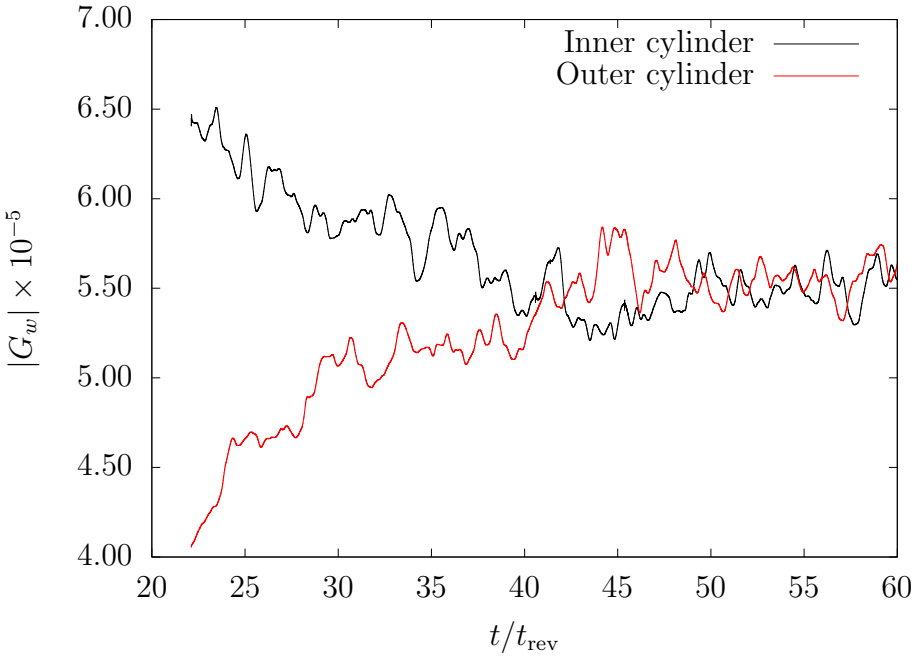

Figure 7.8: Inner and outer cylinder (non-dimensional) torques Vs time for the Taylor-Couette configuration with $\eta = 0.5$ and $Re = 5000$. The absolute value $|G_w|$ is plotted here to compare between the two walls. The statistically stationary regime is approximately reached after 50 revolutions.

is made non-dimensional with the cylinders axial length and with the liquid density and viscosity:

$$G_w^{\text{in,out}} = \frac{T_w^{\text{in,out}}}{\rho_c \nu_c^2 L_z} \tag{7.28}$$

The mean torque values for all the tested configurations at their equilibrium points are compared against the experimental formula proposed by Wendt, 1933 (which was already introduced in section 2.2.2 in terms of torque coefficient and is reported here in the equivalent form for the non-dimensional torque), where G_w scales as $Re^{3/2}$:

$$G_w^{\text{Wendt}} = 1.45 \left[\frac{\eta^{3/2}}{(1-\eta)^{7/4}} \right] Re^{3/2} \tag{7.29}$$

and the corresponding results are reported in Figure 7.9, where, for all the simulated

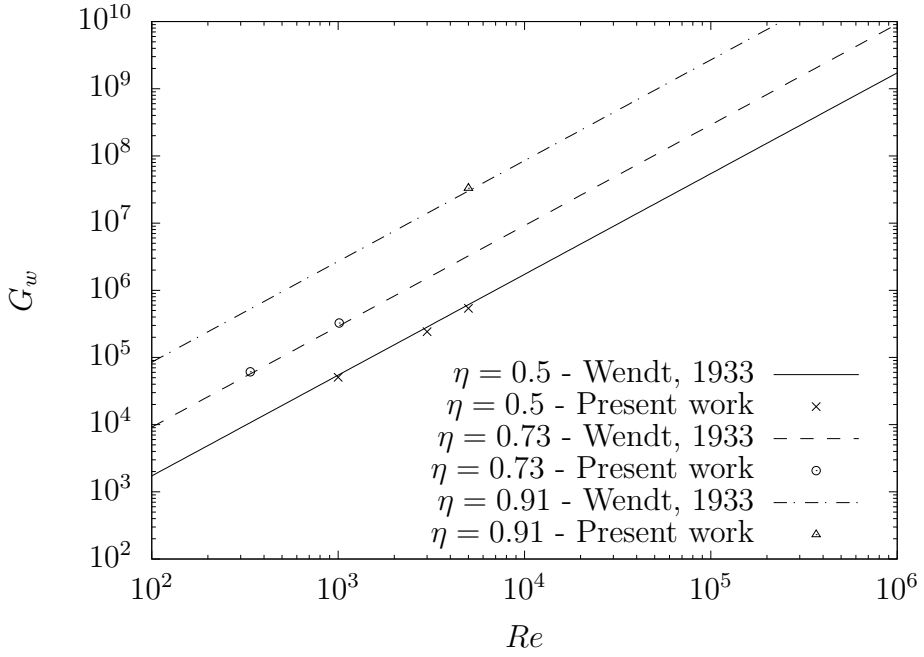

Figure 7.9: Comparison of the (non-dimensional) torque exerted on the inner cylinder against the experimental work of Wendt, 1933 (equation 7.29).

cases, a good comparison against the experimental data is observed, confirming that the statistically stationary regime is reached for all the tested radius ratios and Reynolds numbers.

The mean azimuthal velocity $< u_\theta >_{z\theta t}$ and fluctuation $\sqrt{< u_\theta'^{\,2} >_{z\theta t}}$ for the configurations with $\eta = 0.5$ and $\eta = 0.91$ are compared against the available numerical data of Dong, 2007 and Chouippe et al., 2014 and results are reported in Figure 7.10 and Figure 7.11. A good comparison is observed for almost all the selected configurations, for both the average azimuthal velocity and the corresponding fluctuation. The profiles of velocity fluctuations show the characteristic shape with two local peaks near the inner and outer walls and an (almost) uniform value in the bulk of the liquid; similar profiles are observed for different turbulent channels configurations (see Moser and Moin, 1987 or Hoyas and Jiménez, 2006). As the Reynolds number increases, the magnitude of the (normalised) fluctuations decreases and the

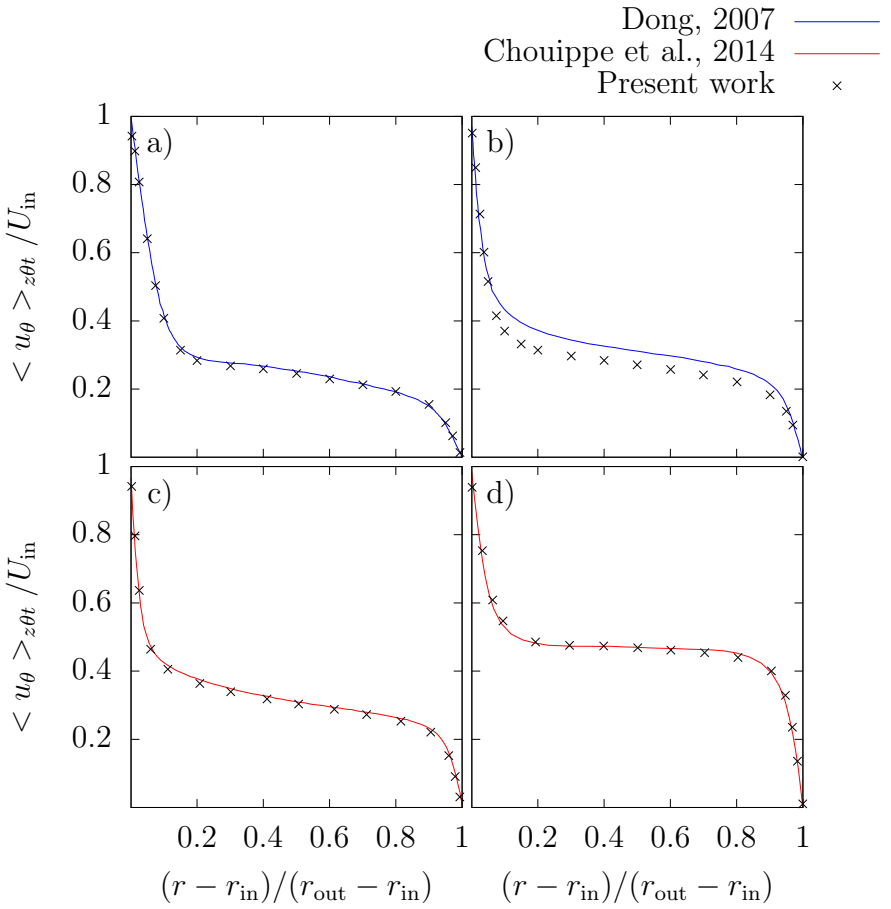

Figure 7.10: Average radial profiles of the azimuthal velocity component for the configurations with $\eta = 0.5$, $Re = 1000$ (a), $\eta = 0.5$, $Re = 3000$ (b), $\eta = 0.5$, $Re = 5000$ (c) and $\eta = 0.91$, $Re = 5000$ (d).

peaks move closer to the respective walls. The configuration with $\eta = 0.5$, $Re = 1000$ shows a significant deviation for the azimuthal fluctuation (but not for the main velocity component) from the work of Dong, 2007 (Figure 7.11a). However, the same case compared to the results reported in Chouippe et al., 2014 shows an excellent agreement at every distance from the walls. Surprisingly, the radial profile of average azimuthal velocity for the configuration with $\eta = 0.5$, $Re = 3000$ (Figure 7.10b) does not match the reference data of Dong, 2007 within the bulk of the liquid, where

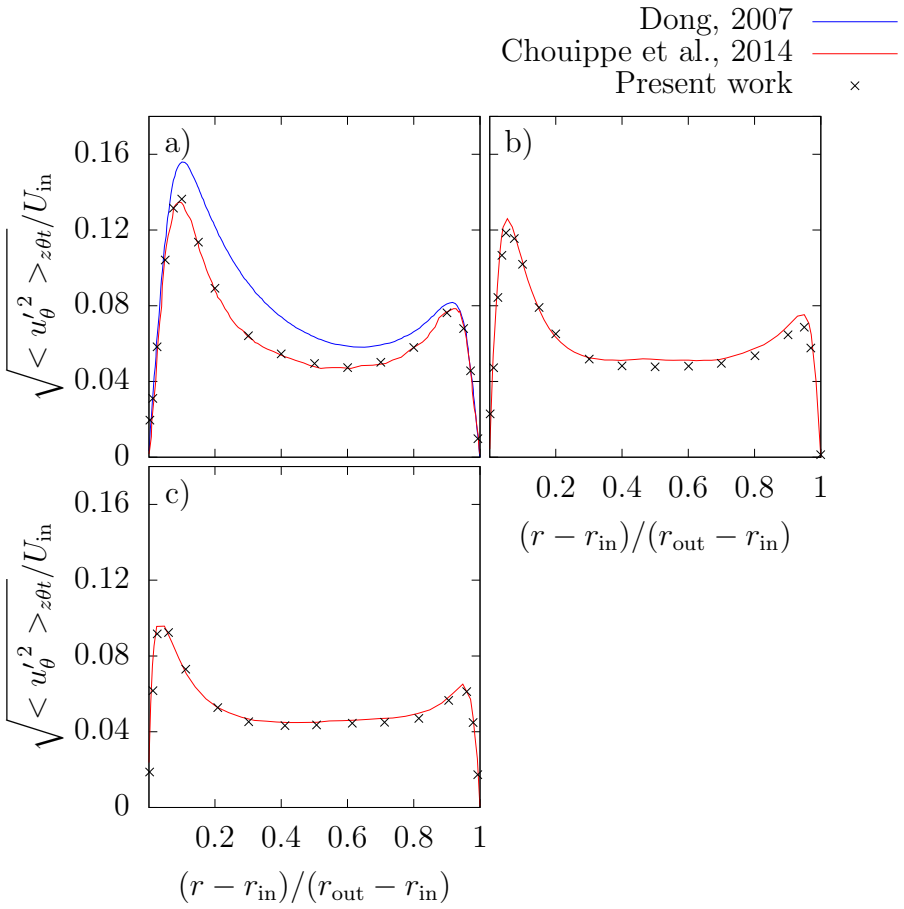

Figure 7.11: Average radial profiles of the azimuthal velocity fluctuation for the configurations with $\eta = 0.5$, $Re = 1000$ (a), $\eta = 0.5$, $Re = 3000$ (b) and $\eta = 0.5$, $Re = 5000$ (c).

the velocity is underpredicted, but a good agreement is reached in the regions close to the inner and outer walls. To further investigate this configuration, results in terms of average azimuthal velocity, made non-dimensional with the friction velocity (equation 7.26) at the inner wall, i.e. $< u_\theta >_{z\theta t} / u^*_{in}$, are compared against the work of Chouippe et al., 2014 and reported in Figure 7.12. In this case, a good comparison between the present work and the reference data is observed and this, along with the velocity fluctuations reported in Figure 7.11b, suggests that the numerical setup

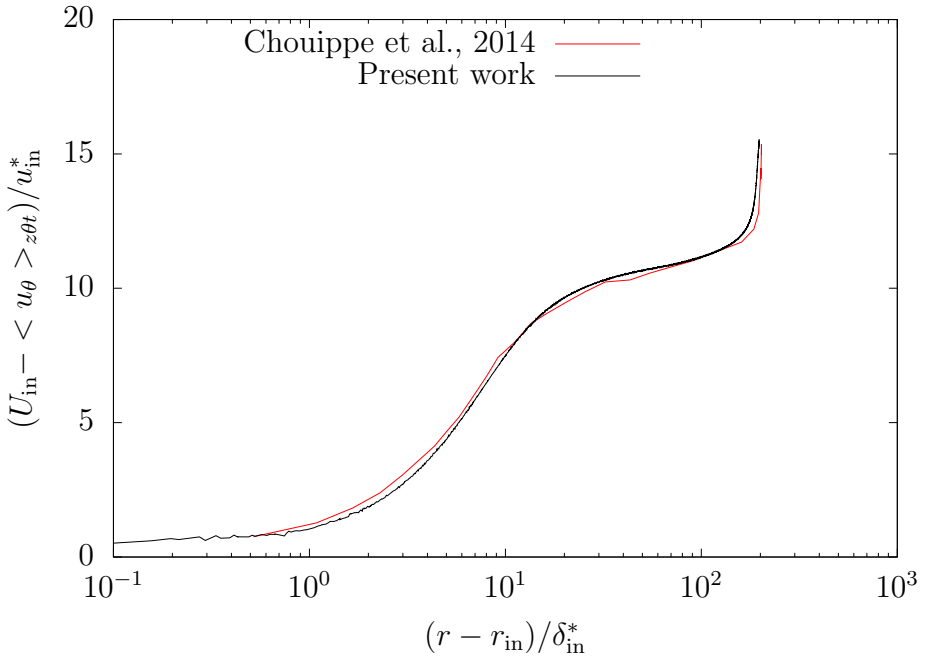

Figure 7.12: Average radial profile of the azimuthal velocity component for the configuration $\eta = 0.5$, $Re = 3000$. Velocity and radial coordinate are made non-dimensional with the inner friction velocity and wall unit respectively.

is able to capture the flow features of this Taylor-Couette configuration in the range $Re < 5000$.

To conclude the validation for the geometry with $\eta = 0.5$, the velocity boundary layers at the inner and outer cylinders are investigated and results are compared against the work of Chouippe et al., 2014 in Figure 7.13. A good correlation is reached for all the Reynolds numbers. The profiles evolve linearly at both the inner and outer walls, following the linear law $u^+ = r^+$, and then they deviate from such trend as the radial distance from the cylinders increases.

A qualitative representation of the flow field and the effect of the Reynolds number for the configurations with $\eta = 0.5$ and $\eta = 0.91$ is reported in Figure 7.14, where the contours of axial velocity (u_z) on a cylindrical surface with constant r are compared in a (planar) 2D plot on the corresponding $z-\theta$ plane. Figures 7.14a, 7.14b and 7.14c show the effect of the Reynolds number on the topology of Taylor vortices as the flow

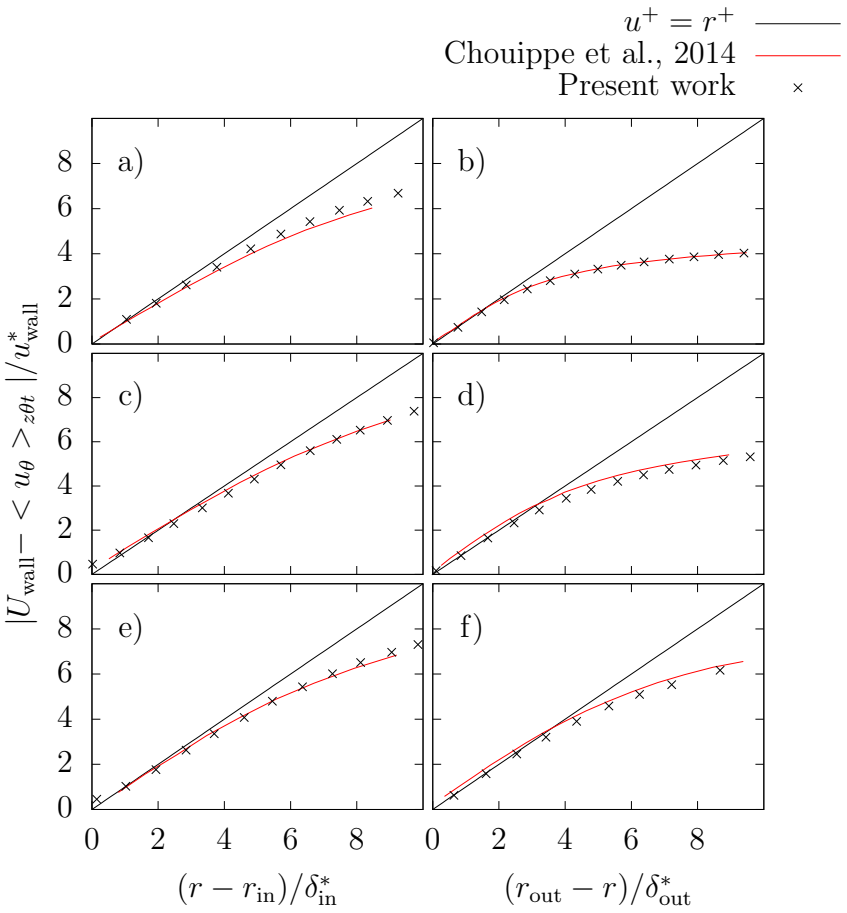

Figure 7.13: Velocity boundary layer profiles at the inner (left) and outer (right) walls for the configuration with $\eta = 0.5$ and $Re = 1000$ (a-b), $Re = 3000$ (c-d) and $Re = 5000$ (e-f). For the inner wall $U_{wall} = U_{in}$, whilst for the outer cylinder $U_{wall} = 0$.

regime evolves from WVF to TTVF (see Table 7.3). For $Re = 1000$ (Figure 7.14a) two organised pairs of counter rotating voritces develop within the annulus and a thin region of null axial velocity separates each vortex from the adjacent (counter rotating) one. The axial extension of the computational domain was set to twice the expected wavelength (see Table 7.3) and the qualitative results reported here (two pairs of vortices) confirm that the axial length of Taylor cells matches the expected one. The travelling trajectory along the azimuthal direction of each vortex is almost

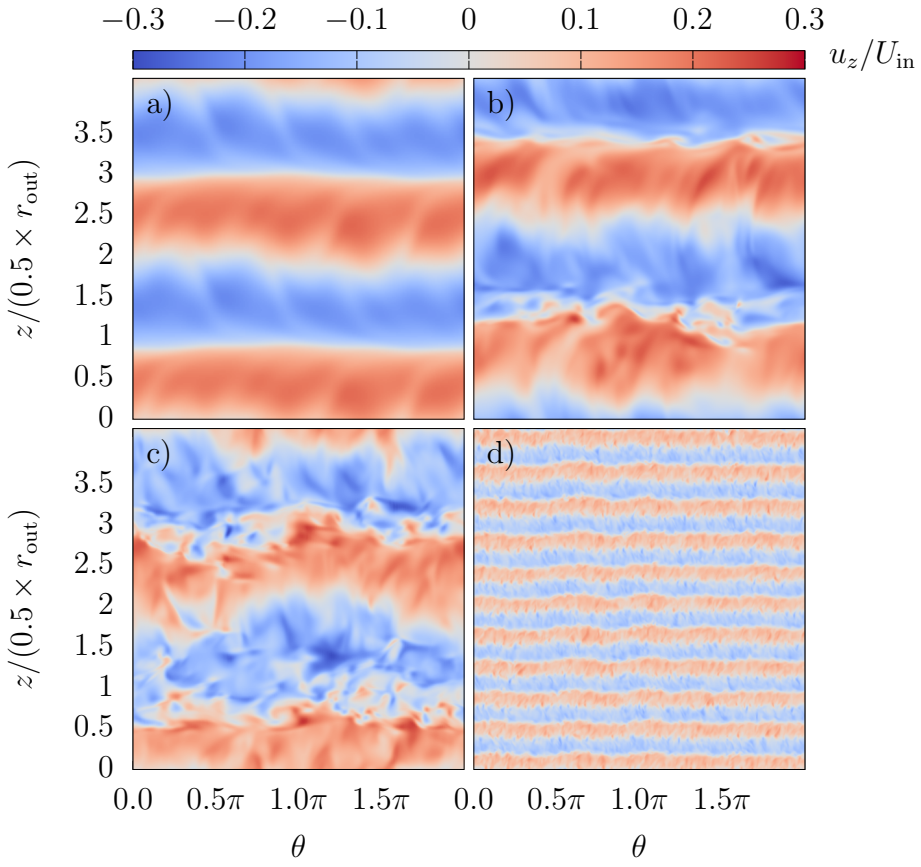

Figure 7.14: Contours of axial velocity on the $z-\theta$ plane for the configurations with $\eta = 0.5$, $Re = 1000$ (a), $Re = 3000$ (b), $Re = 5000$ (c) and $\eta = 0.91$, $Re = 5000$ (d). These plots are obtained from the corresponding cylindrical surface with radius $r_{\text{in}} + 0.1(r_{\text{out}} - r_{\text{in}})$ for cases a,b,c and radius $r_{\text{in}} + 0.25(r_{\text{out}} - r_{\text{in}})$ for case d.

straight, but the onset of a wavy motion is visible from the oscillating boundaries of the vortices, suggesting that the reactor is in a transitional state from TVF to WVF. As the Reynolds number is increased to $Re = 3000$ (Figure 7.14b), the flow is fully turbulent and the shape of the vortices is distorted. However, two main regions of counter rotating velocities can still be identified, although Taylor cells are not well defined as in the case with $Re = 1000$. Finally, for $Re = 5000$ (Figure 7.14c) the flow appears chaotic with many flow structures distributed in a random way and

Taylor vortices do not form into an organised and clear pattern; these observations are qualitatively confirmed by the results reported in Dong, 2007. The effect of the gap size is clearly visible from the comparison between Figure 7.14c ($\eta = 0.5$) and Figure 7.14d ($\eta = 0.91$), which both run at $Re = 5000$. For larger radius ratios, the small gap within the cylinders represents a geometric constraint for the formation of Taylor vortices, whose topology appears (even for large and fully turbulent Reynolds numbers) well organised into stable and clearly recognisable pairs of alternating axial velocities.

So far, the investigation of single-phase Taylor-Couette flows has been limited to the main (average) azimuthal component of the velocity field (and the relative fluctuation). Profiles of axial and radial velocity are investigated for the two configurations with $\eta = 0.73$ and $Re = 3000, 5000$ and compared against the available data from the experimental work of L. Wang, Marchisio, et al., 2005. Due to the non-uniqueness feature of Taylor-Couette flows, the authors adopt a specific procedure for the start up of the reactor that ensures that the observed number of Taylor vortices is always the same for all the tested rotor speeds. Such procedure consists of an acceleration of the inner rotor from rest up to $Re = 4648$, followed by a deceleration to the desired rotating speed; both the acceleration and deceleration steps are performed with a constant (but different) acceleration rate. The torque exerted by the fluid on the inner and outer cylinders follows the aforementioned startup procedure, as it increases with the acceleration of the rotor and decreases when the rotor is decelerated. This is confirmed in the present work by the torque profile reported in Figure 7.15 for the configuration with $\eta = 0.73$ and $Re = 1014$, but a similar profile is also observed for the case with $Re = 338$. After the (transient) start up procedure, where the rotor is first accelerated and then decelerated, the TCR reaches a steady state regime and the inner and outer torques converge to the same value. It is interesting to observe here that the torque on the inner cylinder increases as soon as the rotor is started, whilst the outer wall does not experience a significant torque for the first seven revolutions. The formation of Taylor vortices suddenly increases the friction on the cylinders and this is clearly visible from the plot between the sixth and seventh revolution, where a jump in both torque profiles appears. This first occurs for the

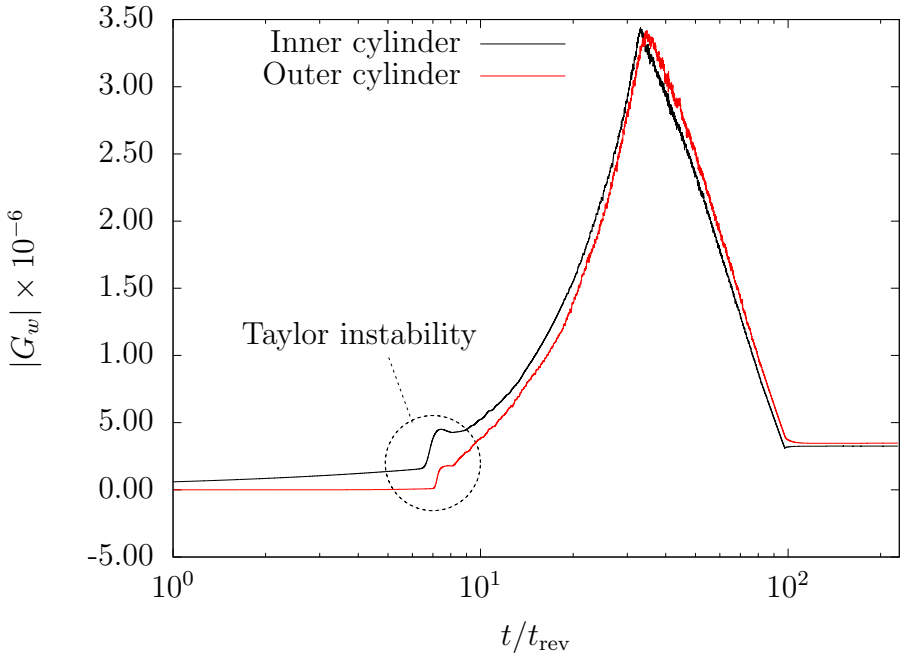

Figure 7.15: Inner and outer cylinder (non-dimensional) torques Vs time for the Taylor-Couette configuration with $\eta = 0.73$ and $Re = 1014$. The torques follow the start up procedure of the rector and the formation of Taylor vortices is clearly visible from the sudden increases in the torque profiles between the sixth and seventh revolution.

inner rotor, since the instability that leads to the formation of Taylor cells originates from the rotating wall and a small amount of time, which corresponds to the time needed for the propagation of vortices across the gap, is required to see the effect of such vortices on the outer cylinder.

Time and space average profiles along the axial direction for the radial ($< u_r >_{\theta t}$) and axial ($< u_z >_{\theta t}$) velocity components are compared in Figure 7.16 against the corresponding experimental measurements of L. Wang, Marchisio, et al., 2005. The profiles are plotted along the axial line at a distance from the inner rotor of $0.35(r_{\text{out}} - r_{\text{in}})$ and $0.37(r_{\text{out}} - r_{\text{in}})$ for $Re = 338$ and $Re = 1014$ respectively. Time averaging is performed with a time interval of one revolution for $Re = 338$ and one hundred revolutions for $Re = 1014$. Such difference is justified by the fact that the flow

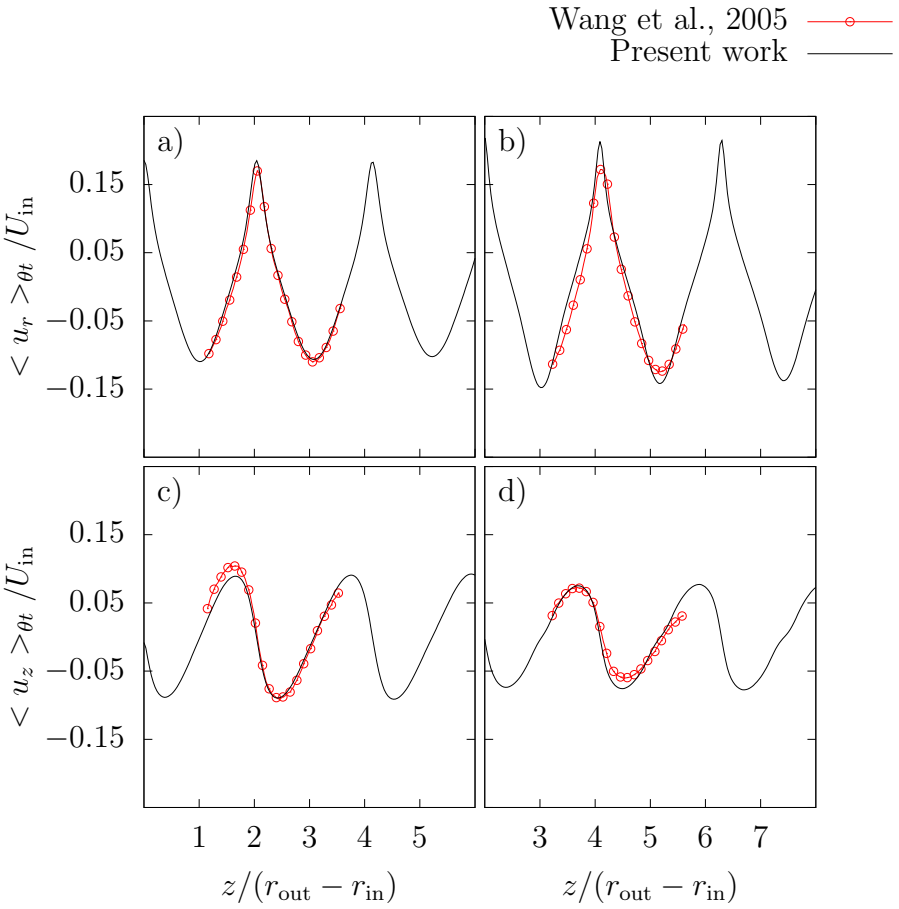

Figure 7.16: Average profiles of radial (top) and axial (bottom) velocity for the configurations with $\eta = 0.73$, $Re = 338$ (left) and $Re = 1014$ (right). The profiles are averaged in time and over the azimuthal direction at a distance from the rotor of $0.35(r_{\text{out}} - r_{\text{in}})$ and $0.37(r_{\text{out}} - r_{\text{in}})$ for $Re = 338$ and $Re = 1014$, respectively. Note that the reference velocity U_{in} is the same for both configurations ($U_{\text{in}} = 1$), but the fluid viscosity is not, i.e. $\mu^{Re=338} = 3\mu^{Re=1014}$.

is steady (TVF) for the lower Reynolds number, but a wavy (unsteady) regime (WVF) appears for the larger Reynolds case and more time is needed to reach a time-independent average profile (although the number of revolutions for $Re = 1014$ could be probably reduced here). The results reported in Figure 7.16 show a good agreement with the experimental data for both the radial (Figures 7.16a-b) and

axial (Figures 7.16c-d) components. The measurements of the vortex wavelength cannot be performed from these plots since the profiles are not sampled along the gap midline. However, a comparison of the vortex size can be done by measuring the distance between two adjacent minimum and maximum peaks in the profiles of radial velocity, which is shown to agree well with the measurements reported in L. Wang, Marchisio, et al., 2005. It is therefore concluded that modelling the same reactor start up procedure as the experiments ensures that the same number of Taylor vortices is obtained in the numerical computations. In the plots of axial velocity, the computations slightly underpredict the maximum peak for $Re = 338$ (Figure 7.16c) and the minimum peak for $Re = 1014$ (Figure 7.16d). However, for the two Taylor-Couette regimes considered here, i.e. TVF and WVF, the time-average axial velocity profiles are expected to be symmetric (for a sufficient number of data samples) as observed from the results of the present work. Therefore, a possible explanations for this (minor) mismatch is that the number of velocity fields used for the time averaging procedure in the experiments is not large enough to reach a fully time-independent average profile.

Finally, a qualitative representation of the flow fields within the annulus is shown in Figure 7.17 for the radial (Figures 7.17a-b) and axial (Figures 7.17c-d) velocity components. The plots represent instantaneous (non-averaged) snapshots of the flow

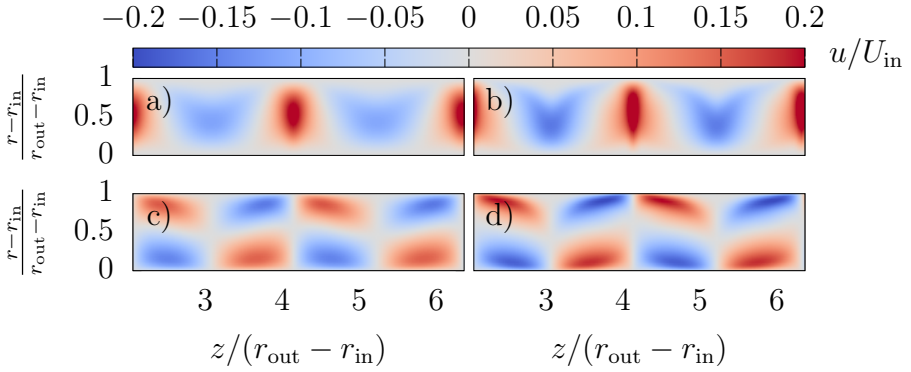

Figure 7.17: Contours of radial (top) and axial (bottom) velocities for the configurations with $\eta = 0.73$, $Re = 338$ (left) and $Re = 1014$ (right).

pattern, which clearly show the presence of stable and well organised Taylor vortices. The increase in the Reynolds number leads to slightly sharper high and low velocity regions, whereas in the low Reynolds case the boundaries of such regions appear more diffuse; however, the instantaneous flow patterns for $Re = 338$ and $Re = 1014$ appear similar to each other and no major differences can be observed between these two configurations.

The results presented in this section show that the numerical methodology used in the present work to model single-phase Taylor-Couette flows is able to accurately reproduce the features of the main flow regimes for different geometries (radius ratios) and rotating speeds (Reynolds numbers). In the following section, the validated approach is coupled with the phase-change solver presented in chapter 5 to model the mass transfer of a single bubble in a TCR.

7.2.3 Mass transfer of a bubble in a Taylor-Couette reactor

In this section, a single (pure) gas bubble is injected at the bottom of a TCR and is let free to exchange mass with the surrounding liquid. The mesh requirements for the mass transfer of soluble species are generally different (and more expensive) than those related to the hydrodynamic part and can be quantified in terms of number of grid points per bubble diameter for a given Péclet number (see section 6.2.4). The selected reactor geometry for this study is the one with radius ratio of $\eta = 0.5$, since the large gap of this configuration allows to model larger bubbles, which are less expensive in terms of grid resolution. The properties of the gas-liquid system are reported in Table 7.7, where the diffusivity of the (generic) gas in the liquid phase has been increased (with respect to typical values) to speed up the mass transfer process and reduce the computational cost of the simulations. The initial bubble diameter is set to $D_b^{t=0} = (r_{\text{out}} - r_{\text{in}})/3 = 0.005\,\text{m}$ and the center of the bubble is placed in the middle of the gap at $z_b^{t=0} = r_{\text{out}}/3$ from the bottom of the reactor (it is reminded here that the axis of the TCR is aligned to the $z-$direction). The reactor is oriented vertically and standard gravitational acceleration is assumed here, i.e. $\mathbf{g} = -9.81\,\text{m}\,\text{s}^{-2}\mathbf{e_z}$. The characteristic non-dimensional numbers of the

Phase	Density ($\mathrm{kg\,m^{-3}}$)	Viscosity ($\mathrm{N\,s\,m^{-2}}$)	Diffusivity ($\mathrm{m^2\,s^{-1}}$)	M ($\mathrm{kg\,mol^{-1}}$)	σ ($\mathrm{N\,m^{-1}}$)	H_e
Liquid	998	1.05×10^{-3}			0.072	
Gas	1.3	2.01×10^{-5}	2.3×10^{-6}	0.032		1.2

Table 7.7: Gas-liquid properties for a dissolving bubble in a TCR.

bubble (based on the initial diameter) are $Ga = 1050.7$ and $Bo = 3.4$; the Schmidt number of the gas-liquid system is $Sc = 0.458$ and the solution is assumed initially under-saturated, with no concentration of gas at $t = 0$, i.e. $\zeta^{t=0} = 0$. The goal of this investigation is to quantify the effect of the reactor Reynolds number (and the corresponding Taylor-Couette regimes) on the mass transfer and dissolution rate of a single bubble. Therefore, the focus is on how the interaction between the bubble and Taylor vortices affects the transport of species released into the liquid. Simulations are first started from rest (null liquid velocity) and the bubble is kept fixed until a (statistically) stationary regime is reached (see section 7.2.2) and Taylor vortices are completely formed. During this initialisation stage, the surface tension term is neglected (since the bubble interface is frozen) and the simulations can be advanced in time with the same time-step used for the single-phase case, avoiding, in this way, the restriction given by the explicit scheme used for the surface tension term (equation 4.47); transport of species and volume change are also not computed at this stage. After the Taylor-Couette regime is established, the bubble is set free to move within the reactor and the full phase-change solver is run. As the volume of the bubble decreases, more liquid needs to be introduced within the reactor for the conservation of mass. However, the considered TCR is a closed system in the sense that the boundaries of the fluid domain consist of two solid walls (inner and outer cylinders) and two periodic boundaries (top and bottom), which do not allow for any net flow of liquid towards the reactor. This issue is solved by making a small circular hole (with diameter $r_{\mathrm{out}}/12$) halfway along the reactor length (i.e. at $L_z/2$) on the external cylinder, where an outflow boundary condition is set and the liquid is set free to enter the domain as the bubble dissolves (see Figure 7.18).

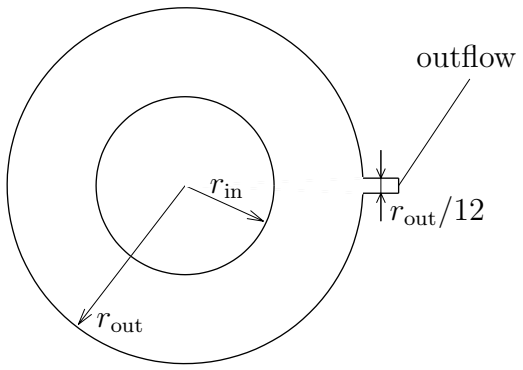

Figure 7.18: Opening of the outer cylinder for the passage of liquid (section taken at $z = L_z/2$). This modification is necessary to ensure the continuity of mass when the volume of the gas fraction decreases.

A different physical process (i.e. the mass transfer at the interface) requires a new mesh sensitivity study to find a suitable grid for mesh independent solutions. This can be done independently of the grid density needed for the single-phase Taylor-Couette flow and the selected configuration for this analysis is the one with steady rotor (i.e. $Re = 0$), which consists of a bubble rising in a quiescent flow bounded by cylindrical walls. The advantage of this configuration is that the finest mesh resolution is only needed around the bubble (with an AMR technique) and it is therefore significantly cheaper to run compared to the cases with Taylor vortices. At this point, it is important to remind here that the requirements in terms of grid density for the mass transfer depend on the Péclet number (see section 6.2.4) and this can obviously be affected by the rotor speed. However, for the considered bubble size ($D_b^{t=0} = 0.005\,\mathrm{m}$), the bubble Reynolds number (Re_b) is mainly determined by the rising velocity and, therefore, the Pe number is weakly dependent on the rotor speed. Three different mesh refinements are compared here and the list of cases for the grid sensitivity study is reported in Table 7.8. Results in terms of volume dissolution rates for the three considered meshes are reported in Figure 7.19. Mesh M.1 over-predicts the volume ratio as a result of the under-resolved concentration boundary layer at the

Case	Re	$D_B^{t=0}$ (m)	$l^{\max}$	$\Delta(l^{\max})$ (m)	cells/$D_b^{t=0}$
M.1	0	0.005	10	6.10×10^{-5}	≈ 82
M.2	0	0.005	11	3.05×10^{-5}	≈ 164
M.3	0	0.005	12	1.53×10^{-5}	≈ 328

Table 7.8: List of cases for the grid convergence analysis of a dissolving bubble in a TCR with no rotation.

gas-liquid interface, whilst meshes M.2 and M.3 are indistinguishable until $t \approx 0.05\,\mathrm{s}$ and produce similar results for $t < 0.07\,\mathrm{s}$. As the bubble volume is further reduced, mesh M.2 deviates from mesh M.3 because not enough points are distributed around the interface. This is a common issue for dissolving bubbles, since no mesh can be fine enough to capture the mass transfer until complete dissolution. However, given the mesh-independent solution obtained for a volume reduction of up to 70% (i.e. $V_b(t)/V_b^{t=0} = 0.3$) and the cheaper computational cost compared to case M.3, mesh M.2 is selected for all the other cases presented in this section. It is worth reminding here that, according to the review presented in section 2.2.2, the presence of bubbles in a TCR is expected to interact with the turbulent features near the walls. Small bubbles are found to decrease the inner cylinder drag by breaking up the dissipative structures at the wall and this mechanism is effective as long as the perturbations induced by the bubbles overwhelm the turbulent fluctuations. However, in the cases presented in this section, only a single (large) bubble is considered and the interaction with the near wall region is limited to a small portion of the reactor and to the time interval during which the bubble is close to one of the cylinders. Therefore, possible alterations of the characteristic turbulent length scales (due to the presence of the bubble) are not investigated here and the mesh sensitivity analysis based on the volume dissolution rate (Figure 7.19) is considered sufficient for the objectives of the present investigation.

The effect of the reactor Reynolds number is investigated by comparing the cases with $Re = 0$ (no rotation) and $Re = 1000, 3000, 5000$, where the TC flow regime within the reactor moves from WVF to TTVF (see Table 7.3). The complete list

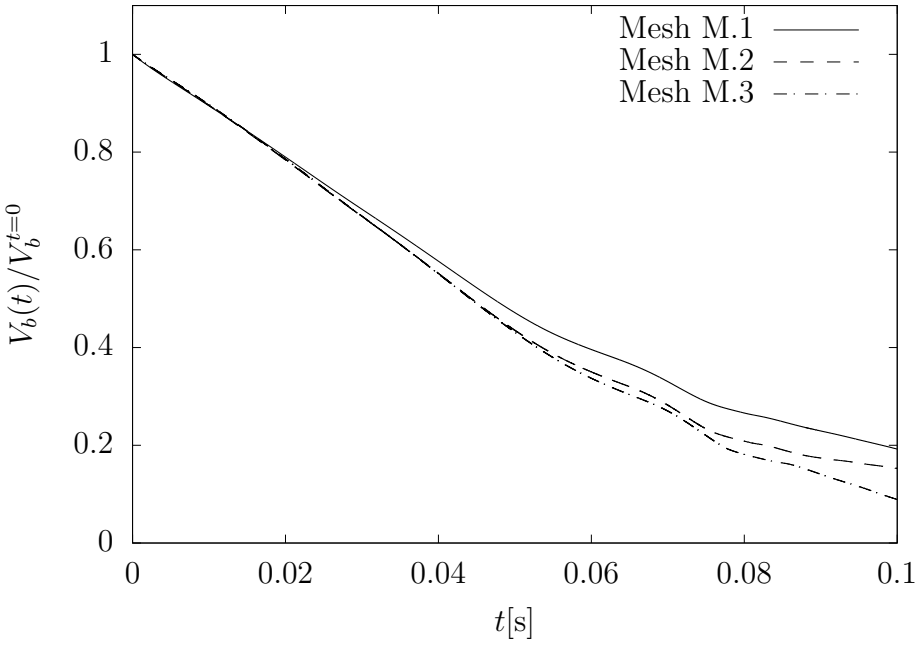

Figure 7.19: Grid convergence for a dissolving bubble in a TCR with no rotation. Plot of bubble volume ratio Vs time.

of cases presented in the rest of this section is summarised in Table 7.9. Cases A-D represent a realistic reactor configuration, where the motion of the bubble is determined by two major components: the gravitational acceleration and the transport induced by the carrier liquid (TC flow). Although the effects on the distribution of the dissolved species within the reactor are clearly dependent on the rotor speed (as will be shown later), for the selected bubble dimension ($D_b^{t=0} = 0.005\,\mathrm{m}$) the motion is dominated by the gravitational component and the effect of the TC regime is marginal. Therefore, to investigate the role of Taylor vortices on the mass transfer of bubbles, gravity has been neglected in cases E-G and the bubble motion is made completely dependent on the carrier flow. An alternative to this approach would be the modelling of smaller bubbles that have a lower buoyancy force and are mainly driven by the rotor-induced flow. However, the latter approach has the disadvantage of requiring a finer mesh to reach a grid-independent solution and would make the

Case	η	Re	$D_b^{t=0}$ (m)	$l^{\max}$	cells/$D_b^{t=0}$	TC regime	g $\mathrm{m\,s^{-2}}$
A	0.5	0	0.005	11	≈ 164	N/A	9.81
B	0.5	1000	0.005	11	≈ 164	WVF	9.81
C	0.5	3000	0.005	11	≈ 164	TTVF	9.81
D	0.5	5000	0.005	11	≈ 164	TTVF	9.81
E	0.5	1000	0.005	11	≈ 164	WVF	0
F	0.5	3000	0.005	11	≈ 164	TTVF	0
G	0.5	5000	0.005	11	≈ 164	TTVF	0

Table 7.9: List of cases for the study of a dissolving bubble in a TCR at different rotating speeds and gravitational accelerations.

cost of the simulations significantly higher; on the other hand, neglecting gravity removes the buoyancy force and allows to quantify the contribution of the Taylor-Couette flow itself on the mass transfer process. Results are first presented for the cases with gravity (cases A-D) and subsequently the removal of the buoyancy force is discussed in cases E-G.

Cases with gravity

Results for cases A-D in terms of volume ratio against time are reported in Figure 7.20. As was anticipated before, the velocity magnitude of the bubble is basically determined by the rising component and the volume dissolution rate for these cases is not significantly affected by the rotation of the inner cylinder (minor differences are observed at the start and at the end of the simulation, where cases C,D dissolve slightly faster than cases A,B, coherently with the larger rotating speed). The plot of the volume ratio shows a linear trend until $V_b(t)/V_b^{t=0} \approx 0.4$ and, after that, the slope progressively decreases as the bubble dissolves; a similar behaviour was observed for the mass transfer of a rising bubble in a quiescent flow (Figure 6.32), confirming the predominance of gravity in cases A-D.

The (time-dependent) Sherwood number (equation 6.8) is monitored during the simulation and results are plotted in Figure 7.21. The reference length used for the

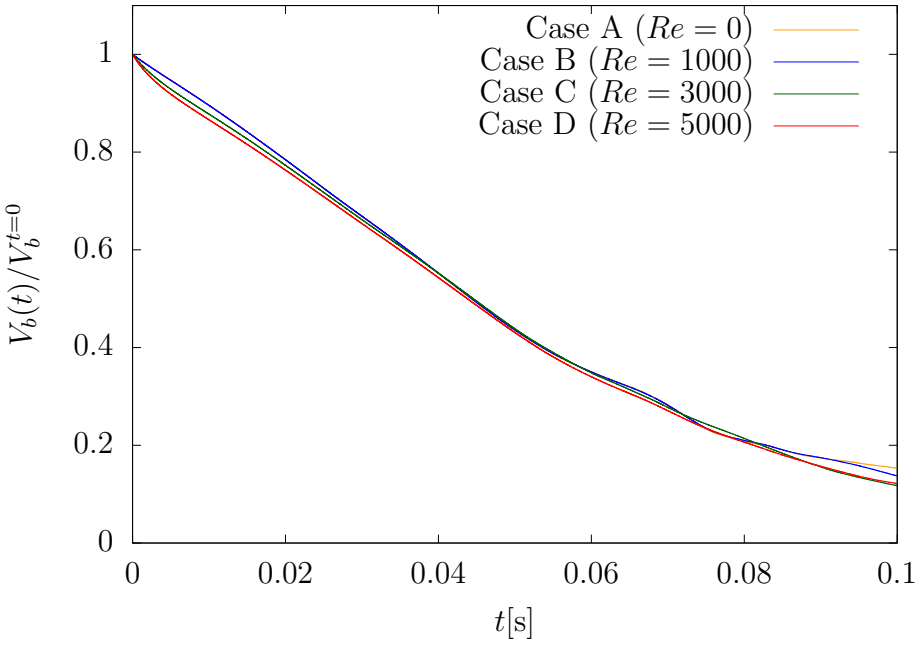

Figure 7.20: Volume ratio Vs time for a dissolving bubble in a TCR at different rotating speeds. For the selected configuration, gravity is dominant and the TC flow plays a marginal role in the dissolution rate.

computation of Sh is based on the equivalent (time-dependent) diameter of a sphere with the same volume, i.e. $L_{\text{ref}}(t) = 2(3V_b/(4\pi))^{1/3}$, but the reference area used for the mass transfer coefficient (k_m) is the effective area of the interface A_Σ. The plots of the Sherwood number show a similar profile until $t \approx 0.06\,\text{s}$, where the size of the bubble is larger and the buoyancy effects are more relevant. However, for $t > 0.06\,\text{s}$, two different patterns that characterise cases A,B and C,D respectively are clearly observable. In the higher rotating speed cases ($Re = 3000, 5000$), the Sh number is enhanced by the turbulent Taylor-Couette flow structures that develop within the reactor, whilst almost no difference is observed between the steady case ($Re = 0$) and the laminar wavy vortex regime ($Re = 1000$). Interestingly, for $Re = 3000$ the Sh number is larger than for $Re = 5000$, meaning that no benefits are obtained by further increasing the rotating speed of the reactors. However, such differences occur when the bubble volume is already significantly reduced ($V_b/V_b^{t=0} < 0.3$) and

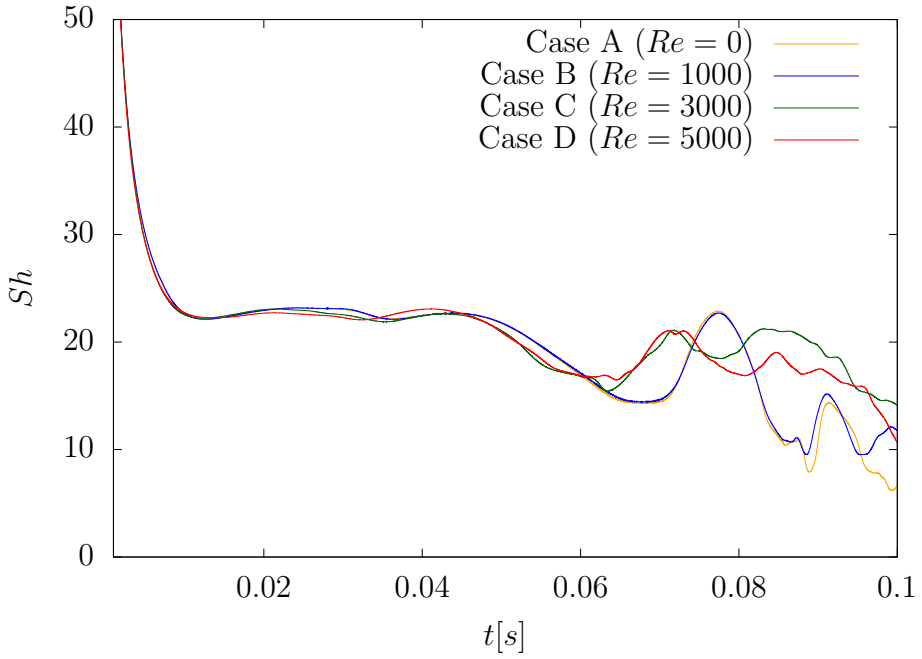

Figure 7.21: Sherwood number Vs time for a dissolving bubble in a TCR at different rotating speeds. The Sh number is based on the diameter of the equivalent sphere (see text).

no relevant effects in terms of dissolution rates can be observed afterwards. Cases A-B show a local peak around $t \approx 0.08\,\mathrm{s}$ that is larger than the values of Sh for cases C-D; as will be shown later, this effect is due to the corresponding rising speed of the bubble.

When the rotating speed of the inner cylinder is increased, the magnitude of the main (azimuthal) velocity component of the carrier fluid grows and the motion of the bubble is affected accordingly. Figure 7.22 compares the trajectory of the bubble centre on the horizontal XY plane for cases A-D (it is reminded here that the axis of the reactor is aligned with the z-direction). When no rotation is used, the bubble rises following an almost perfect rectilinear trajectory and no path can be identified on the horizontal plane. As the reactor Reynolds number is increased, the liquid velocity (combined with gravity) induces a zigzag motion of the bubble, which results in a net anticlockwise displacement on the XY plane (according to

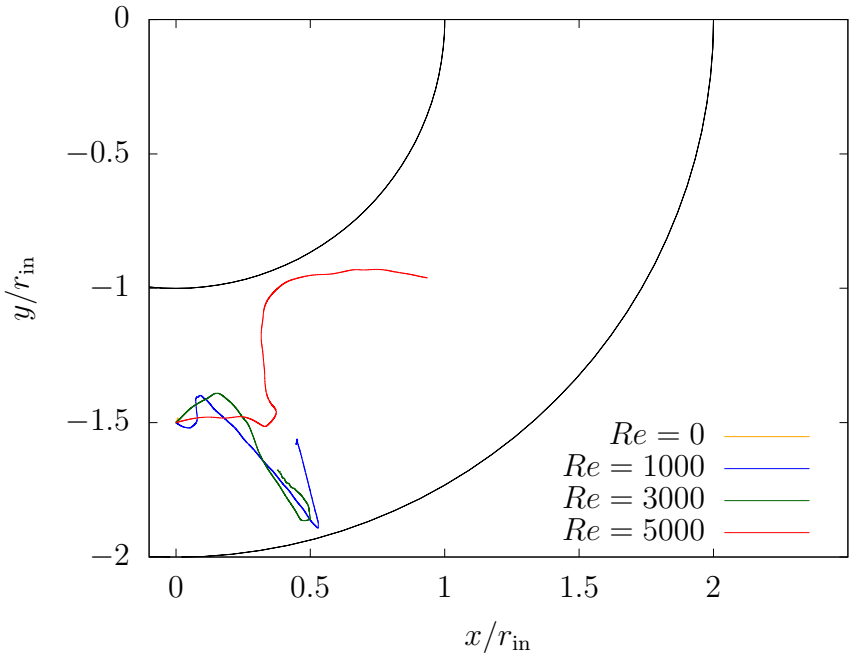

Figure 7.22: Bubble trajectories on the horizontal XY plane in a TCR at different rotating speeds. Bubbles are initialised at $x = 0, y = -1.5r_{\text{in}}$.

the rotation of the rotor). The cases with $Re = 1000$ and 3000 show a very similar path, whilst the largest rotating speed case exhibits a significantly more developed trajectory. In all the configurations with rotation, the bubble bounces off the reactor walls, which act as a container for the bubble motion.

Although the volume dissolution rates are basically the same for cases A-D, such different trajectories provide some useful information for the operation of the reactor. Indeed, when the gas extracted from the disperse phase is needed to perform a chemical reaction within the liquid phase, the more the distribution of the dissolved species is spread in a wide area the more likely is that the reagents react and produce the desired product. The case with $Re = 5000$ results in a more extended trajectory compared to the other cases, which helps distribute the gas in a wider region within the reaction vessel and, eventually, promote reactions. The effects of the trajectory on the (3D) distribution of species is shown in Figure 7.23, where the iso-surfaces

of the gas released into the liquid are compared for cases A-D, along with a contour plot of axial velocity on the YZ plane, which shows the increasing complexity of the TC flow as Re increases (i.e. the transition from WVF to TTVF). The iso-surfaces

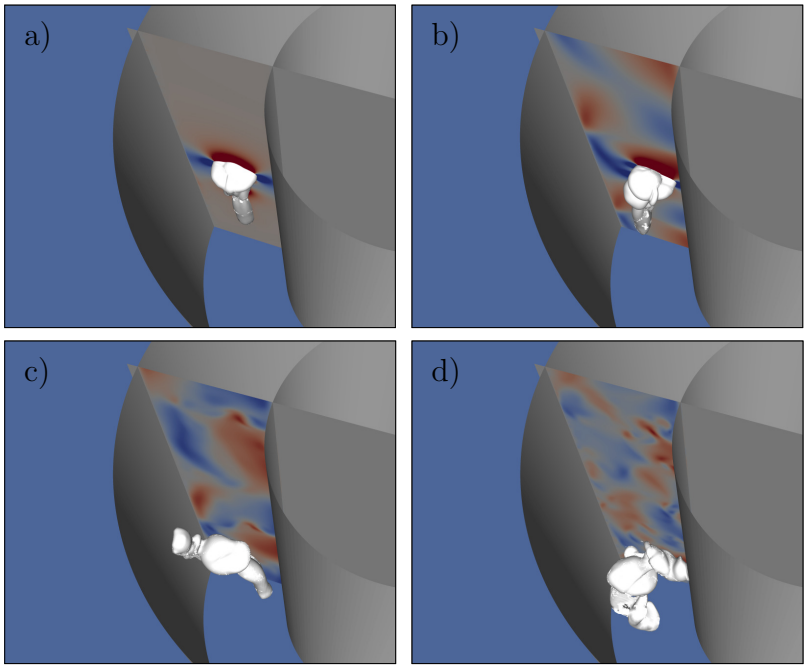

Figure 7.23: Iso-surfaces ($c_c = 0.1\rho_d/M$) of dissolved gas concentration and contours of axial velocity on the YZ plane in a TCR at $Re = 0$ (a), $Re = 1000$ (b), $Re = 3000$ (c) and $Re = 5000$ (d). Snapshots taken at $t = 0.1\,\mathrm{s}$.

clearly show the effect of the rotor speed (and the corresponding TC regimes) on the species distribution. When the rotor is steady (Figure 7.23a), a symmetric iso-surface develops around the bubble and inside the wake. As the rotor is accelerated, the topology of the iso-surface becomes more distorted and, in the fully turbulent case at $Re = 5000$ (Figure 7.23d), the distribution of species results well mixed within a wide region below the bubble. As explained earlier, this is the most desirable scenario for the enhancement of the production yield of a chemical reaction when the dissolved gas is one of the reactant species. Therefore, it can be concluded that, although no major differences are observed in these cases for the dissolution rates, the promotion of turbulent (chaotic) Taylor vortices is a desirable feature for the

enhancement of species mixing within the reactor and, eventually, the production of chemical compounds.

Many attempts have been made in the literature to provide formulae for the prediction of Sherwood numbers in rising bubbly flows and, although no formula can be generic enough to be independent of the specific flow configuration, most of the available correlations relate Sherwood and Reynolds numbers in a sort of proportionality law of the type $Sh \propto Re_b^{\lambda}$, where λ is a configuration-specific coefficient (see section 2.3.1). To the best of the author's knowledge, no specific relationships have been investigated for the mass transfer of a single bubble in a Taylor-Couette flow at different rotating speeds (and TC flow regimes). Here, the correlation between Sherwood and Reynolds numbers is first investigated for cases A-D and the results are reported in Figure 7.24, where the reference length used for Re_b is the equivalent diameter of a sphere (as is done for Sh). In all the tested configurations, the plots of the Reynolds numbers exhibit a similar trend until $t \approx 0.07\,\mathrm{s}$, where a maximum peak is observed. In the first part of the simulation, the buoyancy force makes the bubble less sensitive to the carrier flow, which explains why the plots have a similar shape but, interestingly, the magnitude of the maximum Re is larger for the no rotation (Figure 7.24a) and $Re = 1000$ (Figure 7.24b) cases than for the high speed configurations ($Re = 3000, 5000$ in Figures 7.24c-d respectively). The reason for this is due to the presence of Taylor vortices, which tend to move the bubble towards stable (outflow) regions where the downward liquid velocity of a vortex counteracts the upward (rising) component induced by gravity (this phenomenon is more relevant for a population of small bubbles that accumulates into clouds of particles, as reported by Murai et al., 2005 - see the discussion in section 2.2.2). This effect is significantly stronger as the strength of Taylor vortices increases and explains why the maximum observed peak of Reynolds number is larger in cases A-B than the fully turbulent cases C-D, where the rising speed is limited by the flow structures. For $t > 0.07\,\mathrm{s}$, cases A-B have a similar trend with a strong fluctuating profile and an almost constant mean value, whilst cases C-D have weaker oscillations but an average decreasing value of Re over time. The plots of Sherwood numbers in Figure 7.24 clearly show that Sh and Re are intrinsically related, since both profiles appear

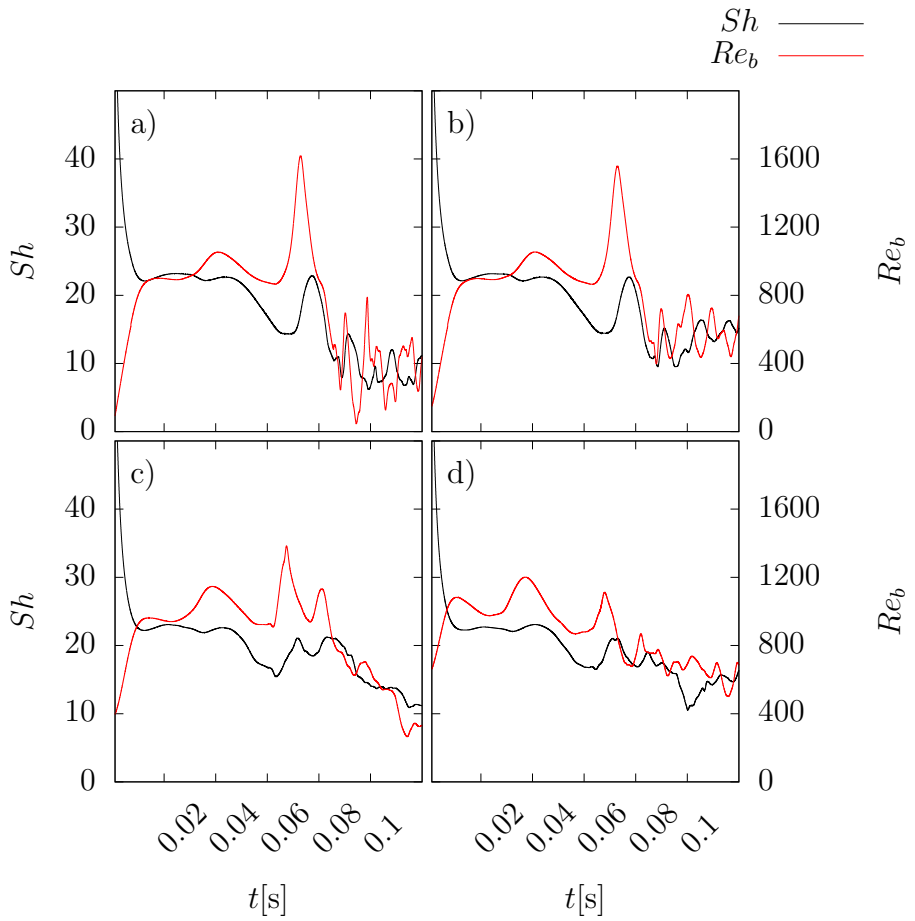

Figure 7.24: Plots of Sh and Re numbers Vs time for a dissolving bubble in a TCR at $Re = 0$ (a), $Re = 1000$ (b), $Re = 3000$ (c) and $Re = 5000$ (d). The similarity of the profiles suggests a functional relationship between Sh and Re, as found for rising bubbles in (unbounded) quiescent flows.

similar to each other and the peaks occur approximately at the same time (with a small delay in the Sherwood plot) for all the tested configurations. Given this correlation, it is not surprising that cases A-B show a larger Sh number than cases C-D at $t \approx 0.07\,\mathrm{s}$, as was observed (but not explained) in Figure 7.21.

Following the qualitative results presented in Figure 7.24, a conceptually equivalent proportionality law between Sh and Re to the ones proposed in the literature for a rising bubble is expected to be valid also in the case of a TC flow. Here the Sher-

wood profiles for cases A-D are compared against the theoretical formulae proposed by Oellrich et al., 1973 for small bubbles:

$$Sh = 2 + 0.651 \frac{Pe^{1.72}}{1 + Pe^{1.22}} \quad \text{for } Re_b \to 0, Sc \to \infty \tag{7.30}$$

and for large bubbles:

$$Sh = 2 + \frac{0.232 Pe^{1.72}}{1 + 0.205 Pe^{1.22}} \quad \text{for } Re_b \to \infty, Sc \to 0 \tag{7.31}$$

Equations 7.30 - 7.31 provide two opposite range limits for Sh and are generally used to predict the mass transfer of a single rising bubble in a steady-state regime, i.e. when Pe is time-independent (see Deising et al., 2018). For the considered application, the Péclet number ($= ReSc$) changes over time and formulae 7.30 - 7.31 are compared against the numerical results by replacing Pe with $Pe(t)$ in Figure 7.25. Since correlation formulae for Sh are generally based on the surface of the equivalent sphere (A_{sphere}), a correction factor (Sr) is needed for the numerical results (which are based on the effective surface A_Σ) to compare against the theoretical equations:

$$Sr = \frac{A_\Sigma}{A_{\text{sphere}}} \tag{7.32}$$

Sr, which is always ≥ 1, is also known as shape factor and provides a parameter for the estimation of the bubble distortion. As the bubble dissolves, the surface tension becomes more relevant (larger curvature) and the bubble approaches the spherical shape, i.e. $Sr \to 1$. The results reported in Figure 7.25 show that the qualitative trend of the corrected Sherwood number (i.e. $Sh \times Sr$) is correctly reproduced by the theoretical formulae of Oellrich et al., 1973, where the solution is closer to equation 7.31 in the first part of the simulation (where the bubble is larger) and progressively approaches equation 7.30 as the bubble dissolves, coherently with the range of validity of these formulae. The trend of a decreasing Sherwood when the Reynolds number reduces (e.g. in the last part of the simulation, for $t > 0.08\,\text{s}$) is also correctly reproduced. Similar conclusions are obtained in Maes and Soulaine,

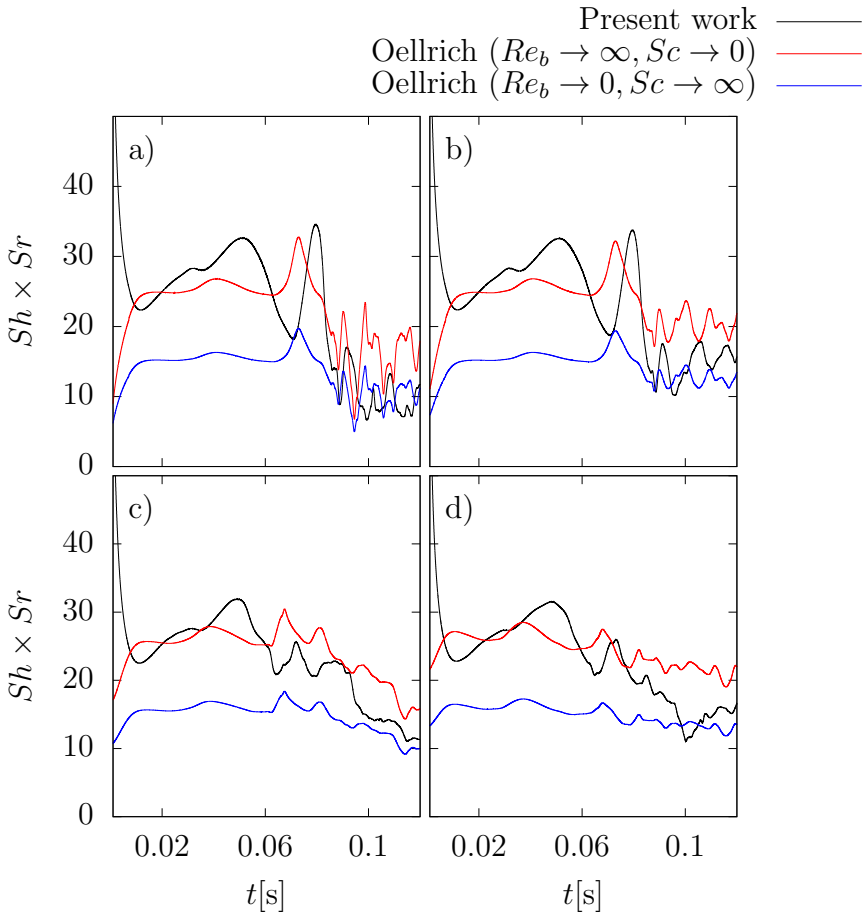

Figure 7.25: Comparison of the corrected Sherwood number against the theoretical formulae proposed by Oellrich et al., 1973 for $Re = 0$ (a), $Re = 1000$ (b), $Re = 3000$ (c) and $Re = 5000$ (d).

2020 for a dissolving bubble rising in a quiescent flow and the present results confirm that volume change effects can be qualitatively taken into account by replacing the steady-state non-dimensional numbers with the corresponding time-dependent ones in the appropriate correlation formulae.

As is shown in Figure 7.25, equations 7.30 - 7.31 can be used as qualitative references for the expected Sherwood number of a rising bubble in a TCR. However, a quantitative accurate match between the present results and these correlations can-

not be obtained, as the theoretical formulae are derived assuming a spherical shape of the bubbles and a rectilinear rising trajectory. For the analysed configurations, the combined effect of gravity, TC flow and phase-change induce strong deformations ($Sr > 1$) in the bubble shape, which are compared in Figure 7.26 for cases A-D, along with the corresponding shape factors. Bubbles are initialised as perfect

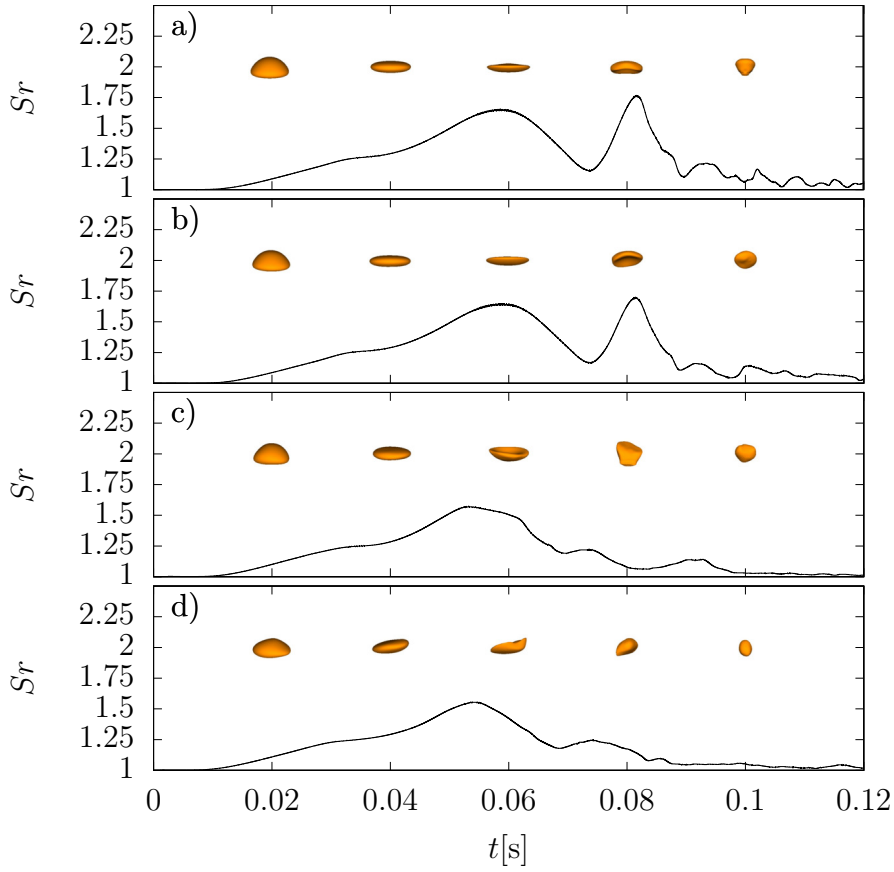

Figure 7.26: Shape factor and bubble shapes Vs time for a dissolving bubble in a TCR at $Re = 0$ (a), $Re = 1000$ (b), $Re = 3000$ (c) and $Re = 5000$ (d).

spheres (i.e. $Sr^{t=0} = 1$) and, as soon as the buoyancy force makes the bubble rise, the interface assumes the typical dimple shape that can be observed at $t \approx 0.02\,\mathrm{s}$. The shape factor increases accordingly until $t \approx 0.06\,\mathrm{s}$ for cases A-B (Figures 7.26a-

b) and $t \approx 0.055\,\mathrm{s}$ for cases C-D (Figures 7.26c-d), where a local maximum peak is reached. The corresponding deformations are different between the first two cases (ellipsoidal shape) and the fully turbulent ones (reverse dimple); the relative shape factors also differ and are stronger for cases A-B ($Sr \approx 1.65$) than for configurations C-D ($Sr \approx 1.56$). After this peak, two different behaviours can be observed: for the no rotation and $Re = 1000$ cases, a second maximum peak is reached slightly after $t = 0.08\,\mathrm{s}$ of approximately $Sr \approx 1.75$, where the bubbles approach a (less pronounced) dimple shape, whilst for cases $Re = 3000, 5000$ the profiles don't have such a significant peak and irregular shapes can be observed. As the volume of the bubble decreases, the surface tension force becomes dominant and all the bubbles move towards a spherical shape ($Sr \to 1$).

Cases without gravity

As was discussed at the beginning of this section, the motion induced by the buoyancy force is the most relevant component for the configurations analysed so far, i.e. cases A-D. For the rest of the section, the focus is on cases E-G (see Table 7.9), where the initial bubble size is kept the same (i.e. $D_b^{t=0} = 0.005\,\mathrm{m}$) and gravity is neglected. The effect of the rotor speed is first investigated by comparing the bubble volume dissolution rates in Figure 7.27 for these cases. The bubble dissolves now significantly faster as the inner cylinder is accelerated, contrary to the cases with gravity (see Figure 7.20) where the dissolution rates were independent of the rotor speed. This is the expected behaviour, since the bubble velocity is now entirely given by the carrier liquid, whose main (azimuthal) velocity component increases with the rotating speed.

The effect of increasing bubble Reynolds number (R_b) on Sh is shown in Figure 7.28 for cases E-G. As expected, the Sherwood number increases as the rotor is accelerated and, after a transient regime where Sh decreases whilst a concentration boundary layer develops around the bubble interface, the profiles approach a steady-state solution with a quasi-constant value over time. Some qualitative differences between the laminar case ($Re = 1000$) and the fully turbulent ones ($Re = 3000, 5000$) can be observed in the plots of Figure 7.28. The presence of unstable and chaotic

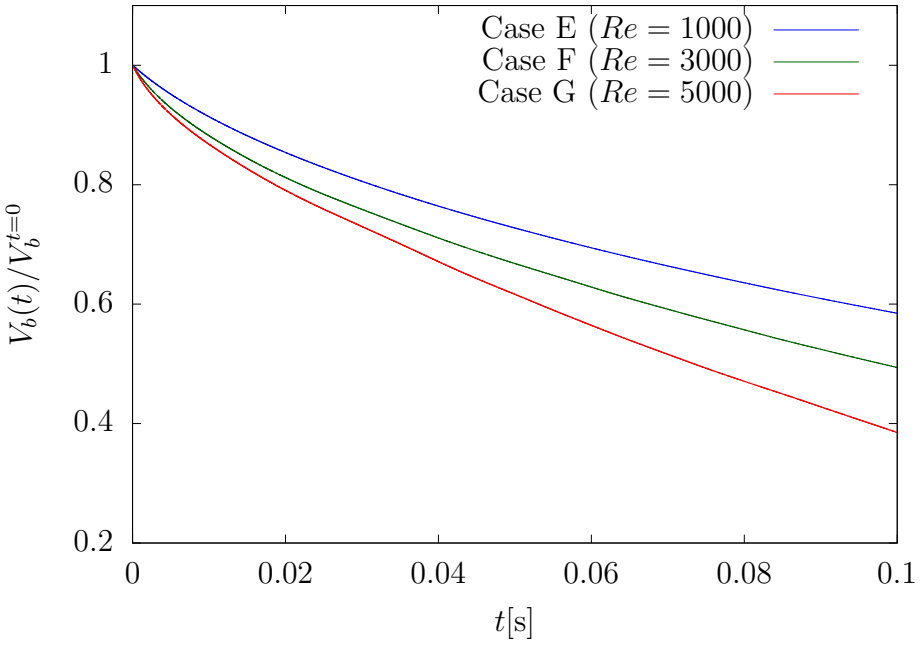

Figure 7.27: Volume ratio Vs time for a dissolving bubble in a TCR at different rotating speeds. Gravity is not taken into account.

Taylor vortices induce some fluctuations in the Sherwood profiles for the turbulent cases, whilst the well organised and steady flow structures that develop in the laminar regime do not introduced analogous perturbations in case E.

Apart from these qualitative observations, the volume ratio and Sherwood number are integral parameters that are mainly affected here by the main component of the TC flow (i.e. the azimuthal velocity) and do not provide insights into the effects of the different TC regimes that characterise the reactor at different Reynolds numbers. To look into the effects of Taylor vortices on the distribution of the dissolved species in the liquid phase, the contours of species concentration for cases E-G are compared in Figure 7.29. The concentration for case E (Figures 7.29a-b) appears uniform around the interface of the bubble and quite similar to the symmetric distribution that characterises a suspended bubble in a stagnant flow (see section 6.2.3), meaning that the effect of Taylor vortices is marginal at $Re = 1000$. On the other hand, in

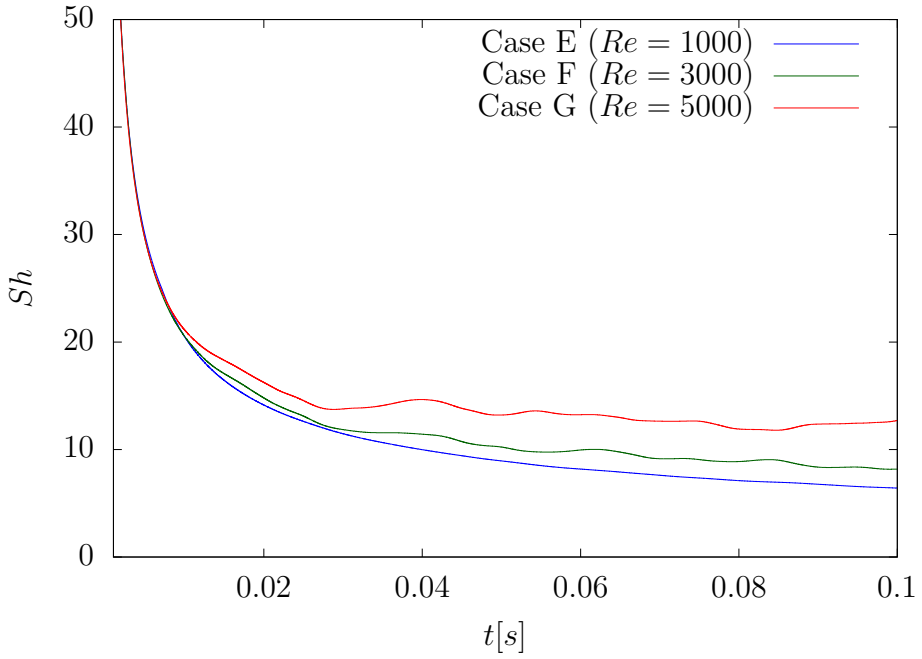

Figure 7.28: Sherwood number Vs time for a dissolving bubble in a TCR at different rotating speeds. Gravity is not taken into account.

cases F (Figures 7.29c-d) and G (Figures 7.29e-f), the effect of the turbulent Taylor cells is clearly visible in the spatial distributions of species concentration, which now assume irregular and non-symmetric shapes around the bubble. The position of the bubble centre in the vertical plane can be tracked by looking at the wake left by the dissolution of species (Figures 7.29b-d-f), and it can be observed that the bubble stays at a constant axial position for $Re = 1000$, whilst in the turbulent cases ($Re = 3000, 5000$) it moves upwards, transported by the upward velocity induced by the vortices. These results confirm that, in case E, Taylor cells play a marginal role and the bubble behaves as a particle transported by the azimuthal velocity component, whilst for the TTVF regime (cases F-G) Taylor vortices actively contribute to the dynamics of the bubble and distribute the concentration of the dissolved species in a wider region around the interface, which is a desirable scenario for a good mixing of the chemicals (as was discussed earlier in this section). It is finally observed that the

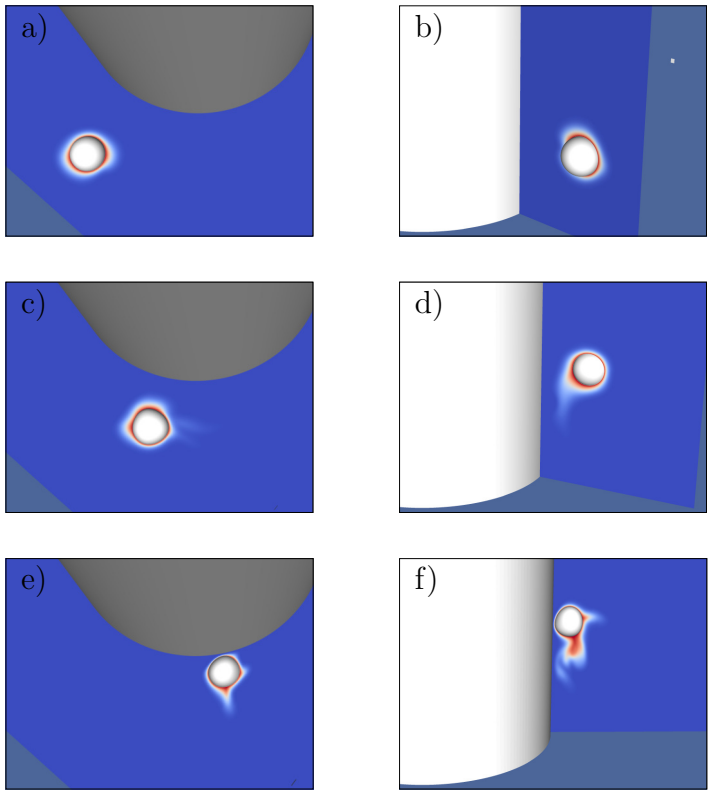

Figure 7.29: Contours of species concentration and bubble interface in a TCR without gravity at $Re = 1000$ (a-b), $Re = 3000$ (c-d) and $Re = 5000$ (e-f). Top view (left) and side view (right). The outer cylinder has been removed for a better visibility.

concentration patterns shown in Figure 7.29 have a significantly different structure compared to the case of a rising bubble. Indeed, for rising bubbles (see section 6.2.4), the concentration boundary layer is thinner on top (where advection counteracts the effect of diffusion) and becomes thicker towards the rear of the bubble. For the case of a bubble transported by a TC flow without gravity, the convective transport induced by the azimuthal velocity component has the same magnitude on both the top and bottom sides of the bubble and its effect is uniform around the interface

(Figures 7.29a-c-e), contrary to the convective component induced by Taylor vortices, which acts on the radial-axial plane and depends on the bubble position and flow configuration.

Figure 7.29 also shows the shape of the bubbles, which appears almost spherical ($Sr \approx 1$) for all the tested configurations. This happens because the shear rate induced by the TC flow is not strong enough to overcome the surface tension and induce significant deformations of the interface, contrary to cases A-D where gravity was responsible for strong deviations from the spherical shape (see Figure 7.26).

Finally, it is concluded that the analysis of the mass transfer of a single bubble in a Taylor-Couette reactor without gravity can provide useful quantitative and qualitative information for the situations in which small bubbles are trapped into stable patterns and the rising velocity is limited by the presence of Taylor vortices. These scenarios have been documented in the literature and the interested reader is referred to Chouippe et al., 2014 and Murai et al., 2008 for more details.

Chapter 8

Conclusions and Future Work

The main goal of the present thesis was to develop a high-fidelity framework for direct numerical simulations of diffusion-driven phase-change problems with soluble species in two-phase flows. The modelling of this class of flows poses some challenges related to the discontinuities that characterise the profiles of concentration and velocity across the gas-liquid interface. A special emphasis was put on the treatment of such discontinuity that led to the development of an original approach for the redistribution of the mass transfer term from the interfacial cells to the neighbouring pure gas ones (chapter 5); this is certainly the most important contribution of this work in terms of numerical methodology. The method is implemented in the open-source code Basilisk (http://basilisk.fr/), which provides a solver for the solution of DNS of incompressible two-phase flows, coupled with a geometric VOF method for the interface tracking (see chapter 4). Given the type of VOF solver implemented in Basilisk (i.e. a geometric method based on the PLIC algorithm), the concentration of species is treated with a two-scalar approach (Bothe and Fleckenstein, 2013), where two transport equations (one for each phase) are solved for each species. This approach guarantees that no artificial mass transfer occurs during the convective transport of molar concentration and a similar strategy is implemented for the treatment of the diffusive term.

The proposed methodology is validated against several analytical, numerical and experimental benchmarks that include the cases of suspended and rising bubbles, the

Stefan problem for a planar interface and the competing mass transfer in a mixture of species (chapter 6). A good agreement is observed for all the proposed test cases and the following conclusions can be inferred.

- The algorithm for the redistribution of the mass transfer term ensures that the velocity field is compliant with the kinematic constraint of the VOF method and guarantees mass conservation during the advection of the interface. On the other hand, if the source term is kept in the interfacial cells, the resulting face velocity field is not consistent with the VOF transport and distorted interfaces are expected, where the mass is no longer conserved.

- The adaptive mesh refinement technique is a valuable tool for the modelling of this type of interfacial phenomena, where a fine mesh resolution is generally needed only around the gas-liquid interface. The Péclet number can be used as an indicator for the grid refinement required to capture the concentration boundary layer. Larger Pe numbers lead to steeper concentration profiles and, therefore, finer spatial resolutions must be employed. In the present thesis, a mesh sensitivity study for rising bubbles at different Pe numbers has shown that more than 2000 cells per diameter are needed for $Pe = 46500$. However, such grid density is only required at the interface and AMR can be used to significantly reduce the computational cost of the simulations.

- In the general case of moving bubbles (e.g. rising bubbles), the distribution of mass transfer is highly non-uniform at the bubble interface, where both positive and negative rates can exist at the same time in different parts of the interface. Therefore, the use of high-fidelity resolved simulations, where local mass transfer is computed for all the interfacial cells, can provide detailed information on the phase-change process that is inherently lost when correlation models are used instead.

- The modelling of non-uniform mixtures of species (where competing mass transfer occurs amongst its components) adds some more challenges to numerical simulations since the transport of species needs to be solved also in

the disperse phase. The redistribution of the mass transfer term introduces a non-null divergence of the velocity field in a layer of pure gas cells adjacent to the interface. In these cells, the convective transport fluxes of the species need to be corrected to preserve the mass of the mixture (see chapter 5.3.1).

The validated methodology has been applied to the study of two industrially relevant applications (chapter 7), namely the growth of bubbles on planar electrodes and the mass transfer of a bubble in a Taylor-Couette reactor.

In the case of electrochemical cells, bubbles nucleate on the electrodes as a result of spontaneous chemical reactions that occur in the electrolytic solution. The generation of bubbles is generally detrimental for the performance of the reactor and strategies to control and remove the formation of gas are currently employed. Due to the increasing demand of certain types of chemicals (e.g. green hydrogen production), the actual trend in industry is to scale-up such devices to larger sizes. This, combined with the use of higher current densities, makes the problem of gas generation even more relevant and new design approaches are currently investigated to keep the efficiency of these devices to a high standard. High-fidelity simulations provide detailed information on the growth of bubbles and can be used to inform low-order models that are currently employed in industrial design processes. In this thesis, a circular electrode is considered and the growth rate of bubbles at different contact angles and current densities are modelled. This study led to the following conclusions:

- The growth rate of small bubbles ($D_b < 0.1\,\mathrm{mm}$) attached to a planar wall follows the functional law of Scriven ($D_b \propto \sqrt{t}$) for suspended bubbles, as found in experiments (Glas and Westwater, 1964).

- When small bubbles are modelled, surface tension effects dominate over the buoyancy force, keeping the shape of the bubble spherical. Gravity can then be neglected and σ can be reduced to a value large enough to preserve the spherical shape. This is particularly helpful to reduce the computational cost of simulations, since larger time steps can be adopted. This approach is clearly

valid until the bubble is attached to the electrode and the volume is small enough to keep the effect of gravity marginal.

- The dynamics of the contact line plays a crucial role in the growth of bubbles attached to a wall. Decreasing the contact angle leads to more elongated bubbles, which are less exposed to the supersaturated region next to the electrode and result in smaller growth rates.

- In practical applications, several bubbles are expected to nucleate at the same time in different locations, due to the presence of multiple defects on the electrode surface. This aspect needs to be taken into account when experiments are replicated, since the growth rate is significantly affected by the number of bubbles that contemporaneously adsorb the gas produced at the electrode. In the present thesis up to four bubbles are considered and, compared to the single bubble cases, a reduction in the growth rate between 31% - 17% is observed in the range of current densities $100\,\mathrm{A\,m^{-2}} - 1000\,\mathrm{A\,m^{-2}}$.

The second part of the applications is devoted to the study of mass transfer in a two-phase Taylor-Couette reactor. This type of reactors have shown excellent mixing properties but some limitations due to the complex design and lack of mass transfer correlations make them difficult to be scaled up and meet industrial production standards. In the present work, several configurations of TCR reactors are modelled and the characteristics of the velocity field are investigated. Then a single bubble is injected at the bottom of the reactor and the effects of the rotor speed on the mass transfer is investigated. The main conclusions from this study are summarised in the following.

- The non-uniqueness feature of Taylor-Couette flows requires a careful treatment of the numerical setup. In this work, periodic boundary conditions are used to model a representative section of the reactor with at least two pairs of counter-rotating vortices. The axial extension of the domain must therefore be selected based on the expected vortex wavelength. A wrong choice would lead the solver to find an alternative stable configuration (i.e. number of vortices) that

does not match the experimental observed state. For the same reason, when a specific experimental procedure is adopted for the start up of the reactor, the same strategy should be implemented in the numerical model to reproduce the same flow configuration.

- In this work, a bubble with diameter $Db = 5\,\text{mm}$ is injected in a reactor with a gap size of 15 mm. For this configuration, the rising speed induced by the buoyancy force is predominant over the main velocity component of the TC flow and the bubble dissolution rate is not significantly affected by the reactor speed in the range $Re = 0 - 5000$.

- On the other hand, the effect of the Reynolds number and the associated TC regimes have a strong impact on the distribution of the dissolved species. As the rotating speed is increased and fully turbulent vortices develop within the reactor, the concentration of species released from the bubble distributes in a wider area around the bubble wake. This improved mixing is beneficial to promote chemical reactions that involve the dissolved gas.

- As for the case of rising bubbles in a quiescent flow (e.g. bubble column reactors), a clear correlation between Sh and Re numbers is observed for all the modelled TC regimes. Theoretical formulas generally assume the bubbles to be spherical and are not directly applicable to this specific flow configuration, where highly distorted interfaces are observed. However, the correlations provided by Oellrich et al., 1973 for small and large bubbles provide two qualitative limits that bound the corrected Sh profile. This result leads to the conclusion that the range of validity of these correlation models can be extended by taking into account the relevant time-dependent quantities and introducing an appropriate correction factor for non-spherical shapes.

- The modelling of a bubble in absence of gravity provides useful information to quantify the effect of the different TC regimes for the cases in which the buoyancy force is marginal (e.g. small bubbles). In this specific case, volume

dissolution occurs significantly faster for increasing rotating speeds. The distribution of species is also positively affected by the fully turbulent regime, where the formation of strong vortices helps to enhance the mixing within the reactor. Although this approach cannot substitute the modelling of actual smaller bubbles, it still provides useful information (at a relatively low computational cost) for the cases in which bubbles are trapped inside a vortex.

From the conclusions drawn in this chapter and, more generally, from the hypothesis behind the phase-change model, it appears evident that there are at least two areas where the proposed methodology could benefit from some improvement, namely the computational cost and the fidelity of the modelled physics. To address these points, the following considerations and suggestions could be taken into account:

- The cost of the simulations for rising bubbles is mainly determined by the Péclet number, which in realistic applications could be as large as 10^5. The reason for that is related to the thickness of the concentration boundary layer, which approximately scales as $\delta_c \propto Pe^{-1/2}$. A possible workaround comes from the consideration that the mesh density required for the hydrodynamic part (i.e. the solution of the Navier-Stokes equations) is generally less expensive (for $Sc > 1$) than the resolution needed to capture the mass transfer. To avoid a further increase in the grid refinement, a subgrid-scale (SGS) modelling of the concentration boundary layer could be implemented. This was performed, for example, in Weiner and Bothe, 2017, where the authors managed to obtain a reduction of a factor of ten for the mesh resolution at the interface.

- The implementation of a SGS model could open the way to a more systematic study on the mass transfer in a Taylor-Couette reactor, where smaller and/or multiple bubbles could be investigated. A particularly interesting configuration is the scenario in which the buoyancy force and TC vortices balance out. In this situation, a stronger sensitivity to the TC regime is expected, as anticipated from the study without gravity effects presented in this work. However, it should be taken into account that this configuration differs significantly from

the case of a rising bubble and a SGS model that works in the last case could not be valid for the former one.

- To derive the phase-change model in this thesis, some simplifying assumptions have been used. More accurate physics should take into account additional phenomena, including:
  - Compressibility effects for mixtures of species, where the density of the disperse phase is not constant due to the non-uniform chemical composition.
  - The evaporation of the liquid phase into the gaseous one.
  - The dependence on interfacial pressure jump (especially for large curvatures) and temperature in Henry's law coefficient, i.e. $H_e = H_e(p_c, p_d, T)$.
  - The implementation of a dynamic contact line model for the case of growing bubbles on walls.

The implementation of these features would make the methodology a step closer to the complex physics that characterises phase-change phenomena and would help to fill the gap between high-fidelity simulations and more industrially-relevant applications.

Appendix A

Spatial grid convergence

The accuracy of the numerical scheme used for the gradient of concentration at the interface (equation 5.36) and the overall (Navier-Stokes + phase-change) solver are tested here for the Stefan problem presented in section 6.2.2.

The gradient scheme consists of two first-order derivatives and is reported here for the reader's convenience (see section 5.4 and Figure 5.7 for more information):

$$-\frac{\partial c_{c(i,j)}}{\partial \mathbf{n}_\Sigma} = f_c \frac{c_c(P_1) - c_c(P)}{\overline{PP_1}} + (1 - f_c) \frac{c_c(P_2) - c_c(P)}{\overline{PP_2}} \tag{A.1}$$

where the volume fraction of the continuous phase is used as weighting factor between the two terms on the RHS. The concentration profile that develops in the liquid region as the interface moves is given by:

$$c_c(y,t) = (c_c)_\Sigma \left(1 - \mathrm{erf}\left(\frac{y - y_\Sigma(t)}{2\sqrt{D_c t}}\right)\right) \tag{A.2}$$

and a qualitative representation is reported in Figure A.1a. The gradient of concentration at the interface follows from equation A.2:

$$\left(\frac{\partial c_c}{\partial y}\right)_{y=y_\Sigma} = -\frac{(c_c)_\Sigma}{\sqrt{\pi D_c t}} \tag{A.3}$$

The numerical derivative is computed for five different meshes with decreasing grid

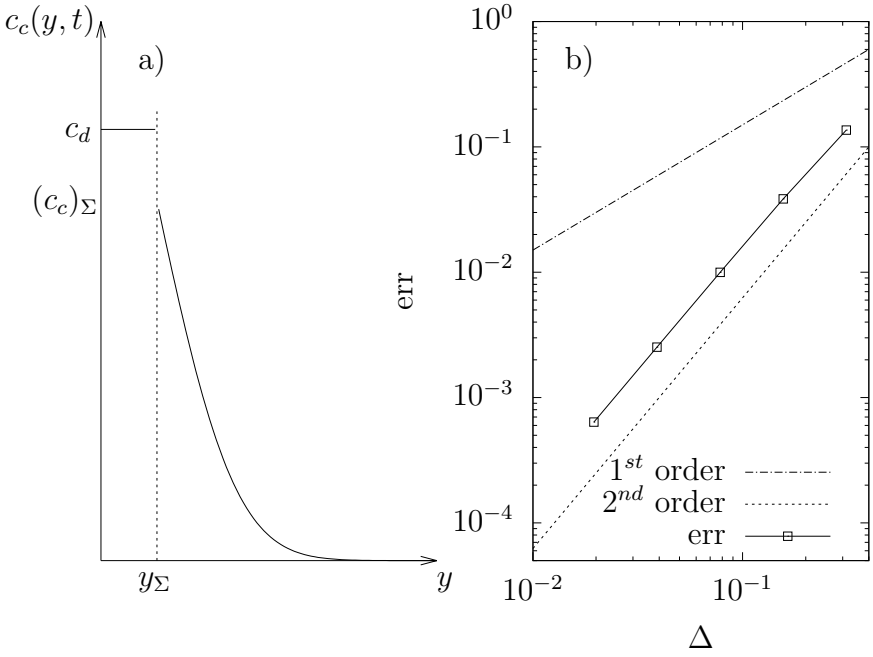

Figure A.1: Characteristic concentration profile of the Stefan problem (a) and grid convergence analysis of the gradient scheme (b). For this specific problem, the method is second-order accurate.

size Δ and the associated discretization error is obtained as

$$\text{err} = \left| \frac{(\partial c_c/\partial y)^{\text{Analyt.}}_{y=y_\Sigma} - (\partial c_c/\partial y)^{\text{Num.}}_{y=y_\Sigma}(\Delta)}{(\partial c_c/\partial y)^{\text{Analyt.}}_{y=y_\Sigma}} \right| \tag{A.4}$$

where $(\partial c_c/\partial y)^{\text{Analyt.}}_{y=y_\Sigma}$ refers to the exact gradient given by equation A.3. The results of the grid convergence analysis are reported in Figure A.1b, where second-order accuracy is reached. The scheme of equation A.1 consists of the weighted average of two-first order terms and is generally expected to be first-order as well. However, for this specific case, the second derivative of species concentration at the interface is null, i.e. $(\partial^2 c_c/\partial y^2)_{y=y_\Sigma} = 0$, and this makes the scheme converge with second-order accuracy.

The overall grid convergence rate of the solver is reported in Figure A.2 for the

Stefan problem discussed in section 6.2.2 (Case A, with $Sc = 5.26$). Five different

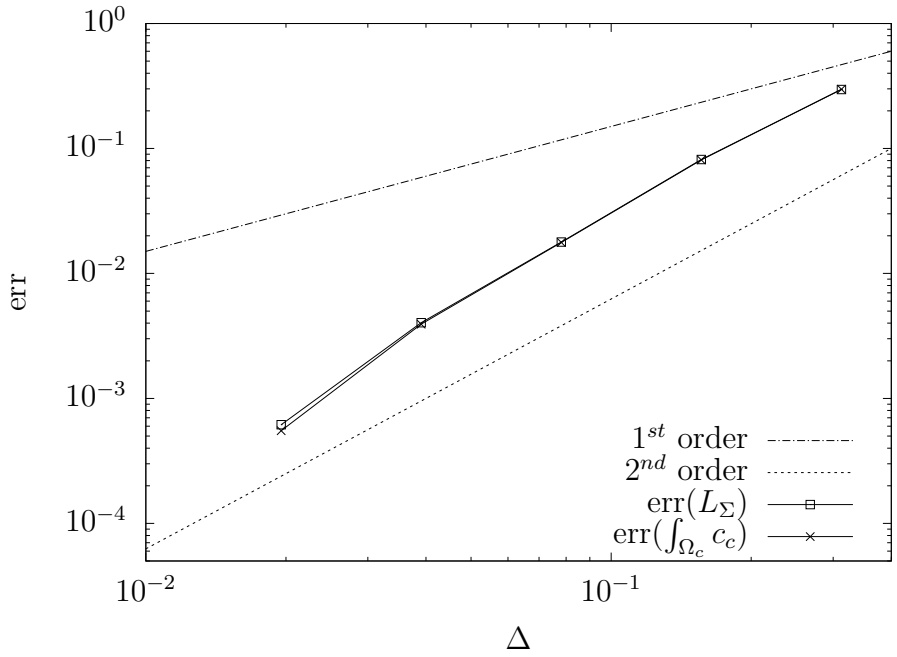

Figure A.2: Grid convergence analysis of the overall solver (NS + phase-change) for the Stefan problem (Case A, section 6.2.2). The global accuracy is second-order.

grids are tested and the analysis of the numerical error is carried out for the interface displacement:

$$L_\Sigma(t) = \frac{2}{H_e}\sqrt{\frac{D_c t}{\pi}} \tag{A.5}$$

and global amount of gas moles dissolved in the continuous region (Ω_c):

$$\begin{aligned}\int_{\Omega_c} c_c(y,t)\,dV \;&= (c_c)_\Sigma L0\left[\left(\frac{L0}{2} - y_\Sigma\right)\operatorname{erfc}\left(\frac{L0/2 - y_\Sigma}{2\sqrt{D_c t}}\right) + \right. \\ &\left. - 2\sqrt{\frac{D_c t}{\pi}}\, e^{\frac{-(L0/2-y_\Sigma)^2}{2\sqrt{D_c t}}} + 2\sqrt{\frac{D_c t}{\pi}}\right]\end{aligned} \tag{A.6}$$

The results show that the method converges with second-order accuracy for both quantities, consistently with the previous analysis and the general order of the Navier-

Stokes solver (see section 4.3). Finally, it is reminded here that the convergence rate is second-order accurate for this specific problem and that the general accuracy of the gradient scheme is first-order only.

Appendix B

A note on the consistency between the transport of volume fraction and momentum

As was pointed out in section 5.4, the projection step that enforces the continuity equation and the transport of the Heaviside function have different source terms related to the interfacial mass transfer ($\dot{m}'$ and $\dot{m}$, respectively). However, the (convective) transports of the interface and momentum are performed with the same face-centred velocity field obtained from the projection step, which makes these two terms consistent to each other.

Here, such consistency property is demonstrated for the case presented in section 6.2.1 of an expanding bubble with a constant mass transfer rate. As the bubble grows, part of the liquid is pushed across the external boundaries and leaves the computational domain (see Figure B.1). This happens because when an element of liquid is converted into gas, its volume increases (due to the lower density of gas, i.e. $\rho_d < \rho_c$) and, given the incompressibility of the phases, part of the liquid is forced to exit the domain. The amount of liquid (dm) that crosses the boundaries in a

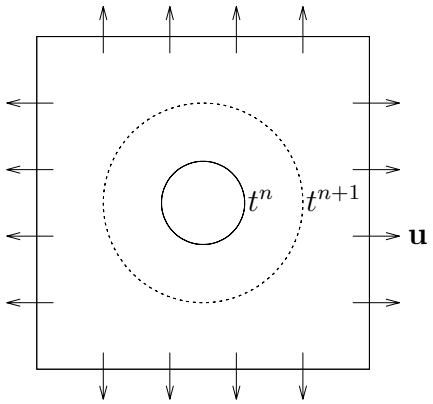

Figure B.1: Growing bubble with a constant mass transfer rate. As the bubble expands, part of the surrounding liquid leaves the domain.

timestep Δt can be quantified from both the fluxes of momentum:

$$dm^{\text{flux}} = \Delta t \oint_{\partial\Omega_c \setminus \Sigma} \rho_c |\mathbf{u} \cdot \mathbf{n}| \, dS \tag{B.1}$$

and from the evolution of the liquid volume fraction field (f):

$$dm^f = \left| \int_\Omega \tilde{f} \rho_c \, dV \; - \int_\Omega f^{n-1/2} \rho_c \, dV \; \right| \tag{B.2}$$

where $\tilde{f}$ is the volume fraction at time $t^{n+1/2}$ right after the advection step, but before the phase-change term is applied (see section 5.1). It is reminded here that f is advanced in time from $t^{n-1/2}$ to $t^{n+1/2}$ (see section 4.2.2). The imbalance between dm^{flux} and dm^f is monitored during the simulation as:

$$\text{err} = \left| \frac{dm^f - dm^{\text{flux}}}{dm^f} \right| \tag{B.3}$$

and the profile reported in Figure B.2 shows that the relative error decreases constantly and approaches a value below 0.01% at the end of the simulation. This test, therefore, demonstrates that the advection of the interface and momentum fields are performed in a consistent way.

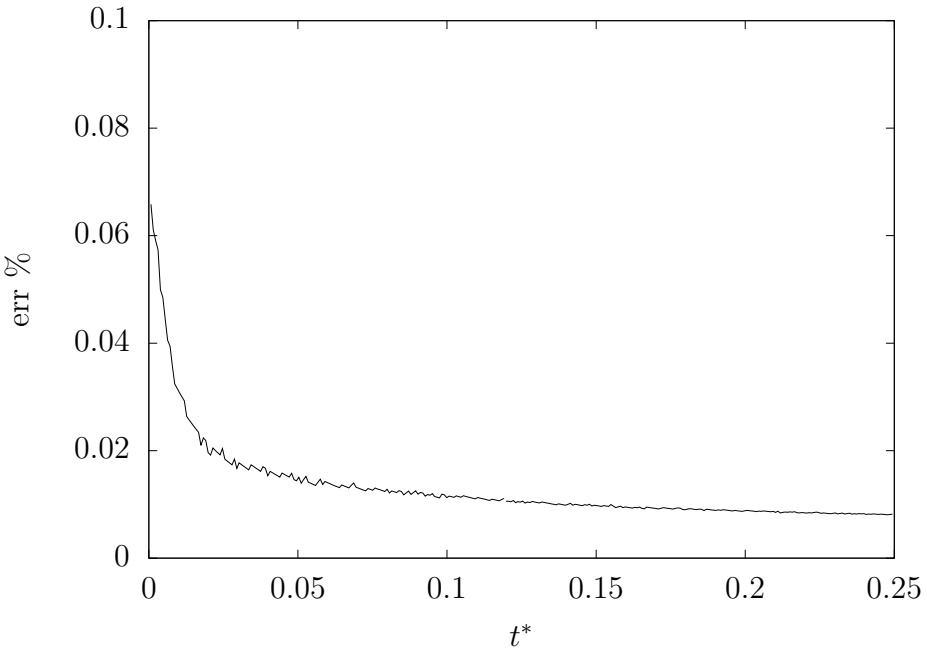

Figure B.2: Relative error of the imbalance between the amount of liquid that leaves the domain based on the boundary fluxes of momentum (dm^{flux}) and volume fraction field (dm^f).

Bibliography

Afkhami, S., & Bussmann, M. (2009). Height functions for applying contact angles to 3d vof simulations. *International Journal for Numerical Methods in Fluids*, *61*(8), 827–847. https://doi.org/https://doi.org/10.1002/fld.1974

Alke, A., Bothe, D., Kroeger, M., & Warnecke, H. (2009). Vof-based simulation of conjugate mass transfer from freely moving fluid particles. *WIT transactions on engineering sciences*, *63*, 157–168.

Andereck, C. D., Liu, S. S., & Swinney, H. L. (1986). Flow regimes in a circular couette system with independently rotating cylinders. *Journal of Fluid Mechanics*, *164*, 155–183. https://doi.org/10.1017/S0022112086002513

Angulo, A., van der Linde, P., Gardeniers, H., Modestino, M., & Fernández Rivas, D. (2020). Influence of bubbles on the energy conversion efficiency of electrochemical reactors. *Joule*, *4*(3), 555–579. https://doi.org/https://doi.org/10.1016/j.joule.2020.01.005

Atykhan, M., Kabdenova (Dauyeshova), B., Rojas-Solorzano, L., & Monaco, E. (2020). *Lattice Boltzmann Model Simulation of Bubble Deformation and Breakup Induced by Micro-Scale Couette Flow* (Vol. Volume 10: Fluids Engineering) [V010T10A008]. https://doi.org/10.1115/IMECE2020-23772

Barcilon, A., Brindley, J., Lessen, M., & Mobbs, F. R. (1979). Marginal instability in taylor–couette flows at a very high taylor number. *Journal of Fluid Mechanics*, *94*(3), 453–463. https://doi.org/10.1017/S0022112079001129

Batten, W. M. J., Bressloff, N. W., & Turnock, S. R. (2002). Transition from vortex to wall driven turbulence production in the taylor–couette system with a rotating

inner cylinder. *International Journal for Numerical Methods in Fluids*, *38*(3), 207–226. https://doi.org/10.1002/fld.208

Bell, J. B., Colella, P., & Glaz, H. M. (1989). A second order projection method for the incompressible navier-stokes equations. *Journal of Computational Physics*, *85*, 257.

Bhaga, D., & Weber, M. E. (1981). Bubbles in viscous liquids: Shapes, wakes and velocities. *Journal of Fluid Mechanics*, *105*, 61–85. https://doi.org/10.1017/S002211208100311X

Bilgen, E., & Boulos, R. (1973). Functional dependence of torque coefficient of coaxial cylinders on gap width and reynolds numbers. *Journal of Fluids Engineering*, *95*(1), 122–126. https://doi.org/10.1115/1.3446944

Bilson, M., & Bremhorst, K. (2007). Direct numerical simulation of turbulent taylor–couette flow. *Journal of Fluid Mechanics*, *579*, 227–270. https://doi.org/10.1017/S0022112007004971

Blanco, A., & Magnaudet, J. (1995). The structure of the axisymmetric high-reynolds number flow around an ellipsoidal bubble of fixed shape. *Physics of Fluids*, *7*(6), 1265–1274. https://doi.org/10.1063/1.868515

Bothe, D. (2015). On the multiphysics of mass transfer across fluid interfaces. *7th International Workshop - IBW7 on Transport Phenomena with Moving Boundaries and More, Fortschr.-Ber. VDI Reihe 3, Nr. 947*, 1–23.

Bothe, D., Koebe, M., Wielage, K., Prüss, J., & Warnecke, H.-J. (2004). Direct numerical simulation of mass transfer between rising gas bubbles and water. In M. Sommerfeld (Ed.), *Bubbly flows: Analysis, modelling and calculation* (pp. 159–174). Springer Berlin Heidelberg. https://doi.org/10.1007/978-3-642-18540-3_13

Bothe, D., & Fleckenstein, S. (2013). A volume-of-fluid-based method for mass transfer processes at fluid particles. *Chemical Engineering Science*, *101*, 283–302. https://doi.org/https://doi.org/10.1016/j.ces.2013.05.029

Brackbill, J. U., Kothe, D. B., & Zemach, C. (1992). A continuum method for modeling surface tension. *Journal of Computational Physics*, *100*(2), 335–354. https://doi.org/https://doi.org/10.1016/0021-9991(92)90240-Y

Britton, J., & Raston, C. L. (2017). Multi-step continuous-flow synthesis. *Chemical Society Reviews*, *46*(5), 1250–1271. https://doi.org/10.1039/C6CS00830E

Bruijn, d. R. A. (1989). *Deformation and breakup of drops in simple shear flows* (Thesis). https://doi.org/10.6100/IR318702

Bunner, B., & Tryggvason, G. (2002). Dynamics of homogeneous bubbly flows part 1. rise velocity and microstructure of the bubbles. *Journal of Fluid Mechanics*, *466*, 17–52. https://doi.org/10.1017/S0022112002001179

Buresti, G. (2012). *Elements of fluid dynamics*. IMPERIAL COLLEGE PRESS. https://doi.org/10.1142/p848

Cadogan, S. P., Maitland, G. C., & Trusler, J. P. M. (2014). Diffusion coefficients of co2 and n2 in water at temperatures between 298.15 k and 423.15 k at pressures up to 45 mpa. *J. Chem. Eng. Data*, *59*(2), 519–525. https://doi.org/10.1021/je401008s

Canedo, E. L., Favelukis, M., Tadmor, Z., & Talmon, Y. (1993). An experimental study of bubble deformation in viscous liquids in simple shear flow. *AIChE Journal*, *39*(4), 553–559. https://doi.org/https://doi.org/10.1002/aic.690390403

Cano-Lozano, J. C., Bohorquez, P., & Martínez-Bazán, C. (2013). Wake instability of a fixed axisymmetric bubble of realistic shape. *International Journal of Multiphase Flow*, *51*, 11–21. https://doi.org/https://doi.org/10.1016/j.ijmultiphaseflow.2012.11.005

Cano-Lozano, J. C., Martínez-Bazán, C., Magnaudet, J., & Tchoufag, J. (2016). Paths and wakes of deformable nearly spheroidal rising bubbles close to the transition to path instability. *Physical Review Fluids*, *1*(5), 053604. https://doi.org/10.1103/PhysRevFluids.1.053604

Childs, P. R. N. (2011). Chapter 6 - rotating cylinders, annuli, and spheres. In P. R. N. Childs (Ed.), *Rotating flow* (pp. 177–247). Butterworth-Heinemann. https://doi.org/https://doi.org/10.1016/B978-0-12-382098-3.00006-8

Chouippe, A., Climent, E., Legendre, D., & Gabillet, C. (2014). Numerical simulation of bubble dispersion in turbulent taylor-couette flow. *Physics of Fluids*, *26*(4), 043304. https://doi.org/10.1063/1.4871728

Chu, P., Finch, J., Bournival, G., Ata, S., Hamlett, C., & Pugh, R. J. (2019). A review of bubble break-up. *Advances in Colloid and Interface Science*, *270*, 108–122. https://doi.org/https://doi.org/10.1016/j.cis.2019.05.010

Clift, R., Grace, J. R., & Weber, M. E. (1978). *Bubbles, drops, and particles*.

Climent, E., Simonnet, M., & Magnaudet, J. (2007). Preferential accumulation of bubbles in couette-taylor flow patterns. *Physics of Fluids*, *19*(8), 083301. https://doi.org/10.1063/1.2752839

Cole, J. A. (1976). Taylor-vortex instability and annulus-length effects. *Journal of Fluid Mechanics*, *75*(1), 1–15. https://doi.org/10.1017/S0022112076000098

Coles, D. (1965). Transition in circular couette flow. *Journal of Fluid Mechanics*, *21*(3), 385–425. https://doi.org/10.1017/S0022112065000241

Couette, M. (1890). *Etudes sur le frottement des liquides* (Thesis).

Crank, J. (1975). *The mathematics of diffusion / by j. crank*. Clarendon Press.

Cussler, E. L. (2009). *Diffusion: Mass transfer in fluid systems*. Cambridge university press.

Danckwerts, P. V. (1951). Significance of liquid-film coefficients in gas absorption. *Industrial & Engineering Chemistry*, *43*(6), 1460–1467. https://doi.org/10.1021/ie50498a055

Dani, A., Guiraud, P., & Cockx, A. (2007). Local measurement of oxygen transfer around a single bubble by planar laser-induced fluorescence. *Chemical Engineering Science*, *62*(24), 7245–7252. https://doi.org/https://doi.org/10.1016/j.ces.2007.08.047

Davies, R. M., & Taylor, G. I. (1950). The mechanics of large bubbles rising through extended liquids and through liquids in tubes. *Proceedings of the Royal Society of London. Series A. Mathematical and Physical Sciences*, *200*(1062), 375–390. https://doi.org/doi:10.1098/rspa.1950.0023

Deckwer, W. D., Burckhart, R., & Zoll, G. (1974). Mixing and mass transfer in tall bubble columns. *Chemical Engineering Science*, *29*(11), 2177–2188. https://doi.org/https://doi.org/10.1016/0009-2509(74)80025-4

Deising, D., Bothe, D., & Marschall, H. (2018). Direct numerical simulation of mass transfer in bubbly flows. *Comput. Fluids*, *172*, 524–537. https://doi.org/https://doi.org/10.1016/j.compfluid.2018.03.041

Deising, D., Marschall, H., & Bothe, D. (2016). A unified single-field model framework for volume-of-fluid simulations of interfacial species transfer applied to bubbly flows. *Chemical Engineering Science*, *139*, 173–195. https://doi.org/https://doi.org/10.1016/j.ces.2015.06.021

de Vries, A. W. G. (2001). *Path and wake of a rising bubble* (Thesis).

Dey, S., Ali, S. Z., & Padhi, E. (2019). Terminal fall velocity: The legacy of stokes from the perspective of fluvial hydraulics. *Proceedings of the Royal Society A: Mathematical, Physical and Engineering Sciences*, *475*(2228), 20190277. https://doi.org/doi:10.1098/rspa.2019.0277

Di Prima, R. C., & Swinney, H. L. (1981). Instabilities and transition in flow between concentric rotating cylinders. In H. L. Swinney & J. P. Gollub (Eds.), *Hydrodynamic instabilities and the transition to turbulence* (pp. 139–180). Springer Berlin Heidelberg. https://doi.org/10.1007/3-540-13319-4_16

Dijkhuizen, W., Roghair, I., Van Sint Annaland, M., & Kuipers, J. A. M. (2010). Dns of gas bubbles behaviour using an improved 3d front tracking model—drag force on isolated bubbles and comparison with experiments. *Chemical Engineering Science*, *65*(4), 1415–1426. https://doi.org/https://doi.org/10.1016/j.ces.2009.10.021

Djeridi, H., Gabillet, C., & Billard, J. Y. (2004). Two-phase couette–taylor flow: Arrangement of the dispersed phase and effects on the flow structures. *Physics of Fluids*, *16*(1), 128–139. https://doi.org/10.1063/1.1630323

Dłuska, E., Wroński, S., & Hubacz, R. (2001). Mass transfer in gas–liquid couette–taylor flow reactor. *Chemical Engineering Science*, *56*(3), 1131–1136. https://doi.org/https://doi.org/10.1016/S0009-2509(00)00331-6

Dong, S. (2007). Direct numerical simulation of turbulent taylor–couette flow. *Journal of Fluid Mechanics*, *587*, 373–393. https://doi.org/10.1017/S0022112007007367

Dong, S. (2008). Turbulent flow between counter-rotating concentric cylinders: A direct numerical simulation study. *Journal of Fluid Mechanics*, *615*, 371–399.

Donnelly, R. J., & Simon, N. J. (1960). An empirical torque relation for supercritical flow between rotating cylinders. *Journal of Fluid Mechanics*, *7*(3), 401–418. https://doi.org/10.1017/S0022112060000177

Donnelly, R. J., Schwarz, K. W., Roberts, P. H., & Chandrasekhar, S. (1965). Experiments on the stability of viscous flow between rotating cylinders - vi. finite-amplitude experiments. *Proceedings of the Royal Society of London. Series A. Mathematical and Physical Sciences*, *283*(1395), 531–556. https://doi.org/doi:10.1098/rspa.1965.0044

Duda, J. L., & Vrentas, J. S. (1971). Heat or mass transfer-controlled dissolution of an isolated sphere. *International Journal of Heat and Mass Transfer*, *14*(3), 395–407. https://doi.org/https://doi.org/10.1016/0017-9310(71)90159-1

Duineveld, P. C. (1995). The rise velocity and shape of bubbles in pure water at high reynolds number. *Journal of Fluid Mechanics*, *292*, 325–332. https://doi.org/10.1017/S0022112095001546

Duncan, P. B., & Needham, D. (2004). Test of the epstein-plesset model for gas microparticle dissolution in aqueous media: Effect of surface tension and gas undersaturation in solution. *Langmuir*, *20*(7), 2567–2578. https://doi.org/10.1021/la034930i

Epstein, P. S., & Plesset, M. S. (1950). On the stability of gas bubbles in liquid-gas solutions. *The Journal of Chemical Physics*, *18*(11), 1505–1509. https://doi.org/10.1063/1.1747520

European Commission. (2020). *A hydrogen strategy for a climate-neutral europe* (Report). https://eur-lex.europa.eu/legal-content/EN/TXT/?uri=CELEX:52020DC0301

Farsoiya, P. K., Magdelaine, Q., Antkowiak, A., Popinet, S., & Deike, L. (2023). Direct numerical simulations of bubble-mediated gas transfer and dissolution in quiescent and turbulent flows. *Journal of Fluid Mechanics*, *954*, A29. https://doi.org/10.1017/jfm.2022.994

Farsoiya, P. K., Popinet, S., & Deike, L. (2021). Bubble-mediated transfer of dilute gas in turbulence. *Journal of Fluid Mechanics*, *920*, A34. https://doi.org/10.1017/jfm.2021.447

Fdhila, R. B., & Duineveld, P. C. (1996). The effect of surfactant on the rise of a spherical bubble at high reynolds and peclet numbers. *Physics of Fluids*, *8*(2), 310–321. https://doi.org/10.1063/1.868787

Fedkiw, R. P., Aslam, T., Merriman, B., & Osher, S. (1999). A non-oscillatory eulerian approach to interfaces in multimaterial flows (the ghost fluid method). *Journal of Computational Physics*, *152*(2), 457–492. https://doi.org/https://doi.org/10.1006/jcph.1999.6236

Fenstermacher, P. R., Swinney, H. L., & Gollub, J. P. (1979). Dynamical instabilities and the transition to chaotic taylor vortex flow. *Journal of Fluid Mechanics*, *94*(1), 103–128. https://doi.org/10.1017/S0022112079000963

Ferrante, A., & Elghobashi, S. (2004). On the physical mechanisms of drag reduction in a spatially developing turbulent boundary layer laden with microbubbles. *Journal of Fluid Mechanics*, *503*, 345–355. https://doi.org/10.1017/S0022112004007943

Fick, A. (1855). Ueber diffusion. *Annalen der Physik*, *170*(1), 59–86. https://doi.org/https://doi.org/10.1002/andp.18551700105

Fleckenstein, S., & Bothe, D. (2015). A volume-of-fluid-based numerical method for multi-component mass transfer with local volume changes. *Journal of Computational Physics*, *301*, 35–58. https://doi.org/https://doi.org/10.1016/j.jcp.2015.08.011

Francois, J., Dietrich, N., Guiraud, P., & Cockx, A. (2011). Direct measurement of mass transfer around a single bubble by micro-plifi. *Chemical Engineering Science*, *66*(14), 3328–3338. https://doi.org/https://doi.org/10.1016/j.ces.2011.01.049

Gao, X., Kong, B., & Dennis Vigil, R. (2016). Cfd simulation of bubbly turbulent tayor–couette flow. *Chinese Journal of Chemical Engineering*, *24*(6), 719–727. https://doi.org/https://doi.org/10.1016/j.cjche.2016.01.013

Gao, X., Kong, B., Ramezani, M., Olsen, M. G., & Vigil, R. D. (2015). An adaptive model for gas–liquid mass transfer in a taylor vortex reactor. *International Journal of Heat and Mass Transfer*, *91*, 433–445. https://doi.org/https://doi.org/10.1016/j.ijheatmasstransfer.2015.07.125

Gao, X., Kong, B., & Vigil, R. D. (2015). Cfd investigation of bubble effects on taylor–couette flow patterns in the weakly turbulent vortex regime. *Chemical Engineering Journal*, *270*, 508–518. https://doi.org/https://doi.org/10.1016/j.cej.2015.02.061

Gennari, G., Jefferson-Loveday, R., & Pickering, S. J. (2022a). A phase-change model for diffusion-driven mass transfer problems in incompressible two-phase flows. *4th Int. Conference on Numerical Methods in Multiphase Flows, Venice, Italy, 28-30 September*.

Gennari, G., Jefferson-Loveday, R., & Pickering, S. J. (2022b). A phase-change model for diffusion-driven mass transfer problems in incompressible two-phase flows. *Chemical Engineering Science*, *259*, 117791. https://doi.org/https://doi.org/10.1016/j.ces.2022.117791

Ghidersa, B., & Dušek, J. A. N. (2000). Breaking of axisymmetry and onset of unsteadiness in the wake of a sphere. *Journal of Fluid Mechanics*, *423*, 33–69. https://doi.org/10.1017/S0022112000001701

Glas, J. P., & Westwater, J. W. (1964). Measurements of the growth of electrolytic bubbles. *International Journal of Heat and Mass Transfer*, *7*(12), 1427–1443. https://doi.org/https://doi.org/10.1016/0017-9310(64)90130-9

Gollub, J. P., & Swinney, H. L. (1975). Onset of turbulence in a rotating fluid. *Physical Review Letters*, *35*(14), 927–930. https://doi.org/10.1103/PhysRevLett.35.927

Gorman, M., & Swinney, H. L. (1982). Spatial and temporal characteristics of modulated waves in the circular couette system. *Journal of Fluid Mechanics*, *117*, 123–142. https://doi.org/10.1017/S0022112082001554

Grace, H. P. (1982). Dispersion phenomena in high viscosity immiscible fluid systems and application of static mixers as dispersion devices in such systems. *Chemical Engineering Communications*, *14*(3-6), 225–277. https://doi.org/10.1080/00986448208911047

Grafschafter, A., & Siebenhofer, M. (2017). Design rules for the taylor-couette disc contactor. *Chemie Ingenieur Technik*, *89*(4), 409–415. https://doi.org/https://doi.org/10.1002/cite.201600142

Groß, T. F., & Pelz, P. F. (2017). Diffusion-driven nucleation from surface nuclei in hydrodynamic cavitation. *Journal of Fluid Mechanics*, *830*, 138–164. https://doi.org/10.1017/jfm.2017.587

Grossmann, S., Lohse, D., & Sun, C. (2016). High–reynolds number taylor-couette turbulence. *Annual Review of Fluid Mechanics*, *48*(1), 53–80. https://doi.org/10.1146/annurev-fluid-122414-034353

Guido, S., & Greco, F. (2001). Drop shape under slow steady shear flow and during relaxation. experimental results and comparison with theory. *Rheologica Acta*, *40*(2), 176–184. https://doi.org/10.1007/s003970000144

Gumulya, M., Joshi, J. B., Utikar, R. P., Evans, G. M., & Pareek, V. (2016). Bubbles in viscous liquids: Time dependent behaviour and wake characteristics. *Chemical Engineering Science*, *144*, 298–309. https://doi.org/https://doi.org/10.1016/j.ces.2016.01.051

Guo, L. (2020). *Numerical investigation of taylor bubble and development of phase change model* (Thesis). Université de Lyon. https://tel.archives-ouvertes.fr/tel-03177304

Hadamard, J. (1911). Mouvement permanent lent d'une sphère liquide et visqueuse dans un liquide visqueux. *C.R. Acad. Sci. Paris*, *152*, 1735–1738.

Hardt, S., & Wondra, F. (2008). Evaporation model for interfacial flows based on a continuum-field representation of the source terms. *Journal of Computational Physics*, *227*(11), 5871–5895. https://doi.org/https://doi.org/10.1016/j.jcp.2008.02.020

Haroun, Y., Legendre, D., & Raynal, L. (2010). Volume of fluid method for interfacial reactive mass transfer: Application to stable liquid film. *Chemical Engineering Science*, *65*, 2896–2909.

Hartunian, R. A., & Sears, W. R. (1957). On the instability of small gas bubbles moving uniformly in various liquids. *Journal of Fluid Mechanics*, *3*(1), 27–47. https://doi.org/10.1017/S0022112057000464

Higbie, R. (1935). The rate of absorption of a pure gas into a still liquid during short periods of exposure. *Trans. AIChE*, *31*, 365–389.

Hinch, E. J., & Acrivos, A. (1980). Long slender drops in a simple shear flow. *Journal of Fluid Mechanics*, *98*(2), 305–328. https://doi.org/10.1017/S0022112080000171

Hirt, C. W., & Nichols, B. D. (1981). Volume of fluid (vof) method for the dynamics of free boundaries. *Journal of Computational Physics*, *39*(1), 201–225. https://doi.org/https://doi.org/10.1016/0021-9991(81)90145-5

Hosoda, S., Tryggvason, G., Hosokawa, S., & Tomiyama, A. (2015). Dissolution of single carbon dioxide bubbles in a vertical pipe. *JOURNAL OF CHEMICAL ENGINEERING OF JAPAN*, *48*(6), 418–426. https://doi.org/10.1252/jcej.14we241

Hoyas, S., & Jiménez, J. (2006). Scaling of the velocity fluctuations in turbulent channels up to $\mathrm{Re}_\tau = 2003$. *Physics of Fluids*, *18*(1), 011702. https://doi.org/10.1063/1.2162185

Huang, Q., Yang, C., Yu, G., & Mao, Z.-S. (2010). Cfd simulation of hydrodynamics and mass transfer in an internal airlift loop reactor using a steady two-fluid model. *Chemical Engineering Science*, *65*(20), 5527–5536. https://doi.org/https://doi.org/10.1016/j.ces.2010.07.021

Janssen, J. J. M., Boon, A., & Agterof, W. G. M. (1994). Influence of dynamic interfacial properties on droplet breakup in simple shear flow. *AIChE Journal*, *40*(12), 1929–1939. https://doi.org/https://doi.org/10.1002/aic.690401202

Koschmieder, E. L. (1979). Turbulent taylor vortex flow. *Journal of Fluid Mechanics*, *93*(3), 515–527. https://doi.org/10.1017/S0022112079002639

Krauß, M., & Rzehak, R. (2018). Reactive absorption of co2 in naoh: An euler-euler simulation study. *Chemical Engineering Science*, *181*, 199–214. https://doi.org/https://doi.org/10.1016/j.ces.2018.01.009

Kunkelmann, C., & Stephan, P. (2009). Cfd simulation of boiling flows using the volume-of-fluid method within openfoam. *Numerical Heat Transfer, Part A: Applications*, *56*(8), 631–646. https://doi.org/10.1080/10407780903423908

Leal, L. G. (1989). Vorticity transport and wake structure for bluff bodies at finite reynolds number. *Physics of Fluids A: Fluid Dynamics*, *1*(1), 124–131. https://doi.org/10.1063/1.857540

Lee, D. S., Amara, Z., Clark, C. A., Xu, Z., Kakimpa, B., Morvan, H. P., Pickering, S. J., Poliakoff, M., & George, M. W. (2017). Continuous photo-oxidation in a vortex reactor: Efficient operations using air drawn from the laboratory. *Organic Process Research & Development*, *21*(7), 1042–1050. https://doi.org/10.1021/acs.oprd.7b00153

Lee, D. S., Love, A., Mansouri, Z., Waldron Clarke, T. H., Harrowven, D. C., Jefferson-Loveday, R., Pickering, S. J., Poliakoff, M., & George, M. W. (2022). High-productivity single-pass electrochemical birch reduction of naphthalenes in a continuous flow electrochemical taylor vortex reactor. *Organic Process Research & Development*, *26*(9), 2674–2684. https://doi.org/10.1021/acs.oprd.2c00108

Lee, D. S., Sharabi, M., Jefferson-Loveday, R., Pickering, S. J., Poliakoff, M., & George, M. W. (2020). Scalable continuous vortex reactor for gram to kilo scale for uv and visible photochemistry. *Organic Process Research & Development*, *24*(2), 201–206. https://doi.org/10.1021/acs.oprd.9b00475

Levenspiel, O. (1998). *Chemical reaction engineering*. John wiley & sons.

Levich, V. G. (1949). The motion of bubbles at high reynolds numbers. *Zh. Eksp. Teor. Fiz*, *19*(18), 436ff.

Levich, V. G. (1962). Physicochemical hydrodynamics.

Liao, Y. (2013). *Development and validation of models for bubble coalescence and breakup* (Report No. 2191-8708). http://inis.iaea.org/search/search.aspx?orig_q=RN:46010905

Liao, Y., & Lucas, D. (2009). A literature review of theoretical models for drop and bubble breakup in turbulent dispersions. *Chemical Engineering Science*, *64*(15), 3389–3406. https://doi.org/https://doi.org/10.1016/j.ces.2009.04.026

Liu, H.-b., Pan, L.-m., & Wen, J. (2016). Numerical simulation of hydrogen bubble growth at an electrode surface. *Canadian Journal of Chemical Engineering*, *94*, 192–199.

Lochiel, A. C., & Calderbank, P. H. (1964). Mass transfer in the continuous phase around axisymmetric bodies of revolution. *Chemical Engineering Science*,

19(7), 471–484. https://doi.org/https://doi.org/10.1016/0009-2509(64)85074-0

López-Herrera, J. M., Gañán-Calvo, A. M., Popinet, S., & Herrada, M. A. (2015). Electrokinetic effects in the breakup of electrified jets: A volume-of-fluid numerical study. *International Journal of Multiphase Flow*, *71*, 14–22. https://doi.org/https://doi.org/10.1016/j.ijmultiphaseflow.2014.12.005

Love, A., Lee, D. S., Gennari, G., Jefferson-Loveday, R., Pickering, S. J., Poliakoff, M., & George, M. (2021). A continuous-flow electrochemical taylor vortex reactor: A laboratory-scale high-throughput flow reactor with enhanced mixing for scalable electrosynthesis. *Organic Process Research & Development*, *25*(7), 1619–1627. https://doi.org/10.1021/acs.oprd.1c00102

Lu, J., Fernández, A., & Tryggvason, G. (2005). The effect of bubbles on the wall drag in a turbulent channel flow. *Physics of Fluids*, *17*(9), 095102. https://doi.org/10.1063/1.2033547

Lunde, K., & Perkins, R. J. (1998). Shape oscillations of rising bubbles. In A. Biesheuvel & G. F. van Heijst (Eds.), *In fascination of fluid dynamics: A symposium in honour of leen van wijngaarden* (pp. 387–408). Springer Netherlands. https://doi.org/10.1007/978-94-011-4986-0_20

Ma, C., & Bothe, D. (2013). Numerical modeling of thermocapillary two-phase flows with evaporation using a two-scalar approach for heat transfer. *Journal of Computational Physics*, *233*, 552–573. https://doi.org/https://doi.org/10.1016/j.jcp.2012.09.011

Maes, J., & Soulaine, C. (2018). A new compressive scheme to simulate species transfer across fluid interfaces using the volume-of-fluid method. *Chemical Engineering Science*, *190*, 405–418. https://doi.org/https://doi.org/10.1016/j.ces.2018.06.026

Maes, J., & Soulaine, C. (2020). A unified single-field volume-of-fluid-based formulation for multi-component interfacial transfer with local volume changes. *Journal of Computational Physics*, *402*, 109024. https://doi.org/https://doi.org/10.1016/j.jcp.2019.109024

Magdelaine-Guillot de Suduiraut, Q. (2019). *Hydrodynamique des films liquides hétérogènes* (Thesis). Sorbonne université. http://www.theses.fr/2019SORUS531/document

Magnaudet, J., & Eames, I. (2000). The motion of high-reynolds-number bubbles in inhomogeneous flows. *Annual Review of Fluid Mechanics*, *32*(1), 659–708. https://doi.org/10.1146/annurev.fluid.32.1.659

Magnaudet, J., & Mougin, G. (2007). Wake instability of a fixed spheroidal bubble. *Journal of Fluid Mechanics*, *572*, 311–337. https://doi.org/10.1017/S0022112006003442

Magnini, M., Pulvirenti, B., & Thome, J. R. (2013). Numerical investigation of hydrodynamics and heat transfer of elongated bubbles during flow boiling in a microchannel. *International Journal of Heat and Mass Transfer*, *59*, 451–471. https://doi.org/https://doi.org/10.1016/j.ijheatmasstransfer.2012.12.010

Malan, L. C., Malan, A. G., Zaleski, S., & Rousseau, P. G. (2021). A geometric vof method for interface resolved phase change and conservative thermal energy advection. *Journal of Computational Physics*, *426*, 109920. https://doi.org/https://doi.org/10.1016/j.jcp.2020.109920

Marschall, H., Hinterberger, K., Schüler, C., Habla, F., & Hinrichsen, O. (2012). Numerical simulation of species transfer across fluid interfaces in free-surface flows using openfoam. *Chemical Engineering Science*, *78*, 111–127. https://doi.org/https://doi.org/10.1016/j.ces.2012.02.034

Mehel, A., Gabillet, C., & Djeridi, H. (2007). Analysis of the flow pattern modifications in a bubbly couette-taylor flow. *Physics of Fluids*, *19*(11), 118101. https://doi.org/10.1063/1.2786584

Mei, R., Klausner, J. F., & Lawrence, C. J. (1994). A note on the history force on a spherical bubble at finite reynolds number. *Physics of Fluids*, *6*(1), 418–420. https://doi.org/10.1063/1.868039

Moore, D. W. (1959). The rise of a gas bubble in a viscous liquid. *Journal of Fluid Mechanics*, *6*(1), 113–130. https://doi.org/10.1017/S0022112059000520

Moore, D. W. (1963). The boundary layer on a spherical gas bubble. *Journal of Fluid Mechanics*, *16*(2), 161–176. https://doi.org/10.1017/S0022112063000665

Moore, D. W. (1965). The velocity of rise of distorted gas bubbles in a liquid of small viscosity. *Journal of Fluid Mechanics*, *23*(4), 749–766. https://doi.org/10.1017/S0022112065001660

Moser, R. D., & Moin, P. (1987). The effects of curvature in wall-bounded turbulent flows. *Journal of Fluid Mechanics*, *175*, 479–510. https://doi.org/10.1017/S0022112087000491

Mougin, G., & Magnaudet, J. (2001). Path instability of a rising bubble. *Physical Review Letters*, *88*(1), 014502. https://doi.org/10.1103/PhysRevLett.88.014502

Mougin, G., & Magnaudet, J. (2006). Wake-induced forces and torques on a zigzagging/spiralling bubble. *Journal of Fluid Mechanics*, *567*, 185–194. https://doi.org/10.1017/S0022112006002266

Müller-Fischer, N., Tobler, P., Dressler, M., Fischer, P., & Windhab, E. J. (2008). Single bubble deformation and breakup in simple shear flow. *Experiments in Fluids*, *45*(5), 917–926. https://doi.org/10.1007/s00348-008-0509-1

Murai, Y., Oiwa, H., & Takeda, Y. (2005). Bubble behavior in a vertical taylor-couette flow. *Journal of Physics: Conference Series*, *14*(1), 143. https://doi.org/10.1088/1742-6596/14/1/018

Murai, Y. (2014). Frictional drag reduction by bubble injection. *Experiments in Fluids*, *55*(7), 1773. https://doi.org/10.1007/s00348-014-1773-x

Murai, Y., Oiwa, H., & Takeda, Y. (2008). Frictional drag reduction in bubbly couette–taylor flow. *Physics of Fluids*, *20*(3), 034101. https://doi.org/10.1063/1.2884471

Nemri, M., Charton, S., & Climent, E. (2016). Mixing and axial dispersion in taylor–couette flows: The effect of the flow regime. *Chemical Engineering Science*, *139*, 109–124. https://doi.org/https://doi.org/10.1016/j.ces.2015.09.022

Nemri, M., Climent, E., Charton, S., Lanoë, J.-Y., & Ode, D. (2013). Experimental and numerical investigation on mixing and axial dispersion in taylor–couette flow patterns. *Chemical Engineering Research and Design*, *91*(12), 2346–2354. https://doi.org/https://doi.org/10.1016/j.cherd.2012.11.010

Nguyen, D. Q., Fedkiw, R. P., & Kang, M. (2001). A boundary condition capturing method for incompressible flame discontinuities. *Journal of Computational Physics*, *172*(1), 71–98. https://doi.org/https://doi.org/10.1006/jcph.2001.6812

Nicoli, A., Johnson, K., & Jefferson-Loveday, R. (2022). Computational modelling of turbulent taylor–couette flow for bearing chamber applications: A comparison of unsteady reynolds-averaged navier–stokes models. *Proceedings of the Institution of Mechanical Engineers, Part A: Journal of Power and Energy*, *236*(5), 985–1005. https://doi.org/10.1177/09576509221075516

Oellrich, L., Schmidt-Traub, H., & Brauer, H. (1973). Theoretische berechnung des stofftransports in der umgebung einer einzelblase. *Chemical Engineering Science*, *28*(3), 711–721. https://doi.org/https://doi.org/10.1016/0009-2509(77)80005-5

Oseen, C. (1910). On stokes' formula and a related problem in hydrodynamics. *Arkiv filr Mathematik Astronomi och Fysik*, *6*.

Ostilla-Mónico, R., Poel, E. P. v. d., Verzicco, R., Grossmann, S., & Lohse, D. (2014). Boundary layer dynamics at the transition between the classical and the ultimate regime of taylor-couette flow. *Physics of Fluids*, *26*(1), 015114. https://doi.org/10.1063/1.4863312

Ostilla-Mónico, R., Verzicco, R., & Lohse, D. (2015). Effects of the computational domain size on direct numerical simulations of taylor-couette turbulence with stationary outer cylinder. *Physics of Fluids*, *27*(2), 025110. https://doi.org/10.1063/1.4913231

Pereiro, I., Fomitcheva Khartchenko, A., Petrini, L., & Kaigala, G. V. (2019). Nip the bubble in the bud: A guide to avoid gas nucleation in microfluidics. *Lab on a Chip*, *19*(14), 2296–2314. https://doi.org/10.1039/C9LC00211A

Pesci, C., Weiner, A., Marschall, H., & Bothe, D. (2018). Computational analysis of single rising bubbles influenced by soluble surfactant. *Journal of Fluid Mechanics*, *856*, 709–763. https://doi.org/10.1017/jfm.2018.723

Pirrò, D., & Quadrio, M. (2008). Direct numerical simulation of turbulent taylor–couette flow. *European Journal of Mechanics - B/Fluids*, *27*(5), 552–566. https://doi.org/https://doi.org/10.1016/j.euromechflu.2007.10.005

Popinet, S. (2003). Gerris: A tree-based adaptive solver for the incompressible euler equations in complex geometries. *Journal of Computational Physics*, *190*(2), 572–600. https://doi.org/https://doi.org/10.1016/S0021-9991(03)00298-5

Popinet, S. (2009). An accurate adaptive solver for surface-tension-driven interfacial flows. *Journal of Computational Physics*, *228*(16), 5838–5866. https://doi.org/https://doi.org/10.1016/j.jcp.2009.04.042

Popinet, S. (2015). A quadtree-adaptive multigrid solver for the serre–green–naghdi equations. *Journal of Computational Physics*, *302*, 336–358. https://doi.org/https://doi.org/10.1016/j.jcp.2015.09.009

Popinet, S. (2018). Numerical models of surface tension. *Annual Review of Fluid Mechanics*, *50*(1), 49–75. https://doi.org/10.1146/annurev-fluid-122316-045034

Popinet, S., & collaborators. (2013–2023). *Basilisk*. http://basilisk.fr

Prausnitz, J., Lichtenthaler, R., & de Azevedo, E. (1998). *Molecular thermodynamics of fluid-phase equilibria*. Pearson Education. https://books.google.co.uk/books?id=VSwc1XUmYpcC

Pritchard, D. T., & Currie, J. A. (1982). Diffusion of coefficients of carbon dioxide, nitrous oxide, ethylene and ethane in air and their measurement. *Journal of Soil Science*, *33*(2), 175–184. https://doi.org/https://doi.org/10.1111/j.1365-2389.1982.tb01757.x

Prosperetti, A. (2004). Bubbles. *Physics of Fluids*, *16*(6), 1852–1865. https://doi.org/10.1063/1.1695308

Qiao, J., Yan, W.-C., Teoh, J. H., Tong, Y. W., & Wang, C.-H. (2018). Experimental and computational studies of oxygen transport in a taylor-couette bioreactor. *Chemical Engineering Journal*, *334*, 1954–1964. https://doi.org/https://doi.org/10.1016/j.cej.2017.11.137

Rallison, J. M. (1981). A numerical study of the deformation and burst of a viscous drop in general shear flows. *Journal of Fluid Mechanics*, *109*, 465–482. https://doi.org/10.1017/S002211208100116X

Rallison, J. M. (1984). The deformation of small viscous drops and bubbles in shear flows. *Annual Review of Fluid Mechanics*, *16*(1), 45–66. https://doi.org/10.1146/annurev.fl.16.010184.000401

Ramezani, M., Kong, B., Gao, X., Olsen, M. G., & Vigil, R. D. (2015). Experimental measurement of oxygen mass transfer and bubble size distribution in an air–water multiphase taylor–couette vortex bioreactor. *Chemical Engineering Journal*, *279*, 286–296. https://doi.org/https://doi.org/10.1016/j.cej.2015.05.007

Razzak, M. A., C.Khoo, B., & B.Lua, K. (2019). Numerical study on wide gap taylor couette flow with flow transition. *Physics of Fluids*, *31*(11), 113606. https://doi.org/10.1063/1.5125640

Roghair, I., Lau, Y. M., Deen, N. G., Slagter, H. M., Baltussen, M. W., Van Sint Annaland, M., & Kuipers, J. A. M. (2011). On the drag force of bubbles in bubble swarms at intermediate and high reynolds numbers. *Chemical Engineering Science*, *66*(14), 3204–3211. https://doi.org/https://doi.org/10.1016/j.ces.2011.02.030

Rust, A. C., & Manga, M. (2002). Bubble shapes and orientations in low re simple shear flow. *Journal of Colloid and Interface Science*, *249*(2), 476–480. https://doi.org/https://doi.org/10.1006/jcis.2002.8292

Rybczynski, W. (1911). On the translatory motion of a fluid sphere in a viscous medium. *Bull. Acad. Sci. Cracovie*, 40–46.

Saffman, P. G. (1956). On the rise of small air bubbles in water. *Journal of Fluid Mechanics*, *1*(3), 249–275. https://doi.org/10.1017/S0022112056000159

Scapin, N., Costa, P., & Brandt, L. (2020). A volume-of-fluid method for interface-resolved simulations of phase-changing two-fluid flows. *Journal of Computational Physics*, *407*, 109251. https://doi.org/https://doi.org/10.1016/j.jcp.2020.109251

Scardovelli, R., & Zaleski, S. (1999). Direct numerical simulation of free-surface and interfacial flow. *Annual Review of Fluid Mechanics*, *31*(1), 567–603. https://doi.org/10.1146/annurev.fluid.31.1.567

Schlottke, J., & Weigand, B. (2008). Direct numerical simulation of evaporating droplets. *Journal of Computational Physics*, *227*(10), 5215–5237. https://doi.org/https://doi.org/10.1016/j.jcp.2008.01.042

Schrimpf, M., Esteban, J., Warmeling, H., Färber, T., Behr, A., & Vorholt, A. J. (2021). Taylor-couette reactor: Principles, design, and applications. *AIChE Journal*, *67*(5), e17228. https://doi.org/https://doi.org/10.1002/aic.17228

Schulz, A., Wecker, C., Inguva, V., Lopatin, A. S., & Kenig, E. Y. (2022). A plic-based method for species mass transfer at free fluid interfaces. *Chemical Engineering Science*, *251*, 117357. https://doi.org/https://doi.org/10.1016/j.ces.2021.117357

Schwartz, P., Barad, M., Colella, P., & Ligocki, T. (2006). A cartesian grid embedded boundary method for the heat equation and poisson's equation in three dimensions. *Journal of Computational Physics*, *211*(2), 531–550. https://doi.org/https://doi.org/10.1016/j.jcp.2005.06.010

Scriven, L. E. (1959). On the dynamics of phase growth. *Chemical Engineering Science*, *10*(1), 1–13. https://doi.org/https://doi.org/10.1016/0009-2509(59)80019-1

Sharaborin, E. L., Rogozin, O. A., & Kasimov, A. R. (2021). The coupled volume of fluid and brinkman penalization methods for simulation of incompressible multiphase flows. *Fluids*, *6*(9), 334.

Shew, L., Woodrow, Poncet, S., & Pinton, J.-F. (2005). *Path instability and wake of a rising bubble* (Unpublished Work). https://hal.archives-ouvertes.fr/hal-00013378

Shiomi, Y., Kutsuna, H., Akagawa, K., & Ozawa, M. (1993). Two-phase flow in an annulus with a rotating inner cylinder (flow pattern in bubbly flow region). *Nuclear Engineering and Design*, *141*(1), 27–34. https://doi.org/https://doi.org/10.1016/0029-5493(93)90089-R

Smith, G. P., & Townsend, A. A. (1982). Turbulent couette flow between concentric cylinders at large taylor numbers. *Journal of Fluid Mechanics*, *123*, 187–217. https://doi.org/10.1017/S0022112082003024

Snyder, H. A. (1968). Stability of rotating couette flow. ii. comparison with numerical results. *The Physics of Fluids*, *11*(8), 1599–1605. https://doi.org/10.1063/1.1692167

Spandan, V., Verzicco, R., & Lohse, D. (2017). Deformable ellipsoidal bubbles in taylor-couette flow with enhanced euler-lagrangian tracking. *Physical Review Fluids*, *2*(10), 104304. https://doi.org/10.1103/PhysRevFluids.2.104304

Stokes, G. (1850). On the effect of internal friction of fluids on the motion of pendulums. *Trans. Camb. phi1. S0c*, *9*(8), 106.

Sugiyama, K., Calzavarini, E., & Lohse, D. (2008). Microbubbly drag reduction in taylor–couette flow in the wavy vortex regime. *Journal of Fluid Mechanics*, *608*, 21–41. https://doi.org/10.1017/S0022112008001183

Sui, Y., Ding, H., & Spelt, P. D. (2014). Numerical simulations of flows with moving contact lines. *Annual Review of Fluid Mechanics*, *46*(1), 97–119. https://doi.org/10.1146/annurev-fluid-010313-141338

Sussman, M. (2003). A second order coupled level set and volume-of-fluid method for computing growth and collapse of vapor bubbles. *Journal of Computational Physics*, *187*(1), 110–136. https://doi.org/https://doi.org/10.1016/S0021-9991(03)00087-1

Sussman, M., Smereka, P., & Osher, S. (1994). A level set approach for computing solutions to incompressible two-phase flow. *Journal of Computational Physics*, *114*(1), 146–159. https://doi.org/https://doi.org/10.1006/jcph.1994.1155

Takemura, F., & Yabe, A. (1999). Rising speed and dissolution rate of a carbon dioxide bubble in slightly contaminated water. *Journal of Fluid Mechanics*, *378*, 319–334. https://doi.org/10.1017/S0022112098003358

Takemura, F., & Matsumoto, Y. (2000). Dissolution rate of spherical carbon dioxide bubbles in strong alkaline solutions. *Chemical Engineering Science*, *55*(18), 3907–3917. https://doi.org/https://doi.org/10.1016/S0009-2509(00)00022-1

Takemura, F., & Yabe, A. (1998). Gas dissolution process of spherical rising gas bubbles. *Chemical Engineering Science*, *53*(15), 2691–2699. https://doi.org/https://doi.org/10.1016/S0009-2509(98)00094-3

Tanguy, S., Ménard, T., & Berlemont, A. (2007). A level set method for vaporizing two-phase flows. *Journal of Computational Physics*, *221*(2), 837–853. https://doi.org/https://doi.org/10.1016/j.jcp.2006.07.003

Taqieddin, A., Liu, Y., Alshawabkeh, A. N., & Allshouse, M. R. (2020). Computational modeling of bubbles growth using the coupled level set—volume of fluid method. *Fluids*, *5*(3), 120.

Taylor, G. I. (1923). Viii. stability of a viscous liquid contained between two rotating cylinders. *Philosophical Transactions of the Royal Society of London. Series A, Containing Papers of a Mathematical or Physical Character*, *223*(605-615), 289–343. https://doi.org/doi:10.1098/rsta.1923.0008

Taylor, G. I. (1934). The formation of emulsions in definable fields of flow. *Proceedings of the Royal Society of London. Series A, Containing Papers of a Mathematical and Physical Character*, *146*(858), 501–523. https://doi.org/doi:10.1098/rspa.1934.0169

Teuber, K., Broecker, T., Bentzen, T. R., Stephan, D., Nützmann, G., & Hinkelmann, R. (2019). Using computational fluid dynamics to describe h2s mass transfer across the water–air interface in sewers. *Water Science and Technology*, *79*(10), 1934–1946. https://doi.org/10.2166/wst.2019.193

Tomiyama, A., Kataoka, I., Zun, I., & Sakaguchi, T. (1998). Drag coefficients of single bubbles under normal and micro gravity conditions. *JSME International Journal Series B*, *41*(2), 472–479. https://doi.org/10.1299/jsmeb.41.472

Townsend, A. A. (1984). Axisymmetric couette flow at large taylor numbers. *Journal of Fluid Mechanics*, *144*, 329–362. https://doi.org/10.1017/S0022112084001634

Tripathi, M. K., Sahu, K. C., & Govindarajan, R. (2015). Dynamics of an initially spherical bubble rising in quiescent liquid. *Nature Communications*, *6*(1), 6268. https://doi.org/10.1038/ncomms7268

Tryggvason, G., Bunner, B., Esmaeeli, A., Juric, D., Al-Rawahi, N., Tauber, W., Han, J., Nas, S., & Jan, Y. J. (2001). A front-tracking method for the computations

of multiphase flow. *Journal of Computational Physics*, *169*(2), 708–759. https://doi.org/https://doi.org/10.1006/jcph.2001.6726

Tryggvason, G., Scardovelli, R., & Zaleski, S. (2011). *Direct numerical simulations of gas–liquid multiphase flows*. Cambridge University Press. https://doi.org/DOI:10.1017/CBO9780511975264

Tsuge, H., & Hibino, S.-I. (1977). The onset conditions of oscillatory motion of single gas bubbles rising in various liquids. *Journal of Chemical Engineering of Japan*, *10*(1), 66–68. https://doi.org/10.1252/jcej.10.66

Ubbink, O., & Issa, R. I. (1999). A method for capturing sharp fluid interfaces on arbitrary meshes. *Journal of Computational Physics*, *153*(1), 26–50. https://doi.org/https://doi.org/10.1006/jcph.1999.6276

Vachaparambil, K. J. (2020). *Interface resolved simulations of continuum scale electrochemical hydrogen evolution* (Thesis). https://ntnuopen.ntnu.no/ntnu-xmlui/handle/11250/2723231

Vachaparambil, K. J., & Einarsrud, K. E. (2020). Numerical simulation of bubble growth in a supersaturated solution. *Applied Mathematical Modelling*, *81*, 690–710. https://doi.org/https://doi.org/10.1016/j.apm.2020.01.017

Van den Berg, T. H., Luther, S., Lathrop, D. P., & Lohse, D. (2005). Drag reduction in bubbly taylor-couette turbulence. *Physical Review Letters*, *94*(4), 044501. https://doi.org/10.1103/PhysRevLett.94.044501

Van Gils, D. P. M., Narezo Guzman, D., Sun, C., & Lohse, D. (2013). The importance of bubble deformability for strong drag reduction in bubbly turbulent taylor–couette flow. *Journal of Fluid Mechanics*, *722*, 317–347. https://doi.org/10.1017/jfm.2013.96

van Hooft, J. A., Popinet, S., van Heerwaarden, C. C., van der Linden, S. J. A., de Roode, S. R., & van de Wiel, B. J. H. (2018). Towards adaptive grids for atmospheric boundary-layer simulations. *Boundary-Layer Meteorology*, *167*(3), 421–443. https://doi.org/10.1007/s10546-018-0335-9

Wang, C., Xu, Z., Lai, C., & Sun, X. (2018). Beyond the standard two-film theory: Computational fluid dynamics simulations for carbon dioxide capture in a

wetted wall column. *Chemical Engineering Science*, *184*, 103–110. https://doi.org/https://doi.org/10.1016/j.ces.2018.03.021

Wang, H., Wang, K., & Liu, G. (2022). Drag reduction by gas lubrication with bubbles. *Ocean Engineering*, *258*, 111833. https://doi.org/https://doi.org/10.1016/j.oceaneng.2022.111833

Wang, H. (2015). *Experimental and numerical study of taylor-couette flow* (Thesis). https://doi.org/https://doi.org/10.31274/etd-180810-4013

Wang, L., Marchisio, D. L., Vigil, R. D., & Fox, R. O. (2005). Cfd simulation of aggregation and breakage processes in laminar taylor–couette flow. *Journal of Colloid and Interface Science*, *282*(2), 380–396. https://doi.org/https://doi.org/10.1016/j.jcis.2004.08.127

Wang, L., Vigil, R. D., & Fox, R. O. (2005). Cfd simulation of shear-induced aggregation and breakage in turbulent taylor–couette flow. *Journal of Colloid and Interface Science*, *285*(1), 167–178. https://doi.org/https://doi.org/10.1016/j.jcis.2004.10.075

Wei, T., Kline, E. M., Lee, S. H. K., & Woodruff, S. (1992). Görtler vortex formation at the inner cylinder in taylor–couette flow. *Journal of Fluid Mechanics*, *245*, 47–68. https://doi.org/10.1017/S002211209200034X

Wei, Y. k., Qian, Y., & Xu, H. (2012). Lattice boltzmann simulations of single bubble deformation and breakup in a shear flow. *The Journal of Computational Multiphase Flows*, *4*(1), 111–117. https://doi.org/10.1260/1757-482x.4.1.111

Weiner, A. (2020). *Modeling and simulation of convection-dominated species transfer at rising bubbles* (Thesis). http://tuprints.ulb.tu-darmstadt.de/11405/

Weiner, A., & Bothe, D. (2017). Advanced subgrid-scale modeling for convection-dominated species transport at fluid interfaces with application to mass transfer from rising bubbles. *Journal of Computational Physics*, *347*, 261–289. https://doi.org/https://doi.org/10.1016/j.jcp.2017.06.040

Welch, S. W. J., & Wilson, J. (2000). A volume of fluid based method for fluid flows with phase change. *Journal of Computational Physics*, *160*(2), 662–682. https://doi.org/https://doi.org/10.1006/jcph.2000.6481

Wendt, F. (1933). Turbulente strömungen zwischen zwei rotierenden konaxialen zylindern. *Ingenieur-Archiv*, *4*(6), 577–595. https://doi.org/10.1007/BF02084936

Weymouth, G. D., & Yue, D. K. P. (2010). Conservative volume-of-fluid method for free-surface simulations on cartesian-grids. *Journal of Computational Physics*, *229*(8), 2853–2865. https://doi.org/https://doi.org/10.1016/j.jcp.2009.12.018

Whitman, W. G. (1923). The two-film theory of gas absorption. *Chem. Metall. Eng.*, *29*, 146–148.

Wichterle, K., Večeř, M., & Růžička, M. C. (2014). Asymmetric deformation of bubble shape: Cause or effect of vortex-shedding? *Chemical Papers*, *68*(1), 74–79. https://doi.org/10.2478/s11696-013-0406-9

Wild, P. M., Djilali, N., & Vickers, G. W. (1996). Experimental and computational assessment of windage losses in rotating machinery. *Journal of Fluids Engineering*, *118*(1), 116–122. https://doi.org/10.1115/1.2817488

Xu, F., Zhao, P., Sun, C., He, Y., & Wang, J. (2022). Direct numerical simulation of taylor-couette flow: Regime-dependent role of axial walls. *Chemical Engineering Science*, *263*, 118075. https://doi.org/https://doi.org/10.1016/j.ces.2022.118075

Yamamoto, T., & Ishii, T. (1987). Effect of surface active materials on the drag coefficients and shapes of single large gas bubbles. *Chemical Engineering Science*, *42*(6), 1297–1303. https://doi.org/https://doi.org/10.1016/0009-2509(87)85002-9

Ymawaki, K., Hosoi, H., Takigawa, T., Noui-Mehidi, M. N., & Ohmura, N. (2007). Gas-liquid two-phase flow in a taylor vortex flow reactor. *ICheaP-8: the 8th Italian Conference on Chemical and Process Engineering*, 24–27.

Youngs, D. L. (1984). *An interface tracking method for a 3d eulerian hydrodynamics code* (Report No. 44/92/35). AWRE.

Zanutto, C. P., Evrard, F., van Wachem, B., Denner, F., & Paladino, E. E. (2022). Modeling interfacial mass transfer of highly non-ideal mixtures using an algebraic vof method. *Chemical Engineering Science*, *251*, 117458. https://doi.org/https://doi.org/10.1016/j.ces.2022.117458

Zanutto, C. P., Paladino, E. E., Evrard, F., van Wachem, B., & Denner, F. (2022). Modeling of interfacial mass transfer based on a single-field formulation and an algebraic vof method considering non-isothermal systems and large volume changes. *Chemical Engineering Science*, *247*, 116855. https://doi.org/https://doi.org/10.1016/j.ces.2021.116855

Zenit, R., & Magnaudet, J. (2008). Path instability of rising spheroidal air bubbles: A shape-controlled process. *Physics of Fluids*, *20*(6), 061702. https://doi.org/10.1063/1.2940368

Zhou, Y., Zhao, C., & Bo, H. (2020). Analyses and modified models for bubble shape and drag coefficient covering a wide range of working conditions. *International Journal of Multiphase Flow*, *127*, 103265. https://doi.org/https://doi.org/10.1016/j.ijmultiphaseflow.2020.103265

Publications

Journal articles

- Love, A., Lee, D. S., Gennari, G., Jefferson-Loveday, R., Pickering, S. J., Poliakoff, M., & George, M. (2021). A continuous-flow electrochemical taylor vortex reactor: A laboratory-scale high-throughput flow reactor with enhanced mixing for scalable electrosynthesis. *Organic Process Research & Development*, *25*(7), 1619–1627. https://doi.org/10.1021/acs.oprd.1c00102

- Gennari, G., Jefferson-Loveday, R., & Pickering, S. J. (2022b). A phase-change model for diffusion-driven mass transfer problems in incompressible two-phase flows. *Chemical Engineering Science*, *259*, 117791. https://doi.org/https://doi.org/10.1016/j.ces.2022.117791

Conference presentation

- Gennari, G., Jefferson-Loveday, R., & Pickering, S. J. (2022a). A phase-change model for diffusion-driven mass transfer problems in incompressible two-phase flows. *4th Int. Conference on Numerical Methods in Multiphase Flows, Venice, Italy, 28-30 September*